ABSTRACT

Title of dissertation: GAMMA RAY BURST FOLLOW UP USING GROUND BASED METHODS: INSTRUMENTATION, OBSERVATION AND ANALYSIS

Joseph Durbak
Doctor of Philosophy, 2025

Dissertation directed by: Professor Sylvain Veilleux
Department of Astronomy

Since the 1973 announcement of the initial Vela detection of Gamma-Ray Bursts (GRBs) in 1967, these powerful events have been of significant interest. The study of GRBs has advanced our knowledge of plasma physics, particle physics, cosmology, among many other fields. However, even with the advancement in understanding gained through various detections, both multi-wavelength and multi-messenger, there is still much to be learned by observing these transients in as many different ways as possible. This dissertation will explore the development of instrumentation (RIMAS and PRIME), operational software, data reduction software, and observations aimed at furthering the study of GRBs.

Rapid infrared IMAger Spectrometer (RIMAS) is a near-infrared (NIR) imager spectrometer operating in wavelengths from 0.97 to 2.37 µm, and will be installed on the 4.3 m Lowell Discovery Telescope (LDT) in Happy Jack, Arizona. Among other features, RIMAS has four broad band filters (Y, J, H, K), and three spectral modes (spectral resolving powers, R$\sim$30, 300 and 5000). Completing this instrument required the development, integration and testing of multiple detector readout systems, cryogenic systems, spectral

and imaging modes, communication systems, and cooling systems. Furthermore, software needed to be developed to reduce RIMAS data so that it will be ready to contribute to scientific discoveries shortly after commissioning. Due to the development of this software, observers will quickly obtain high signal-to-noise exposures, astronomically and photometrically calibrated stacked images, and one-dimensional spectra that are flux and wavelength calibrated.

PRime-focus Infrared Microlensing Experiments (PRIME) is a 1.8 m telescope with 1.56 square degree field of view (FOV) (0.5″/pixel) operating in the NIR (0.82-1.78 µm) located in Sutherland, South Africa at the South African Astronomical Observatory (SAAO). The primary science objective for PRIME is to perform a time-domain survey of the Galactic Bulge for the purpose of observing microlensing events caused by transiting exoplanets. In doing so, it will support the Nancy Grace Roman Space Telescope (RST) mission by taking baseline measurements of this field before RST launch, while testing the performance of RST package H4RG-10 detectors. After RST launch, PRIME will perform simultaneous observation with RST of the Galactic Bulge to perform parallax measurements. PRIME is also continuously available for Target of Opportunity (ToO) observations, making it a powerful tool for observing GRB and gravitational wave (GW) counterparts. Since commissioning in October 2022, PRIME has been observing a time domain survey of the Galactic Bulge searching for microlensing events, observing high-energy transients (GRBs, X-ray bursts, GWs, and supernovae), and performing an all-sky survey in J-band. During the course of this thesis work, the development of PRIME's camera greatly mirrors that of RIMAS, with lessons learned shared between them. Most notable in this development is the integration and testing of PRIME's detectors and detector readout system. This is the

first instance of these detectors and electronics being used on-sky, and as such required the development of custom software and thorough testing.

Beyond these instrumentation efforts, photometric and spectroscopic observations were performed in the optical for various GRB afterglows, GRB host galaxies, and GW counterpart candidates using LDT's optical imager, Large Monolithic Imager (LMI), and optical spectrograph, DeVeny. After the commissioning of PRIME, over 40 high-energy transients (GRBs, X-ray Bursts, LIGO/Virgo/KAGRA (LVK) probability fields) were observed with the new telescope. These events were observed as soon as possible after initial detection, and observed over multiple epochs when assessing the evolution of detected counterparts. Further observations were also obtained when sources were not well localized, and further observations could lead to the detection of variable sources. These have resulted in the PRIME detection of the brightest GRB of all time, GRB 221009A, the night after PRIME's first light, and helped determine that this extreme GRB was powered by structured jet. PRIME observations of GRB 230307A helped determine that the progenitor system was a lanthanide rich kilonova despite its long duration. Observations and software developed for LDT during this thesis work searched for and categorized potential optical GW counterparts, analyzed the environments surrounding GRBs, and searched for a supernova associated with GRB 221009A.

GAMMA RAY BURST FOLLOW UP USING GROUND BASED METHODS: INSTRUMENTATION, OBSERVATION AND ANALYSIS

by

Joseph Durbak

Dissertation submitted to the Faculty of the Graduate School of the
University of Maryland, College Park in partial fulfillment
of the requirements for the degree of
Doctor of Philosophy
2025

Advisory Committee:

Professor Sylvain Veilleux, Chair/Advisor
Dr. Alexander Kutyrev, Co-Advisor
Professor Peter Shawhan
Professor Daniel Lathrop
Professor Jordan Goodman
Professor Mario Dagenais, Dean's Representative

© Copyright by
Joseph Durbak
2025

Preface

Portions of Chapters 2, 3, and 4 appear in non-refereed SPIE conference proceedings manuscripts[1, 2, 3], and in a successful *Swift* Guest Investigator proposal[4]. RIMAS's progress has also been presented at meetings of the American Astronomical Society (AAS)[5].

Sometimes, if you pay real close attention to the pebbles you find out about the ocean.

Terry Pratchett, Lords and Ladies

To my wife, whose support and seemingly endless patience got me through this.

Acknowledgments

Completing this dissertation has been a long and fruitful journey, and I am deeply grateful to the many individuals who have supported and guided me along the way. Their contributions, both big and small, have been invaluable in shaping this work.

First and foremost, I would like to express my sincere gratitude to my supervisors, Alexander Kutyrev and Sylvain Veilleux, for their support, insightful feedback, and constant encouragement. Their expertise in astrophysics instrumentation and conducting astronomical experiments were instrumental in shaping my research direction and refining my arguments. I am particularly grateful for their encouragement and support as I tackled ever evolving challenges in finishing these projects.

I would also like to thank my committee members for taking the time to read and critique my work.

I am deeply indebted to NASA Goddard Space Flight Center, University of Maryland Department of Physics, and Department of Astronomy for providing me with the resources and support necessary to conduct this research. I would like to acknowledge the contributions of everyone who worked on these projects with me. Alexander Kutyrev, as PI of both RIMAS and the PRIME camera for having the vision needed to begin and complete these instruments. Greg Mosby for his expertise, guidance, and collaboration in integrating, configuring and testing the detectors for both PRIME and RIMAS. Gennadiy Lotkin for leading the mechanical design of both RIMAS and PRIME. Eric Lyness and Steve Maher for writing much of the software needed to operate RIMAS and PRIME. John Capone, Vicky Toy and everyone else who contributed to RIMAS before I started working on the

project. The rest of the PRIME camera team: Dale Fixsen, Giuseppe Cataldo, Yuki Hirao, Elmer Sharp, Sam Mosley, and James Hayes-Wehle. Jillian Kunze for generating initial spectral calibrations for RIMAS's echelle spectrograph I continue to use. Ethan Zack for his efforts in improving RIMAS's photometry pipeline. Orion Guiffreda for doing the lion's share of the PRIME photometry pipeline development. Nathan Miller for updating and debugging the RIMAS echelle spectroscopy pipeline. Pradip Gatkine, and Simone Dichiara for their collaboration in GRB follow-up studies with the Lowell Discovery Telescope.

I am also grateful to the various grants I have worked under for their generous financial support.

A special thank you to Lowell Observatory, Osaka University, and South African Astronomical Observatory. Their collaboration and support were crucial for completing RIMAS and PRIME, as well as acquiring the observations discussed in this dissertation.

Beyond the academic realm, I would like to express my heartfelt gratitude to my family and friends for their unwavering love, support, and understanding throughout this challenging process. Their encouragement and belief in me kept me going even when I felt overwhelmed. I am particularly grateful to my wife, Leah, for her support and seemingly endless patience.

Finally, I would like to acknowledge the authors and researchers whose work has inspired and informed this dissertation. Their contributions to the field of Gamma Ray Bursts have paved the way for my own research.

While I have made every effort to acknowledge all those who have contributed to this dissertation, any omissions are unintentional. The completion of this work is a testament to the collective support and guidance I have received, and I am truly grateful to everyone

who has been a part of this journey.

Table of Contents

Preface ii

Foreword iii

Dedication iv

Acknowledgements v

Table of Contents viii

List of Tables xii

List of Figures xiii

List of Abbreviations xvi

1 Introduction 1
1.1 Gamma-ray Burst Background . . . 1
1.1.1 History . . . 1
1.1.2 Afterglow Discoveries . . . 4
1.1.3 The "Fireball" Model . . . 6
1.1.4 Afterglow Observations and the "Fireball" Model . . . 8
1.2 Thesis Overview . . . 9

2 RIMAS Instrumentation 12
2.1 Overview . . . 12
2.2 RIMAS project background . . . 14
2.2.1 Science Goals . . . 14
2.2.2 Design . . . 19
2.3 Detector Background . . . 20
2.3.1 Detector Array Description . . . 20
2.3.2 Detector Parameters . . . 25
2.3.2.1 Non-Destructive Reads . . . 25
2.3.2.2 Read Noise . . . 25
2.3.2.3 Dark Current . . . 26
2.3.2.4 Total Noise . . . 26
2.3.2.5 Bias . . . 26

2.3.2.6 Saturation . . . 27
2.3.2.7 Dynamic Range . . . 27
2.3.2.8 Quantum Efficiency . . . 27
2.3.2.9 Persistence . . . 28
2.3.2.10 Conversion Gain . . . 28
2.3.2.11 Linearity . . . 28
2.3.2.12 Hot and Cold Pixels . . . 29
2.4 Integration and Testing . . . 29
2.4.1 Detector Testing . . . 29
2.4.1.1 JDEM H2RG Detectors . . . 30
2.4.1.2 NIRCAM H2RG Detectors . . . 32
2.4.1.3 RST Test Package H4RG Detectors . . . 32
2.4.1.4 Leach Generation II Readout Electronics . . . 44
2.4.1.5 MACIE-ACADIA Readout Electronics . . . 44
2.4.1.6 Harness Testing . . . 45
2.4.2 Echelle Spectrograph Testing . . . 45
2.4.2.1 Lab Spectra Acquisition . . . 48
2.4.2.2 Dispersion . . . 51
2.4.2.3 Reflections and Ghosting . . . 51
2.4.2.4 Resolving Power . . . 53
2.4.2.5 Efficiency . . . 56
2.4.2.6 Slit Quality . . . 57
2.4.3 Low Resolution VPH Spectrograph . . . 60
2.4.4 Moderate Resolution VPH and Prism Spectrograph Testing . . . 61
2.4.5 Imaging . . . 62
2.4.5.1 Point Spread Function . . . 62
2.4.5.2 Focusing Curve . . . 62
2.4.6 Mechanism Testing . . . 64
2.4.6.1 Filter Wheel Mechanisms . . . 64
2.4.6.2 Focus Stage Mechanisms . . . 66
2.4.7 Housekeeping Electronics . . . 69
2.4.7.1 Thermometry . . . 69
2.4.7.2 Pressure . . . 76
2.4.7.3 Communications . . . 78
2.4.7.4 Power Supply . . . 82
2.4.7.5 Mechanical . . . 84
2.4.7.6 Motor Controllers . . . 86
2.4.8 Cryogenics . . . 86
2.4.8.1 Thermal Isolation . . . 89
2.4.8.2 Cryocoolers . . . 92
2.4.9 User Interface . . . 95

3 RIMAS Data Reduction 99
3.1 Overview . . . 99
3.2 Detector Data Reduction . . . 99
3.2.1 Sample Up the Ramp . . . 100
3.2.2 Fowler Sampling . . . 101
3.2.3 Ramp Fitting . . . 103
3.2.4 Reference Pixel Correction . . . 103
3.3 Cross-Dispersed Spectrograph Data Reduction . . . 105
3.3.1 Echelle Quick Reduce Pipeline . . . 105
3.3.2 Echelle Science pipeline . . . 110
3.3.2.1 Pipeline Overview . . . 110
3.3.2.2 Pipeline Algorithm: Preprocessing . . . 111
3.3.2.3 One-Dimensional Spectrum Acquisition . . . 112
3.3.2.4 Telluric Correction . . . 113
3.3.2.5 Flux Calibration . . . 114
3.3.3 RIMAS calibration . . . 114
3.3.3.1 Calibration Data Acquisition and Preprocessing . . . 114
3.3.3.2 One-Dimensional Spectra Generation . . . 116
3.3.3.3 Emission Line Detection . . . 117
3.3.3.4 Atomic Lines List Catalog . . . 119
3.3.3.5 Line Identification . . . 121
3.3.3.6 Wavelength Solution . . . 121
3.3.4 Science Pipeline Testing . . . 123
3.3.4.1 RIMAS H2RG Lab Spectra . . . 126
3.3.4.2 Echelle++ Simulated Spectra . . . 126
3.3.4.3 RIMAS H4RG Lab Spectra . . . 127
3.3.4.4 DeVeny NIR Data . . . 127
3.4 Imaging Data Reduction . . . 128

4 PRIME Instrumentation 131
4.1 Overview . . . 132
4.1.1 Observatory Overview . . . 132
4.1.2 Instrument Overview . . . 133
4.1.3 Commissioning and Servicing . . . 137
4.2 Camera Design . . . 138
4.2.1 Cryogenic Assembly . . . 140
4.2.2 Electronics Assembly . . . 141
4.2.2.1 Thermometry . . . 141
4.2.2.2 Communications . . . 141
4.2.2.3 PRIME Power Distribution . . . 142
4.2.2.4 Motor Controllers . . . 144
4.3 Detectors . . . 144
4.3.1 Detector Readout System . . . 144
4.3.2 Detector readout software . . . 148
4.3.3 Detector Characterization . . . 149

4.4 Data Reduction . . . 150
4.4.1 PRIME Ramp Reduction . . . 153
4.4.2 PRIME Photometry Pipeline . . . 153
4.5 Performance . . . 154
4.6 Current Observations . . . 156
4.6.1 Observing Strategy . . . 156
4.6.2 All Sky Coverage . . . 159
4.6.3 Observation Software . . . 160
4.7 PRIME Transient Follow-Up . . . 161

5 Final Considerations 166
5.1 Summary . . . 166
5.2 Future Work . . . 169
5.2.1 RIMAS . . . 169
5.2.2 PRIME . . . 170

A Gamma Ray Burst and Gravitational Wave Follow Up with the Lowell Discovery Telescope 172
A.1 Instruments . . . 172
A.2 GRB Follow-Up Efforts . . . 173
A.2.1 GRB observations . . . 173
A.3 GW Follow-Up Efforts . . . 174
A.3.1 LDT GW observations . . . 175

B RIMAS Lab Data 177
B.1 Various Lab Spectra . . . 177
B.1.1 Echelle Spectra . . . 177
B.1.1.1 Reduced Echelle Lamp Spectra . . . 177
B.1.1.2 Additional Echelle Lamp Spectra . . . 197
B.1.2 Low Resolution VPH Spectra . . . 197
B.1.2.1 R≈30 Spectra . . . 197
B.1.2.2 R≈300 Spectra . . . 197

List of Tables

2.1 Detector Packages Summary 30
2.2 H2RG Characterization 31
2.3 Resolving power 56

3.1 Alignment parameters 106
3.2 Wavelength Solution Error 123

4.1 Specifications for both the telescope and camera 133
4.2 Single Detector CDS Noise Test 150
4.3 Single Detector Dark Current Test 153
4.4 PRIME Transient Follow Up 163

A.1 LDT GRB Follow-Up 174
A.2 LDT GW Follow-Up 176

List of Figures

1.1 BATSE GRBs . . . 3
1.2 BATSE T_{90} . . . 3
1.3 Gamma-ray Burst Mechanism . . . 8

2.1 Lowell Discovery Telescope . . . 14
2.2 GRB afterglows used a line-of-sight probe . . . 16
2.3 High Redshift GRBs . . . 18
2.4 LDT Cube Model with RIMAS Mounted . . . 21
2.5 RIMAS Model optical path . . . 22
2.6 RIMAS optical layout . . . 23
2.7 RIMAS aperture, filter and grating wheels . . . 24
2.8 CDS Noise: YJ Detector . . . 38
2.9 CDS Noise: HK Detector . . . 39
2.10 Dark Current: YJ Detector . . . 40
2.11 Dark Current: HK Detector . . . 41
2.12 Total Noise: YJ Detector . . . 42
2.13 Total Noise: HK Detector . . . 43
2.14 Echelle Spectrograph Diagram . . . 46
2.15 Grism Diagram . . . 47
2.16 Grism Assembly . . . 48
2.17 Continuous Source Spectrum . . . 50
2.18 Solar Spectrum Test Setup . . . 52
2.19 YJ echelle spectrograph ghosting . . . 54
2.20 HK echelle spectrograph ghosting . . . 55
2.21 Resolving power . . . 56
2.22 Blackbody Source Echelle Spectrum . . . 58
2.23 UV Fused Silica . . . 59
2.24 Slit Quality . . . 59
2.25 Low Resolution Spectra . . . 60
2.26 Medium Resolution Spectra . . . 61
2.27 Focusing . . . 63
2.28 Filter Wheel Mechanism . . . 67
2.29 Focus Stage . . . 70

2.30 RIMAS Temperature Measurement and Control . . . 72
2.31 RIMAS PID Controlled Detector Temperatures . . . 74
2.32 RIMAS Dewar Internal Temperatures . . . 75
2.33 Pyboard Humidity and Temperature Monitor . . . 77
2.34 Vacuum Gauges . . . 79
2.35 RIMAS Communications Diagram . . . 81
2.36 RIMAS Alternate Communications Diagram . . . 82
2.37 Rack Mount Communications Module . . . 83
2.38 Power Distribution Unit . . . 85
2.39 Electronics Rack . . . 87
2.40 Chilled Water Plumbing . . . 88
2.41 Chilled Water Plumbing . . . 91
2.42 Cryocoolers . . . 94
2.43 GCN Diagram . . . 96
2.44 GCN Alert VI . . . 98

3.1 Sample Up The Ramp . . . 100
3.2 Fowler Sampling . . . 102
3.3 Raw Frames with Reference Pixels and Voltages . . . 104
3.4 Wavelength maps . . . 106
3.5 Echelle lab spectrum compared with model . . . 107
3.6 Quick reduced lab spectra . . . 108
3.7 Quick Reduced Spectrum . . . 109
3.8 Wavelength calibration flowchart . . . 115
3.9 Echelle order maps . . . 117
3.10 Calibration 1D spectra by order . . . 118
3.11 Gaussian fit peaks . . . 120
3.12 Calibration line matching . . . 122
3.13 Calibration residuals . . . 124
3.14 Calibration residuals . . . 125
3.15 Photometry Pipeline Flowchart . . . 130

4.1 PRIME observatory . . . 134
4.2 PRIME camera . . . 135
4.3 PRIME cold assembly . . . 136
4.4 PRIME filters . . . 136
4.5 Early PRIME observations . . . 138
4.6 PRIME Block Diagram . . . 139
4.7 PRIME Communications Diagram . . . 143
4.8 PRIME Power Distribution . . . 145
4.9 PRIME Detector Readout Assembly . . . 147
4.10 PRIME CDS Noise . . . 151
4.11 PRIME Dark Current . . . 152
4.12 PRIME photometry pipeline . . . 155
4.13 Photometric Fit of Cross-matched sources . . . 157

4.14 PRIME J-band detected sources histogram . . . 157
4.15 PRIME J-band limiting magnitude . . . 158
4.16 PRIME Observation Grids . . . 159
4.17 PRIME J-band Survey Coverage . . . 160
4.18 S240422ed Tiling . . . 162

B.1 HgAr Lamp Echelle YJ Echelle Spectrum . . . 178
B.2 Labeled HgAr Lamp Echelle YJ Echelle Spectrum . . . 179
B.3 Ar Lamp Echelle YJ Echelle Spectrum . . . 180
B.4 Labeled Ar Lamp Echelle YJ Echelle Spectrum . . . 181
B.5 Kr Lamp Echelle YJ Echelle Spectrum . . . 182
B.6 Labeled Kr Lamp Echelle YJ Echelle Spectrum . . . 183
B.7 Xe Lamp Echelle YJ Echelle Spectrum . . . 184
B.8 Labeled Xe Lamp Echelle YJ Echelle Spectrum . . . 185
B.9 HgAr Lamp Echelle HK Echelle Spectrum . . . 186
B.10 Labeled HgAr Lamp Echelle HK Echelle Spectrum . . . 187
B.11 Ar Lamp Echelle HK Echelle Spectrum . . . 188
B.12 Labeled Ar Lamp Echelle HK Echelle Spectrum . . . 189
B.13 Kr Lamp Echelle HK Echelle Spectrum . . . 190
B.14 Labeled Kr Lamp Echelle HK Echelle Spectrum . . . 191
B.15 Xe Lamp Echelle HK Echelle Spectrum . . . 192
B.16 Labeled Xe Lamp Echelle HK Echelle Spectrum . . . 193
B.17 Cross Dispersed Spectra with 80 µm slit . . . 194
B.18 Cross Dispersed Spectra with 130 µm slit . . . 195
B.19 Cross Dispersed Spectra with 250 µm slit . . . 196
B.20 R≈30 VPH Spectra with 80 µm slit . . . 198
B.21 R≈30 VPH Spectra with 130 µm slit . . . 199
B.22 R≈30 VPH Spectra with 250 µm slit . . . 200
B.23 R≈30 VPH Spectra with long slit . . . 201
B.24 R≈300 VPH Spectra with 80 µm slit . . . 202
B.25 R≈300 VPH Spectra with 130 µm slit . . . 203
B.26 R≈300 VPH Spectra with 250 µm slit . . . 204
B.27 R≈300 VPH Spectra with long slit . . . 205

List of Abbreviations

AAS	American Astronomical Society
AAVSO	American Association of Variable Star Observers
ACADIA	ASIC for Control And Digitization of Imagers for Astronomy
ADC	Analog to Digital Converter
ADU	Analog Digital Unit
APASS	AAVSO Photometric All-Sky Survey
ARC	Astronomical Research Camera
ASIC	Application Specific Integrated Circuit
ATel	Astronomer's Telegram
BAT	Burst Alert Telescope
BATSE	Burst and Transient Source Experiment
BETTI	Balloon Experimental Twin Telescopes for Infrared Interferometry
CBM	Circumburst Medium
CCD	Charge Coupled Devices
CDS	Correlated Double Sampling
CGM	Circumgalactic Medium
CGRO	Compton Gamma Ray Observatory
CLI	Command Line Interface
CMB	Cosmic Microwave Background
COTS	Commercial Off-The-Shelf
DCT	Discovery Channel Telescope
DCL	Detector Characterization Laboratory
DOF	Degrees of Freedom
EP	Einstein Probe
FOV	Field Of View
FPGA	Field Programmable Gate Array
FWHM	Full Width at Half Maximum
GB	Galactic Bulge
GBM	Gamma-ray Burst Monitor
GCN	General Coordinates Network
GRB	Gamma-Ray Burst
GRBM	Gamma-Ray Burst Monitor
GUI	Graphical User Interface

GW	Gravitational Wave
HAWAII	HgCdTe Astronomy Wide Area Infrared Imager
HK	H and K optical arm
HTML	HyperText Markup Language
HxRG	HAWAII xk x xk Readout with Reference Pixels and Guide mode
I2C	Inter-Integrated Circuit
IDL	Interactive Data Language
IGM	Intergalactic Medium
IGRINS	Immersion GRating INfrared Spectrometer
IIR	Imaging infrared
IR	Infrared
JAXA	Japan Aerospace Exploration Agency
JDEM	Joint Dark Energy Mission
JWST	James Webb Space Telescope
KAGRA	Kamioka Gravitational Wave Detector
KMTNet	Korea Microlensing Telescope Network
LAN	Local Area Network
LDT	Lowell Discovery Telescope
LED	Light Emitting Diode
LIGO	Laser Interferometer Gravitational-Wave Observatory
LVK	LIGO/Virgo/KAGRA
MACIE	Multi-purpose ASIC Control and Interface Electronics
MOA	Microlensing Observations in Astrophysics
NASA	National Aeronautics and Space Administration
NC	Normally Closed
NIR	Near Infrared
NIRCam	Near Infrared Camera
NIST	National Institute of Standards and Technology
NO	Normally Open
OGLE	Optical Gravitational Lensing Experiment

Pan-STARRS	Panoramic Survey Telescope and Rapid Response System
PCB	Printed Circuit Board
PDU	Power Distribution Unit
PID	Proportional Integral Derivative
PnP	Plug and Play
PRIME	PRime-focus Infrared Microlensing Experiments
QE	Quantum Efficiency
QSO	Quasi-Stellar Object or Quasar
RATIR	Reionization and Transients Infrared/Optical
RIMAS	Rapid infrared IMAger Spectrometer
ROIC	Readout Integrated Circuit
RST	Nancy Grace Roman Space Telescope
SAAO	South African Astronomical Observatory
SDSS	Sloan Digital Sky Survey
SIRC	Simple Improved Reference Pixel Correction
SNe	Supernovae
SNR	Signal-to-Noise-Ratio
SUTR	Sample Up The Ramp
TCP	Transmission Control Protocol
USB	Universal Serial Bus
USNO	US Naval Observatory
UVOT	Ultra-Violet Optical Telescope
VI	Virtual Instrument
VOEvent	Virtual Observatory Event
VPH	Volume Phase Holographic
WFIRST	Wide-Field Infrared Survey Telescope
XML	eXtensible Markup Language
XRT	X-Ray Telescope
YJ	Y and J optical arm

Chapter 1: Introduction

1.1 Gamma-ray Burst Background

Gamma-ray Bursts (GRBs) are defined by how they are observed; they are brief γ-ray events (a few to tens of seconds) that are many magnitudes brighter than the background γ-ray sky outshining even the sun. GRBs occur daily, and have an electromagnetic (EM) output in a few seconds comparable to the Sun's output over the order of 10^{10} years. Studying GRBs gives an insight into physics occurring at much higher energies than can be observed in laboratories on Earth. Furthermore, the brightness of these events makes them observable at high redshifts outshining quasars and galaxies. This makes them useful as line-of-sight probes into the early universe.

1.1.1 History

The first three pairs of Vela satellites were launched in 1963 to monitor the Earth for nuclear weapons testing that would violate the Nuclear Test Ban Treaty.[6] These satellites first detected a strong γ-ray signal in 1967.[7] In 1973, Klebesadel et al. informed the community of this detection along with their determination, through triangulation, that these γ-rays were not from nuclear weapons testing on Earth, but were in fact cosmic in origin.[7]

Due to the difficulty in locating γ-rays, follow-up observations by other instruments were not able to be performed during this period.

Nearly 25 years after the initial discovery announcement, in 1991, the Compton Gamma Ray Observatory (CGRO) was launched. The Burst and Transient Source Experiment (BATSE) instrument on the CGRO showed that these GRBs are isotropically distributed [8], and therefore are not limited to the Milky Way. This is well demonstrated in the plot shown in Figure 1.1. During the 9-year lifespan of CGRO, over 2700 GRBs were observed giving a rate of $\approx$1 per day.[9] Observing the light curves for this population by the T_{90} values (the time over which the burst emits 5% to 95% of its counts), showed (Figure 1.2) that there were two distinct populations of GRBs with T_{90} durations: less than 2 s, and greater than 2 s.[10] These populations are referred to as short GRBs (sGRBs), and long GRBs (lGRBs) respectively. Furthermore, using BATSE light curves, the Band function was empirically derived, which showed the GRB spectrum could be fit by joining two power laws.[11]

Later, *BeppoSAX* was the first satellite to detect GRBs in X-rays [12] using its Wide-Field Camera to observe the fading X-ray counterpart to the Gamma-Ray Burst Monitor (GRBM), and thus have much better localization of a few arcminutes. This improved localization led to the first observations of an afterglow a few hours later via optical telescopes.[12, 13]

In 2004, *Swift* observatory launched [14], with the Burst Alert Telescope (BAT), X-Ray Telescope (XRT) and Ultraviolet/Optical Telescope (UVOT). BAT is capable of localizing detected bursts within $\approx 3'$ [14], and then autonomously slews the XRT and UVOT common boresight towards the detected source and can localize a detected X-ray coun-

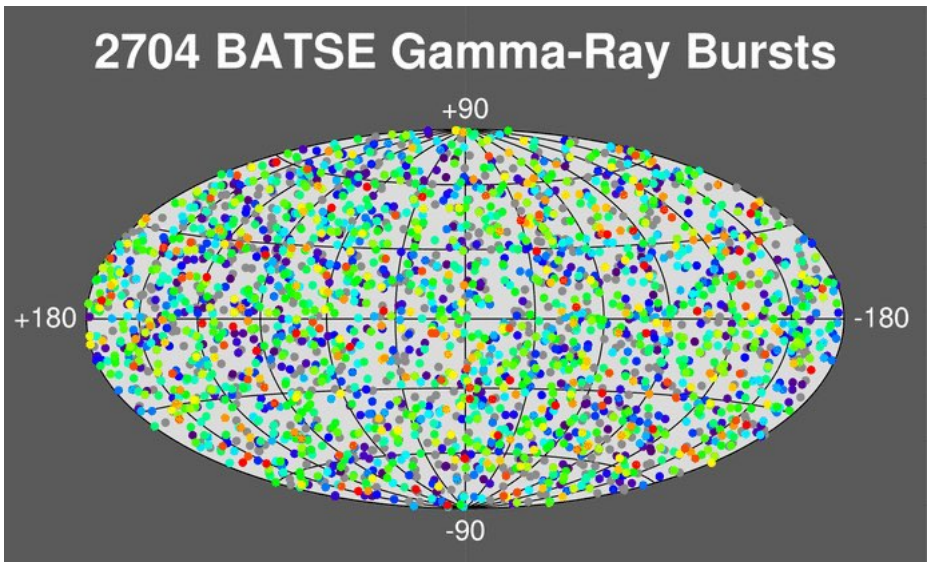


Figure 1.1: GRBs detected by the BATSE instrument during the CGRO 9 year mission projected in Galactic Coordinates. As can be seen here, there is no increased density of GRBs located in the Milky Way's galactic plane. Image sourced from `https://gammaray.nsstc.nasa.gov/batse/grb/skymap/images/fig2_2704.pdf`.

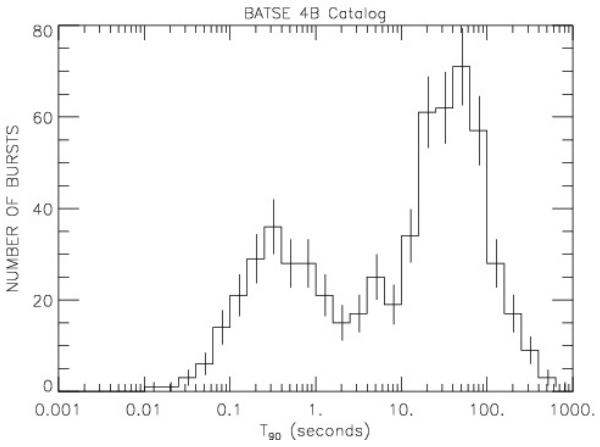


Figure 1.2: Histogram of the measured T_{90} values of GRBs observed by BATSE. As can be seen here, there are 2 distinct populations below and above 2 s. Image sourced from `https://gammaray.nsstc.nasa.gov/batse/grb/duration/images/4b_t90.gif`.

terpart within ≈3″ [15] using XRT and to sub arcseconds with UVOT [16] for a detected UV/optical counterpart[1]. *Swift* observes ≈100 GRBs per year [17], and quickly providing their locations has allowed the community to quickly and effectively perform follow-up observations. This has allowed the community to study both GRBs and their host galaxies throughout the electromagnetic spectrum. These multi-wavelength observations have led to important breakthroughs in understanding GRBs, such as measuring the redshifts, detecting that lGRBs can be produced by extreme Type Ic SNe [18], and showing the cooling of the afterglow is achromatic [19].

The final observational breakthrough covered here is the first high-significance EM and gravitational wave (GW) multi-messenger observation of a sGRB by *Swift*, Fermi, INTEGRAL and other EM instruments alongside LIGO, GRB/GW 170817. This multi-messenger observation conclusively showed the origin of sGRBs to be from binary neutron star mergers.[20] This discovery has led to great interest in studying short GRBs as the physics of these events can be explored using EM and GW observations.

1.1.2 Afterglow Discoveries

Prompt to late afterglow observations are needed to gain detailed understanding of GRBs, including the high energy physics taking place, and the local environments of these events. As discussed earlier in this chapter, thanks to improved localization of GRBs starting with *BeppoSAX* detection of the X-ray afterglow from the GRB detected by BATSE, and continued with projects like *Swift*, many of the recent GRB discoveries have come from studying the afterglow. The *BeppoSAX* afterglow X-ray detection's improved localization

[1] X-ray and UV/optical counterparts are not always detectable

of GRB 970228 [21] led to the first detection of a GRB's optical counterpart [12], and the first measurement of a GRB's redshift, z=0.695,using the Keck telescopes [22]. Another big step forward was accomplished when the extremely bright GRB 030329 was detected by the High Energy Transient Explorer satellite (HETE), which managed to report its $2'$ localization within 73 minutes of initial detection. This quick localization and reporting led to the detection of the counterpart in the optical and radio [18]. Multi-wavelength coverage of this GRB's afterglow led to measurement of the redshift, z=0.1685, the detection of an associated supernova, and the establishment that lGRBs can be produced by extreme Type Ic SNe. Hubble Space Telescope (HST) observations of the error box regions for lGRBs show that they occur in UV-bright star-forming regions of host galaxies, which suggests that lGRBs are associated with extremely massive stars and are restricted to galaxies with very little chemical evolution.[23]

The launch of *Swift* has led to a number of multi-wavelength GRB discoveries. The rapid reporting of detections and localizations from *Swift* has allowed the community to make numerous discoveries. This includes the first precise localization and redshift measurements of sGRBs [24], the identification of the highest redshift GRB [25] ($z = 9.4$), a population of low-luminosity GRBs associated with SNe [26, 27], and detailed multi-wavelength light curves (e.g. [28]).

A key attribute of GRBs measured through follow-up observations of afterglows is their redshift. GRBs with measured redshifts span $0.0085 \leq z \leq 9.4$ with mean redshift $\bar{z} \sim 2.5$ as helpfully collated by Greiner.[2] This range and mean is heavily susceptible to selection bias, instrumental and astrophysical, as outlined by Coward et al. [29]. Among

[2] `https://www.mpe.mpg.de/~jcg/grbgen.html`

other instrument selection biases (position in the sky, GRB localization, galactic extinction, and source angular distance from the Sun), there is bias towards afterglows that can be observed in the optical, whereas some of the highest redshifts of GRBs (GRB 090423 and GRB 090429B) have been measured by NIR instruments despite no optical counterpart detection by UVOT. This optical bias extends specifically into redshift-dependent selection effects involving: Malmquist bias, redshift desert, and host galaxy extinction. Malmquist bias arises from telescope and instrument sensitivity, which are favored to observe GRB afterglows with bright luminosity functions. The redshift desert extends from $1.3 < z < 3$ where it is more difficult to observe absorption and emission spectra in the optical. Within the redshift desert, the main rest-frame optical features from host galaxies (e.g. the [O III] λ3727 line, Hα, and Hβ) become more difficult to detect as they move to the IR. Finally, there are GRBs whose afterglows are likely obscured by host galaxy extinction. [30, 31, 32, 33] These "dark burst" afterglows are measured in the NIR, and occur in high redshift galaxies with evidence of dust extinction.

1.1.3 The "Fireball" Model

The dominant model used for interpreting GRB observations has been the jet-like fireball shock model for decades [34]. While initial theories for GRBs assumed spherical symmetry, this model did not provide the required efficiency to generate the powerful events that have been observed. The "fireball" in this context is "an optically thick plasma whose temperature exceeds the electron rest mass and which can produce $e^{\pm}$ pairs and photons in equilibrium with a baryonic plasma."[35] The fireball model for GRBs involves a compact in-

ner engine where injected γ-rays are trapped by electron-positron pair production.[36] This fireball then expands as it cools, causing acceleration of the baryons within this region. As the plasma becomes optically thin, the baryonic matter interacts with the external medium creating shocks that reconvert the expansion kinetic energy into radiative energy.[37, 38]

In this model (represented in Figure 1.3), the expansion occurs in multiple shells with different Lorentz factors, and the internal shocks between these shells create high energy γ-rays via either synchrotron emission or inverse-Compton up-scattering.[36] This first part would be observed as prompt emission of γ-rays and X-rays.[39] The relativistic jet would then experience an external shock when interacting with the surrounding ambient medium, causing a longer lived afterglow emission across the EM spectrum.[37]

The central engine for a collimated ultra-relativistic structured jet requires a very large amount of angular momentum. This requires a rapidly spinning compact source, likely an accreting black hole [40, 41, 42], but possibly a rapidly spinning neutron star [43]. The existence of the two populations of GRBs based on T_{90} shown in Figure 1.2, suggests the existence of two different progenitors for sGRBs and lGRBs. The leading progenitor for sGRBs are two merging compact objects including at least one neutron star.[44] This was long suspected to be the case for this population [17], and was confirmed with the near simultaneous detection of GW 170817 in which a NS-NS merger was detected by LIGO, and short GRB 170817A was detected by Fermi and INTEGRAL.[20, 45] The kilonova and afterglow associated with this GW event were then detected by *Swift*, and other EM instruments.[20, 45] Long GRBs are typically associated with the extreme core-collapse supernova of a massive star (hypernova), which was determined through measurements discussed in § 1.1.2. These are not strict associations, as demonstrated by GRB 230307A,

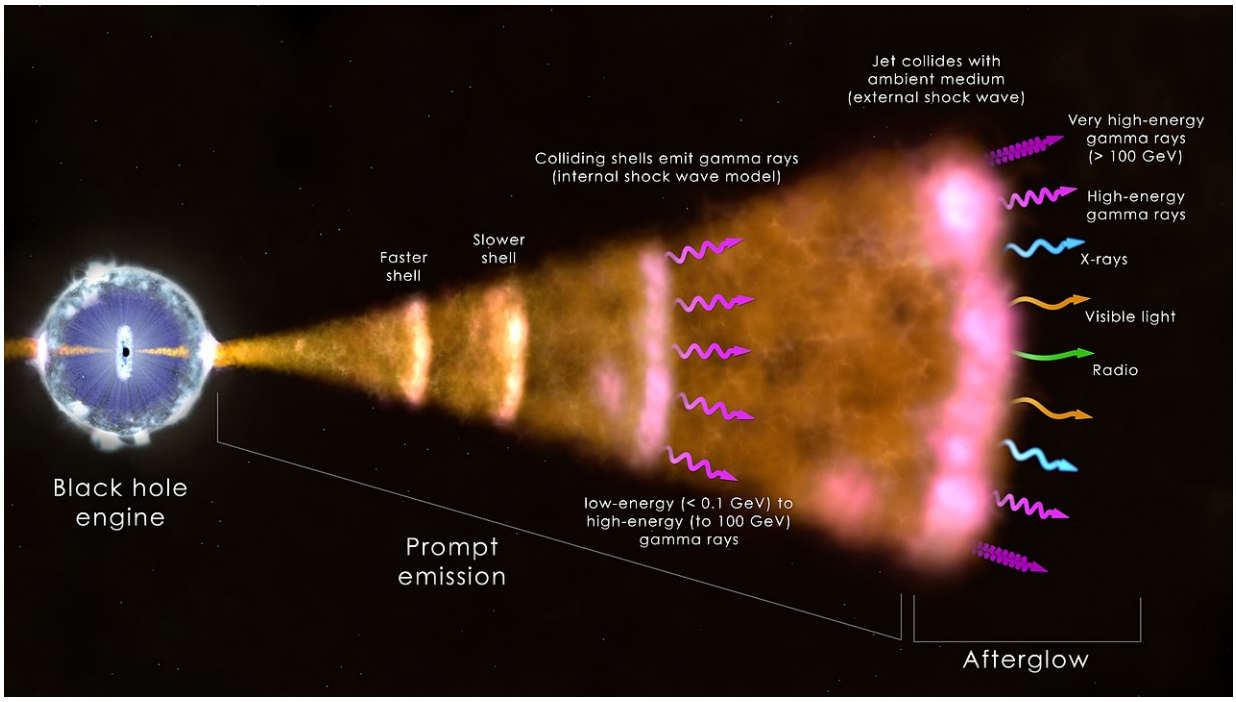


Figure 1.3: Depiction of the fireball model for GRBs. In this image it shows black hole acting as a compact engine powering a jet of ultra-relativistic particles that is released in several shells. This then shows how collisions between these shells can create internal shocks, causing fluctuations in the released photons. It also shows external shocks created when the jet collides with the external ambient medium, which then creates the afterglow. Image Credit: By NASA/Goddard Space Flight Center/ICRAR. - `https://en.es-static.us/upl/2019/11/gamma-ray-burst-mechanism-lg.jpg`

for which the optical/IR counterpart was classified as a lanthanide-rich kilonova despite its long duration.[46]

1.1.4 Afterglow Observations and the "Fireball" Model

As discussed above, the fireball model has been a key framework in understanding GRBs. Each of its components have mechanisms that need to be verified, and quantified with observation. Afterglows provide powerful insight into these mechanisms. Depending on the jet collimation angle, the jet-break time can be observed in the optical/IR, as

accomplished for the brightest GRB of all time, GRB 221009A [47]. Also, the rise and peak of the GRB afterglow are observable in the optical/IR, whereas the rise and peak of the X-ray afterglow are obscured by the tail of the higher energy γ-ray prompt emission. As discussed above, lower energy photons are assumed to be from the reverse shock, thus the optical/IR afterglow is assumed to correspond to the decelerating radius of the expanding fireball. The fireball Lorentz factor at the time of the peak afterglow, t_d, is half the initial Lorentz factor, Γ_0.[48] Using this method for inferring the deceleration radius, the radii of both GRB 060418 and GRB 060607A is $\approx 10^{17}$ cm, and the initial Lorentz factor is $\Gamma_0 \sim 400$, thus confirming the highly relativistic nature of these fireballs.[49] With this Lorentz factor calculation, the total isotropic energy of the burst, E_{iso} can also be derived [50], along with a correlation between isotropic luminosity, peak energy emission, and Γ_0 [51]. It is worth noting that E_{iso} is a standard quantity that is calculated assuming that the observed energy is isotropic, but this is not a statement of the actual emitted energy or that the energy is really emitted isotropically.

1.2 Thesis Overview

This thesis focuses on the development of instrumentation, software, and observations with the aim of studying GRB counterparts in the NIR. The instrumentation effort has been quite successful as PRIME is already on-sky observing transients, and RIMAS has been accepted by Lowell Observatory pending a few minor adjustments. Each of the data reduction pipelines for these instruments have been completed, and the imaging data reduction software is already in use.

Chapter 2 – RIMAS Instrumentation Most of this thesis work is concentrated on developing, testing and characterizing RIMAS so that it can be deployed to LDT and used to study transients. RIMAS is an imager spectrometer operating in the NIR (0.97-2.37 µm), and is designed specifically to follow-up detections made by *Swift*. Using its simultaneous multi-band observations, it can quickly identify and classify objects in imaging mode, and then can quickly switch to one of its spectral modes to gain further valuable information about transients. This chapter discusses the effort to get RIMAS to the point where it will be mounted to the telescope and acquiring observations as accomplished through the development and testing of detector systems, imaging and spectral modes, cryogenics, cryogenic mechanisms, and housekeeping electronics. Furthermore, each of these items needed to be fully characterized in order to understand the quality of data expected from RIMAS, and ensure reliability of the instrument. Through these efforts, RIMAS has become a much more sensitive and reliable instrument that will be installed on LDT within the next few months.

Chapter 3 – RIMAS Data Reduction A key component of preparing RIMAS to be immediately useful after commissioning is the development of data reduction software prior to deployment. RIMAS required development of three types of data reduction software: detector data reduction, spectral data reduction, and photometry data reduction. The detector data reduction software is key to creating single images from sample-up-the-ramp (SUTR) frames with the lowest possible noise levels. This reduction is done by integrating tools and methods developed for Nancy Grace Roman Space Telescope and James Webb Space Telescope (JWST) that use multiple techniques to remove correlated noise, and artifacts from cosmic rays. This software is well integrated into the data acquisition software,

making its use seamless for observers. Spectral data reduction creates both wavelength and flux calibrated spectra from the initial images taken of these spectra. The spectral data reduction was based off of code already developed for IGRINS [52], another ground based NIR cross-dispersed spectrograph. Adapting this for RIMAS involved precise calibration of the echelle spectrograph, and heavy edits to the overall code. Photometry data reduction software calibrates each set of exposures for flux and astrometry. RIMAS's pipeline was developed in Vicki Toy's thesis work [53], but was heavily updated during the course of this thesis as well.

Chapter 4 – PRIME Instrumentation This chapter discusses the development, testing, commissioning, and operation of the camera for the PRIME telescope. PRIME is a 1.8 m telescope with 1.56 square degree FOV (0.5″/pixel) operating in the NIR (0.82-1.78 µm) located in Sutherland, South Africa at the South African Astronomical Observatory (SAAO).[3, 54, 55] After a couple of years of development, the PRIME camera was commissioned in October 2022. Since then PRIME has been carrying out a time domain survey of the Galactic Bulge searching for microlensing events, following up high energy transients (GRBs, X-ray bursts, gravitational waves, and supernovae), and performing an all-sky survey in J-band. The instrumentation and software efforts described in this chapter greatly overlap with RIMAS instrumentation efforts as they were developed in parallel. There were a lot of lessons learned from each project that were able to inform the other. This overlap has led to the development of two robust instruments.

Chapter 5 – Final Considerations This chapter summarizes the goals and efforts made in this thesis. It also discusses future work that should be done so that the primary projects, RIMAS and PRIME, can reach their full potential in studying GRBs.

Chapter 2: RIMAS Instrumentation

2.1 Overview

Rapid infrared IMAger Spectrometer (RIMAS) is a flexible tool for a variety of imaging and spectroscopic studies that require fast reaction ($\Delta t \lessapprox 3$ min) in the near infrared (NIR), such as GRB afterglows.[56, 57] It will acquire these observations using the Lowell Discovery Telescope (LDT)2.1, a 4.3 m telescope operated by Lowell Observatory in Happy Jack, Arizona. RIMAS is a fully cryogenic instrument and operates simultaneously along two optical arms: one covering H and K bands (HK) and the other covering Y and J bands (YJ). RIMAS is designed for photometry, low resolution spectroscopy (spectral resolving power, R$\sim$30 and 300), and moderate resolution spectroscopy (R$\sim$5000). Where spectral resolving power, R, is a measurement of the ability of a spectrograph to resolve features in an observed spectrum, and is defined in Eq. 2.1 where λ is the wavelength and $\Delta\lambda$ is the smallest difference in wavelengths that can be resolved. It accomplishes this using a continuously running Stirling cryocooler, a dichroic mirror, Y, J, H and K broadband filters, two Volume Phase Holographic (VPH) gratings, ZnSe grisms with cross dispersers, and HgCdTe Astronomy Wide Area Infrared Imager (HAWAII) 4k x 4k Readout with Reference Pixels and Guide mode (H4RG) detectors, shown in Figure 2.6. RIMAS is a flexible tool with both imaging and spectral modes available. Commissioning of this instrument is

scheduled to begin during the first half of 2025.

$$R = \frac{\lambda}{\Delta\lambda} \tag{2.1}$$

Throughout the course of working on this thesis, much has been done to complete this instrument. This has involved replacing RIMAS's previous science detectors, readout electronics, cryocoolers, vacuum gauge, temperature monitor and controllers, communications equipment, cryogenic mechanisms, cold plate, and optical bench based on testing and desired improvements. Various upgrades were also made during RIMAS's development, the baffling was enhanced to improve background, the R$\sim$300 spectral mode was added, insulation was improved, the electronics mounting was completed, and the water cooling system was added. Discoveries during integration also necessitated the replacement of the cold plate and optical bench. During all of these replacements, upgrades, developments and repairs, the entire system was characterized, tested, and brought to the point of being ready for deployment at LDT. This involved measuring detector properties, characterizing the dispersion from the spectrographs, analyzing the image quality, measuring the thermal regimes, and measuring filter backgrounds. Although there are always more improvements that can be done, RIMAS has become ready for deployment during the course of this thesis work.



Figure 2.1: Photographs of the LDT observatory and telescope, and a map showing LDT's location in Happy Jack, Arizona outside of Flagstaff, Arizona.

2.2 RIMAS project background

2.2.1 Science Goals

RIMAS is designed specifically to identify and study high-redshift GRBs detected by *Swift*.[56, 57] RIMAS's NIR multicolor imaging [58] and spectroscopy modes make it well suited to this task. The imaging mode has a field of view (FOV) of 3′x3′, which is well suited to *Swift* BAT localizations (error diameter 1′ to 5′ [59]). This allows for RIMAS follow-up observations before *Swift* XRT localization, 5″ diameter, is available. If the detected GRB afterglows are bright enough, RIMAS can quickly (tens of seconds) switch to one of its spectroscopy modes. With spectral resolving power options across three different orders of magnitude, RIMAS is well suited to maximizing the data that can be acquired from any

individual event.

Rapid follow-up using multiple observation methods is crucial for identifying a new transient and promoting additional follow-up from other instruments within the General Coordinates Network (GCN). GRB afterglows can be quickly identified via multicolor photometry and spectroscopy. Furthermore, spectroscopy can identify the redshift of an object and help illuminate the type of transient being observed. This is especially helpful when following up potential electromagnetic counterparts of LIGO/Virgo/KAGRA (LVK) events, in order to determine whether the observed distance is within the LVK's detected distance range, and easily rule out other transients such as supernovae (SNe).

A good case study of interesting science that can be achieved with RIMAS can be found in our successful *Swift* cycle 20 proposal.[4] In this proposal, we outline how RIMAS spectra of high redshift GRB afterglows can be used as line-of-sight probes (Figure 2.2) to study the intergalactic medium (IGM) at high redshifts ($z \gtrsim 7$), which will be used to study the epoch of reionization through measurements of the neutral hydrogen fraction. Understanding both the precise time history and the sources responsible for cosmic reionization remains one of the most sought-after goals of modern cosmology. The discovery of Gunn-Peterson troughs, spectral absorption due to neutral hydrogen, in the spectra of $z \gtrsim 6$ quasars (QSOs [60]) implied at least a modest neutral hydrogen fraction ($x_{\rm HI}$) at this time. However, observations of the cosmic microwave background (CMB [61]) indicate a significantly larger characteristic reionization redshift ($z_{\rm reion} \approx 10$). It may be possible to reconcile these two seemingly contradictory observations if reionization were to occur slowly with a large degree of small-scale variation. Many more sightlines are needed to test this hypothesis, something not possible for QSOs with current instrumentation.[4]

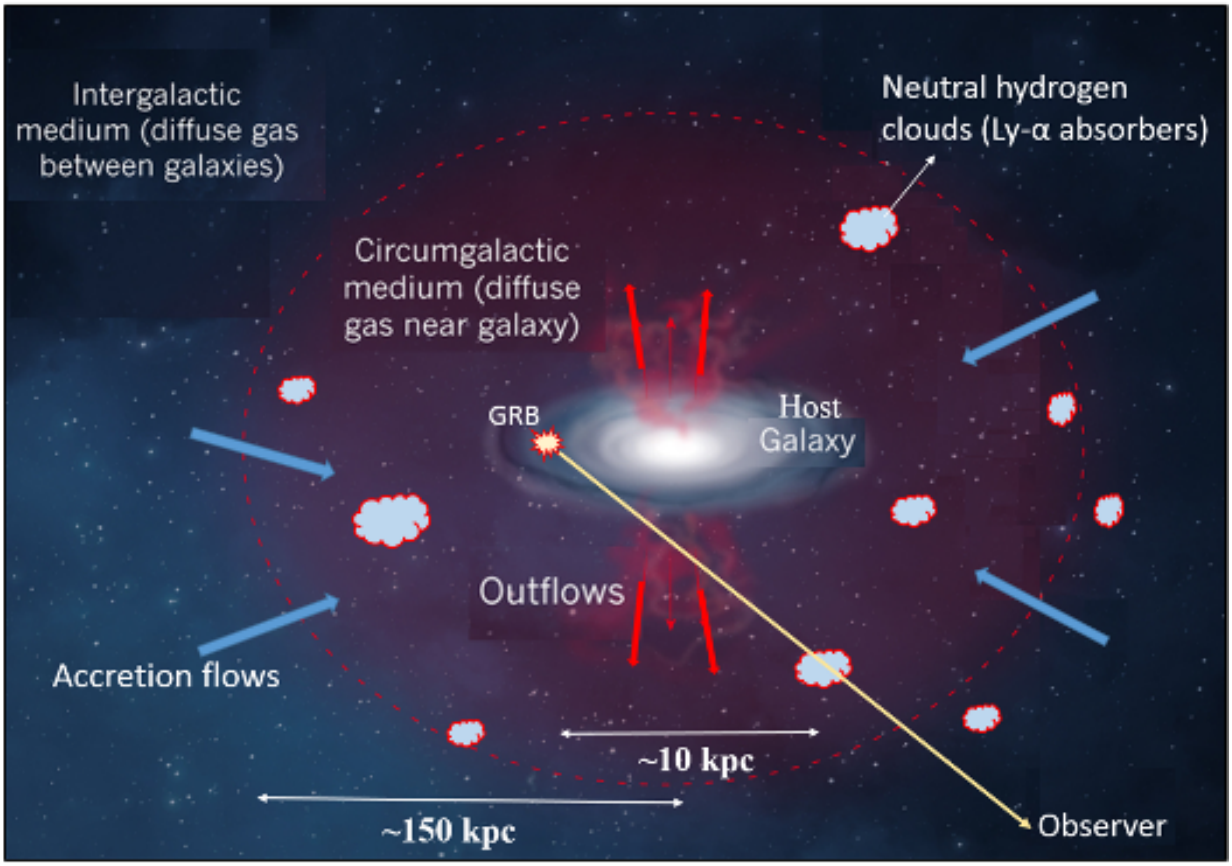


Figure 2.2: Diagram showing how GRB afterglows can be used as a line-of-sight probe to study the CGM, IGM, etc. between the observer and the GRB location. As can be seen here, the light emitted from the GRB afterglow interacts with the matter in this sight-line. This interaction is then observed in the observed afterglow spectrum. Image credit: `https://www.astro.umd.edu/~pgatkine/research.html`

While both QSOs and the CMB have been used to study reionization for some time, long-duration γ-ray bursts (GRBs) are a relatively new probe of the high-redshift universe (e.g. [62]) as studying the absorption features in their afterglow spectrum will illuminate the composition of the IGM. GRBs offer several theoretical advantages over QSOs for constraining $x_{\rm H\,I}$ near the epoch of reionization. First, though short-lived, their afterglow emission can significantly outshine even the brightest QSOs (e.g. [63, 64, 65]). Second, the power-law afterglow spectral energy distributions are significantly simpler to model than QSOs, leading to more precise $x_{\rm H\,I}$ measurements [66]. Third, GRBs are not biased towards the most massive halos [66] because they result from the core-collapse of a single massive star.[4]

Thanks to more than 20 years of painstaking effort from the community, we are finally on the cusp of using GRBs to make meaningful measurements of the neutral hydrogen fraction at cosmologically interesting redshifts ($z \gtrsim 7$). The discovery of GRB 090423 at $z \approx 8.2$ [67, 68], the most distant spectroscopically confirmed source in the universe (Figure 2.3), along with the measurement of a photometric redshift of $z \sim 9.4$ for GRB 090429B [25], unambiguously establish that GRBs explode and are detectable at the relevant redshifts of interest. In fact, we have relatively precise constraints on the rate of such events from unbiased *Swift* samples: approximately a few percent of the *Swift* population resides at $z \gtrsim 7$ (1–2 events per year; [69, 70]). Furthermore, high signal-to-noise ratio (SNR) spectroscopy of the $z = 5.913$ GRB 130606A and $z = 6.33$ GRB 140515A (Figure 2.3) enabled strict upper limits on the neutral hydrogen fraction from the profile of the Lyman-α red damping wing for the first time [71, 72, 73, 74].[4]

Despite these remarkable successes, as a community we still lack the ultimate prize:

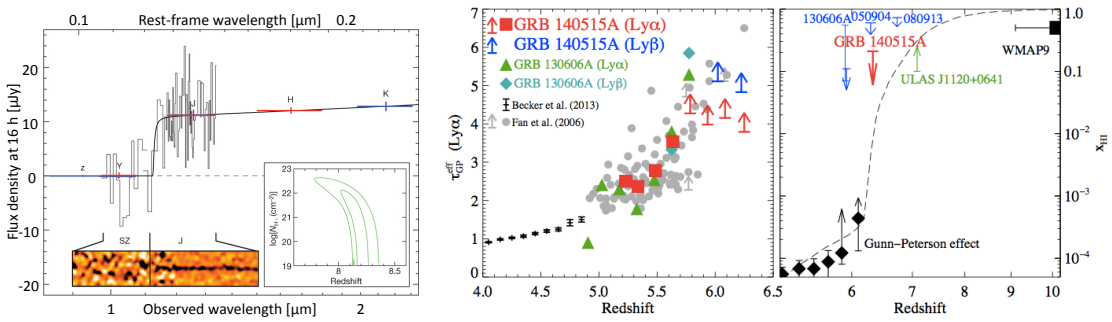


Figure 2.3: *Left panel* : NIR spectrum of the afterglow of the $z = 8.2$ GRB 090423 [67], obtained with ISAAC on the VLT at a full 16 hr after the burst trigger time. While the sharp break in the spectrum (consistent with that obtained from broadband photometry) indicates a redshift of $z \approx 8.2$, the low SNR precludes meaningful constraints on $x_{\rm HI}$. *Right panel* : Redshift evolution of the IGM from GRBs and quasars. Recent observations of GRB 140515A (blue and red [74]) and GRB 130606A (cyan and green [71]) are compared with limits from quasar observations. Even with just a small number of sightlines, GRBs can provide powerful constraints at redshifts $z \lesssim 6$. However, thus far, no high SNR spectra of a GRB afterglow has been obtained at a redshift directly probing the epoch of reionization ($z \gtrsim 7$).

meaningful constraints on $x_{\rm HI}$ at a redshift of interest for reionization ($z \gtrsim 7$). Given that *Swift* has likely detected $\gtrsim 15$ events over the course of its lifetime at these distances, the bottleneck is clear: a lack of promptly available NIR imaging and spectroscopy on moderate/large aperture telescopes. At $z \gtrsim 7$, rest-frame Lyman-α is redshifted into the observer-frame NIR. While many promptly available optical facilities automatically respond to *Swift* GRB alerts, the number of *readily available* NIR imagers, and, to an even larger degree, spectrographs, is remarkably small [GROND, NIRI (Gemini), X-SHOOTER (VLT)]. Without NIR capabilities, which RIMAS is designed to provide, it is nearly impossible to distinguish between events that are optically faint because they are obscured by dust (a significant fraction of the *Swift* population; [69, 70, 75]) and true high-redshift GRBs, let alone measure $x_{\rm HI}$ from the red wing of Lyman-α.[4]

2.2.2 Design

RIMAS is designed to allow for quick and efficient observations across multiple modes and spectral bands. This design is complimented by the design of LDT's Ritchey-Chrétien cube, which allows for the installation of five continuously operating instruments.[76] These instruments can be switched between using its deployable fold mirrors. By choosing one of these fold mirrors to be dichroic, it is possible to simultaneously operate optical and NIR instruments.[77] Due to this design, RIMAS receives NIR light (Figure 2.4), wavelengths $>$ 0.97 µm, from LDT while observations with LDT's optical imager, LMI, are simultaneously available.

Once this light is received from LDT, it takes the path shown in Figures 2.5 and 2.6. First, it passes through the CaF_2 window, into the dewar where all components are kept at cryogenic temperatures around 90 K. At this point, a number of apertures can be selected using the aperture wheel in Figure 2.7[b]. The open aperture for imaging, the short (6″) slits for all spectroscopic modes with varying widths (0.6″, 1.2″ and 2.5″) for different seeing, a long slit (insert dimension here) for low resolution spectroscopic modes, and a blank for calibrations. The slits are reflective and mounted at an angle so that the reflection can be seen by the slit viewing optics. This allows for the location to be viewed while spectra are being acquired, and allows for quick alignment of the spectrograph with the target. Directly after the aperture, there is an auxiliary filter wheel (Figure 2.7[c]) that allows for any 1 inch filter to be installed based on an observer's science case. At the moment, multiple narrow band filters that were available in the lab are installed, another blank and an extra K band filter are included to test the system. Next, the light is collimated

through a five-lens assembly. It is then split along the two optical arms with 0.97 µm through 1.35 µm reflecting towards the YJ filter/grating wheel and the 1.35 µm through 2.37 µm light continuing towards another mirror and the HK filter/grating wheel. Both filter/grating wheels (Figure 2.7[a]) contain two broadband filters and an open slot for imaging, a VPH grating (R $\approx$ 30), a VPH grating and prism assembly (R $\approx$ 300), and an echelle grating assembly. The broadband filters along the YJ path are Y and J, and the broadband filters along the HK path are H and K. The filtered or dispersed light is then focused by another five-lens assembly and detected by an H4RG-10 detector. The detectors are each on a focusing stage that allow for movement of the detector along the beam. There is a steep drop-off in the detectors' Quantum Efficiency (QE) around 2.5 µm so any longer wavelength light passing through the dichroic mirrors is unlikely to cause any issues with instrument performance.[78]

2.3 Detector Background

Throughout this thesis work, there is a lot of discussion and exploration of NIR detectors. To aid with this, a brief description of how these detectors work, detector attributes, and detector readout systems are included in this section.

2.3.1 Detector Array Description

These arrays have two types of pixels, photosensitive and reference. The photosensitive pixels make up the vast majority of the array, and are the pixels used to gather observations. The reference pixels are not photosensitive, but are designed to electrically

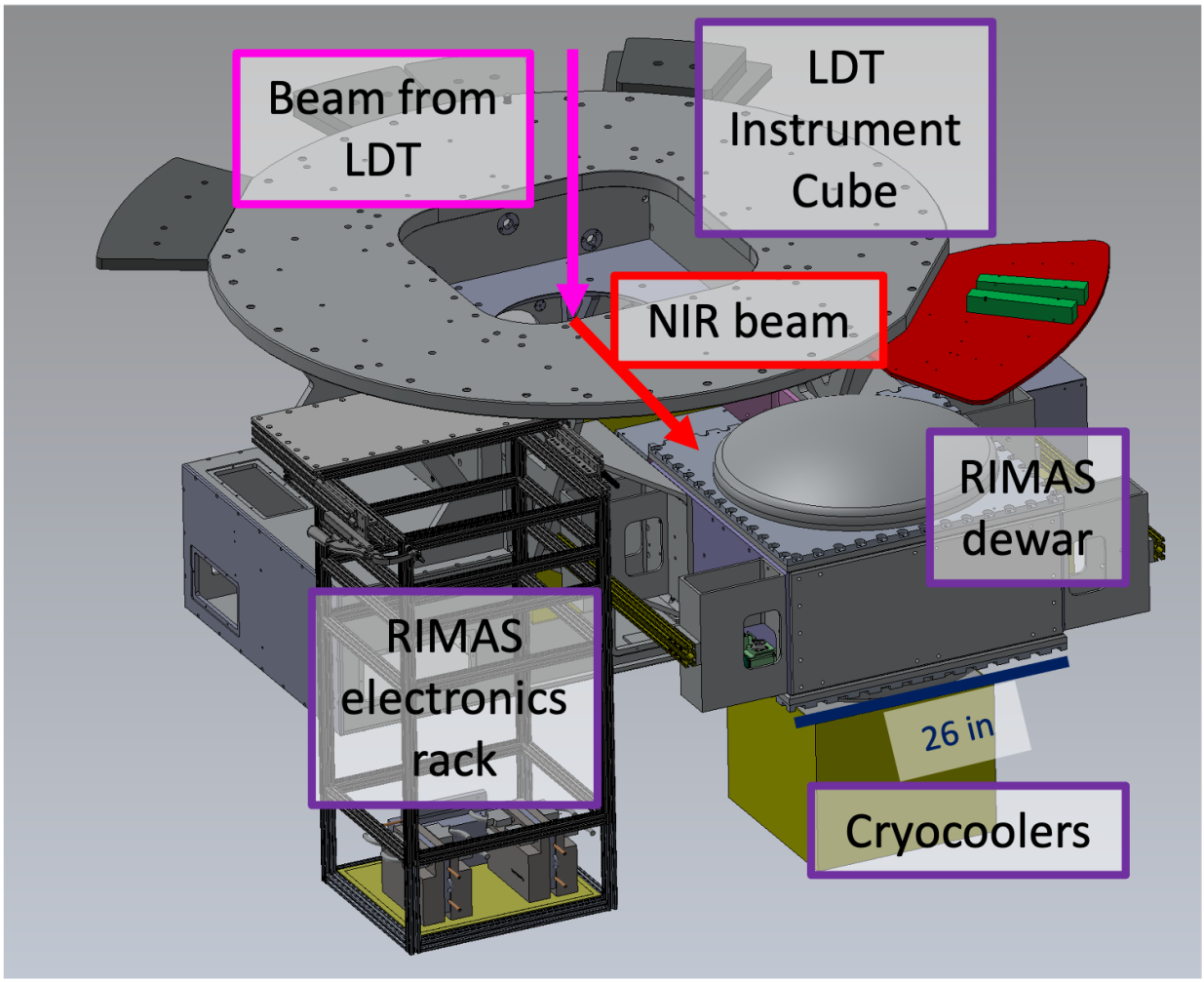


Figure 2.4: Model of LDT's instrument cube showing the beam coming into the cube and NIR light reflecting off of a dichroic mirror into RIMAS's aperture. RIMAS's electronics rack is also shown mounted to the cube.

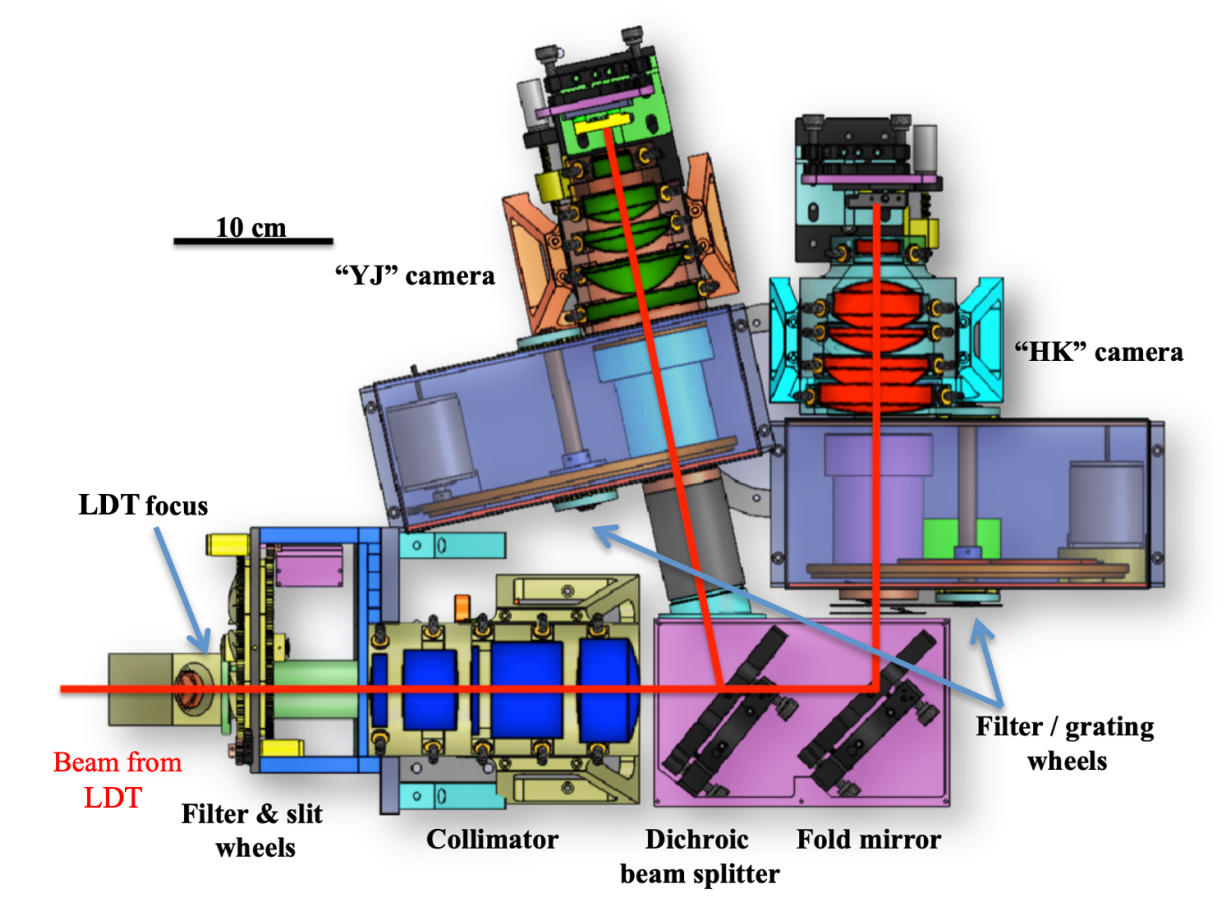


Figure 2.5: Model of RIMAS's optical path after receiving light from LDT lightly edited from John Capone's thesis [79]. As can be seen here, the beam from the telescope passes through (1) the aperture wheel located in the telescope's focal plane, (2) passes through the auxiliary filter wheel directly behind the aperture wheel, (3) becomes a parallel beam after traveling through the 5 lens collimator assembly, and (4) is split by wavelength into shorter (YJ) and longer (HK) wavelengths by a dichroic mirror. Each of these two beams then travel through (5) a filter and grating wheel, (6) are refocused by a 5 lens camera assembly, and (7) finally reach the detector located in the camera assembly's focal plane.

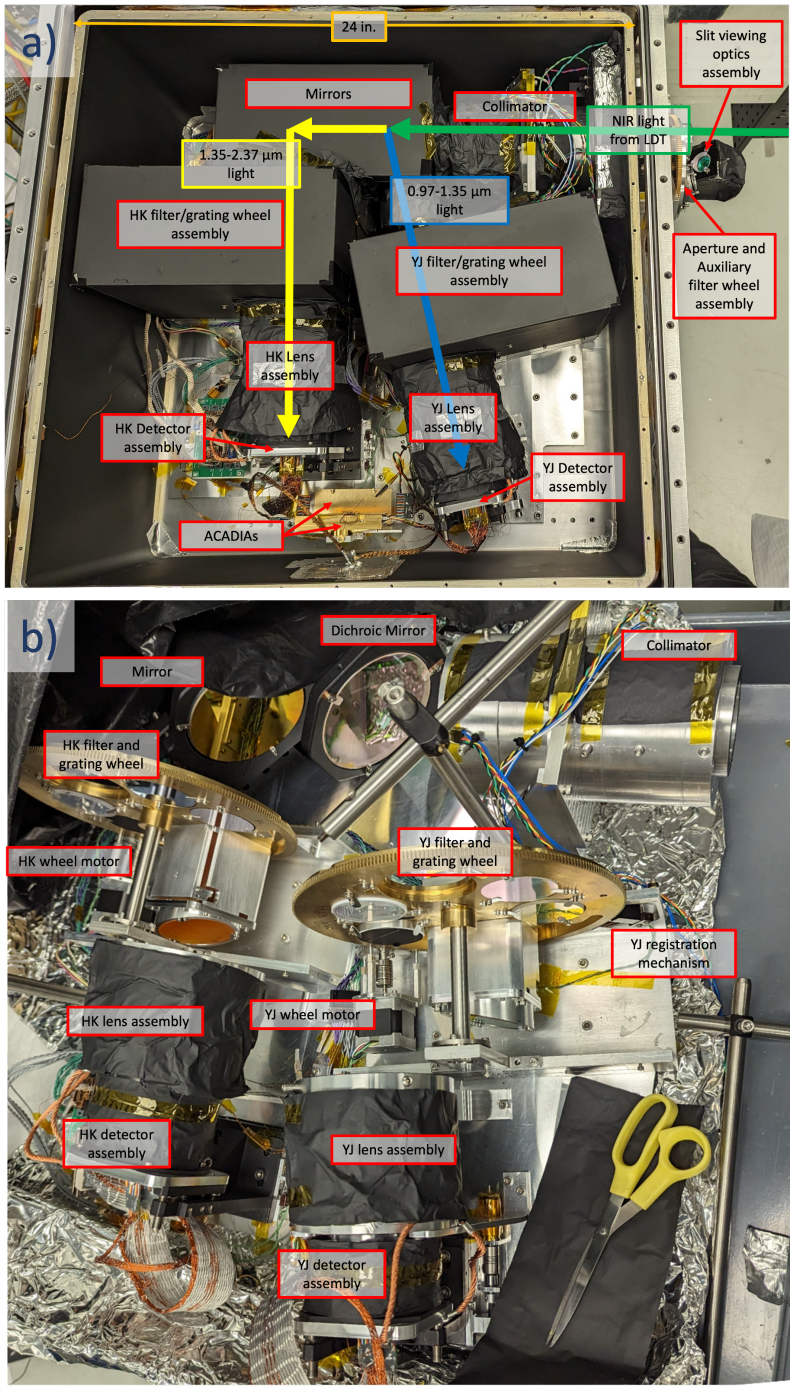


Figure 2.6: (a) Picture of the internal parts of RIMAS with the various optics and detector parts labeled. The path of the incoming light is also shown with the incoming NIR light from LDT (green arrow), the longer wavelengths (yellow arrows) and the shorter wavelengths (blue arrow) shown split by the dichroic mirror. (b) RIMAS optical assembly with fewer baffles installed in order to show more of the components.

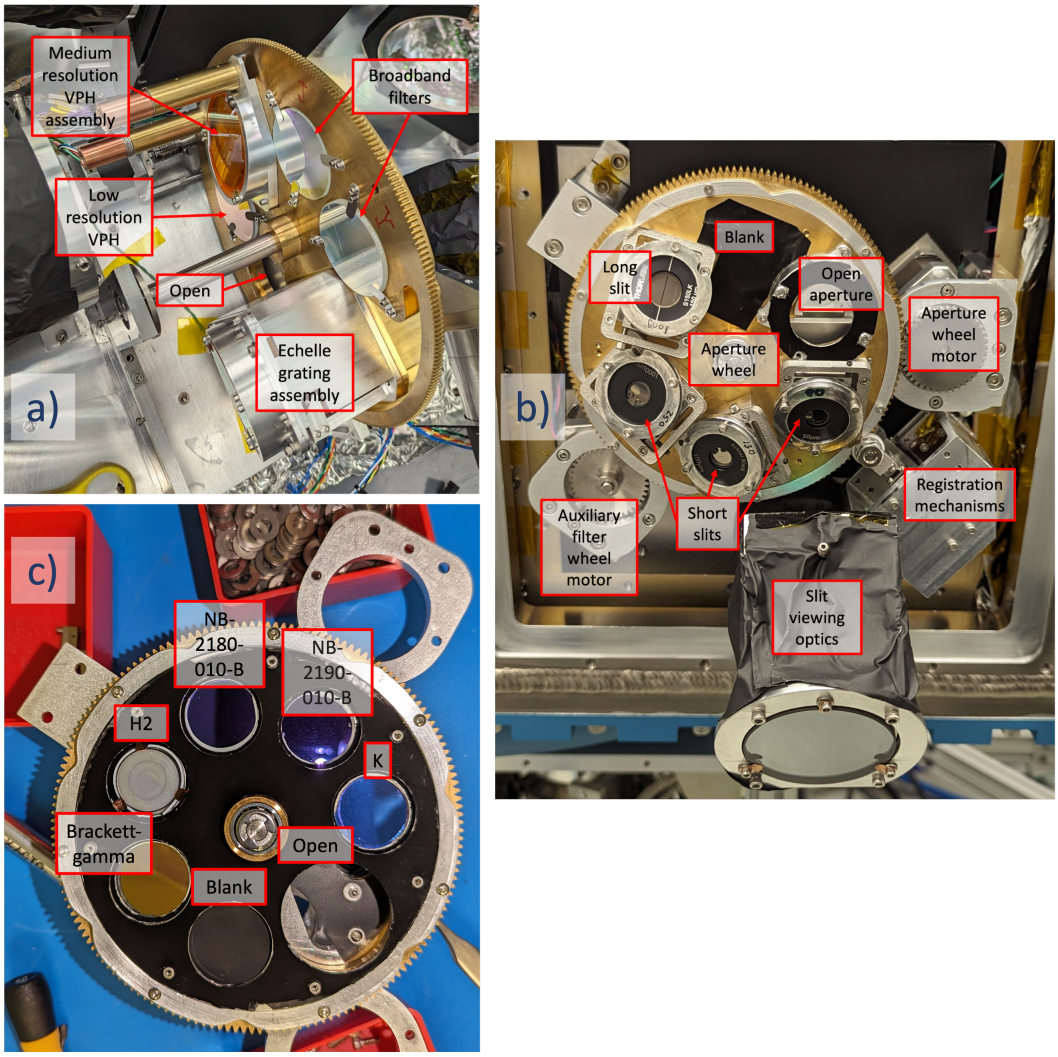


Figure 2.7: Pictures of each type of wheel with the various slots labeled. (a) Broadband filter and grating wheel. There are two of these wheels, one for each wavelength range. Both wheels have the three gratings shown (optimized for the specific wavelength range), and two broadband filters Y and J for the shorter wavelengths, H and K for the longer wavelengths. (b) Aperture wheel. This is the first component light from LDT travels through after the window. It contains an open aperture, a blank, three short slits and one long slit. (c) Auxiliary filter wheel. This wheel is directly behind the aperture wheel. It contains a large aperture for use with the broadband filters shown in (a), and six 1 inch filter slots to be used with the open aperture in (a).

mimic the photosensitive pixels. Since they are read alongside the photosensitive pixels they can be used to remove correlated noise as discussed in §3.2.4. HxRG detectors have a four pixel wide border of reference pixels.

2.3.2 Detector Parameters

Before we discuss the detector testing, it is important to describe and define the various detector properties of interest.

2.3.2.1 Non-Destructive Reads

Unlike charge coupled devices (CCDs), hybrid detectors arrays like the HxRG can read non-destructive. This the accumulated charge on each

2.3.2.2 Read Noise

Read noise is the noise generated by the electronics. This noise is primarily made up of a few types: shot noise, thermal noise, and 1/f noise. Shot noise comes from random events from small particles that occur in discrete packets, mostly electrons and photons[1]. Thermal noise comes from thermal agitation of electrons in a circuit, and is proportional to both the temperature and the bandwidth. 1/f noise, also called pink noise, is noise that is proportional to a power of the inverse frequency ($1/f^{\alpha}$). Given the non-destructive read capabilities, each pixel's charge can be read without eliminating the charge, of these HxRG detectors, the read noise is calculated based on the sampling method, so the values may

[1]Ideally, the read noise is measured in a state where very few detectable photons are present. This is accomplished by blocking light with a dark blank, and by shortening the time where photons can interact with the detector.

be given as correlated double sampling (CDS) read noise or as FowlerX read noise. Both of these sampling methods are described in §3.2.2.

2.3.2.3 Dark Current

Dark current is the small electric current that flows through a photosensitive detector without photons creating the signal. Since our detectors are an array of photodiodes, this can be accurately thought of as the reverse bias leakage current that is present in all diodes. Although this signal can be subtracted off, it has its own shot noise associated with it caused by the quantum tunneling of electrons, and thus adds to the overall noise in an exposure.

2.3.2.4 Total Noise

Total noise is the totality of noise measured over a typical exposure time. This measurement includes read noise, dark current, effects from nonlinearity, light leaks, and anything else that might happen over a typical exposure.

2.3.2.5 Bias

Bias is the base level readout of the detector. This is subtracted off through the use of any of the SUTR data reduction methods described in §3.2.

2.3.2.6 Saturation

Saturation is the level at which the maximum amount of photons has been measured, and thus additional photons no longer change the measured value. For RIMAS's detectors, this is caused by electrons filling the potential well within the ROIC. Each pixel has its own saturation value, but the values are typically quite similar. As such, saturation is sometimes presented as a map, and at other times presented as a singular value.

2.3.2.7 Dynamic Range

Dynamic range is the range over which photon intensity can be measured, which is set by a combination of the detector dynamic range and the readout electronics dynamic range. The detector dynamic range is set by the bias, and the saturation. For these devices, this value is dominated by saturation The readout electronics dynamic range is set by the analog to digital converter (ADC). The ADC limits come from a combination of offset reference voltage, and the amplifier gain value.

2.3.2.8 Quantum Efficiency

Quantum Efficiency (QE) is the measure of the ratio of photons that are converted into electrons by the detector. This value is variable with wavelength. Ideally, this is as close to 100% as possible for the wavelengths of interest, and near 0 for wavelengths outside of this range.

2.3.2.9 Persistence

Persistence, caused by charge trapping, is signal that crosses from one exposure to the next after reset. It is most obvious after exposures to bright sources reaching saturation, and appears as a memory of the previous exposure. In the readout, this appears as a temporary increase in dark current for the pixels that were subject to a bright source. A value related to persistence is burn-in, which is a loss of sensitivity in a region caused by charge trapping.

2.3.2.10 Conversion Gain

ADC conversion gain is the ratio between electrons and analog digital units (ADU). This value is controlled by the ADC, and is needed to obtain the read noise, and dark current values in electrons.

2.3.2.11 Linearity

Linearity refers to the relationship between detector response and the number of incident photons. Ideally, the relationship between the number of photons and the ADUs digitized are directly proportional, i.e. linear. Nonlinearity is mostly noticeable at integrated signal levels near saturation. HxRG detectors do have nonlinearity from charge buildup within the individual capacitors that read each pixel.[80]

2.3.2.12 Hot and Cold Pixels

For any detector array, there are going to be a subset that are unusable, which we refer to as bad pixels. These bad pixels come in two types, hot and cold. Cold pixels are pixels with low photosensitivity, and are typically caused by the photodiode being disconnected from the ROIC. Hot pixels may have some photosensitivity, but they have excessive dark current. Typically it is best to identify these pixels, and exclude them from further analysis.

2.4 Integration and Testing

RIMAS is made up of many separate components that make up its optical, detector, vacuum, cryogenic and housekeeping systems. Each of these components need to be unit tested to ensure that they work to RIMAS's specifications. Once the individual parts are shown to work, they need to be fully integrated into the system, and tested again. This is especially the case with cryogenic components that can be tested well at room temperature, but when they are brought to operating temperature within the dewar they may become inoperable. This section discusses the various tests that were performed during this thesis work, how the components were iterated upon after this testing, and how these components were integrated into the overall system.

2.4.1 Detector Testing

Even after appropriate detectors are selected, there are a number of issues involved when incorporating detectors into an instrument. First, there is the readout hardware,

Detector Package	**JDEM H2RG-18**	**NIRCAM H2RG-18**	**RST H4RG-10**
Array Size	2048x2048	2048x2048	4096x4096
Pixel Pitch (µm)	18	18	10
λ **Range** (µm)	0.6-2.5	0.6-2.3	0.6-2.5
Readout Channels	1, 4, or **32**	1, or **4**	1, 4, **32**, or 64
Readout Time (s)	2.0	5.5	2.8, 2.9
Notes	Degraded	1-year loan	Final detectors

Table 2.1: Table describing the specifications of the different detectors used in RIMAS's development. The actual readout channels used for RIMAS are in bold. The readout time is based on the time needed for readout given the clocking frequency, readout channels and references uses in the lab. The WFIRST H4RG-10 had two different readout electronics, Leach Generation II and MACIE/ACADIA, which is why there are 2 different readout times provided.

which had a couple iterations for this project. Next, it is important to have well made harnesses that add minimal noise for communication and powering of the detectors. After these are settled, robust software that is being maintained is required to keep things running smoothly. Finally, when a well functioning system is established, the detectors need to be evaluated for performance.

2.4.1.1 JDEM H2RG Detectors

The initial science detectors selected for RIMAS were the HgCdTe Astronomy Wide Area Infrared Imager (HAWAII) with 2K x 2K, Reference Pixels and Guide Mode (H2RG) detectors that were initially part of the JDEM (Joint Dark Energy Mission) development lot.[81] JDEM was an early iteration of the mission that was initially named the Wide-

Characteristic	**YJ**	**HK**
Fowler 16 Read Noise (e-)	8.73	7.67
Dark Current (e-/s)	1.2E-3	8.8E-4

Table 2.2: H2RG characterization values from Vicki Toy's thesis. The dark current was measured at 80 K.[53]

Field Infrared Survey Telescope (WFIRST), and eventually became Nancy Grace Roman Space Telescope (RST).[82] These detectors had 2048 x 2048 pixels with 18 µm pixel pitch, wavelength sensitivity cutoff at 2.5 µm and 32 readout channels.[81] The 32 enabled readout channels allowed for quick readout of the detector array, ≈0.7 s. These detectors were read and controlled with the Leach Generation II electronics described in §2.4.1.4 and the system was evaluated by Vicki Toy in her dissertation.[53] The cryogenic harness for these detectors and electronics used 32 stainless steel coaxial lines to read the 32 analog channels from the detector, twisted pair copper wire for the bias signals, and twisted pair phosphor bronze wire for the clocking signals. In this evaluation (summarized in Table 2.2), the the dark current and read noise were low and well within RIMAS's requirements. These detectors were well integrated with RIMAS mechanical, electrical and software systems.

Unfortunately, the detectors experienced significant degradation since this evaluation due to an issue with early iterations of these devices [83] that results in large numbers of shorted pixels. These shorted pixels appear in a couple ways: some have such high dark current that the pixels saturate very quickly, and others have very nonlinear dark current. This degradation caused roughly half of the pixels to photo-insensitive or too noisy for effective use. Despite being fairly confident of the source of these shorted pixels, lower biases across the detector were tested since there is a correlation between dark current and detector bias. When looking at this data qualitatively, there was no apparent change in

the number of shorted pixels. As a result, it was determined that these H2RG detectors were inadequate for our purposes and a different pair were required.

2.4.1.2 NIRCAM H2RG Detectors

While we awaited permanent replacement science detectors, we received a 1 year loan of a pair of NIRCAM short wave package H2RG detectors in February of 2020. These detectors have high QE (90%) from 0.6-2.3 µm, and similar noise statistics to non-degraded JDEM detectors.[84] However, they only have 4 readout channels causing the readout time to increase from ≈0.7 s to ≈5.6 s. Unfortunately, due to the pandemic, integration progress was slow with these detectors. A harness was developed to read these detectors using the same Leach Generation II electronics described in §2.4.1.4, and the same cryogenic harness materials described in §2.4.1.1. The software for the initial JDEM detectors was then edited to work with a 4 channel readout instead of 32.[85] After the harnessing and software changes, these detectors were successfully tested at room temperature. Once these steps were complete, we received the permanent science detectors (§2.4.1.3), so no further testing was performed.

2.4.1.3 RST Test Package H4RG Detectors

The final pair of science detectors used for RIMAS are the evaluation package H4RG-10 detectors developed for RST. These detectors have a 4096x4096 array of pixels with 10 µm pitch, allow up to 64 readout channels, and have QE[2] from 0.6-2.5 µm.[78] This means that the overall array size is only slightly larger than an H2RG-18, and there are

[2]The QE is above 90% over the wavelengths observed by RIMAS.[78]

almost 4 pixels in the space where one pixel was in the previous arrays. The read noise, dark current, crosstalk, QE, etc. are also typically better in these devices than their H2RG counterparts. Even without accounting for the degradation of the previous detectors, these new devices are an improvement over the previous generation.

2.4.1.3.1 Leach Readout Electronics

The initial readout electronics for RIMAS's detectors were the same two Leach Generation II controllers that were in use since the start of the project. Using the Leach controllers with the new detectors required updated harnessing, PCIe cards, and software. This initial setup was appealing since the controllers were already in hand, and a seemingly straightforward path to adjusting the setup for these detectors was apparent.

The new internal harnessing was modeled off of the initial JDEM package detector harnessing, whereas the exterior harnessing remained constant. Stainless steel coaxial cables were used for each of the 32 readout channels with the analog outputs applied to core, and the analog ground applied to the shield. These signals are in turn connected Leach video card positive and negative ADC inputs. Clocking signals were provided using phosphor bronze twisted pairs where each of the clocking signals were paired with the digital ground signal. These signals were controlled by the Leach controller clocking board. The bias signals were provided by copper twisted pairs where each of the bias signals are paired with an analog ground signal.

The next step in integrating the new detectors was to update the detector control software. The software discussed in §2.4.1.1 and §2.4.1.2 was edited to work with the

larger array. Unfortunately, the new detectors require a specific serial command to reset the accumulated voltage in the ROIC, and this software was not configured to send this command. At this point, there were two options: attempt to edit the legacy software, or pivot to new software. Since there was already software from the Detector Characterization Lab (DCL) at NASA GSFC to use Leach controllers with the H4RG devices, we decided to pivot to this new software that was already being used with a Leach Generation III controller in the lab. The only hardware change required for this software change was swapping an ARC-64 PCI card for an ARC-66 PCIe card, which should have been trivial.

Based on recommendations from Bob Leach, we decided to update the software while adapting it for use with a Generation II controller in order to future proof the software. This update was intended to switch from Python 2 to Python 3 (an update that had already been implemented in other systems), switch from Windows/Scientific Linux (discontinued) to Ubuntu, and switch to the latest version of ARC API. This updated software seemed to work initially until the offset voltages were altered such that the readout values were not 0 or 65535. When this change was made, the system would error out. After months of troubleshooting, it was determined that the issue was with the new ARC-66 PCIe cards which contained faulty chips. Once these were repaired, the system was successfully tested with the original Generation III version of the code that was being used in the lab, and the desire to use an updated codebase was abandoned.

Unfortunately, after this successful integration was complete, Bob Leach closed Astronomical Research Cameras, Inc., liquidated its assets and moved to France.[86] This created concerns that replacement parts for damaged components would be very difficult to obtain, and software would go without maintenance. In fact, a few months after this

shutdown, the signature for the ARC-66 PCIe Windows drivers were not renewed, which prevented the ARC-66 cards from being installed in any new Windows systems. On top of this, the internal harnesses were very fragile, and had issues with the coaxial shields becoming electrically disconnected. These disconnections were risky to repair, since the entire output was at risk of permanent damage from possible shorts induced during the repair process. Disconnected shields for outputs outside of the FOV were ignored, but needed outputs were repaired.

Instead of using Leach controllers as readout electronics for its detectors, RST uses Application Specific Integrated Circuits (ASICs) for Control And Digitization of Imagers for Astronomy (ACADIAs), which are in turn controlled by an Field Programmable Gate Arrays (FPGAs). Fortunately, while PRIME was being developed to use ACADIA readout electronics, duplicates of harnessing and a Multi-purpose ASIC Control and Interface Electronics (MACIE) were acquired for RIMAS in case more ACADIAs became available. The MACIE is the FPGA used to control the ACADIAs for both PRIME and RIMAS now, whereas RST uses similar devices more suited to handling its 18 detector array. These ACADIAs did become available, and given the risky nature of the Leach Generation II setup, we decided to pivot to the electronics and hardware that had already been well tested with PRIME.

2.4.1.3.2 MACIE-ACADIA readout system

As mentioned above pivoting to a MACIE-ACADIA readout system was relatively straightforward since the necessary hardware was already in hand in anticipation of ac-

quiring ACADIAs. Also, the detector software had already been developed and tested thoroughly on sky by PRIME. Besides avoiding the Leach Generation II pitfalls discussed above, the MACIE-ACADIA system has a number of upsides. ACADIAs digitize detector data at cryogenic temperatures, which reduces electronic noise. Also, using RST's hardware with RIMAS's H4RG detectors allows us to leverage the noise removal and data reduction pipelines developed for RST. Another benefit of the MACIE-ACADIA system is that this hardware has a mass of a couple small PCB boards, while the Leach controllers and power supplies weigh ≈15 kg. This reduction in mass helps reduce the strain on LDT's hardware.

One downside to switching to this readout system is that each ACADIA emits ≈0.5 W, which increases the heat load in the cryogenic space. This heat was offset by improving the cold shielding as discussed in §2.4.8.1.

Despite already having the harnessing in hand, and having already tested the pinouts to ensure that they were correctly manufactured, there were still a couple issues. Some of the conductors had become disconnected due to poor soldering quality. Once this was discovered, these connections were repaired in house. After the harnessing was repaired, we were able to successfully test the system.

2.4.1.3.3 Characterization

In order to fully understand the capabilities of RIMAS's detectors, some characterization is required. Here, the methods used by RST in their own characterization [78], are duplicated to measure the CDS read noise, total noise, and dark current. To acquire this data, a mirror was put in place to cover the aperture and limit stray light. The filters were

set to blank aperture, with another blank on the auxiliary wheel, and the YJ/HK filter wheels set to grism. This setup minimizes the number of photons with their accompanying shot noise that reach the detectors. CDS noise (Figures 2.8 and 2.9) was measured by taking 5 exposures of 100 frames (286 s) up the ramp[3], subtracting subsequent frames in pairs, and calculating the standard deviation for each pixel across each of these subtracted pairs up the ramp. Finally, a median is taken across the different exposures to determine the CDS noise for each pixel. Total noise (Figure 2.12 and 2.13) was determined by 100 exposures of 55 frames (157 s) up the ramp, and applying a linear fit for each pixel up the ramp. The standard deviation of the slope for each pixel was then calculated across the 100 exposures, giving the total noise for each pixel. Dark current (Figure 2.10 and 2.11) was calculated by taking 4 exposures of 2626 frames ($\approx$2 h) frames, and calculating a linear fit for each exposure. Taking the median of the slope for each pixel across the 4 exposures gives that pixel's dark current. In these measurements, there is a clear signal in the HK data from a light leak. The baffling has been improved since these calculations were done, and this leak is seemingly eliminated. This will improve the dark current and read noise measurements. Improvements could also be made to the read noise by implementing correlated noise removal with methods similar to the Simple Improved Reference-pixel Correction (SIRC) [87] algorithm. Measurements of gain, persistence and crosstalk still need to be conducted.

[3]Frames "up the ramp" refer to images acquired while charge was still accummulating on the detector. More information can be found in §3.2.2

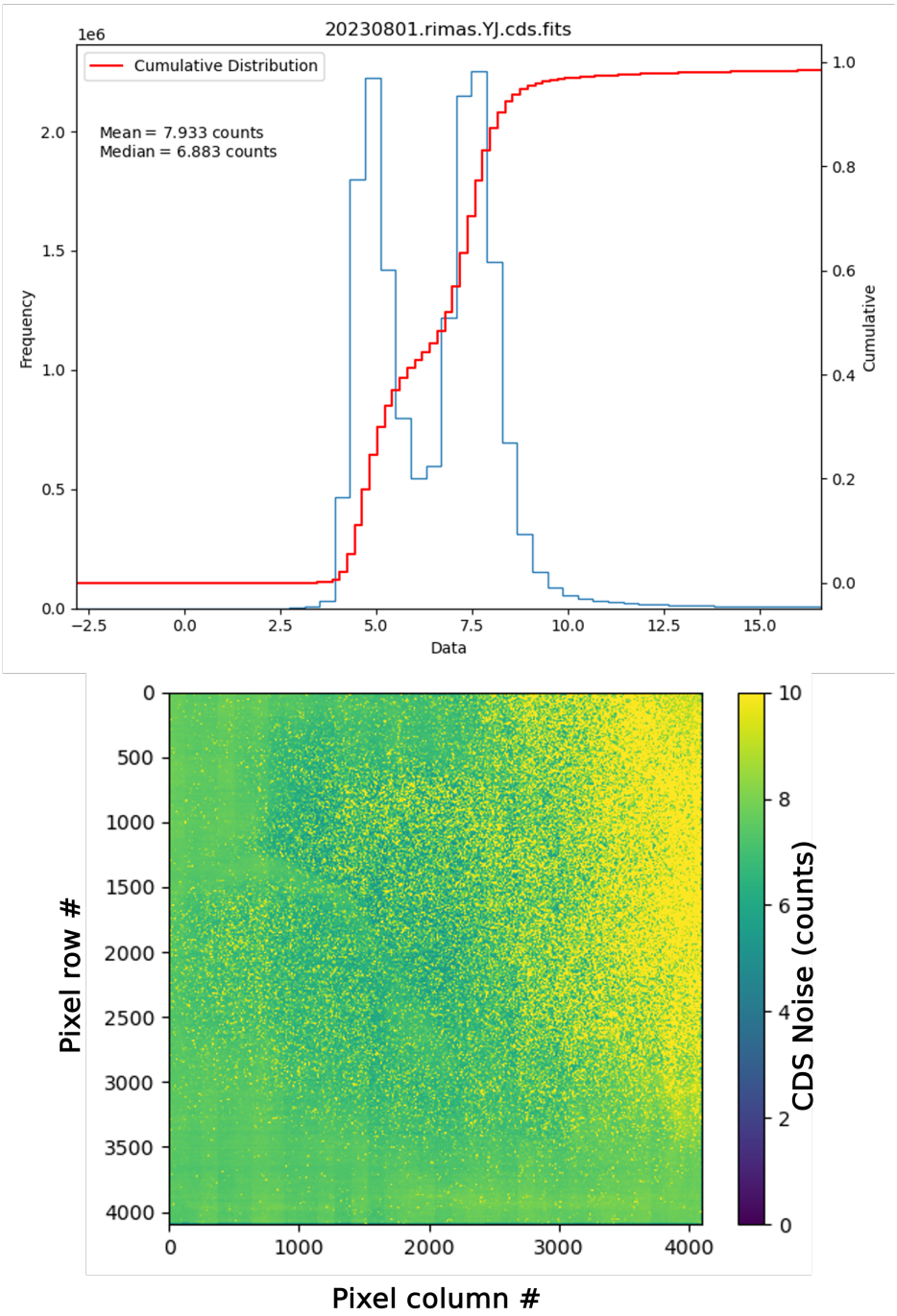


Figure 2.8: (Bottom) The pixel by pixel calculations of the CDS read noise for the YJ detector shown as they appear on the detector array, shown with the (Top) corresponding histogram and cumulative total plots showing the distribution.

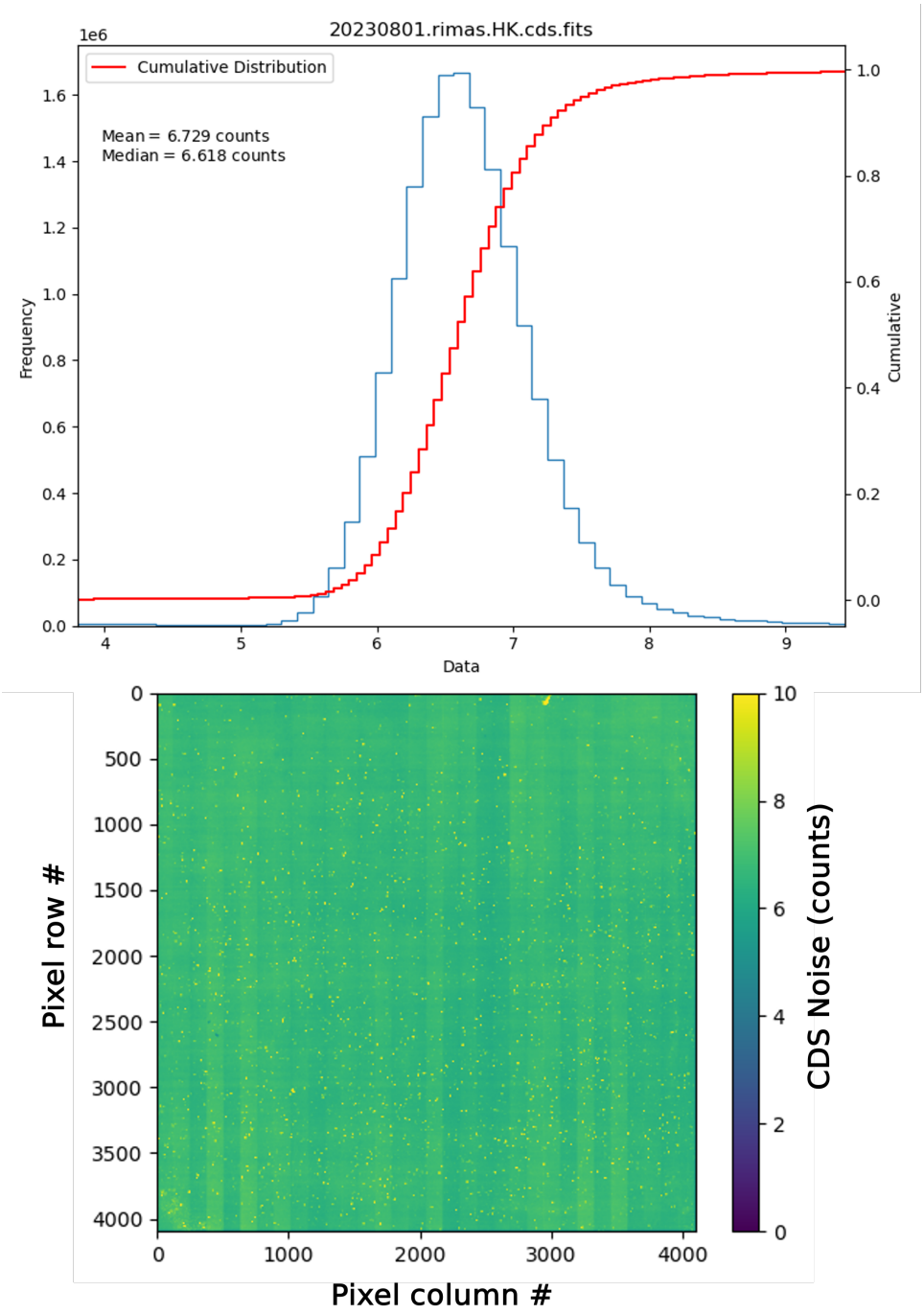


Figure 2.9: (Bottom) The pixel by pixel calculations of the CDS read noise for the HK detector shown as they appear on the detector array, shown with the (Top) corresponding histogram and cumulative total plots showing the distribution.

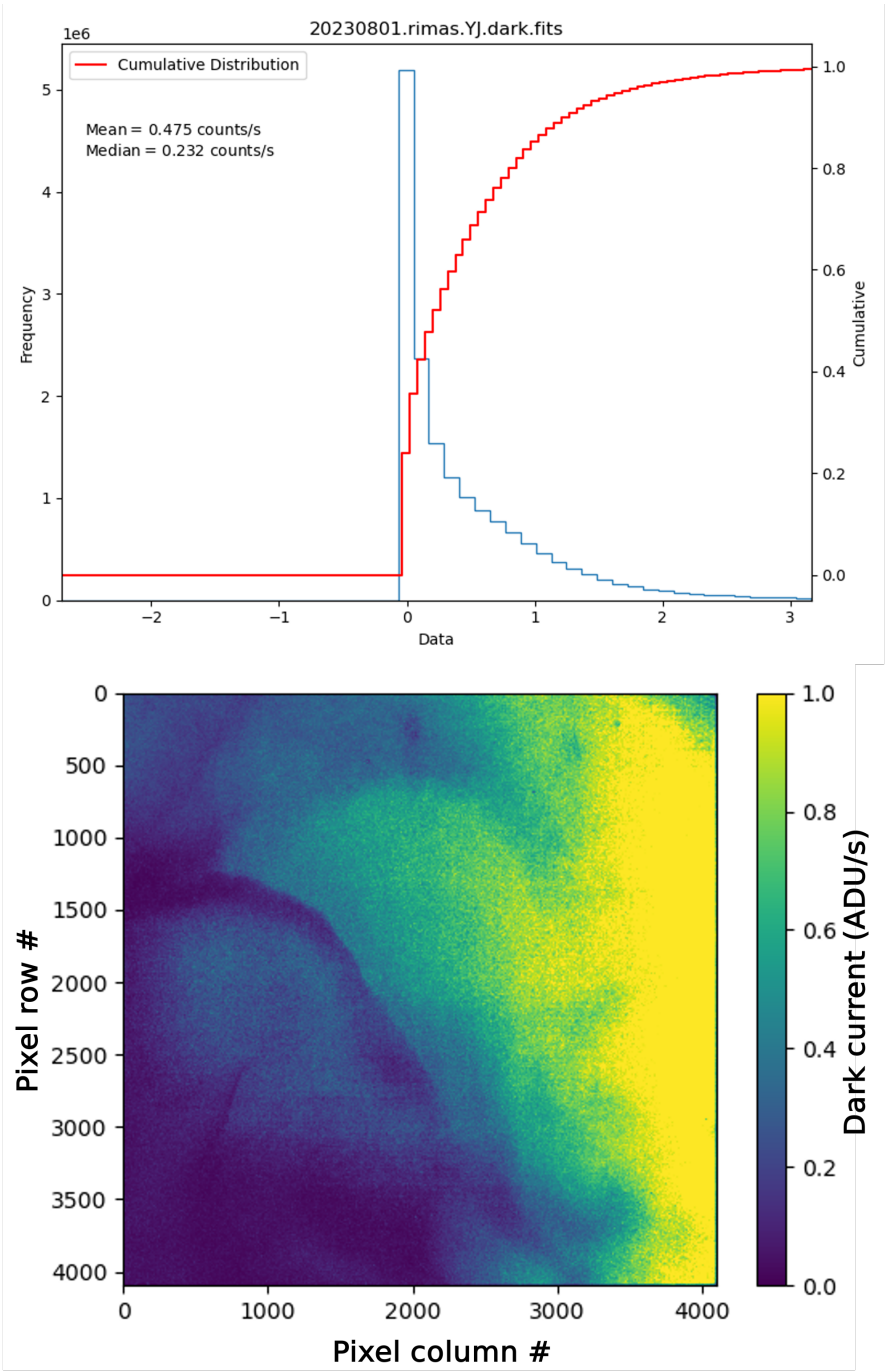


Figure 2.10: (Bottom) The pixel by pixel calculations of the dark current for the YJ detector shown as they appear on the detector array, shown with the (Top) corresponding histogram and cumulative total plots showing the distribution.

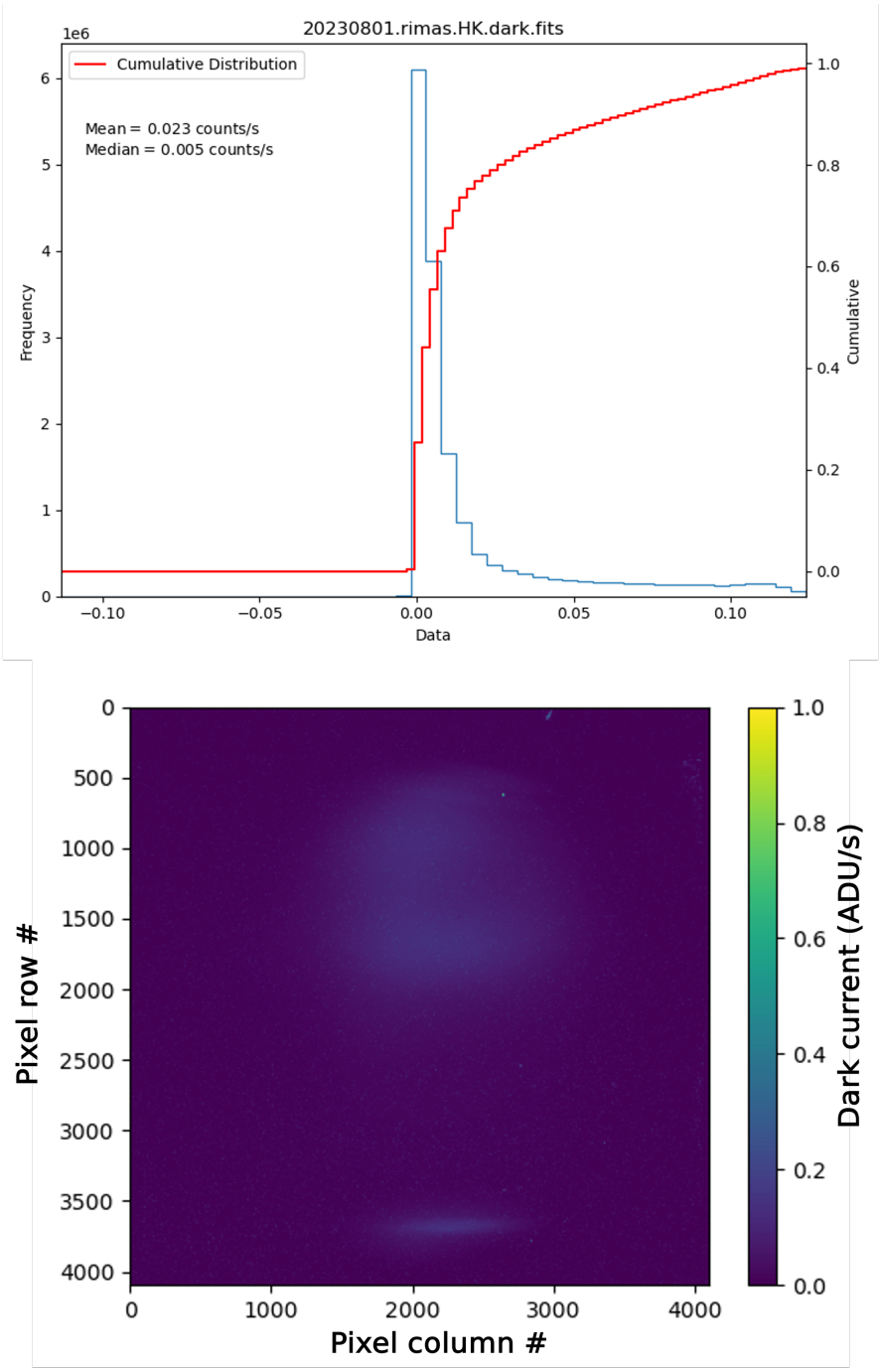


Figure 2.11: (Bottom) The pixel by pixel calculations of the dark current for the HK detector shown as they appear on the detector array, shown with the (Top) corresponding histogram and cumulative total plots showing the distribution.

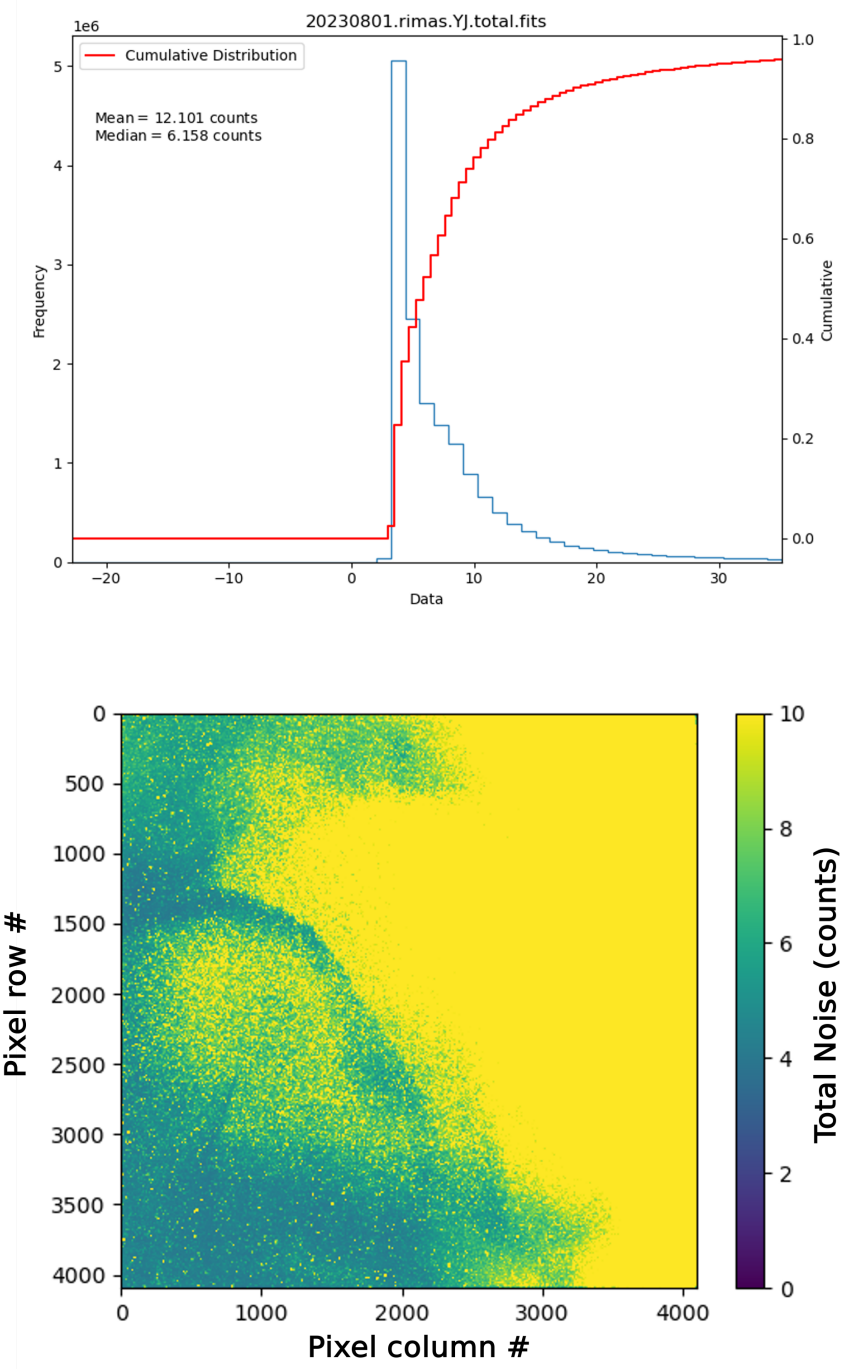


Figure 2.12: (Bottom) The pixel by pixel calculations of the total noise for the YJ detector shown as they appear on the detector array, shown with the (Top) corresponding histogram and cumulative total plots showing the distribution.

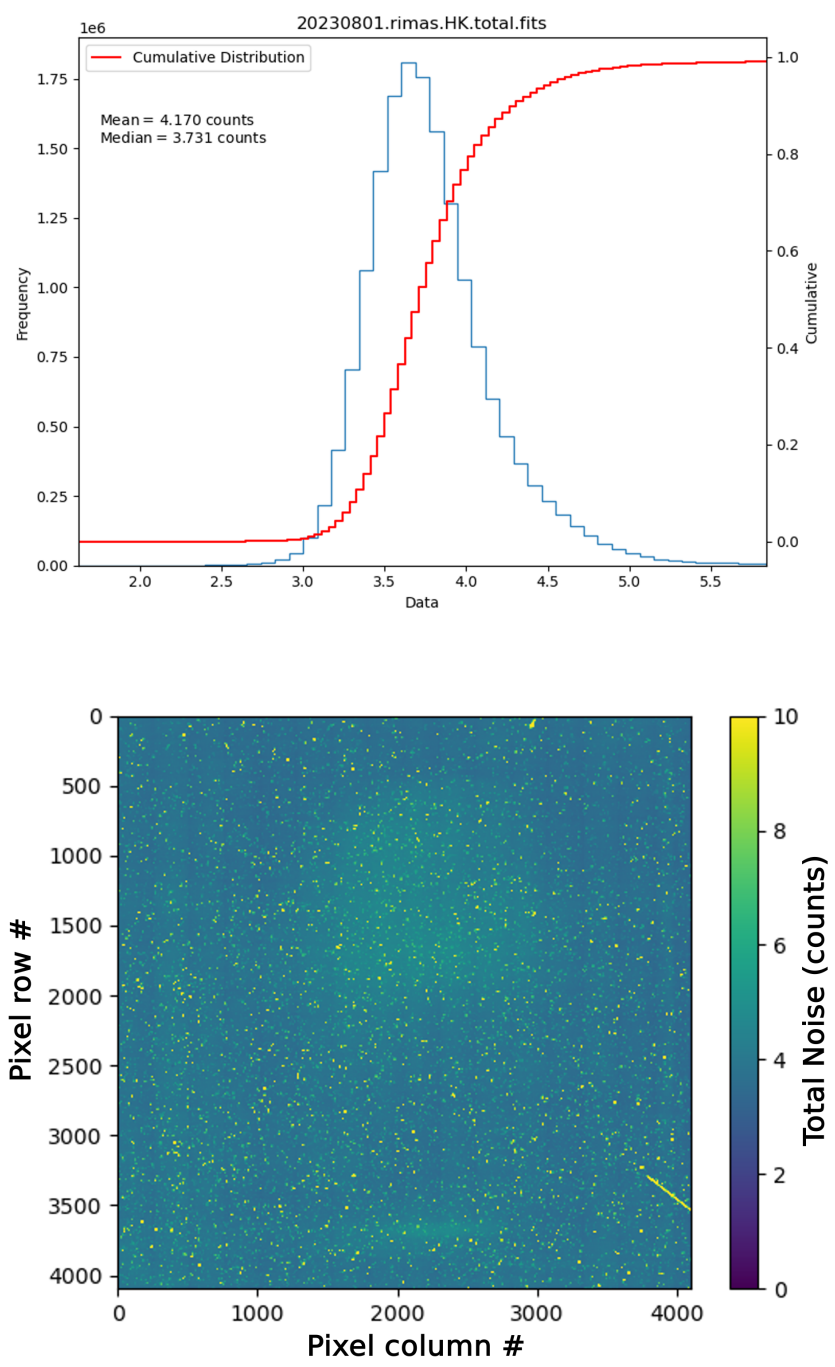


Figure 2.13: (Bottom) The pixel by pixel calculations of the total noise for the HK detector shown as they appear on the detector array, shown with the (Top) corresponding histogram and cumulative total plots showing the distribution.

2.4.1.4 Leach Generation II Readout Electronics

A commonly used system in astronomy for controlling and reading imaging detector arrays are Leach Controllers[4] developed by Bob Leach specifically for this purpose.[86] RIMAS's initial readout electronics were two Leach Generation II controllers, each containing communication, bias, clocking and 4 video cards. Each of the video cards can perform digitization for 8 detector readout channels. External harnessing consists of hermetic MDM-100 pigtail connectors with connections split between the different Leach Controller cards. Internal harnessing uses wire material meant for limiting thermal transfer, as discussed in §2.4.8.1. Stainless steel coaxial cables were used for each of the detector readout channels with the analog outputs applied to core, and the analog ground applied to the shield. These signals are in turn connected Leach video card positive and negative ADC inputs. Clocking signals were provided using phosphor bronze twisted pairs where each of the clocking signals were paired with the digital ground signal. These signals were controlled by the Leach controller clocking board. The bias signals were provided by copper twisted pairs where each of the bias signals are paired with an analog ground signal. The Leach controllers communicate with the control computer via fiber, and an ARC PCI/PCIe card.

2.4.1.5 MACIE-ACADIA Readout Electronics

The MACIE-ACADIA readout electronics harnessing, and software were initially developed for PRIME, so the system is described in better detail in §4.3.1. The differences in integrating these electronics for RIMAS are somewhat trivial: the harnesses are slightly

[4]Leach controllers are also known as Astronomical Research Camera (ARC) Controllers [86]

longer, and the ACADIAs needed to be mounted differently.

2.4.1.6 Harness Testing

All harnesses, including the detector harnesses, needed to be tested to ensure they match specifications. This means they needed to be checked for continuity, resistance, and shorts. Continuity testing ensures that connections between junctions are electrically present. Resistance testing checks that there are no weak connections. Short testing searches for any connections that should not be present. This can be done with an ohmmeter, or with a harness tester such as a CableEye [88]. Most harness testing was done with an ohmmeter, which is particularly time consuming when short testing all possible combinations in harnesses with large numbers of contacts. Eventually, a CableEye was borrowed, and all MACIE-ACADIA harnesses were able to be quickly checked for not only continuity, resistance and shorts, but also crosstalk.

2.4.2 Echelle Spectrograph Testing

One of the more interesting components of RIMAS's design is the moderate resolution (R$\sim$5000) echelle spectrograph. Echelle (based on the French word for ladder, échelle) spectrographs use an echelle grating to disperse light in one direction, and then another grating to cross-disperse the light again in a perpendicular direction (Figure 2.14). This allows the spectrograph to operate at high resolution and large free spectral range, the wavelengths over which different wavelengths' maxima can be distinguished. This spectral mode is created using ruled ZnSe grisms [89] with correcting prisms and VPH cross-

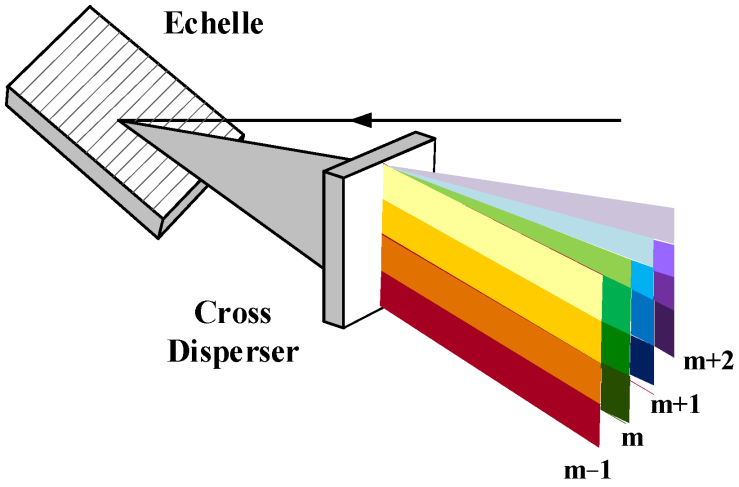


Figure 2.14: Diagram of a grism taken from Zhang, et al. [92]. The echelle grating, a grism in RIMAS's case, disperses the collimated beam in one direction. Then, a cross-dispersing grating, a VPH and prism in RIMAS's case, disperses these spectral orders in a perpendicular direction. As can be seen here, the output spectrum has multiple spectral orders with a spectrum inside of each of those orders.

dispersers. Although JWST's NIRSpec [90], IGRINS [91], and other ground instruments perform cross-dispersed spectroscopy in the NIR, RIMAS will be the first NIR spectrograph to use ruled grisms in cross-dispersed mode for astronomy. A grating prism or grism, is the combination of a grating and a prism as shown in Figure 2.15. This combination allows for dispersion without deviation of the beam, and selection of the wavelengths that will have peak efficiency.

Multiple rounds of testing were performed [1, 2, 5] on this spectrograph. The initial tests [1] were performed as soon as the newly machined grisms [94] were available, but these tests needed to be done using the original degraded detectors discussed in §2.4.1.1. The large additional noise made it difficult to do a thorough inspection, but important qualitative measures could be made of the dispersion to confirm that they were manufac-

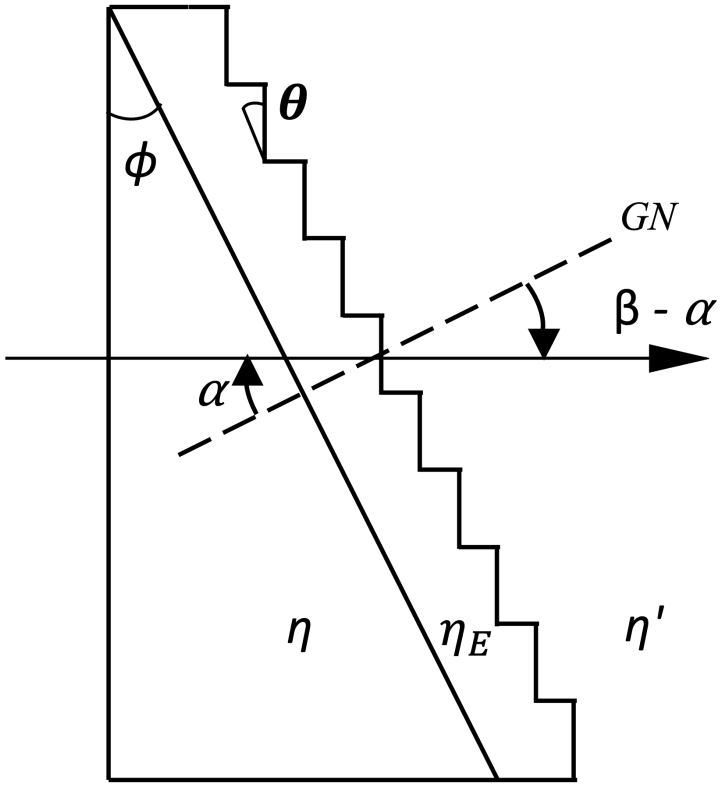


Figure 2.15: Diagram of a grism taken from page 178 of Palmer [93]. The ray path for straight-through operation at one wavelength is shown such that the incidence angle, α, is the opposite of the diffraction angle, β that are measured from GN, the grating normal. The refractive indices of the prism, grating material and surrounding medium are indicated as η, η_E and η'; also, ϕ is the prism angle and θ is the groove angle. For RIMAS, the grating grooves are cut directly into the prism material, ZnSe, so $\eta = \eta_E$. Also, the grism is surrounded by vacuum, thus $\eta' = 1$

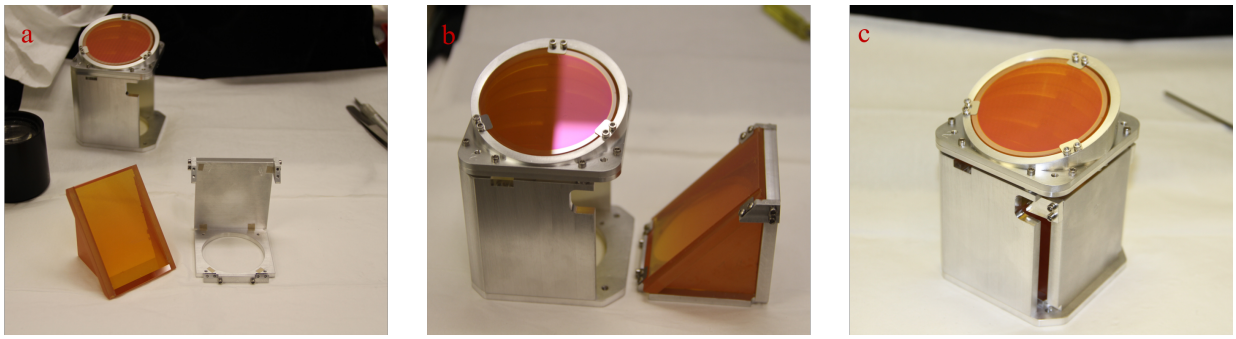


Figure 2.16: RIMAS echelle assembly. (a) Shows an unmounted grism in the foreground, and mounted cross-disperser in the background. (b) and (c) Show a completed echelle assembly.

tured with the expected quality. The next round of tests [2] was much more useful, as the new H4RG detectors (§2.4.1.3) were installed and working at this point. With the new detectors, the first measurements of resolving power were possible along with the ability to detect far more lines than before. There were some much more minor issues with the data at this point due to the detector biases not being optimized, but most measurements were useful. Beyond these issues, more care was put into accurately identifying each of the emission lines (§3.3.3.5) since this round of testing, which allows for a more accurate measure of wavelength dependent properties. This section will discuss the most recent results from RIMAS's echelle spectrograph, which use the new detectors with the final readout electronics and optimized detector biases.

2.4.2.1 Lab Spectra Acquisition

Spectra of a continuum source (with and without narrow band filters), low-pressure gas discharge lamps [95], and multiple broadband NIR LEDs were taken in order to test

various properties of the echelle dispersion. In order to achieve even illumination, multiple brushed glass diffusers are placed in front of the source in a 1 inch lens tube. One the end of this tube, a 3 inch lens tube was used as a baffle to prevent other light sources in the lab from effecting the data acquisition. All exposures of lab sources were acquired in an ON-OFF-OFF-ON pattern to remove any background from the room. An ON-OFF-OFF-ON acquisition pattern in this case means that data was acquired with the light source on, then off, off and on again. This has the benefit of removing any background from the room that is not from the light source, and also removes the dark current. On top of removing background, it increases the SNR of the observations by averaging over multiple observations. Alternating between lights on and lights off exposures in this pattern also allows for the mean time of each pair to be the same. The downside of taking this approach with light sources in the lab, is that it does not allow for the light sources to become thermally stable. Another approach would be to have a shutter in front of the light source to accomplish the same effect while keeping the source illuminated, and thermally stable.

Thermal data was acquired of a broadband IR tungsten bulb, where the temperature and intensity are controlled by an adjustable power supply in the lab. Given that the spectral distribution and intensity of this source can be approximated as blackbody radiation (Figure 2.17), the intensity of the spectrum is quite different at a wavelength of 1 µm versus 2 µm. As such, higher voltage settings were used to gather data for the YJ spectrograph (1.9 V) than the HK spectrograph (0.9 V). This helps keep the observed spectra observable with a high SNR while also avoiding saturation. The thermal data allows for the identification of spectral orders, helps identify ghosting and reflections, and gives some measure

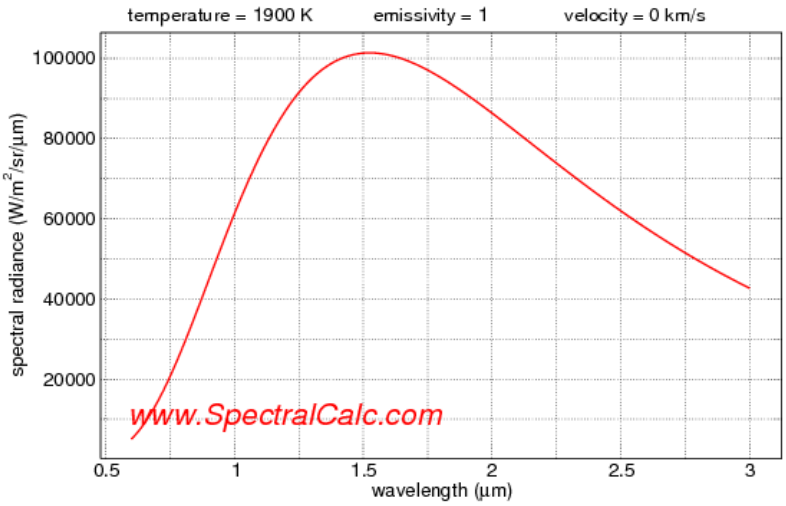


Figure 2.17: Blackbody radiation spectrum of a source with emissivity of 1 at a temperature of 1900 K, which is the color of the tungsten bulb used for data collection when used at its highest current.[96]

of the efficiency. Thermal data was also acquired in combination with each of the auxiliary filters, which gives a detailed measure of the efficiency of these filters. Low-pressure discharge lamp spectra of mercury-argon, argon, krypton and xenon were acquired. Each of these sources were acquired both individually and as a group. This made identifying the individual lines easier, while also having data that was useful for the echelle reduction pipeline described in §3.3.2.2. The emission lines for these sources allowed for the verification of the dispersion, wavelength calibration, and measurement of the resolving power. Spectra of broadband LEDs with central wavelengths of 630, 940, 1050, 1550 nm were also acquired to help identify orders. While multiple iterations of these data were acquired over the past few years, this discussion will focus primarily on the most recent dataset as it would be repetitive to go through the previous data and has multiple improvements to the background and detector readout.

Beyond the lab sources, solar spectra were also acquired by placing large mirrors throughout the building corridors in order to direct sunlight into the lab and ultimately RIMAS's aperture. This allowed for RIMAS's first observation of an astronomical object despite not being mounted to a telescope. This on-sky observation allowed for the analysis of absorption lines in addition to the emission lines observed with the gas lamps.

2.4.2.2 Dispersion

The first item of interest was whether the dispersion from the spectrograph matched the model. For this purpose, and to help identify the emission lines, order and wavelength maps were generated (Figure 3.4) to give the wavelength and order number of each pixel.[97] Using this identification, Jillian Kunze, an undergraduate Physics and Astronomy student at University of Maryland, was able to identify the translation, rotation, and rescaling required (Table 3.1) to match these maps to the dispersion.[97] The fact that the modeled spectra are easily fit to the observed spectra shows that the grisms were manufactured to match specifications. This can be seen more clearly in the echelle quick reduction pipeline discussed in §3.3.1.

2.4.2.3 Reflections and Ghosting

Part of characterizing this spectrograph is searching for detectable unwanted artifacts created by the dispersion, namely reflections and ghosting. Reflections are caused by light reflecting off surfaces, and ghosting is the refocusing of these unwanted echoes. Since the discovery of the JDEM H2RG-18 detector degradation was made directly after receiving

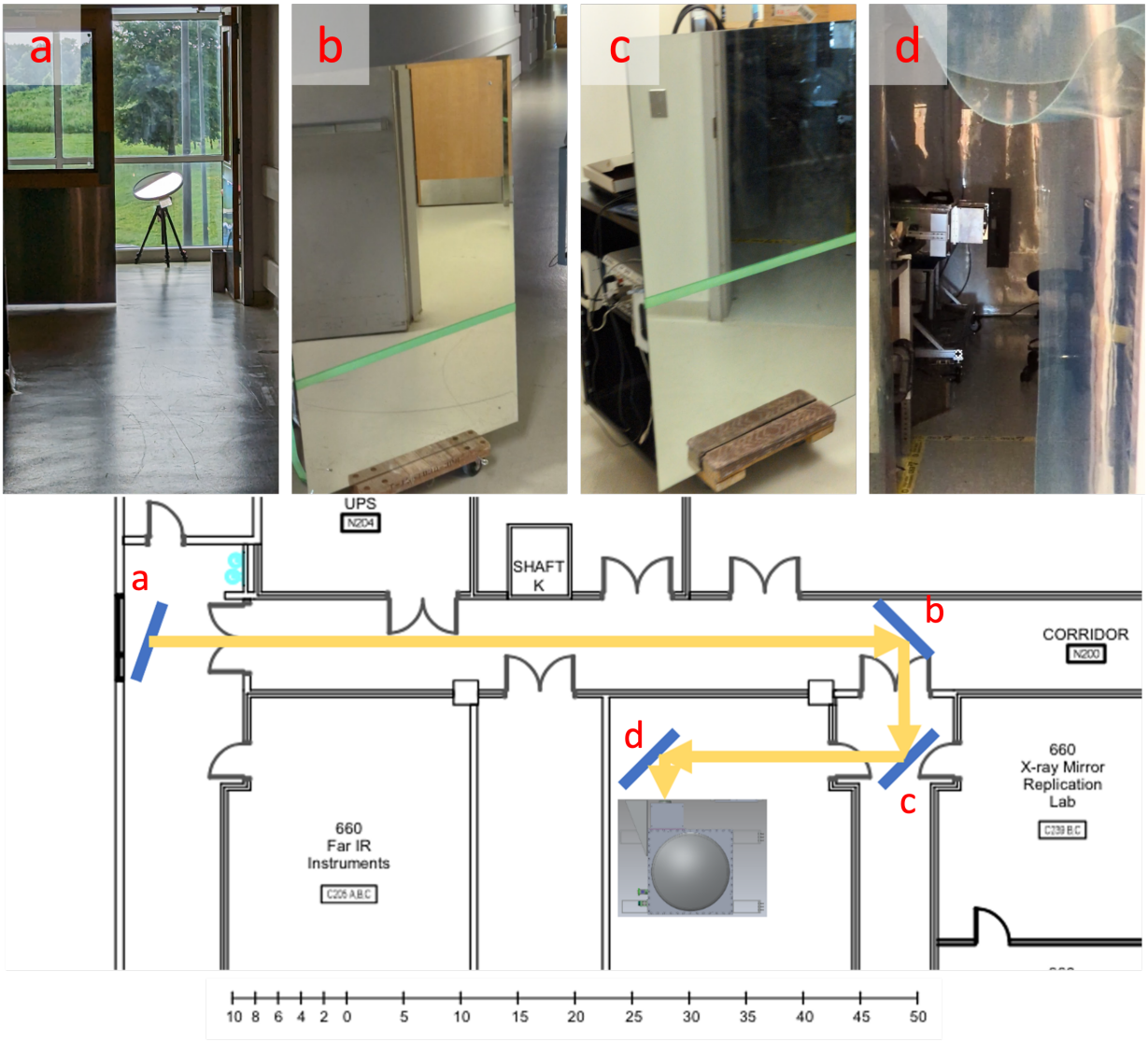


Figure 2.18: The setup used to acquire a solar spectrum in the lab. The top row shows each of the mirrors, and labels them a-d. The second row shows the floor plan with the data acquisition setup diagrammed on top of it. The blue lines represent the mirrors, and are labeled with the corresponding photo from above. The yellow line represents solar light's path to the instrument. The instrument and mirrors in the diagram are not to scale.

the grisms, the initial tests were done with these less sensitive detectors. Due to this lack of sensitivity, our initial determination was that there was no ghosting or reflections, and all detectable light remained in the orders.[1] This would be the ideal scenario. However, after greatly reducing the background noise by replacing the detectors (§2.4.1.3) and improving the baffling, it was discovered that there is ghosting, which can be seen in Figure 2.19 and Figure 2.20. The magnitude of this ghosting is ≈1/10th of the intensity of the dispersion. Efforts were made to determine the cause of this ghosting by blackening more surfaces and removing the YJ high-pass filter, but none of these efforts reduced the effect. The most likely source is from internal reflections from surfaces within the grisms, which is unavoidable.

2.4.2.4 Resolving Power

An important measurement in finding the usefulness of a spectrograph is its resolving power, R, a measurement of the ability of a spectrograph to resolve features in an observed spectrum, and is was previously defined in Equation 2.1. Resolving power is a particularly interesting when combined with the Doppler Effect to obtain a measure of the smallest difference in velocities, Δv, that can be measured as shown in (Eq. 2.2).

$$R = \frac{c}{\Delta v} \tag{2.2}$$

Where c is the speed of light. To find the resolving power for RIMAS's echelle mode, spectral calibration gas lamp emission lines were identified as discussed in §3.3.3.5, and the shape of the lines were determined as discussed in §3.3.3.3. Although there are more

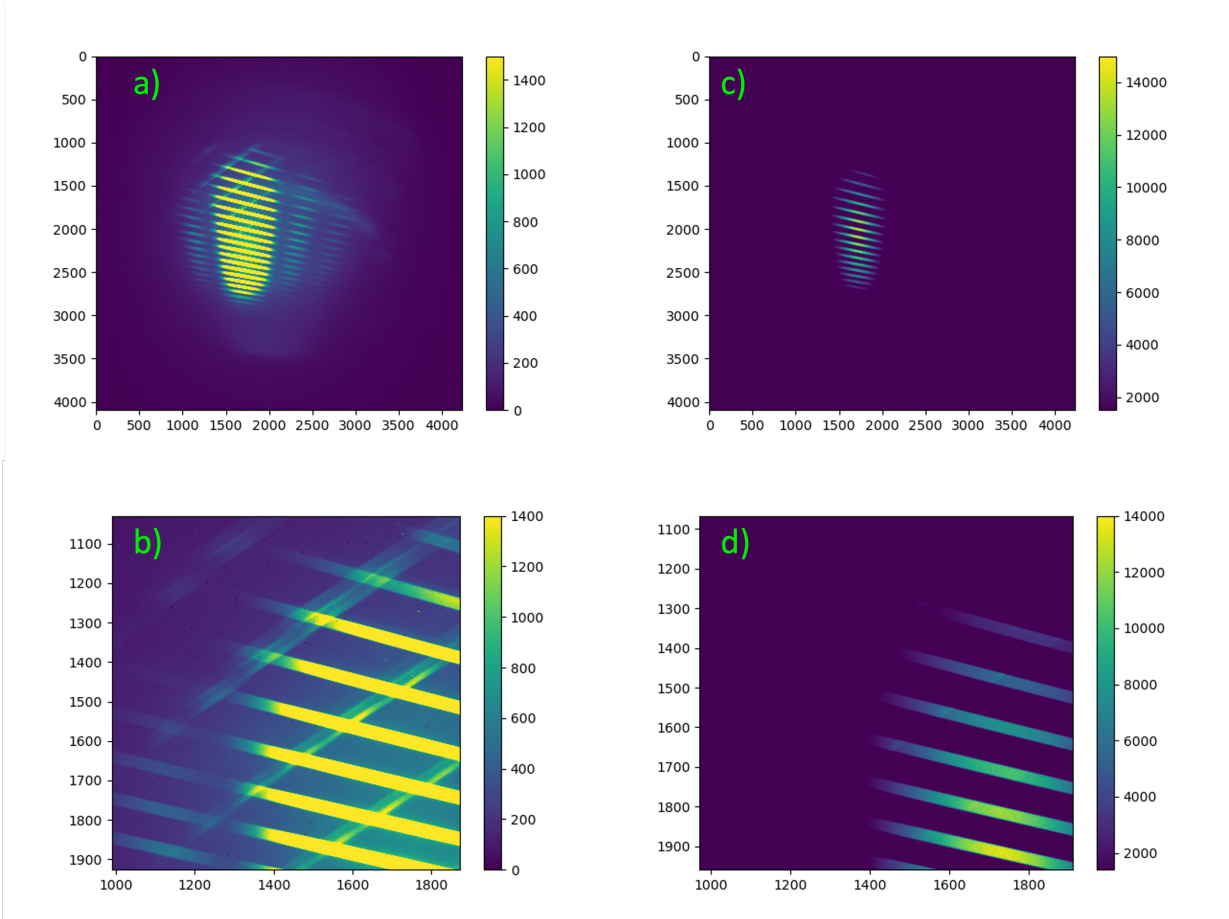


Figure 2.19: A single ON-OFF-OFF-ON reduction of the YJ echelle dispersion of a tungsten lamp shown with different scaling and zooming. (a) and (b) have the color scale set from 0 to 1400 to show the ghosting and reflections outside of the dispersive orders. (c) and (d) have the color scale set from 1400 to 14000 to only show the dispersive orders. This also shows that the reflections and ghosting are ≈1/10th of the intensity of the dispersion.

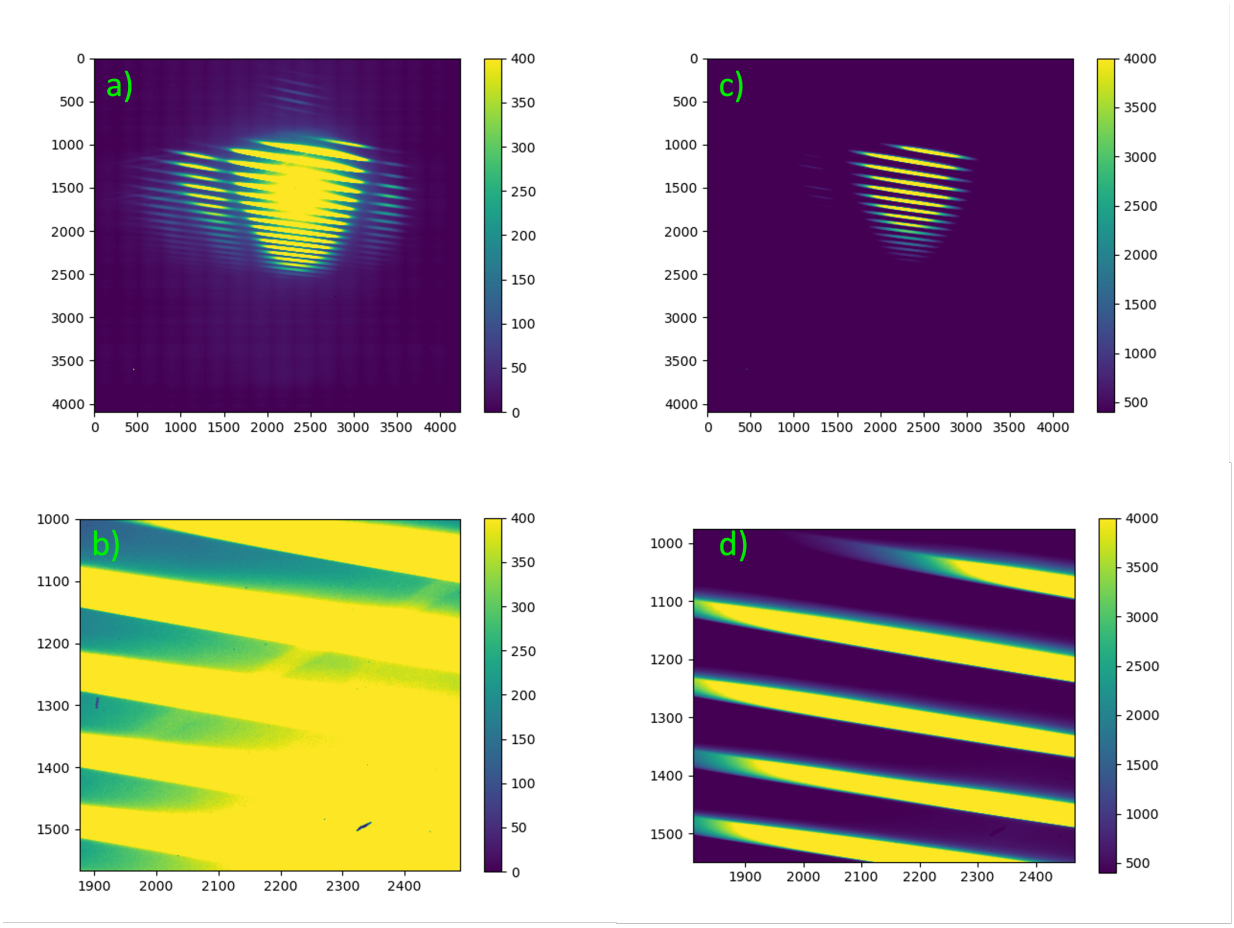


Figure 2.20: A single ON-OFF-OFF-ON reduction of the HK echelle dispersion of a tungsten lamp shown with different scaling and zooming. (a) and (b) have the color scale set from 0 to 400 to show the ghosting and reflections outside of the dispersive orders. (c) and (d) have the color scale set from 400 to 4000 to only show the dispersive orders. This also shows that the reflections and ghosting are ≈1/10th of the intensity of the dispersion.

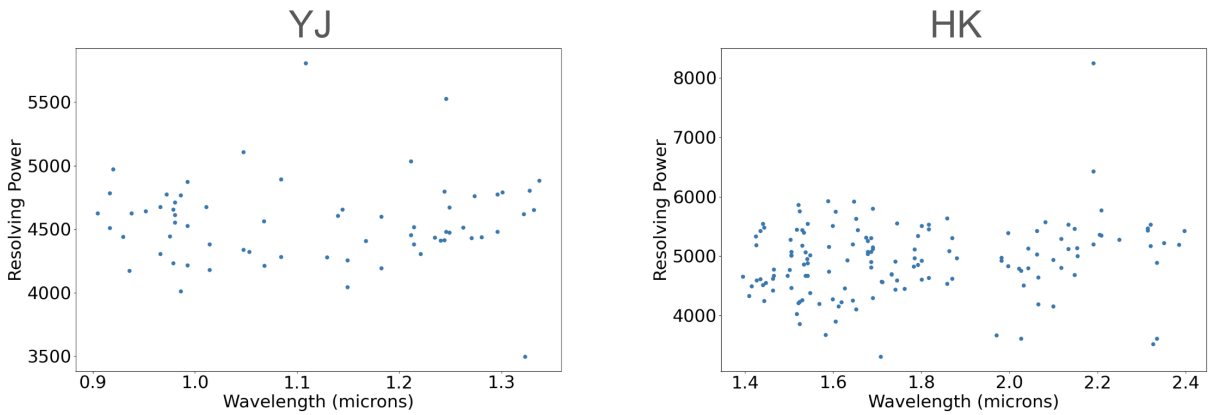


Figure 2.21: Resolving power for the YJ and HK echelle spectrographs calculated using the wavelengths and FWHM each of the gas lamp identified lines.

Band	**YJ**	**HK**
Resolving power	4550+/-40	4950 +/-50
Δv (km/sec)	65.9+/-0.6	60.6+/-0.6

Table 2.3: Resolving power and corresponding Δv for both echelle spectrographs.

sophisticated ways to determine $\Delta\lambda$ [98], a reasonable value to use is the full width at half maximum (FWHM). So, using the mean and sigma determined in §3.3.3.3 along with the wavelength solution determined in §3.3.3.6, the resolving power of each identified line can be calculated as shown in Figure 2.21.

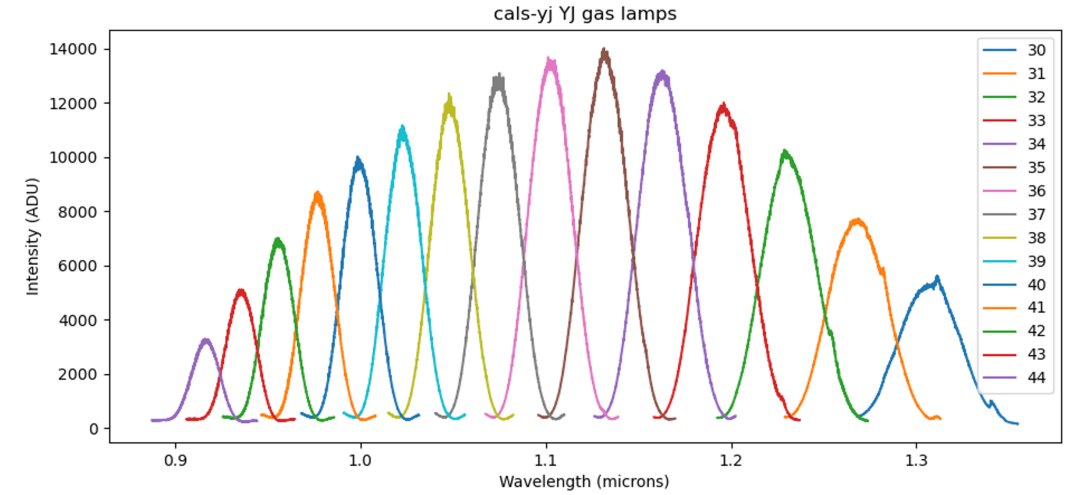
2.4.2.5 Efficiency

An important data point around any astronomical instrument is its efficiency, which limits of what can be observed. Furthermore, if the efficiency does not match the models, it suggests there are issues with the instrument. Unfortunately, without a well calibrated lab source this is a difficult value to measure before the instrument is on sky. However, even with a blackbody source, the edges of the spectral orders, and inherent features of

the spectrograph can be identified. In Figure 2.22, it can be seen that the blackbody source spectrum is fairly smooth, and unremarkable except for an absorption feature in the YJ band at ≈1.35 µm, and an absorption feature at ≈2.3 µm. Comparing with the modeled intensity plots from John Capone's thesis [79], it can be seen that these features are unexpected. Initially, these features were assumed to be from diffusers and optics used for the lab light sources. However, after looking through multiple datasets taken with different sources, it was clear that these features exist regardless of light source and optics. After searching typical glass absorption spectra, it was found that the transmission spectrum for ultraviolet optimized fused silica has a matching absorption pattern (Figure 2.23). The density of RIMAS's window was subsequently measured, and determined to be fused silica instead of the expected CaF_2, which explains this feature. This window was then replaced with a CaF_2 to match specifications, and improve the throughput.

2.4.2.6 Slit Quality

Using the solar spectrum gathering described in §2.4.2.1, the quality of the spectrum could be tested in the lab with an astronomical object. With this test, absorption lines can be observed in a addition to the emission lines. The absorption lines are a good test of the quality of the dispersion, as they show that the wavelength signals are easily differentiated, this can be seen in Figure 2.24.



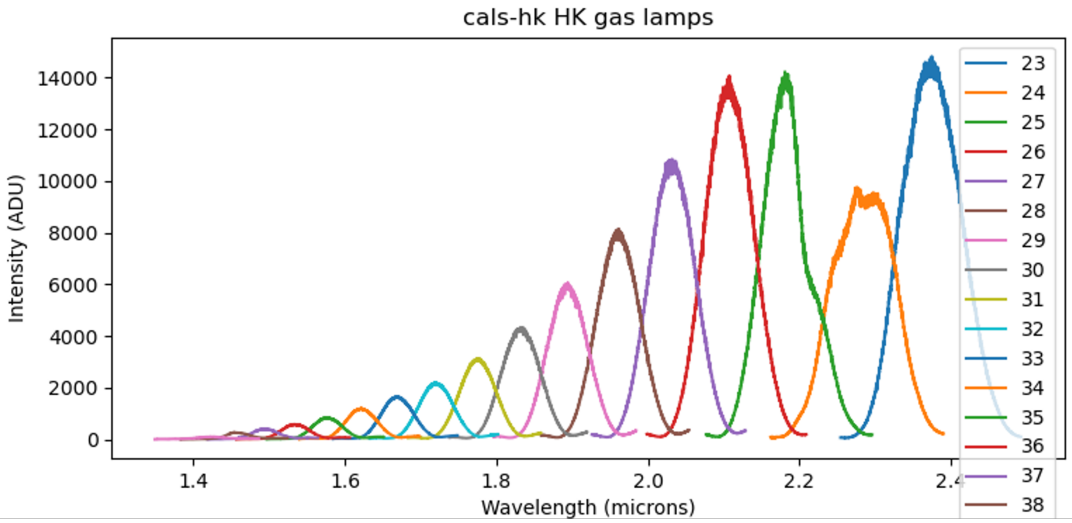


Figure 2.22: Reduced spectra of a tungsten source for both the YJ (a) and HK (b) echelle spectrographs. The legend for both plots identifies the cross-dispersed spectral order. The applied voltage for the YJ spectrum is larger than the HK spectrum in order to increase the intensity.

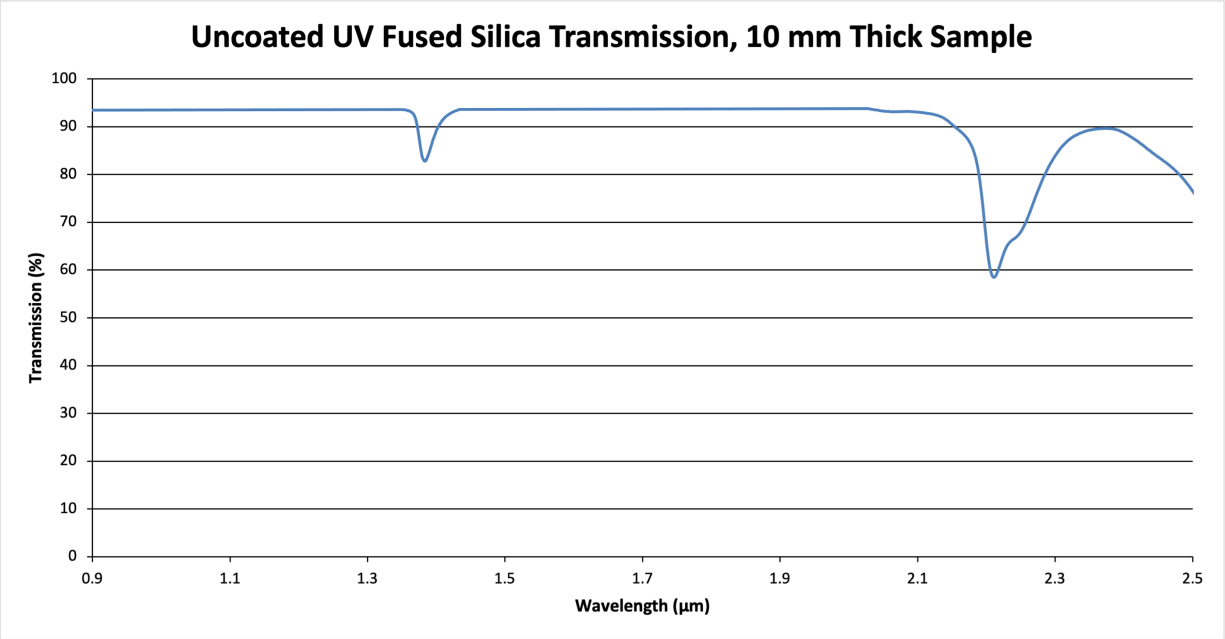


Figure 2.23: Plot showing NIR transmission spectrum of uncoated ultraviolet optimized fused silica using data from newport.com.[99]

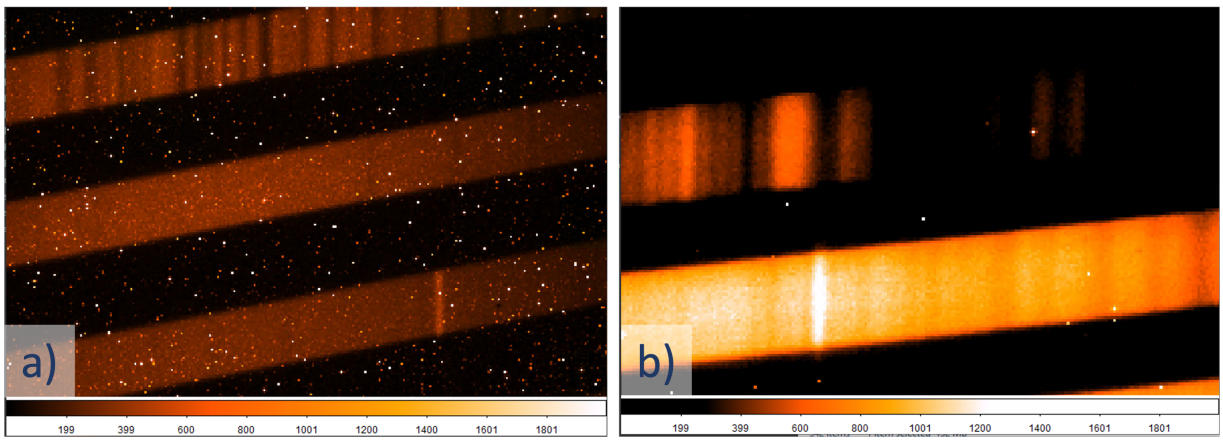
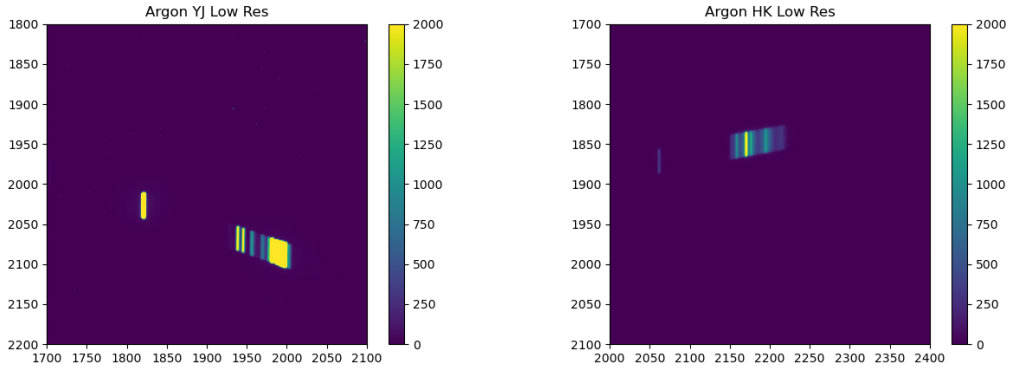


Figure 2.24: Zoomed in solar spectra for both YJ (a) and HK (b) optical arms. The clear definition of the atmospheric absorption lines highlights the quality of the spectrograph. The absorption lines shown here are primarily from atmospheric H_2O [100], and the bright emission lines are from mercury in the building's flourescent lights.

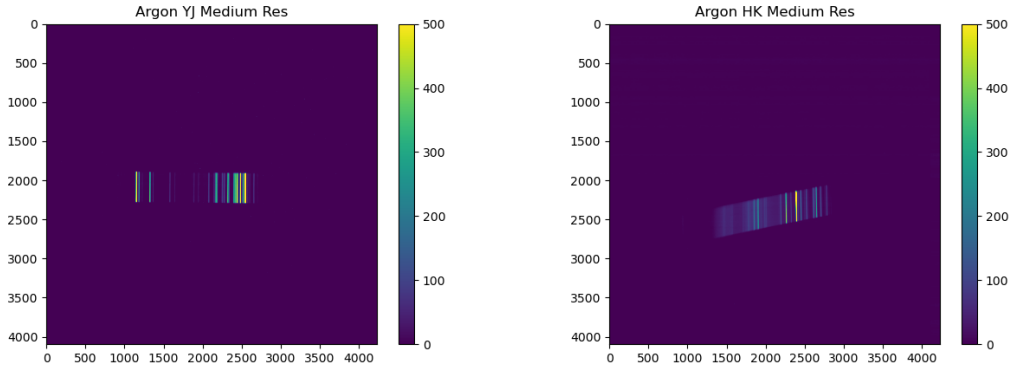


(a) (b)

Figure 2.25: Low resolution VPH spectra of argon taken with the 80 µm wide short slit, acquired with effective exposure times of 2.86 s, CDS reduced, and further reduced from OFF-ON-ON-OFF sampling. (a) The YJ low resolution spectrum. (b) The HK low resolution spectrum.

2.4.3 Low Resolution VPH Spectrograph

RIMAS's low resolution VPH spectrograph is created using a VPH transmission grating from Wasatch Photonics with R∼30 for both optical arms.[101] These were aligned to be perpendicular to the slit by shining a laser through the grating mounted on the filter/grating wheel, and rotating the grating to be in the correct position. After RIMAS was cooled to operating temperature, data was acquired of a continuum source, spectral calibration lamps, and the sun using the same methods described in §2.4.2.1. Using these acquisitions (Figure 2.25), it can be seen that there is clear dispersion, but the spectra is not horizontal for the YJ and HK cameras as expected. The cause of this misalignment is likely due to a previous mistake, but the small loss in spectral resolution does not necessitate the large amount of assembly and disassembly required to fix this issue. This issue should be repaired if any changes are needed around the YJ or HK slit/grating wheels.



(a) (b)

Figure 2.26: Medium resolution VPH spectra of argon taken with the long slit, acquired with effective exposure times of 8.58 s, CDS reduced, and further reduced from OFF-ON-ON-OFF sampling. (a) The YJ low resolution spectrum. (b) The HK low resolution spectrum.

2.4.4 Moderate Resolution VPH and Prism Spectrograph Testing

The moderate resolution spectrograph (R∼300) was not part of the initial design, and was added to cover another order of magnitude of spectral resolution near the end of RIMAS development. Each optical arm compound grating consists duplicates of the VPHs and correcting prisms acquired as spares to the ones used for cross-dispersers in the echelle spectrograph described in §2.4.2. These were aligned using the same laser method described in §2.4.3. After RIMAS was cooled to operating temperature, data was acquired of a continuum source, spectral calibration lamps, and the sun using the same methods described in §2.4.2.1. The results are nearly identical to the low resolution spectrograph results in that using these acquisitions (Figure 2.26), it can be seen that there is clear dispersion, but the spectra is not horizontal for the HK camera as expected. This issue should be repaired if any changes are needed around the YJ or HK slit/grating wheels.

2.4.5 Imaging

RIMAS's imaging mode allows for simultaneous broadband imaging in two bands, while also allowing for auxiliary filters with standard one inch diameter anywhere within RIMAS's sensitivity range. This feature is particularly useful in quickly identifying transients that have not been well localized by previous observations.

2.4.5.1 Point Spread Function

The point spread function (PSF) from RIMAS's optics were determined to be well within specification in John Capone's thesis, so no further lab testing was needed.[79] Qualitatively, it can be seen in the lab data taken over the years that the optics are performing well without major diffraction issues. The defects that had been seen in the lab data were easily solved by adding optics to the test light source to create a beam that simulates the one that would come from the telescope. These test optics are not of high quality, so the best test will ultimately be done on-sky with the actual telescope optics.

2.4.5.2 Focusing Curve

For each optical band, a linear stage is placed after the refocusing optics (referred to as YJ and HK lens assemblies in Figure 2.6) with the detectors mounted to them. These stages function at cryogenic temperatures, and are used to move the detectors into the focus position, as shown by the changing image slit width in Figure 2.27.

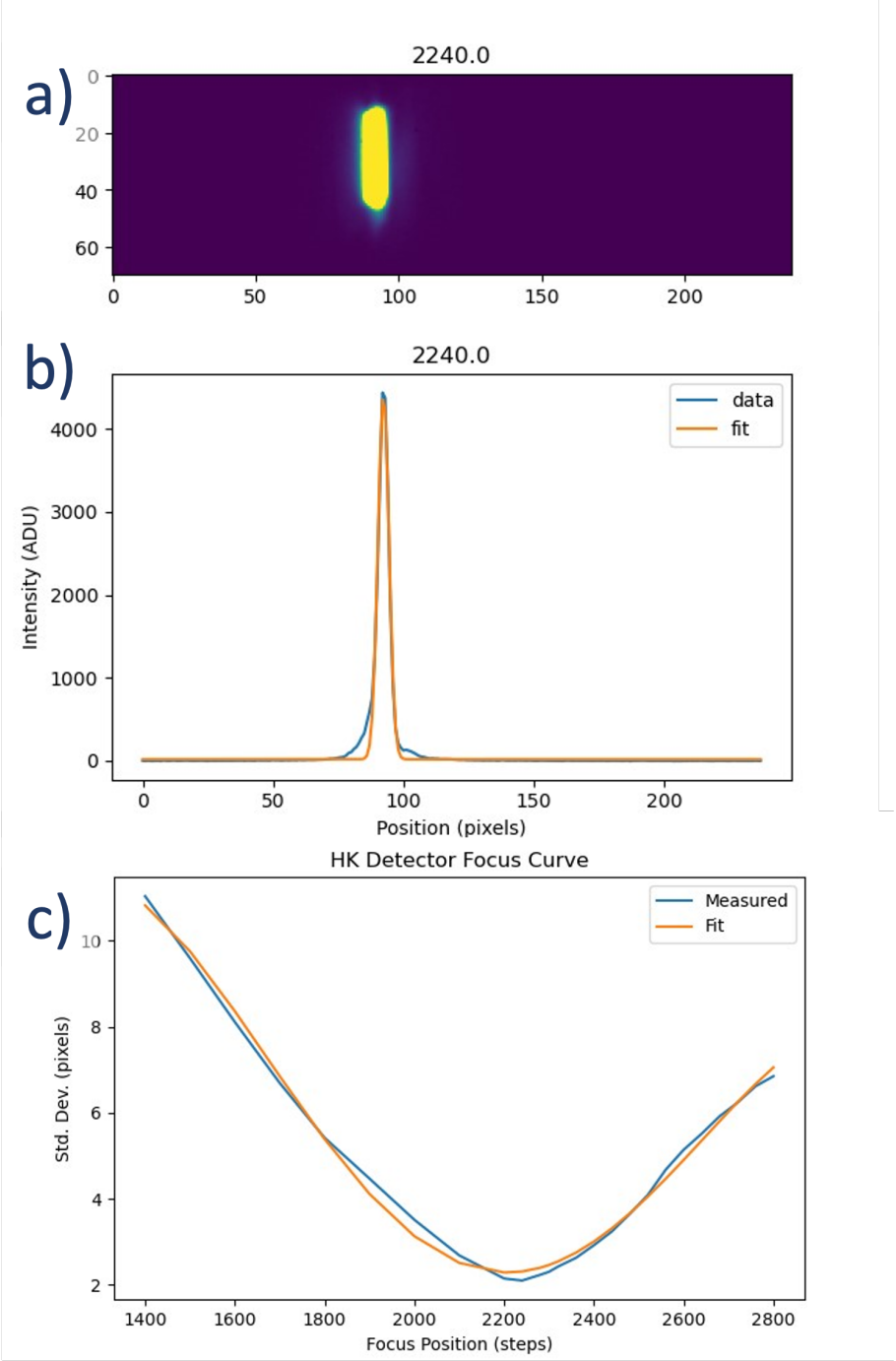


Figure 2.27: (a) Image of the 80 micron slit taken 2240 steps from the home position. The slit was not evenly illuminated during focusing, which is why the slit looks a bit amorphous. (b) Plot of the intensities of the above image totalled along the vertical axis. (c) Plot showing the standard deviation from a gaussian fit of the vertically summed intensity data as the focus position is changed.

2.4.6 Mechanism Testing

As an imager spectrometer, RIMAS requires multiple mechanisms to provide focusing, and change apertures, filters, and gratings. Since RIMAS is fully cryogenic, these filter wheel and focus stages also need to work at cryogenic temperatures. This requires a good initial design, testing at room temperature, testing at cryogenic temperatures, and alterations to the design.

2.4.6.1 Filter Wheel Mechanisms

In order to switch between RIMAS's various apertures, filters, and gratings, cryogenic motorized filter wheels are required. As shown earlier in Figure 2.6, RIMAS has four filter wheels: aperture, auxiliary filter, YJ filter and grating, HK filter and grating. As can be seen in Figure 2.28 and Figure 2.7, each wheel is a brass gear with the various filters, gratings, and apertures mounted. These are driven by a smaller gear mounted on the drive shaft of a stepper motor. The motor has been modified for cryogenic operation by cleaning each of the components in an ultrasonic cleaner, and replacing the steel bearings with ceramic bearings. The motors are run by a stepper motor driver, which is controlled by an Arduino Mega using custom code developed by John Capone.[79] The wheels also have a cam consisting of a smooth circle with grooves machined around the outside, which is used for the registration mechanism. Each of the registration mechanisms consist of a spring/flexure, a limit switch, and a ceramic bearing. For the auxiliary and filter wheels, the ceramic bearing is mounted to a linear slider, which is pushed by a coiled spring. For the YJ and HK filter/grating wheels, the ceramic bearing is mounted to the flexure. The

ceramic bearing runs along the cam as a cam follower, and is pushed into the grooves by the spring/flexure to create registration. When the registration mechanism enters the groove, the limit switch is toggled, which tells the motor controller to stop. After this, wheel position can be determined by the number of grooves passed through.

Each of the wheels went through multiple rounds of testing and development. After assembly, the repeatability of the filter/grating/aperture location using the registration was measured by John Capone using a camera with machine vision.[79] This is especially important for RIMAS's slits and gratings to ensure that the wavelength calibration remains consistent after changing between modes. Next, the wheels were cycled many times, and the number of steps between grooves was checked for consistency. After these successful tests, these mechanisms were tested at cryogenic temperatures. The aperture and auxiliary filter wheel mechanisms (Figure 2.7) are quite similar, and had no issues. The iterations on these wheels were primarily due to desired changes in the number of filters and slits.

The YJ and HK filter/grating wheel mechanisms are similar to each other and the wheels are much larger than the auxiliary filter and aperture wheels. Due to this difference, they had a number of issues not observed with the smaller wheels. First, through testing it was discovered that there was some grinding and jittering at the interface of the gears used to change filter position. As can be seen in Figure 2.28, this was solved by preloading the interface using a spring coupler between the motor shaft and the drive gear. with registration: at cryogenic temperatures the set screw setting for the limit switch did not always trigger the switch when cooled down, the registration was not very strong on the large wheel, the mechanisms would occasionally lock in place, and eventually one of the linear sliders the bearing was mounted to fell apart. As can be seen in Figure 2.28, the

registration mechanism was redesigned so that instead of mounting the ceramic bearing to a linear slider pushed by a coiled spring, it is mounted to a flexure. This has the benefit of reducing the number of moving parts, and increasing the range of motion. The increased range of motion makes adjusting the mechanism much easier. Another benefit to the new design is that the force from flexure and the limit switch are pointed in the same direction, which helps increase the force applied in the groove. This new mechanism also needed to go through a number of iterations after testing. First, care needed to be taken when adjusting the limit screw to prevent it from bottoming out on the limit switch as this would cause the flexure to permanently deform. Second, the limit switch and screw were initially offset from the flexure, and needed to be brought inline to prevent the torque from twisting the flexure. Third, the number of brass shims used in the flexure was increased from two to four in order to double the force in the groove. Fourth, the mounting holes for the registration mechanism needed to be slotted to allow for fine adjustment of the force provided to the groove. Finally, a G-10 slider was fabricated to prevent the possibility of the ceramic bearing leaving the cam.

2.4.6.2 Focus Stage Mechanisms

As with any optical assembly it is important to be able to adjust the focus, and with RIMAS's fixed lens assemblies this is accomplished by moving the detectors. Given that all of the optics and detectors for RIMAS are cryogenic, the distances between optical components change significantly over the ≈200 K change in temperature. As such, it is best to be able to adjust the focus after everything has reached operating temperature.

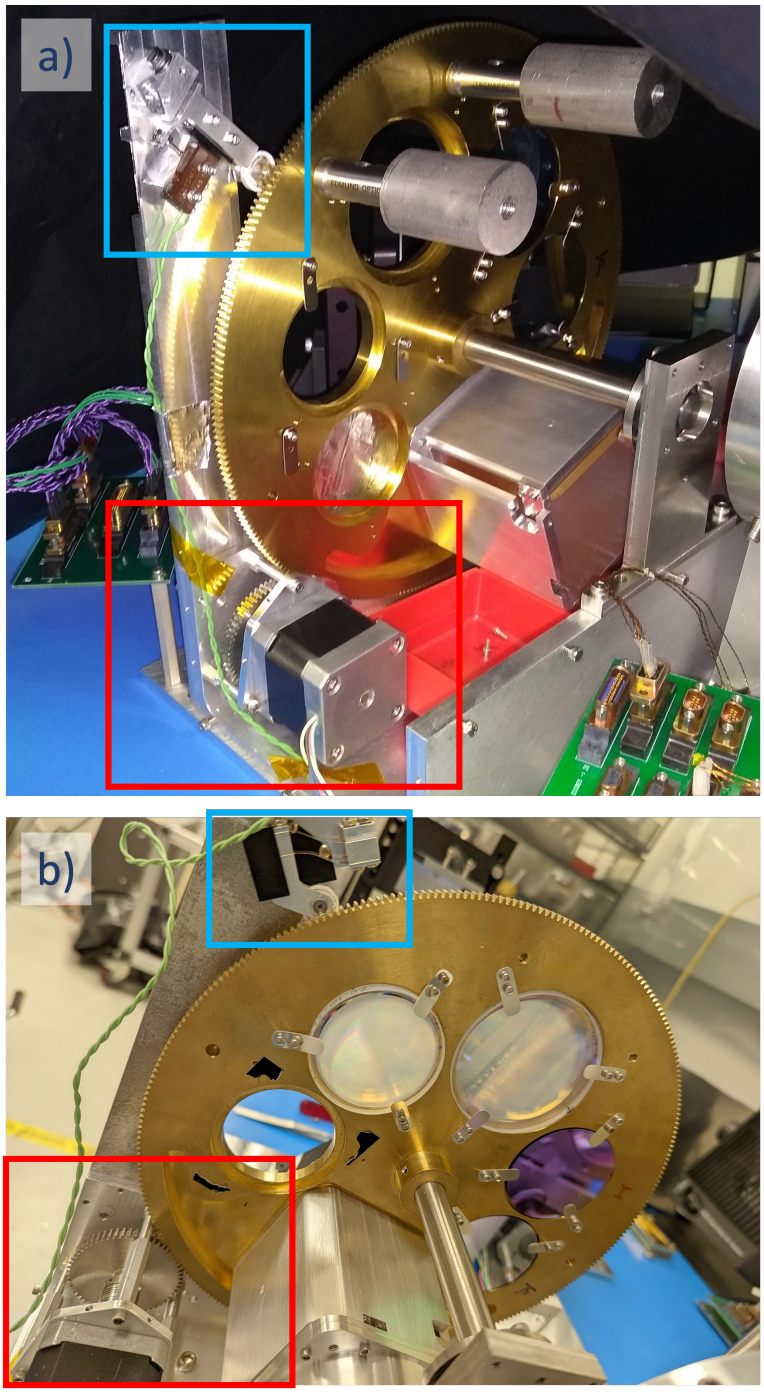


Figure 2.28: Filter wheel mechanism shown (a) early in the project, and (b) after multiple rounds of testing and modification. The motor assembly is circled in red, and the registration mechanism is circled in blue.

To accomplish this cryogenic focus stage assemblies (Figure 2.29) are used to adjust the position of each detector. The linear stage is made of two separate plates that can slide across each other, the bottom plate is mounted to the optical bench, and the detector (not pictured) is mounted to the top plate. The cryogenic Faulhaber stepper motor with its gearbox are mounted to the bottom stage plate, and its motor shaft is connected to the drive screw via spring coupler. The other part of the drive is mounted to the top stage plate, which converts the rotational motion of the motor to linear motion of the stage plate. On the opposite side of the stage, there are two limit switches that can be engaged by the adjustable screw stops. The motor is controlled by a Faulhaber motor driver, which is commanded by an Arduino Mega controller with custom code written by John Capone.[79] The Arduino controller prevents the motor from moving the stage in the direction of an engaged limit switch.

After the initial fabrication, it was important to test and modify these mechanisms to ensure robust repeatability of position, long lifetime, and operation at cryogenic temperatures. After assembly and confirmation of basic functionality, the stages were commanded to cycle from limit to limit many times using a lab weight to simulate the mass of the detector. The number of steps from these cycles were then checked for variability. Since there was very little variability, we could be sure that steps were not being missed, and movements were repeatable. This test was then successfully repeated with focus stages rotated $\pm 45^\circ$ and $\pm 90^\circ$. Once room temperature operation was confirmed, cryogenic tests could be performed. The first few tests at cryogenic temperatures mostly worked, but the positions were not repeatable. Once the mechanisms were warm and able to be inspected, it was discovered that there was excess wear on the gear boxes. Eventually, this issue

was tracked down to be caused by contraction of the aluminum part of the drive around the G-10 fiberglass drive screw. This was solved by re-tapping the threads with a slightly larger pitch diameter tolerance. After cleaning the gearboxes and reassembly, the stages were successfully tested at cryogenic temperatures.

2.4.7 Housekeeping Electronics

In order to ensure continuous function of the instrument, a number of items, need to be controlled and monitored. The electronics that perform these functions are referred to as housekeeping electronics.

2.4.7.1 Thermometry

In general, HgCdTd detectors need to be operated at temperatures of ≈100 K or less. Also, the various properties (dark current, nonlinearity, photosensitivity, etc.) of these detectors are subject to temperature, which makes controlling the temperature within a few millikelvin important in order to reduce read noise from the detectors. The temperatures of the detectors, ACADIAs, cold plate, cold shield, front assembly, camera lens assembly, and filter wheel motors are monitored by diodes. These DT-670 diodes are sensitive to temperatures across a wide range, from 1.4 K to 500 K.[102] The detector temperatures are controlled by 500 Ω resistor heaters. The diodes and resistors are connected to a breakout board developed by Vicki Toy, which allows for a 4-wire measurement of the detector temperature sensors and a 2-wire measurement of the other temperature sensors.[53] Initially, the detectors temperatures were measured and controlled by a Lakeshore 325 [103] and a

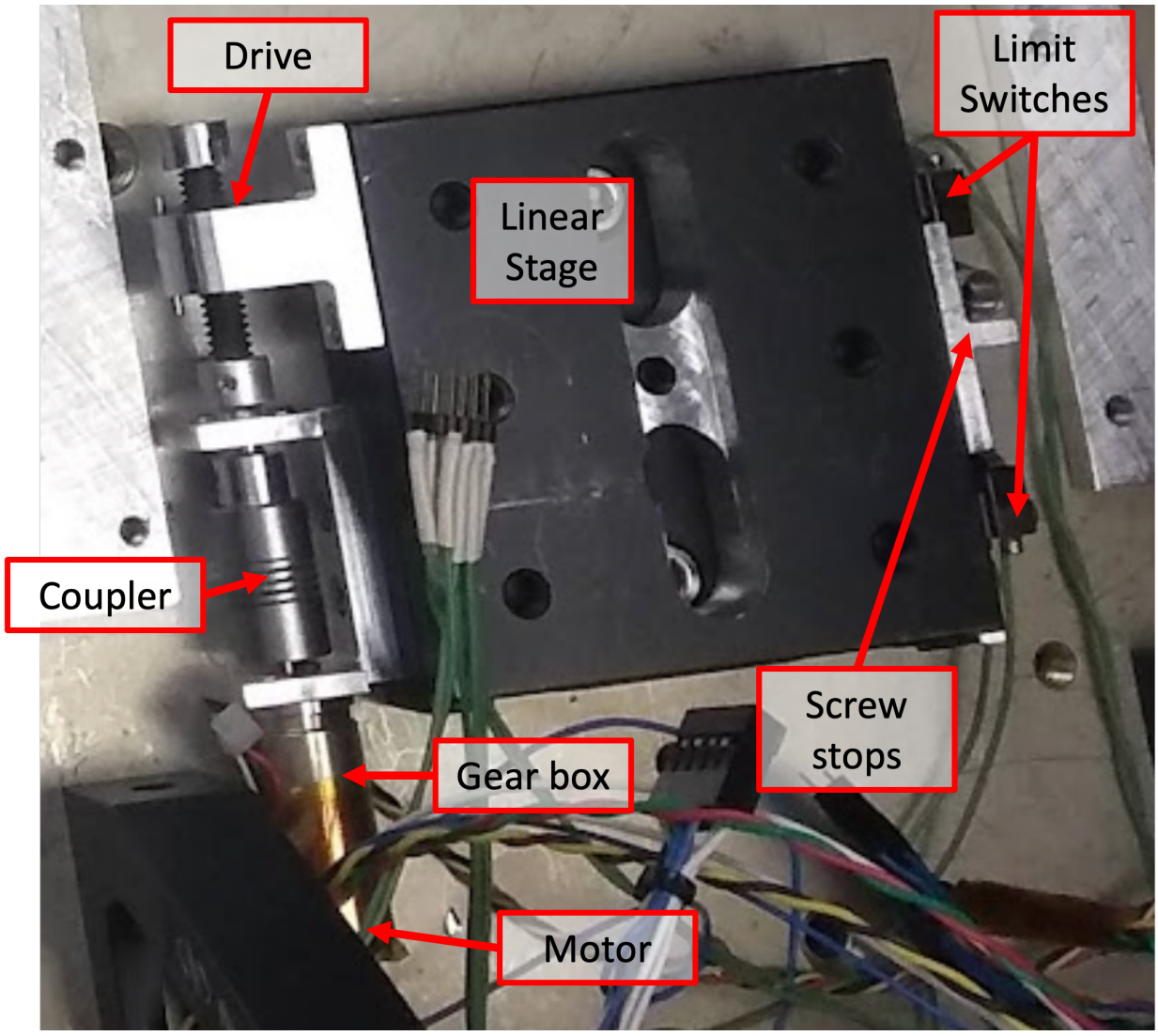


Figure 2.29: Labeled photograph of a focus stage mechanism, designed by Gennadiy Lotkin, showing the different components.

Lakeshore 331 [104] temperature controller, while the other eight temperatures were measured by a Lakeshore 218 [105] temperature monitor. This was done since these Lakeshore devices were already available in the lab, and each Lakeshore controller only had one powered control loop.[5] Over time, the performance of the Lakeshore 331 began to degrade such that the previously tuned Proportional Integral Derivative (PID) parameters no longer worked. As concerns began to grow over the use of multiple devices that could each need to be replaced eventually, a Lakeshore 336 with a four sensor expansion card was selected to do the tasks of all three previous Lakeshore devices. The Lakeshore 336 with expansion card can measure eight thermal sensors, and has two powered control loops.[106] This means that two fewer temperature sensors are measured than with the previous setup, but this was deemed an acceptable tradeoff for the reduction in hardware. After fabricating the necessary harnesses to incorporate the Lakeshore 336, the detector temperatures were able to be controlled within ± 1 mK using the previously tuned PID parameters. A diagram showing this setup can be seen in Figure 2.30.

Each of the detectors' temperatures need to be controlled within a few millikelvin to reduce read noise. This is accomplished by using a temperature sensor, a heater and a Lakeshore controller. The Lakeshore uses a PID control loop to determine the appropriate power to apply to the heater. A PID control loop, as described by Equation 2.3, uses predetermined constants to calculate the power needed to achieve a parameter through the use of three terms: proportional, integral, and derivative.[107]

[5] Each of these Lakeshore controllers have 2 control loops, one powered current loop and one unpowered voltage loop.[103, 104] To save on development time, we decided to use 2 controllers rather than develop and test an amplifier for the unpowered loop.

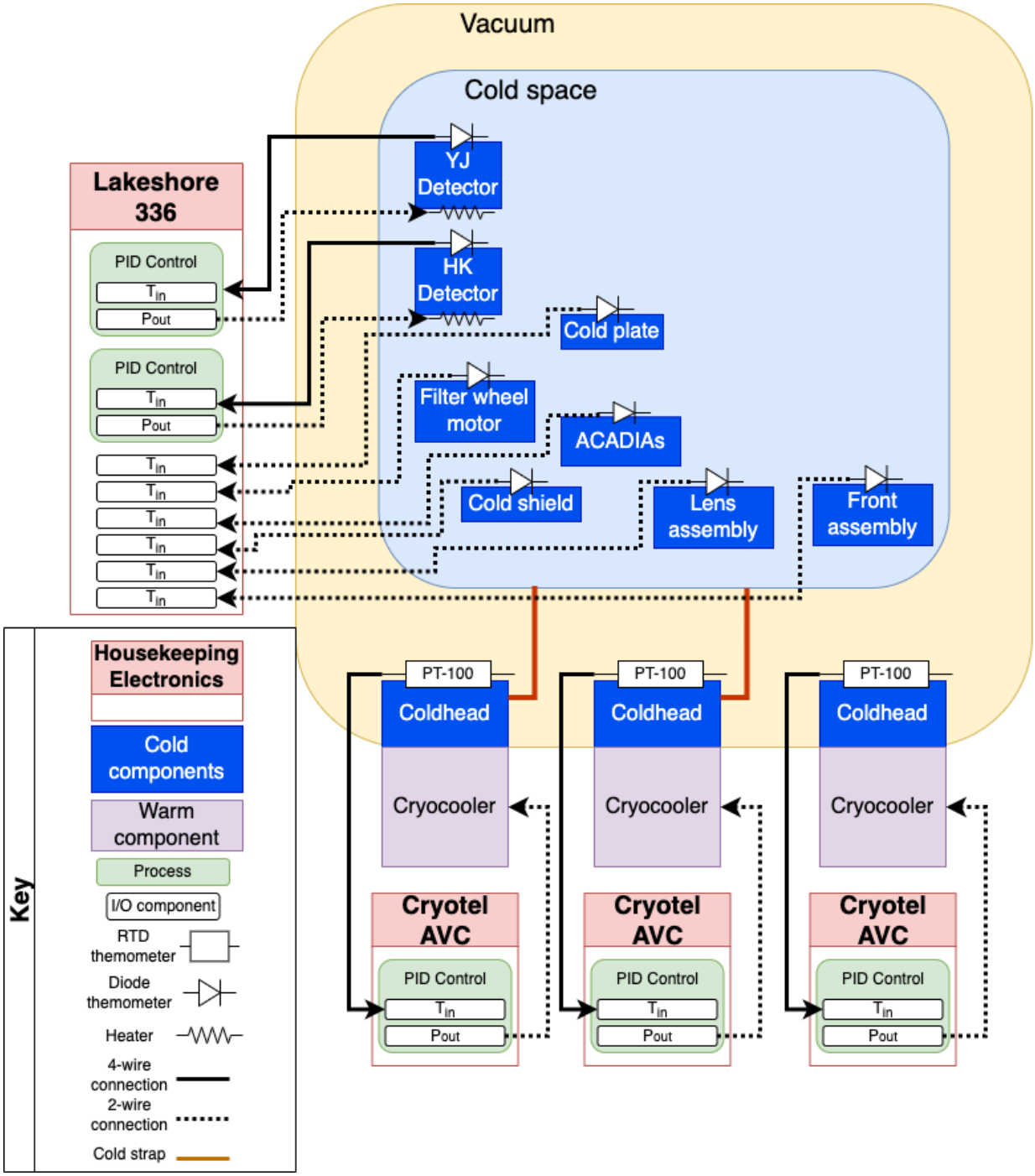


Figure 2.30: Diagram showing how the temperatures of various components are measured, and how they are controlled. The pale blue space is inside of the cold shield. The cold shield is under vacuum as shown by the pale yellow space. Everything else is outside of the dewar. The key describes the other components.

$$\text{Control Power} = P[e(t) + I \int e(t)dt + D\frac{de(t)}{dt}] \tag{2.3}$$

Where P, I, and D are constants, and e(t) is the difference between the set point and measured value for the parameter being controlled, temperature in this case. The proportional term is based on the difference between the current measured value and the control value. The integral is based on the summation of previous differences between the measured values and the control value. The derivative term is based on the rate of change of the difference between the current measured value and the control value. The Lakeshore 325 manual [103] tuning instructions were followed in order to determine the needed PID constants to maintain detector temperature. After choosing a set temperature a few kelvin above the current detector temperature, the proportionality constant, P, was determined by starting at a low value, 5, and doubling the value until sustained oscillations around the set point were achieved. This value, 160, was then halved so that the final value used was $P = 80$. The integral value was determined by taking the oscillating period of the sustained oscillations measured during the P tuning step, ≈60 s, and dividing 1000 by this period to get $I = 17$. Since changes to the set point should be rare, the derivative term is not necessary for this control, and thus $D = 0$. Once these values were determined for one detector, they were successfully tested on the other detector as can be seen in Figure 2.31.

Another part of RIMAS's temperature control is achieved through the use of its Cryotel GT cryocoolers, which are described in §2.4.8. Each of these three cryocoolers are operated by three Cryotel AVC controllers. These controllers measure the cold head temperature through the 4-wire measurement of a platinum resistor's (PT-100) resistance.

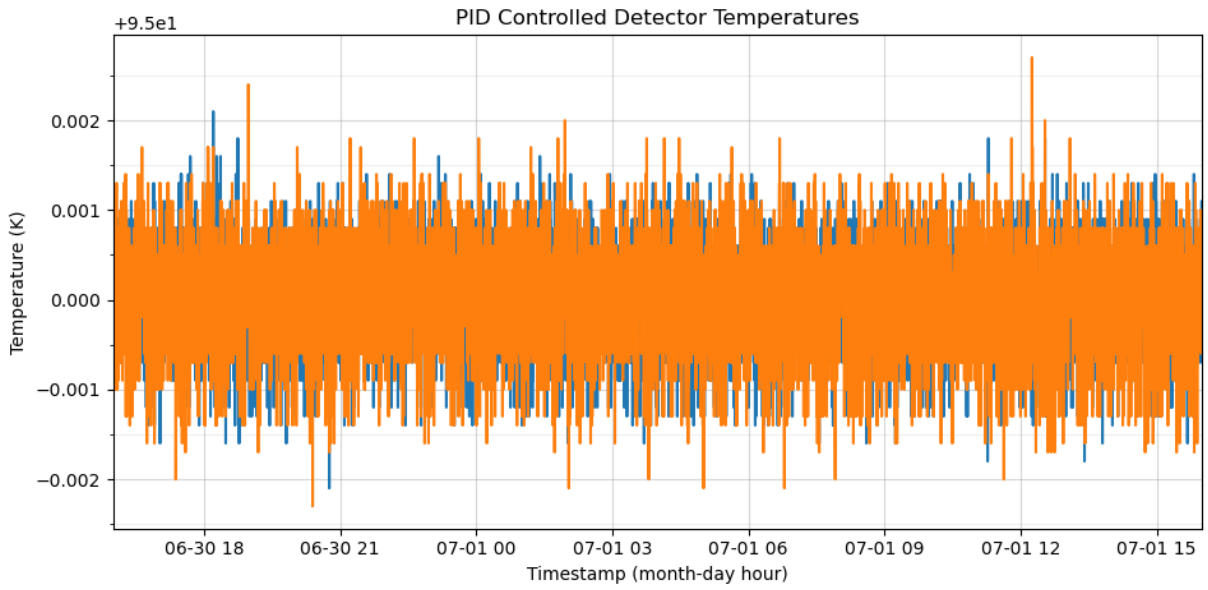


Figure 2.31: Plot showing temperatures of both detectors with the PID control loop enabled. As can be seen here, detector temperatures mostly stay within ±1 mK over a 24 hour period.

It then uses this temperature along with its' own PID control to determine the required power needed for the cryocooler as depicted in Figure 2.30. The factory default values for the PID constants were sufficient, so no further tuning was necessary. By keeping the cold head temperature constant, the rest of the components in the dewar maintain relatively constant temperatures, ±200 mK, as seen in Fig 2.32.

Since many of RIMAS's components are liquid cooled, it is important to ensure there is no condensation occurring that could harm the electronics. To check for this, there was a desire to measure humidity and temperature in each of the liquid cooled containers to check if the cooling lines were reaching the dew point. The initial solution for this was to read an Si7021 temperature and humidity sensor embedded in an Adafruit breakout board using a Micropython pyboard (Figure 2.33). The Si7021 can measure relative humidity

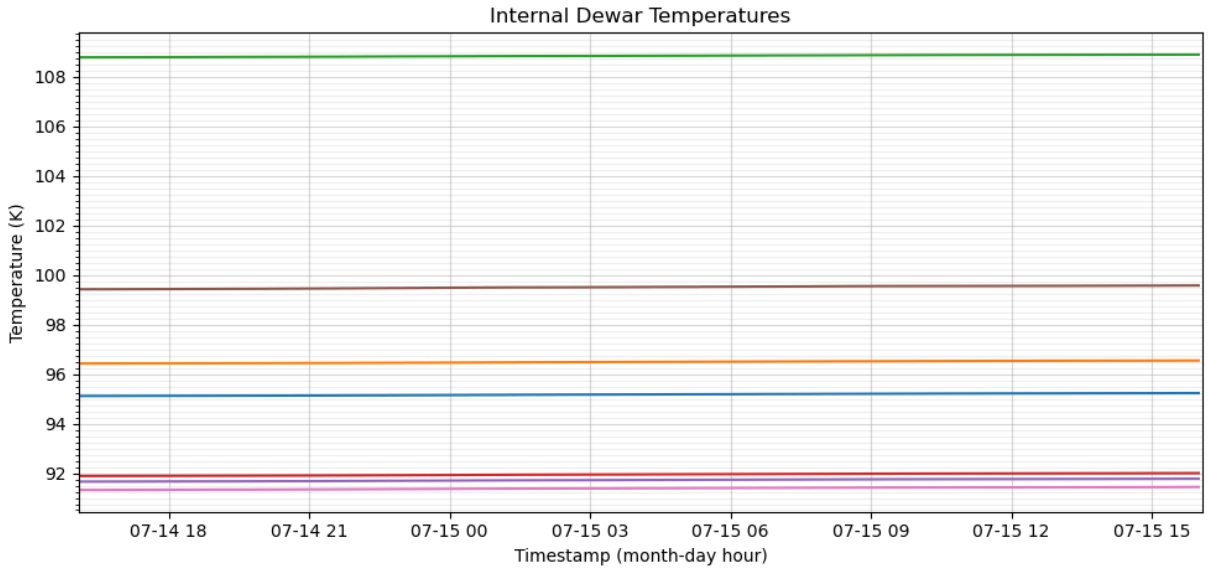


Figure 2.32: Plot showing temperatures of all items within the cold space. The detector PID loops are not enable during this period, so the only temperature control is coming from the cryocoolers. As can be seen here, all temperatures stay within 100 mK over a 24 hour period.

from 0 to 80% with an error of ±3%, and temperatures from -10 to 85 °C with an error of ±0.4 °C.[108] Pyboard is a development microcontroller board, similar to an Arduino, that runs on MicroPython.[109] Micropython is an adaptation of Python 3.4 for use with microcontrollers.[110] These two boards communicate with each other via I2C protocol, and then communicate with the PC via serial connection using custom code[6].[111] This setup worked relatively well for a while, however the code is uploaded to the pyboard as if it were a pyboard. This is convenient, however if the connection to the pyboard was unexpectedly interrupted, the storage would become corrupted. The corrupted file system could only be repaired via factory reset and reinstallation of the code, which would not work well at the observatory. After a lot of searching, a COTS temperature and humidity sensor with serial interface was found, and will be integrated as a replacement. The new temperature and humidity sensors can measure relative humidity from 0 to 100% with an error of ±3%, and temperatures from -40 to 80 °C with an error of ±0.3 °C.[112]

2.4.7.2 Pressure

A major requirement for RIMAS's cryogenics is to reduce thermal transfer by limiting convection. This is accomplished by lowering the dewar pressure into the high vacuum range, $\approx 10^{-6}$ mbar,using the methods discussed in more detail in §2.4.8.1. To be sure the dewar is continuously at this vacuum level, the pressure needs to be measured with a vacuum gauge. Multiple vacuum gauges were used during RIMAS's development, and can be seen in Figure 2.34. At the start of this thesis work, RIMAS's vacuum level was measured by a Pfeiffer FullRange™ Gauge. This gauge measures atmospheric pressure to

[6]https://github.com/joedurbak/htsensor

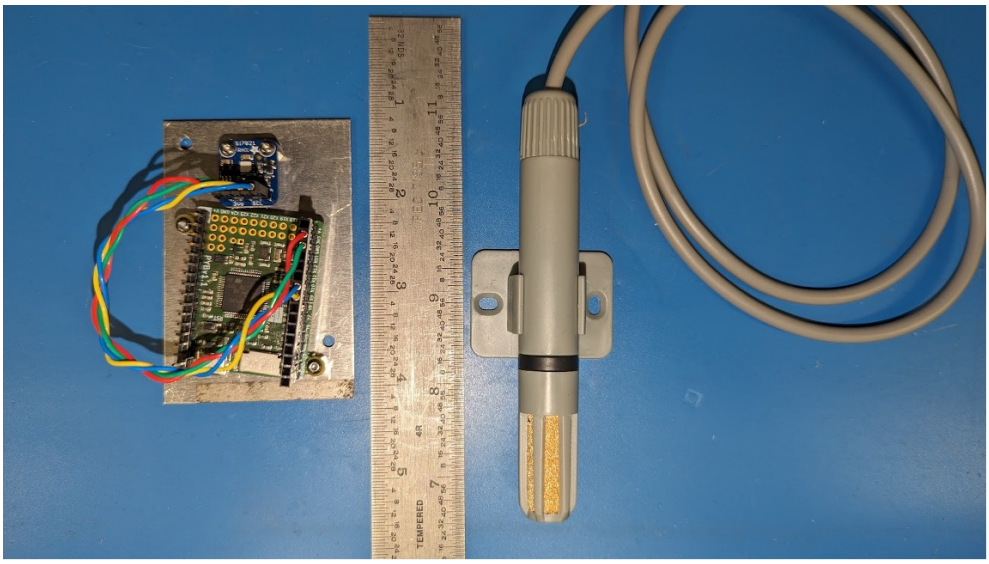


Figure 2.33: Photograph showing the different humidity and temperature monitors used to monitor RIMAS's housekeeping electronics. *Left:* The pyboard version is the green board on the left, and is connected to the Adafruit Si7021 breakout board. *Right:* COTS humidity and temperature sensor that will ship with the instrument.

medium vacuum using a Pirani gauge and measures high vacuum with a cold cathode gauge.[113] This gauge worked well, but required a bulky external controller. Since we found a more compact gauge for PRIME, a KJLC® 392 Series Wide-Range Combination gauge. This gauge seemed to be convenient since the controller and gauge are combined in a compact package, and the logging software was already integrated into the instrument control software for PRIME. The KJLC® 392 measures atmospheric pressure to medium vacuum using a convection enhanced pirani gauge, and high vacuum with an hot cathode ion gauge.[114] Further inspection however showed that the convection gauge is a separate unit that need to be connected separately from the ion gauge/controller package. At first, the ion gauge was used without a vacuum gauge, which only allowed for the measurement of pressures $< 10^{-3}$ mbar, which works for RIMAS's operating pressure. However, it is

difficult to detect when there are vacuum leaks early on in the cooldown without knowing the pressure at rough vacuum, so the convection gauge was installed next to the ion gauge using a KF-40 vacuum tee. Unfortunately, the convection gauge's calibration was poor, and was only useful for obtaining a rough estimate of the pressure trend instead of an exact value. Due to the issues with this bulky gauge assembly, it was replaced with an 972B DualMag™ Vacuum Pressure Transducer. This gauge, like the Pfeiffer FullRange™ Gauge, uses Pirani and cold cathode gauges to measure pressure from atmosphere to high vacuum.[115] Since both gauges and the controller are all in one package, and the pressure measurement was found to be reliable over the full range, this gauge will ship with the instrument.

2.4.7.3 Communications

RIMAS has quite a few components that require communication: MACIE, thermometry, cryocooler controllers, motor controllers, pressure gauges, PDUs, and humidity sensors. As various components have been replaced and upgraded, RIMAS's communication infrastructure has needed to undergo many iterations to handle the various communication protocols, specifically: serial, USB, and ethernet. In order to avoid routing extra communication lines between LDT's instrument cube and the observatory control room, the communication infrastructure for RIMAS was chosen such that all protocols were converted to ethernet in order to take advantage of the instrument cube's already existing network connection (Figure 2.35). The network switch used in the instrument cube was upgraded to accommodate the bandwidth needed for the MACIE detector data acquisition. The main

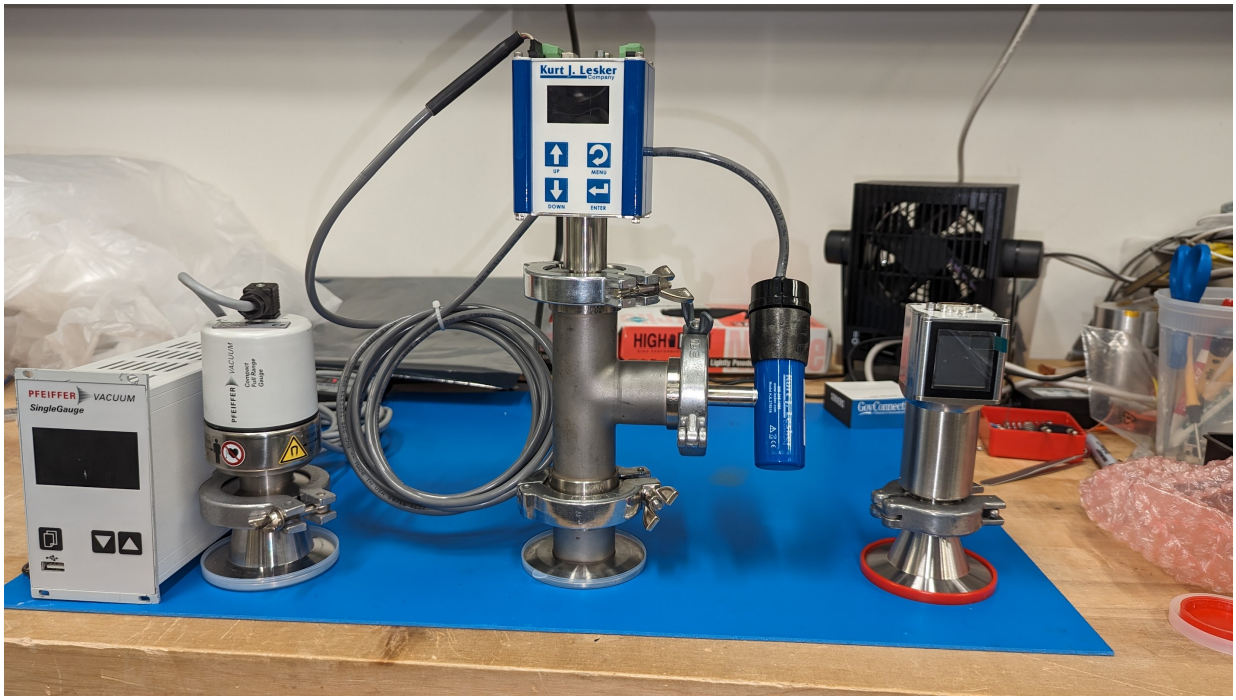


Figure 2.34: Photograph showing the various vacuum gauges that were used to measure RIMAS's vacuum with the needed fittings. *Left:* Pfeiffer FullRange™ Gauge with its controller, and a KF-50 to KF-40 adapter fitting. *Middle:* KJLC® 392 Series Wide-Range Combination gauge with a convection gauge, a KF-40 vacuum tee, and a KF-50 to KF-40 adapter fitting. *Right:* MKS 972B DualMag™ Vacuum Pressure Transducer with a KF-50 to K5-25 adapter fitting. This is the gauge that is shipping with RIMAS.

connection to this network is made via a single GigE connection from a Netgear GS105 ethernet unmanaged switch [116]. The MACIE and another Netgear GS105 (since there are too many ethernet connections for a single one of these 5-port switches) are connected with Cat6 cables capable of speeds >1 Gbps to allow for maximum communication speed. Both PDUs, the Lakeshore 336, and an Icron Ranger REX are connected to this second network switch via Cat5 cables capable of speed up to 100 Mbps. The lower speed for these connections reduces the bandwidth used by these devices, which helps reserve bandwidth for the detectors. The Icron Ranger 2304-LAN is a USB to LAN converter that allows for remote communication with USB devices as if they were plugged directly into the computer.[117] The Icron REX is located with the instrument, and is paired with an Icron Ranger LEX that is located with the control computer. This converter was recommended by Lowell as a replacement our previous converters that were not compatible with Windows 10. All USB devices are either connected directly to the Icron REX, or they are connected via a USB hub mounted to the dewar body. Serial devices are converted to USB using RS-232 and RS-485 serial to USB converters. These converters all use FTDI chipsets since these retain their COM port numbers using unique serial numbers unlike other converters that were tested.

There is an alternative communications setup (shown in Figure 2.36), where the control computer is located in the electronics rack with the instrument. This design is to be used if the Lowell network cannot support the bandwidth needed for RIMAS's detector data acquisition. The alternative setup requires fewer components since the USB to LAN converter and one of the network switches become unnecessary. Even though this design is simpler, it remains a backup option due to the risk of exposing the control computer to

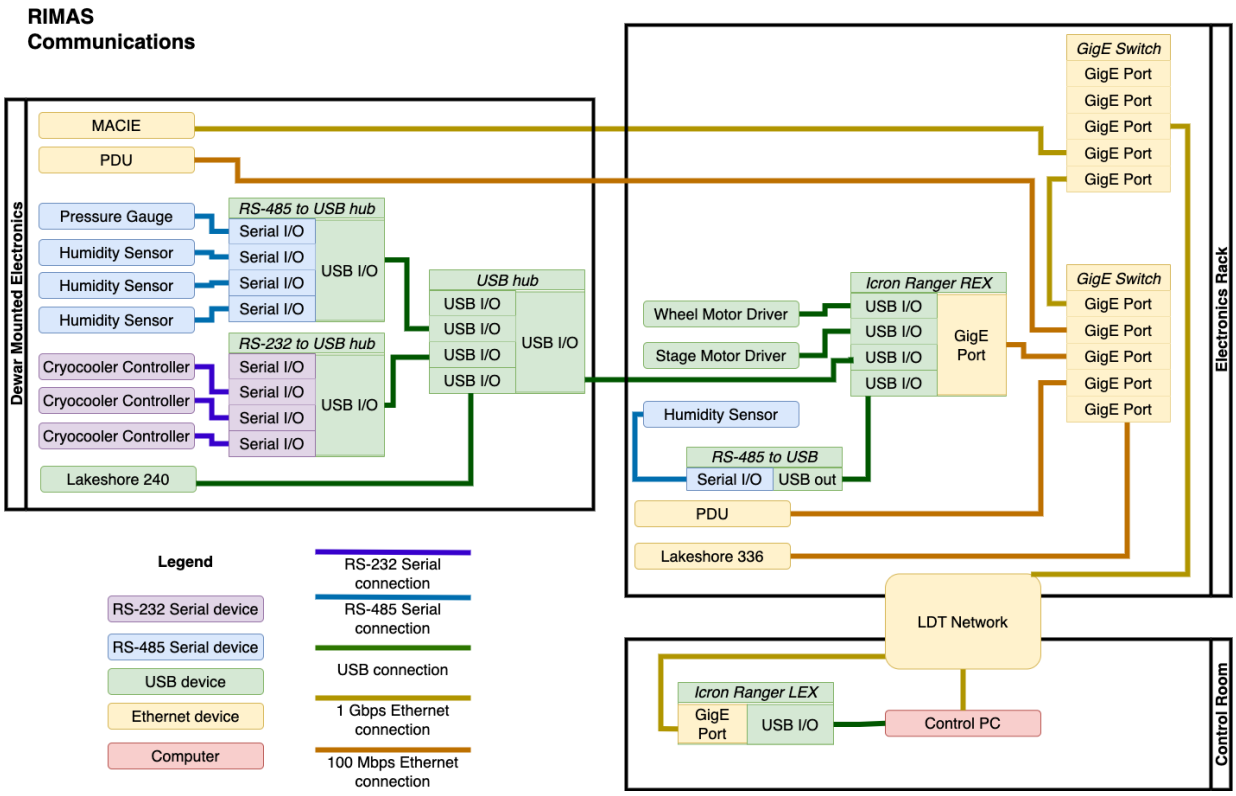


Figure 2.35: Diagram showing the current communication diagram for RIMAS. The dewar and the electronics rack are both under the dome and mounted to LDT's instrument cube. The control room is in a different room within the observatory.

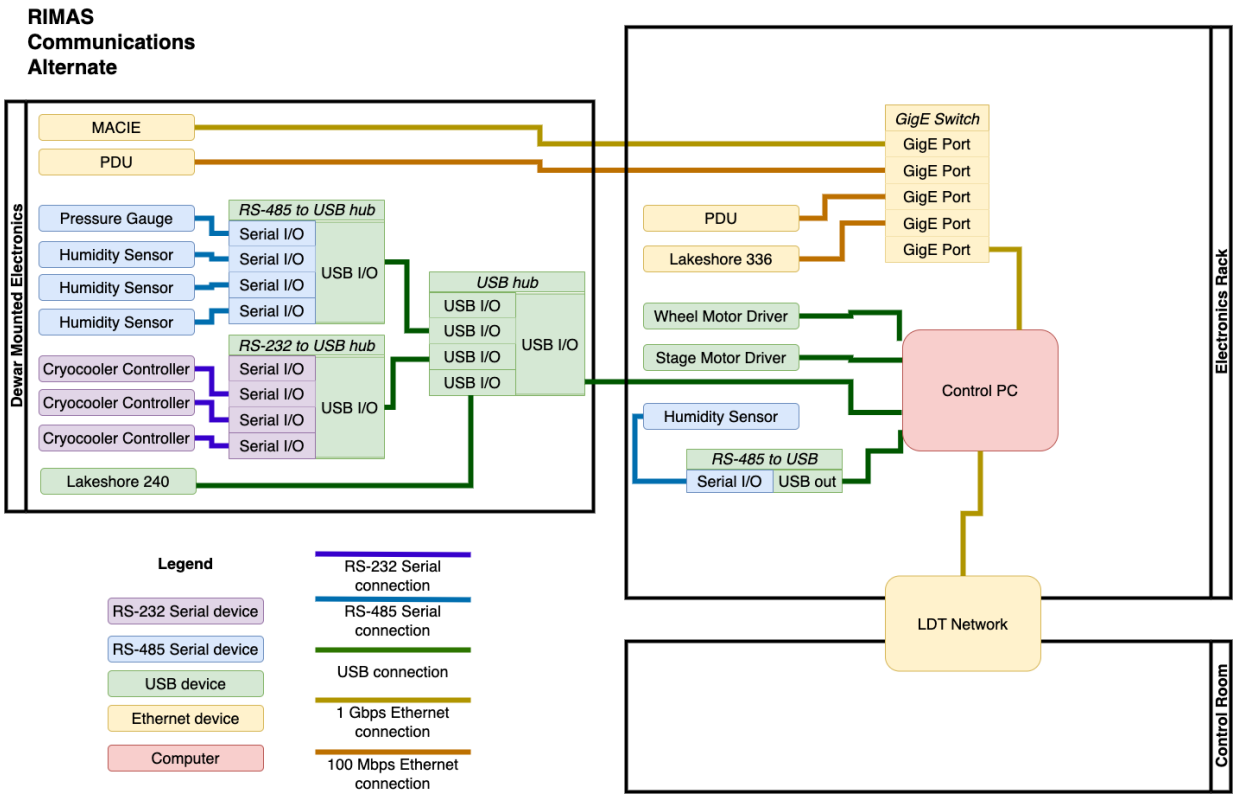


Figure 2.36: Diagram showing the alternate communication diagram for RIMAS where the control computer is located with the instrument.

the weather under the dome.

2.4.7.4 Power Supply

For practical and instrument protection reasons, remotely controlled power distribution units (PDUs) (Figure 2.38) are used to provide power to RIMAS's electronics. In the lab, there was an issue where one of the cryocoolers was permanently damaged because the water cooling lines became clogged by calcium build up. When this happened, the exterior of cryocooler overheated (temperature was above 60 °C), and this eventually caused the cryocooler to fail. There was also an issue, where a dewar was warmed up without turning

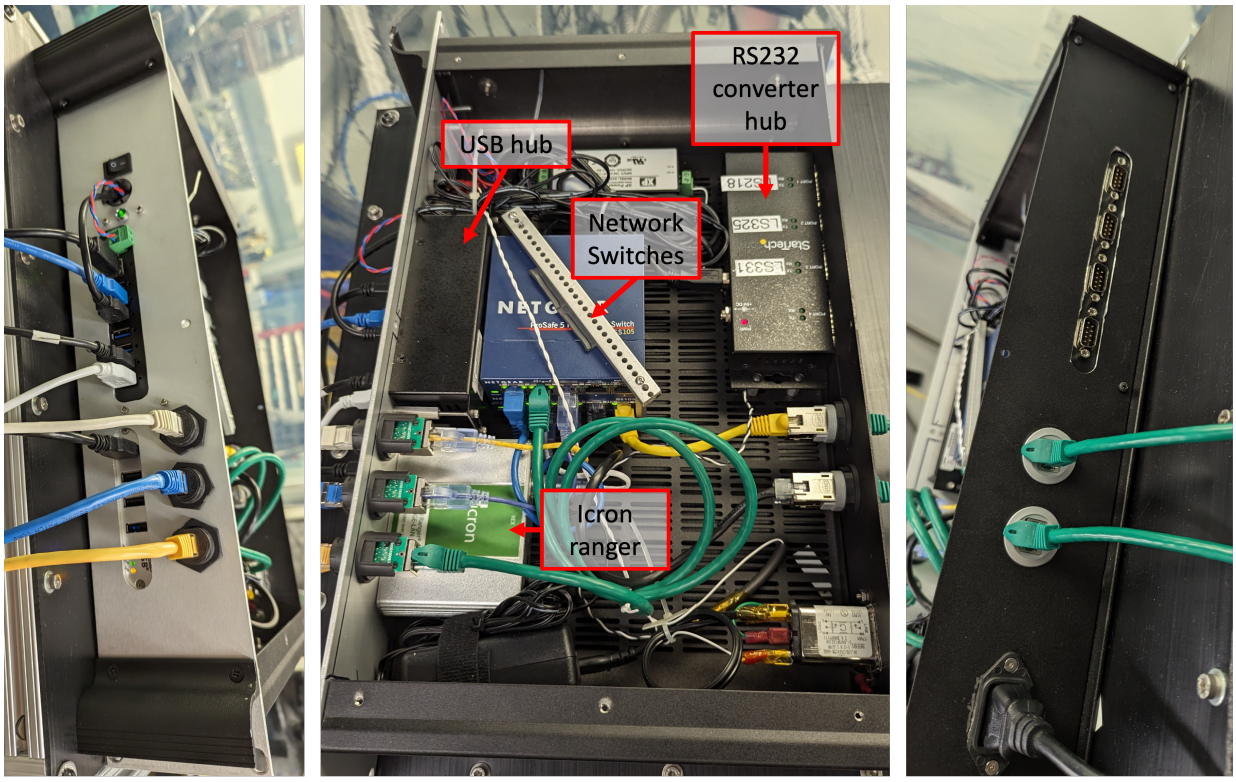


Figure 2.37: Photograph showing the rack mount communications module with the various components labeled.

off the detectors, which can cause increased dark current and hot pixels if left in this state for prolonged periods [83]. With these PDUs, the cryocoolers can be shut off automatically if the cryocoolers are overheating, and the detectors can be shut off if the instrument is too warm. Beyond preserving the instrument, various electronics need to be power cycled occasionally to clear errors, and light sources need to be controlled during calibration. It is impractical to have the telescope operator go under the dome to flip these switches on a regular basis. Another safety precaution taken with supplying power to the instrument is the use of thermostats. The thermostats shut off power to a device if they sense the temperature becoming too high. This is useful layer of security as it does not require software to function.

2.4.7.5 Mechanical

All of these housekeeping components need to be mounted somewhere near or on the instrument. Initially, all housekeeping electronics were stored on the electronics rack show in Figure 2.39. This rack is constructed from 80/20 T-slotted aluminum framing to fit standard width rackmount components, and fit within the space available in the LDT instrument cube. The standard width is useful for mounting COTS components, and the rack design makes it easy to swap out components. The electronics rack is mounted to the telescope using the assembly pictured in Figure 2.39(c). This mount is designed to be mounted to the telescope, while the rack is put into place using the T-Slotted aluminum framing as rails as shown in Figure 2.4. The rack is then locked into place using a toggle clamp, which allows for quick installation and removal of the rack. Other housekeeping elec-



b)

ORION FANS

Total load: 7.1 A , Status: Normal

Information

PDU

System

Control

Outlet

Configuration

PDU

Threshold

User

Network

Mail

SNMP

PDU	Status	
MACIE	ON	☐
Cryo1_3	ON	☐
Cryo2	ON	☐
Lesker	ON	☐
N/C	OFF	☐
N/C	OFF	☐
N/C	OFF	☐
Lamp	OFF	☐

ON OFF OFF/ON

Figure 2.38: (a) Photograph showing the power distribution unit outlet strip that is located in the electronics rack. (b) Screenshot showing the interface to control the outlets remotely.

tronics were added later for the upgraded cryocoolers, and were mounted to the cryocooler vacuum plate as seen in Figure 2.42.

All of these housekeeping components emit heat, and need to be cooled. In the lab at sea level, this is accomplished with airflow for all of the electronics, while the cryocoolers require liquid cooling to improve their efficiency. However, at the observatory the air density is reduced due to altitude, and convection around the telescope worsens seeing. Instead of using ambient airflow, a chilled glycol-water supply is used to cool these components using the plumbing setup shown in Figure 2.40. Using the input and output manifolds, the individual components are chilled in parallel. The cryocoolers have their own water cooling jackets installed, while the other components are chilled using liquid cooled aluminum heat exchanger plates.

2.4.7.6 Motor Controllers

There are two motor controllers, one for the linear stages, and one for the filter wheels. These controllers are essentially unchanged since John Capone's thesis work. Both consist of Arduino Mega 2560 microcontrollers, which command a stepper motor controller specific to the motor being controlled. These controllers communicate with the control computer via serial interface.[79]

2.4.8 Cryogenics

RIMAS is a fully cryogenic instrument, with its optics, filters, gratings, mechanisms, and detectors operating at temperatures ranging from 80 to 100 K. This is important since

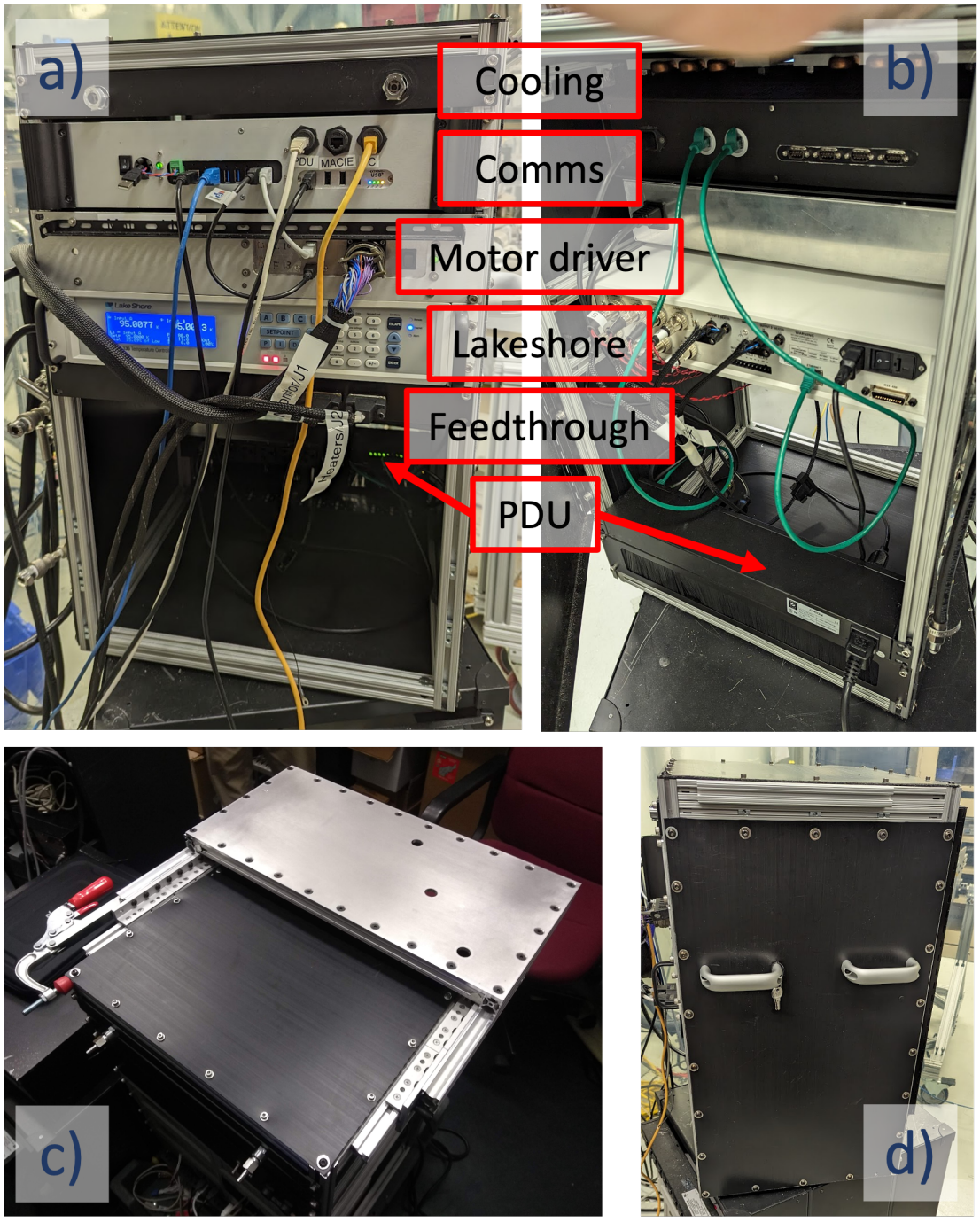


Figure 2.39: Photographs of the electronics rack from multiple angles. (a) Shows the front of the rack with the various rack mount boxes labeled. (b) Shows the back of the rack with the various rack mount boxes labeled. (c) Shows the top of the rack with the telescope interface plate, and slide mount. The toggle clamp locks the rack into place. (d) Shows the side of the rack with the handles to assist with mounting.

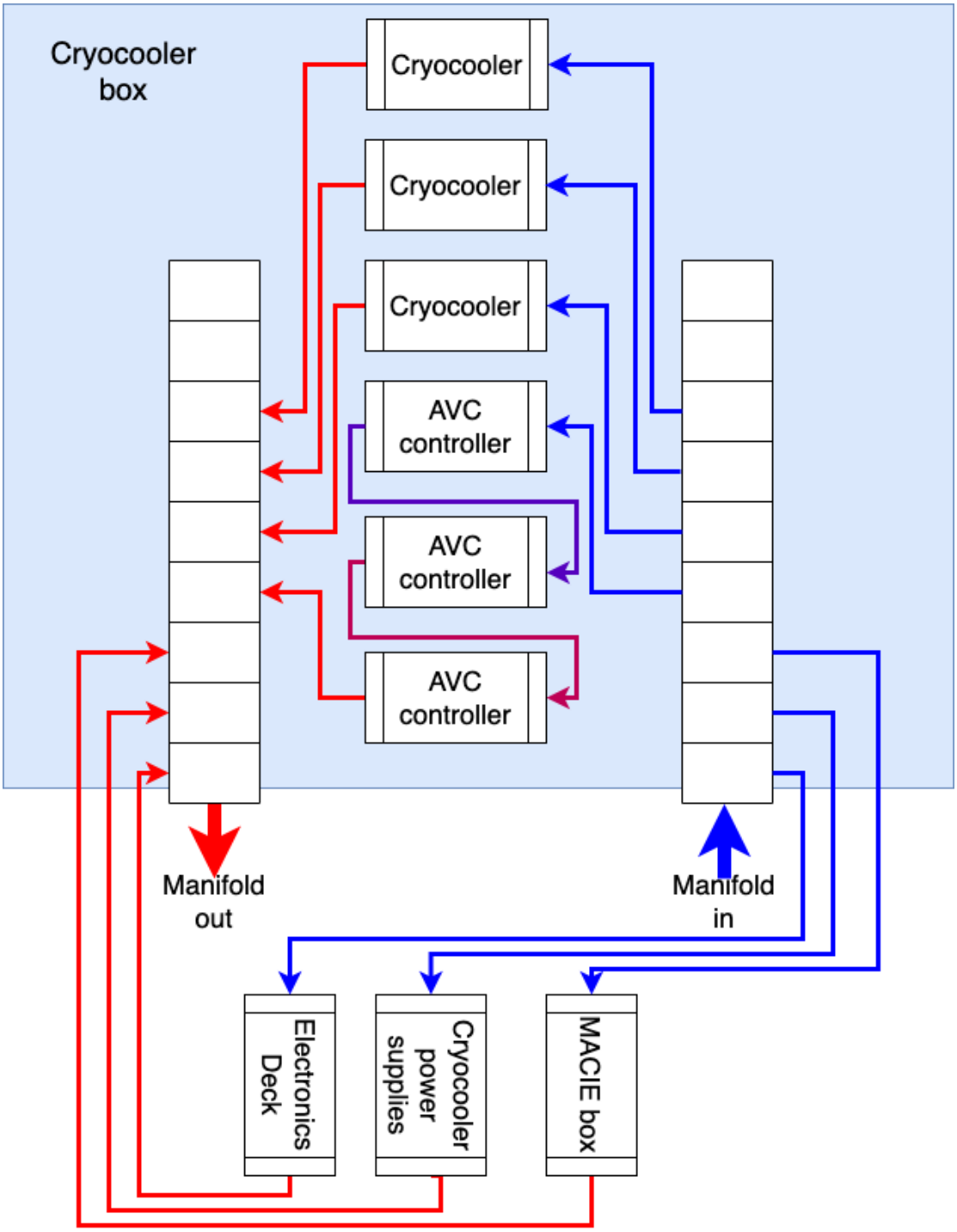


Figure 2.40: Diagram showing the plumbing setup to provide chilled water cooling of various components. There is a valve limiting flow entering the manifold input, and there are also valves limiting flow to every component that is not a cryocooler.

it reduces noise via thermal emission from the components as well as dark current and read noise in the detectors. To accomplish this, a method of cooling and thermal isolation are required.

2.4.8.1 Thermal Isolation

In order to achieve cryogenic temperatures, thermal isolation is a necessity. This involves cutting off all three modes of heat transfer: conduction (Eq. 2.4), convection (Eq. 2.5), and radiation (Eq.2.6). In each of these equations $\dot{Q}$ is the heat transfer rate, T_1 is room temperature, and T_0 is the cryogenic temperature.

$$\dot{Q}_{conduction} = \frac{kA_{conductor}(T_1 - T_0)}{d} \tag{2.4}$$

Where k is the thermal conductivity, $A_{conductor}$ is the cross sectional area of the conductor, d is the length of the conductor.

$$\dot{Q}_{convection} = hA_{coldsurfaces}(T_1 - T_0) \tag{2.5}$$

Where h is the heat transfer coefficient, and $A_{coldsurfaces}$ is the surface area of the cold surfaces. The heat transfer coefficient is dependent on the makeup, density and flow of the fluid.

$$\dot{Q}_{radiation} = \sigma eA(T_1^4 - T_0^4) \tag{2.6}$$

Where e is the emissivity coefficient of the surface, and A is effectively the outermost

cold surface (the cold shield in this case). The emissivity coefficient is dependent on the reflectivity of the surface, so a perfectly absorptive surface would have $e = 1$, and a perfectly reflective surface would have $e = 0$.

Conduction is minimized by mounting the cold assembly within the dewar using low thermal conduction materials for anything creating a mechanical connection from the exterior of the dewar to the cold assembly. For RIMAS, G-10 fiberglass laminate mounts are used to connect the cold assembly to the warm dewar body. Furthermore, high gauge (> 30 AWG) wire is used for the electrical connections in order to keep the diameter (and thus the cross-sectional area, A) of the wires small, and alloy conductors (e.g. phosphor-bronze and manganin) are used when current need are well below the fuse current. Appropriate alloy wire conductors have high electrical conductance, and low thermal conductance, k. Convection is minimized through the use of a high vacuum chamber, a turbomolecular pump, and cryopumping from the cryocoolers. Outgassing is reduced by choosing low-outgassing materials for objects within the dewar, and cleaning parts with an ultrasonic cleaner. The reduction in fluid density created in the high vacuum environment greatly reduces the heat transfer coefficient in Eq. 2.5. Finally, radiation is reduced through the use of multilayer aluminized mylar insulation, which reduces the emissivity constant, e,of the cold surfaces. The RIMAS's outer cold shield surface, anodized aluminum, has an emissivity constant of ≈0.8 [118], whereas the aluminized mylar has an emissivity constant of 0.03 [118]. Mylar also has low thermal conductivity, so the multiple layers help to ensure that there is a smaller thermal gradient between layers, and thus also lower the T^4 term for each layer.

After switching to the new cryocoolers and adding the ACADIAs, the detector tem-

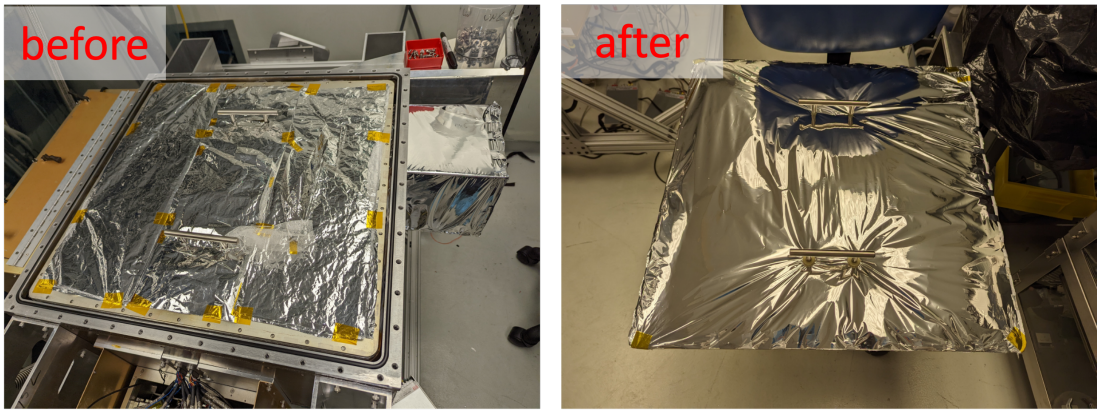


Figure 2.41: Photographs of RIMAS's cold shield lid before and after the radiation load was improved. This is an example of how the entire cold shield multi-layer insulation was improved by reducing the exposed surface area, and increasing the number of mylar layers.

peratures were still above the desired operating temperature of 95 K. The new cryocoolers and cold straps have less cooling power than the initial cryocooler and cold strap. The ACADIAs each output ≈0.5 W, adding a total load of ≈1 W. Although another cryocooler could be added to reduce the temperature by increasing the cooling power, the less resource intensive option is to increase the thermal isolation. Since convection and conduction have already been minimized, and radiation heat transfer is a large term dominated by T_1^4 the simplest option was to improve the thermal isolation from radiation. Given that this term depends on both surface area and the emissivity coefficient, these are the terms left to minimize. This is accomplished by increasing the number of mylar layers to reduce the emissivity coefficient, and ensuring that the mylar covered more of the cold shield to reduce the effective surface area as shown in Figure 2.41.

2.4.8.2 Cryocoolers

Initially, RIMAS used a 2-stage Gifford-McMahon cryocooler [119], where one stage was connected to the cold plate at ≈80 K and the other stage connected to the slit-viewing camera at ≈20 K. This cooler required an external compressor and long helium lines for the cooling cycle and heat exchange. Since this setup was inconvenient for operations at the telescope, a recently developed set of Stirling cryocoolers [120] were chosen as a replacement. These cryocoolers have a number of benefits as they are much more compact, contain a compressor within the single unit, can be controlled with a PID (Proportional Integral Derivative) loop, have active vibration cancellation, and require no servicing. The coolers are more compact since there is no external compressor, and are more convenient for use in the field as they only require already existing water cooling and electrical infrastructure. The PID control of the cryohead allows for very consistent temperatures throughout the instrument, which helps further reduce background noise. Active vibration cancellation is also important as it minimizes shaking of the instrument, and the telescope to which it is mounted. Shaking needs to be minimized in order to avoid spread in the PSF. The closed system prevents contaminants in the helium used as the cryogen. With the previous cryocooler, it was necessary to regularly service the cryocooler by pumping out the lines and replenishing them with ultra-high purity helium. For self evident reasons, this is difficult to accomplish in the field, and is best to be avoided.

These new cryocoolers required thermal, vacuum, electrical, and data integration and testing. After copper cold straps were manufactured and installed to connect the cold heads to the cold plate, the desired maximum operating temperature of ≈90 K was reached using

two cryocoolers. The vacuum integration involved installing the new bottom dewar lid and a vacuum plate with ports for the new cryocoolers and the new PID thermometry hardware. At this point a helium based leak detector was used to find any issues with the large number of new vacuum interfaces that were introduced. When leaks were detected, efforts were made to remove any surface scratches on the vacuum interfaces, and clean any foreign objects from the o-rings. Even with these leaks removed, there were issues maintaining vacuum with the higher base temperature since the lowest temperature in the dewar was now ≈70 K at the cold heads instead of the previous cryocooler coldest temperature of ≈10 K. This increase in base temperature greatly reduced the cryopumping rate, and the gasses that could be removed via cryopumping. To solve this issue, a third cryocooler was added, and instead of connecting it to the cold plate like the other two coolers, a copper container filled with charcoal was mounted to the third cold head. Not strapping the third cryocooler to the cold plate greatly reduces the thermal load on this cooler, and allows for a much colder temperature of ≈40K. The charcoal increases the surface area that is available to condense gasses, and is also more effective at binding gasses at higher temperatures than metallic surfaces.[121] Electrical integration was fairly trivial, as it just required acquiring appropriate DC power supplies that are connected to the PDUs. Data integration required programming the serial interface in LabVIEW so that the status could be logged, and the operating mode (constant power or constant temperature) can be set.

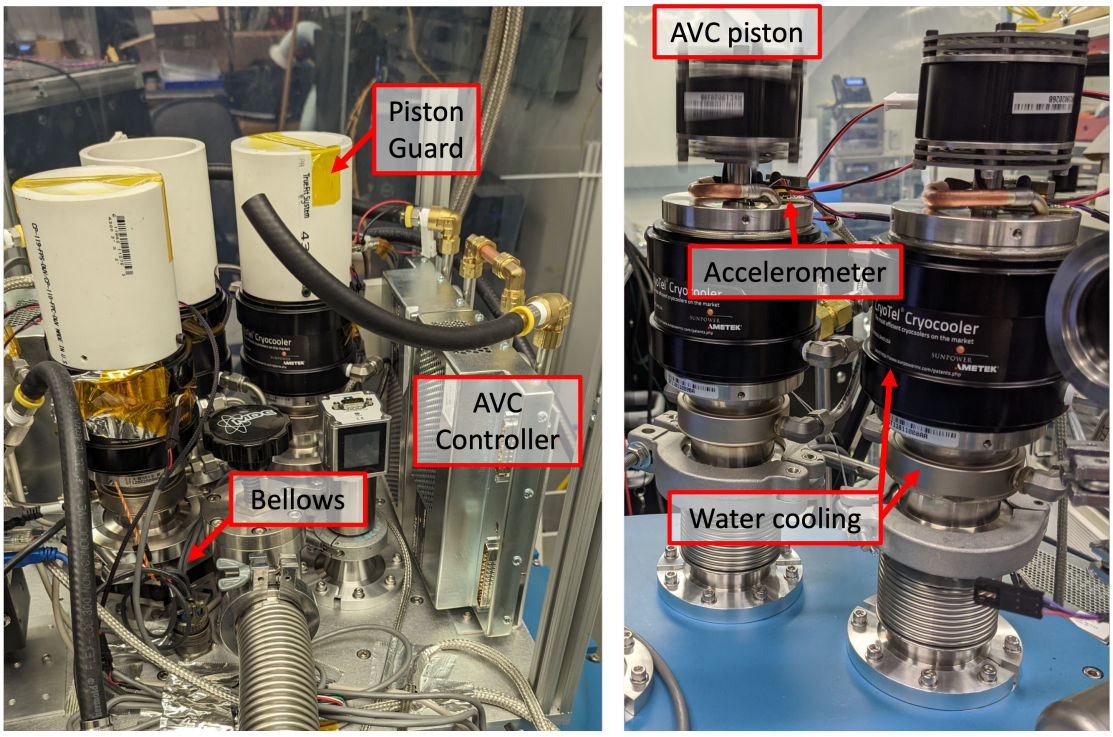


Figure 2.42: Photographs of the Cryotel GT Cryocoolers with interesting parts labeled. The AVC controller provides PID controlled power to the cryocooler with temperature input from the PT-100 sensor located on the cold head (not pictured). This controller also uses a feedback loop given data from the accelerometer to control the vibration cancelling piston. The water jacket cools the cryocooler exterior and is monitored by another temperature sensor. If this exterior temperature is too high, the AVC controller shuts off the cryocooler.

2.4.9 User Interface

Since the primary goal of RIMAS is to quickly follow up Swift detections, it is advantageous to obtain the alerts as quickly as possible. Fortunately, the General Coordinates Network (GCN[7]) exists as a purpose-built communication method between multiple instruments to alert others to interesting astronomical events so that they can be quickly observed by others.[59] These GCN alerts are shared via GRB coordinate notices distributed in real-time, and follow-up message circulars shared between observers.[122] When this interface was developed, GRB coordinate notices were distributed using many methods: socket (0.1-0.5 seconds), email (5-100 seconds), and other methods that are no longer used such as pager, dialed phone/modem.[123] Most of these notices are automatically generated, and are quickly available after detection. Since the development of this software, the GCN migrated over to a new standardized Kafka protocol [124], which has yet to be incorporated. Since the Kafka standardized protocol incorporates VOEvent XML, converting to this system should be relatively uncomplicated. GCN circulars are messages sent between various groups "to share discoveries, observations, quantitative near-term predictions, requests for follow-up observations, or future observing plans related to high-energy, multi-messenger, and variable or transient astrophysical events."[125] These circulars are typically much slower than notices, and require interested parties to actively share information. This happens when a particular team wants to advocate for further observations, or has completed observations/analysis of an event.

To take advantage of the GCN and accomplish RIMAS's science goals more effectively,

[7]GCN was previously known as the Gamma-ray burst Coordinates Network.

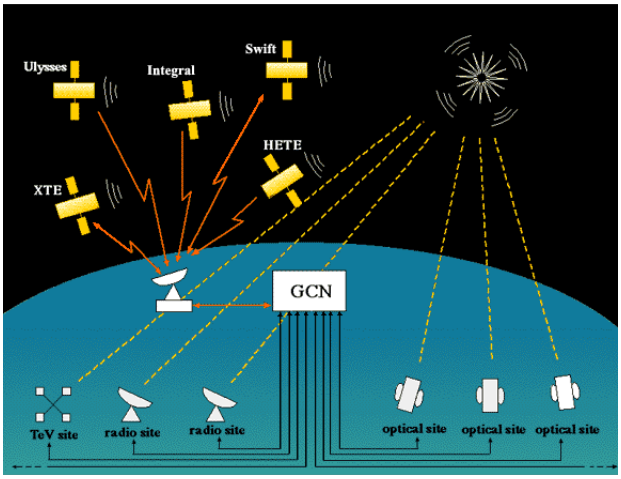


Figure 2.43: Picture showing the layout of the GCN where both space and ground-based telescopes communicate with each other while observing a target.[126]

a GCN listener was developed to alert observers when a new event is currently observable with RIMAS with minimal latency.[127] Since the GCN communication method with the lowest latency is the socket method, this was the method chosen for this listener. Fortunately, there was already an available GCN client written in Python [128] that could be used to retrieve XML formatted VOEvents (Virtual Observatory Events). With this client, the different types of events are easily filtered based on information about the VOEvent such as the notice type. Based on RIMAS's FOV, only SWIFT BAT, XRT and UVOT notices are used for this monitor. After the XML messages are received, they are then converted to HTML to make them human readable. HTML is a subset of XML, which made converting between the two quite natural. During this conversion process, important information, such as the coordinates, is extracted for further calculations and filtering. Using the detected object's coordinates and tools from astroplan [129], important information pertinent to observations can be quickly calculated. This information includes target rise

time, set time, and general observability based on the instrument's location. Once all of this is calculated,the XML has been converted to HTML and the target is determined to be observable, the user is then alerted via the LabVIEW virtual instrument (Figure 2.44) that is easily integrated into RIMAS's LabVIEW user interface.

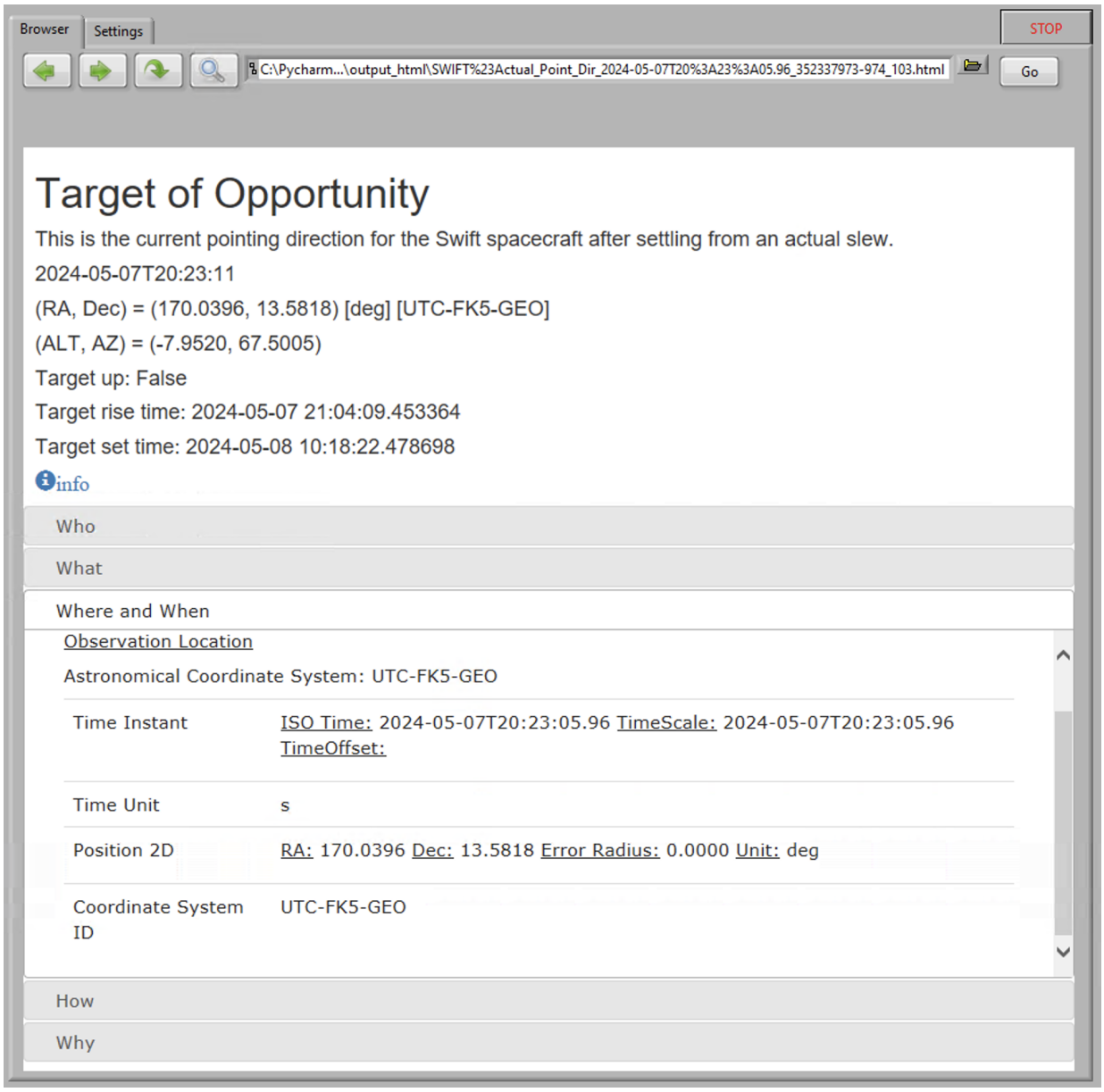


Figure 2.44: Screenshot showing the appearance of the GCN alert after it has been converted to HTML.

Chapter 3: RIMAS Data Reduction

3.1 Overview

With RIMAS's numerous modes of operation (cross-dispersed spectrograph, two low resolution single order spectrographs, and photometric imaging), multiple data reduction pipelines are needed to handle RIMAS's outputs. This section discusses the development of pipelines for both the cross-dispersed spectrographs and photometry. The pipeline for RIMAS's single order spectrographs have yet to be developed.

3.2 Detector Data Reduction

Unlike CCDs, the pixel voltages on these hybrid detector arrays can be read non-destructively, which allows for multiple samplings as data is acquired during an exposure (e.g. sample-up-the-ramp or SUTR). Due to this ability, there are multiple methods that can be used to improve the SNR of any individual exposure using different sampling methods, which are discussed throughout this section. On top of SUTR, these arrays and readout electronics use reference pixels, and reference output voltages to allow for further reduction of noise.

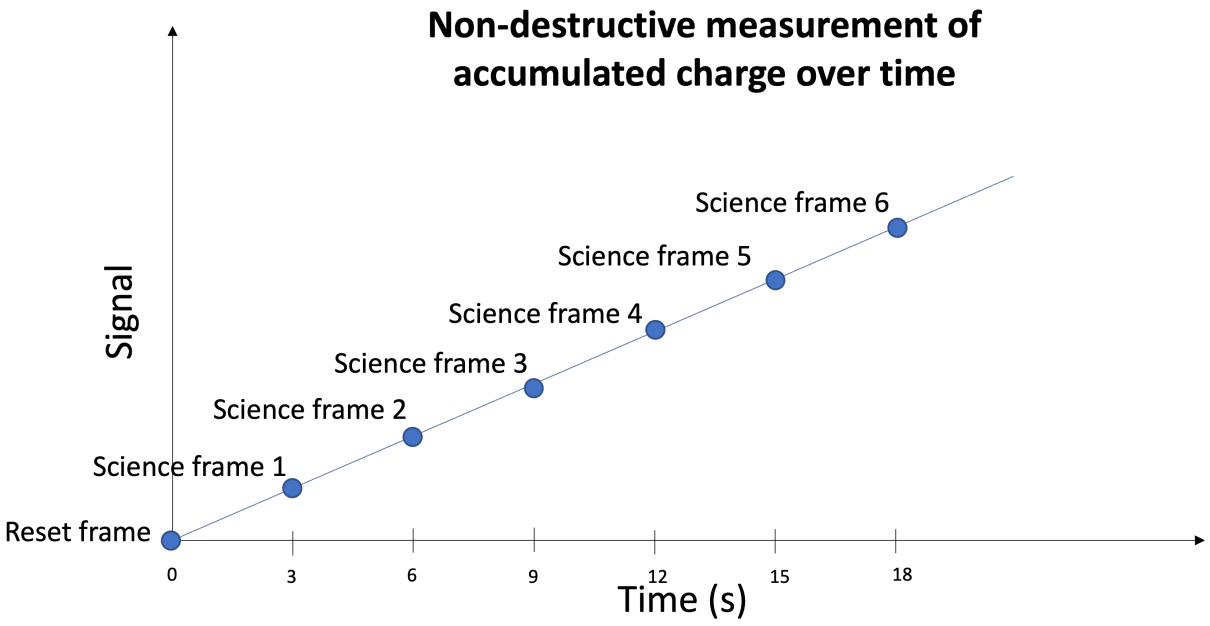


Figure 3.1: Plot showing how signal is measured non-destructively as charge accumulates on the detector array.

3.2.1 Sample Up the Ramp

The ACADIAs are programmed such that they consistently read the detectors at all times in consistent intervals (every 2.86 s with our settings) regardless of whether the detectors are idling, being reset, or acquiring an exposure. All of the frames acquired during the exposure are saved as signal accumulates, as demonstrated in Figure 3.1. Since the pixels are clocked consistently throughout these exposures, the time between each pixel measurement is the same for each pixel. Furthermore, the pixel voltages are reset pixel by pixel using the same clock, so the time since the voltage reset is the same for each pixel as well. Since every frame is saved, a number of different data reduction, and/or sampling methods can be used later on to reduce a set of SUTR frames into a single exposure image

later.

3.2.2 Fowler Sampling

The simplest way to reduce SUTR data is correlated double sampling (CDS) where a pedestal frame (typically the first frame in the exposure) is subtracted from the signal frame (typically the final frame in the exposure). This removes the bias signal from the exposure, and reduces the read noise by sampling each of the pixels twice. A slightly more sophisticated method of sampling is Fowler sampling, where multiple frames are averaged for the pedestal frame, and the same number of frames are averaged for the signal frame in order to further reduce read noise.[130] This Fowler sampling is described by Eq. 3.1, where the resultant value, R, for a pixel, (i, j), is given by averaging the value for that pixel over a number of samples, N, for the signal frames, S_n, and the pedestal frames, P_n, and taking the difference.

$$R^{ij} = \frac{\sum_{n=1}^{N} {S_n}^{ij}}{N} - \frac{\sum_{n=1}^{N} {P_n}^{ij}}{N} \tag{3.1}$$

CDS can be thought of as a special case of Fowler sampling where $N = 1$. An example of Fowler sampling where $N = 4$ is shown in Figure 3.2. This figure also nicely demonstrates how the effective exposure time is calculated as the difference between the starts of each group of samplings. Although increasing N reduces the read noise, it also decreases the amount of signal present in the resultant image for the same total time since resetting the pixel voltages. This balance is important to keep in mind especially for exposure times limited by saturation.

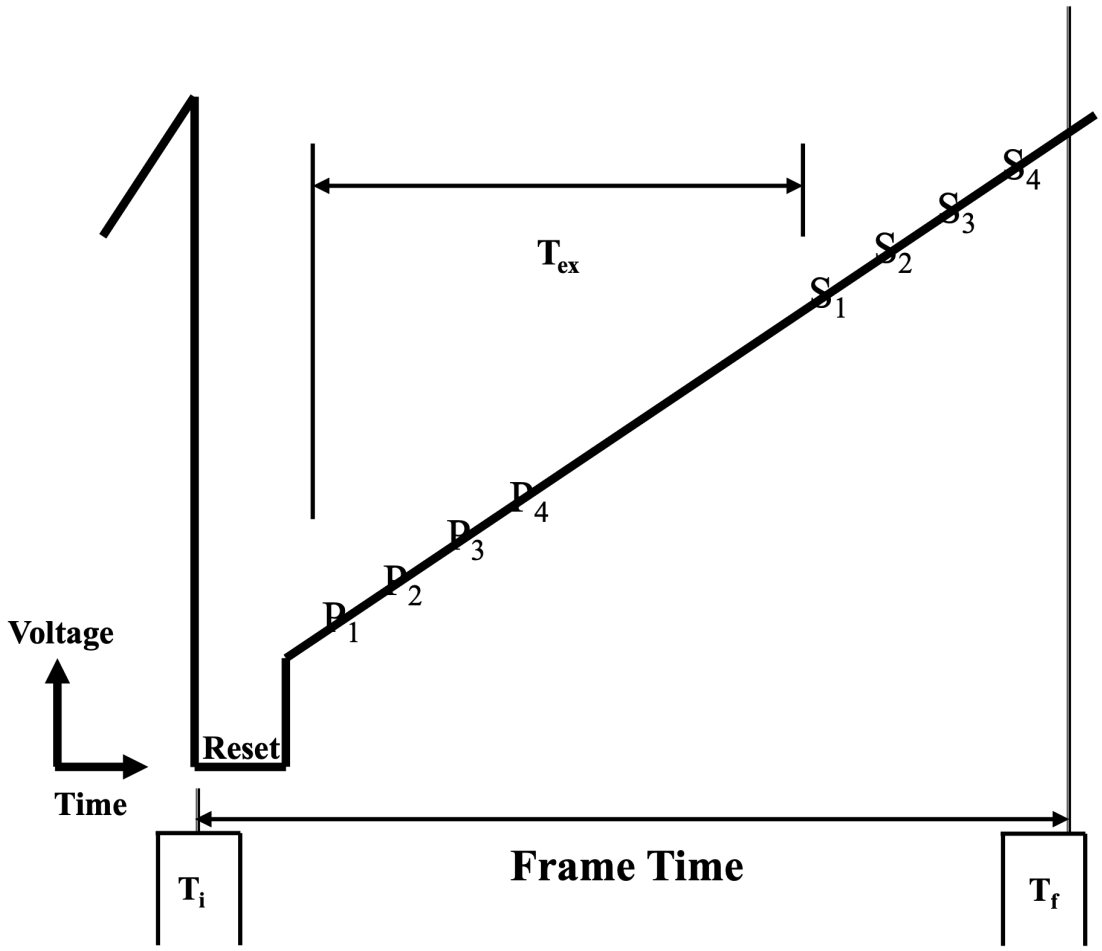


Figure 3.2: An example of Fowler sampling with 4 samples taken for the pedestal (P_1 through P_4) and signal (S_1 through S_4) readouts taken from the Spitzer IRAC handbook. These groups of 4 are averaged, and the difference is taken to give a resultant image with lower read noise.[131]

3.2.3 Ramp Fitting

An alternative SUTR reduction method to Fowler sampling is ramp fitting. Since the rate of photons observed by the detectors is practically constant over the exposure time, a good measure of this photon rate can be acquired by calculating a least squares fit for each pixel as it is sampled up the ramp. This allows every SUTR data point to be incorporated, and thus reduces the read noise even further. Furthermore, non-linearities from saturation and cosmic rays are easily detected, and the samples prior to these effects can be kept.[132] This recovers many of the pixels that would be otherwise unusable when a bright source is present, or a cosmic ray is detected partway through an exposure. Ramp fitting is a bit more resource intensive, but with modern computing power this method is much more desirable.

3.2.4 Reference Pixel Correction

Another way to reduce noise in the raw data is via reference pixel, and reference voltage correction. For HxRG detectors, reference pixels (shown in Figure 3.3(b)) are photo-insensitive pixels located around the border of the detector that are read alongside the rest of the array.[81] This is useful because the reference pixels are subject to the same offset voltages, and sources of noise as the other pixels. The reference voltage is a signal used for digitization, and is read by the ACADIAs simultaneously with each of the detector readout channels (shown in Figure 3.3(a)).[87, 133] Since the reference voltage is read alongside the readout channels, it is also subject to the same noise as the rest of the channels. A simple reference pixel correction method is de-banding where the values of the

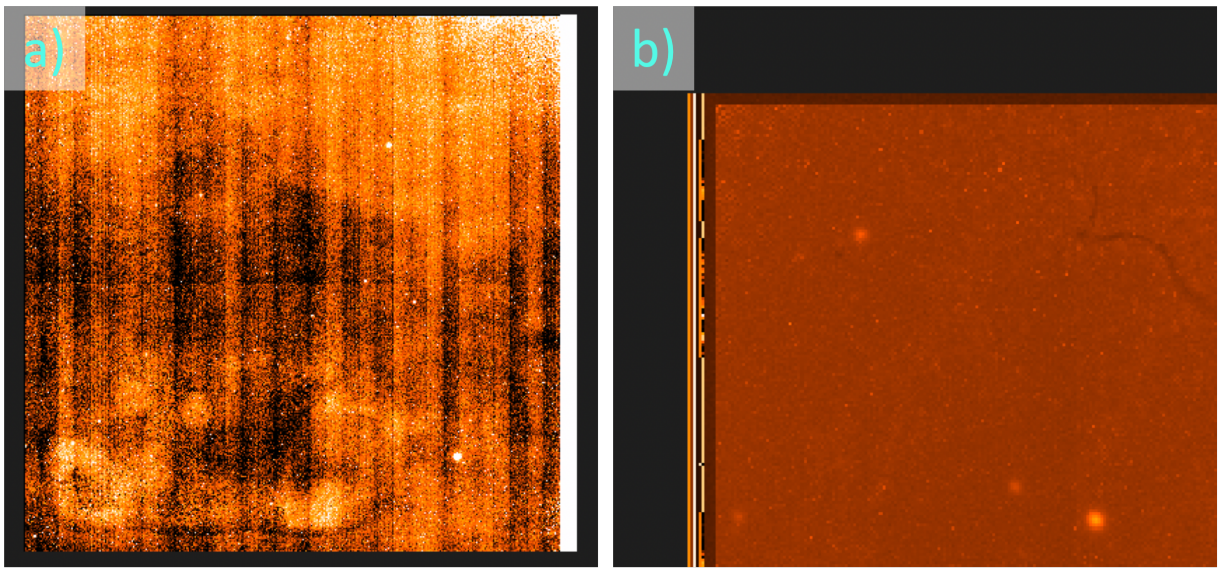


Figure 3.3: a) Full readout of an H4RG-10 taken on-sky with PRIME. The scaling is set so that the each of the 32 readout channels (vertical bands) can be seen. The reference voltage readout is the last (mostly white) band to the right of the array. b) Zoomed in image of the same raw frame so that the individual pixels can be seen. The first 6 columns in this frame are telemetry data generated by the ACADIA. Ignoring these columns, it can be seen that there is a 4-pixel wide border of reference pixels that are distinct from the light sensitive pixels.

reference pixels within a readout channel are averaged, and this average is subtracted from every pixel value within that channel. A more sophisticated method involves detecting the correlated noise (sometimes called pink noise) detected within the reference pixels and voltages in the readout, and subtracting this measured noise from each of the SUTR frames.[87] Code was generated specifically for this ACADIA readout of an HxRG detector by the RST team, and Greg Mosby already implemented this solution for PRIME. This solution will be implemented for RIMAS in the near future.

3.3 Cross-Dispersed Spectrograph Data Reduction

The cross-dispersed spectrograph pipeline was created in two steps. First, a quick-look pipeline was created to get some understanding of the data, and to be useful to obtain a qualitative look at spectra as they are acquired. Second, the science pipeline was developed to obtain high signal-to-noise science outputs from the data.

3.3.1 Echelle Quick Reduce Pipeline

The quick reduce method for the echelle mode is relatively straightforward. First, a wavelength map was created by Jillian Kunze from the Zemax model as shown in Figure 3.4 using the methods from Jillian Kunze's thesis [134]. This map was then used to create a template for the spectral calibration lamps [95] used in the lab. That wavelength map was then rotated, translated and expanded to match the lab acquired spectra as shown in Figure 3.5. The parameters used for this overlap are in Table 3.1. With the parameters gained from this match, the wavelength map is then altered with the same parameters to obtain a rough wavelength solution. Reduced spectra are then acquired by summing the values of pixels with equal wavelength as seen in Figure 3.6. The reduced spectra can then be compared with spectral line lists from NIST [135] for the Y and J bands, and Wavelength Standards in the Infrared [136] for the H and K bands. This comparison shows that the quick reduce wavelength map is reasonably calibrated for this tool's purpose as can be seen in Figure 3.7.

A few items of interest can be found looking at the fit parameters in Table 3.1. First, we can see that the scale is consistent with expectations. The initial map projection was

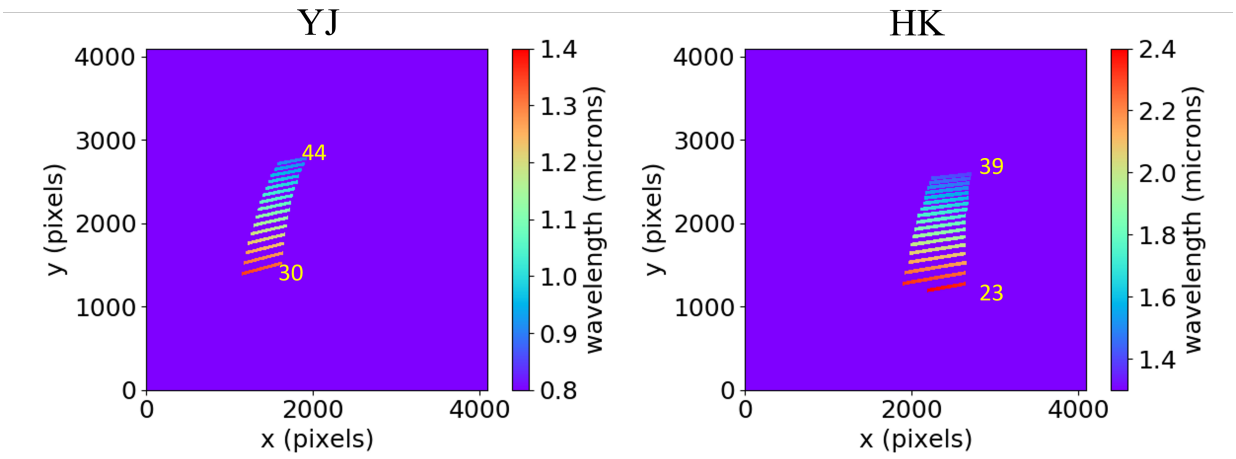


Figure 3.4: Wavelength maps for both the YJ (left) and HK (right) echelle spectrographs with the first and last orders labeled.

Spectrograph	**YJ**	**HK**
Expansion	1.925	1.945
Rotation	0.0	0.5
Horizontal Translation	-447 pixels (-4.47 mm)	278 pixels (2.78 mm)
Vertical Translation	-15 pixels (-0.15 mm)	-208 pixels (-2.08 mm)

Table 3.1: Alignment parameters used to adjust the Zemax model generated.

created for a detector with a 19 µm pixel pitch, but the current detectors have a pixel pitch of 10 µm. Therefore, the expansion factor of ≈ 1.9 is reasonable. Second, the rotation factor of $< 0.5°$ shows that the dispersive elements and the detectors are fairly well aligned rotationally. Finally, the translation factors show that the image is not fully centered on the detector. This is expected, since no effort was made to align the detectors along these axes. No effort was made in this respect because the imaging and spectral dispersion observed by RIMAS is smaller than the detector array size.

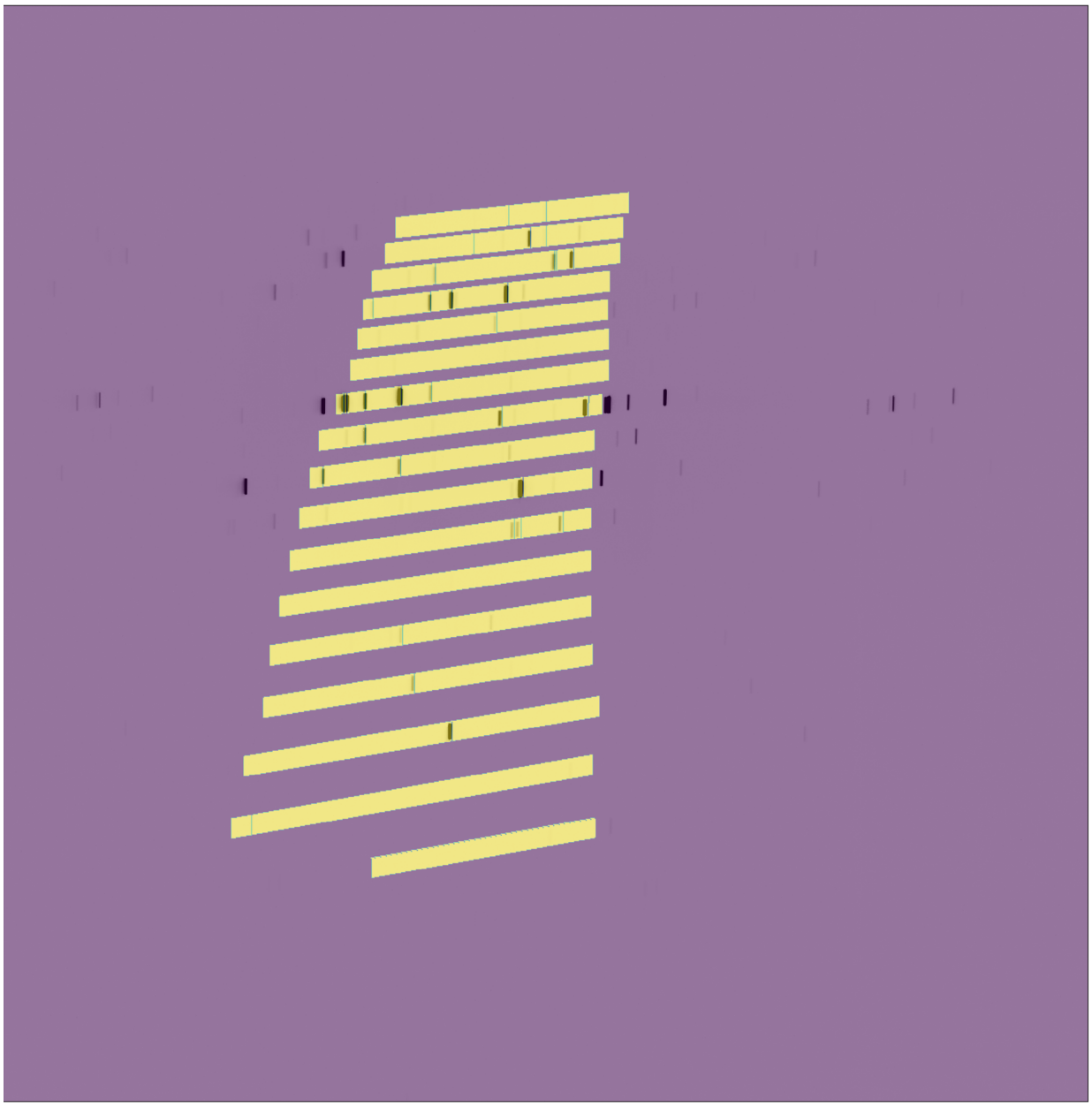


Figure 3.5: HK lab spectrum of krypton taken with with the rotated, translated and expanded template spectra overlaid to show the quality of the fit. The template spectrum shows each of the spectral orders highlighted in yellow, and the emission lines for krypton shown in blue. The thicker gray lines are the actual emission lines measured by the detectors.

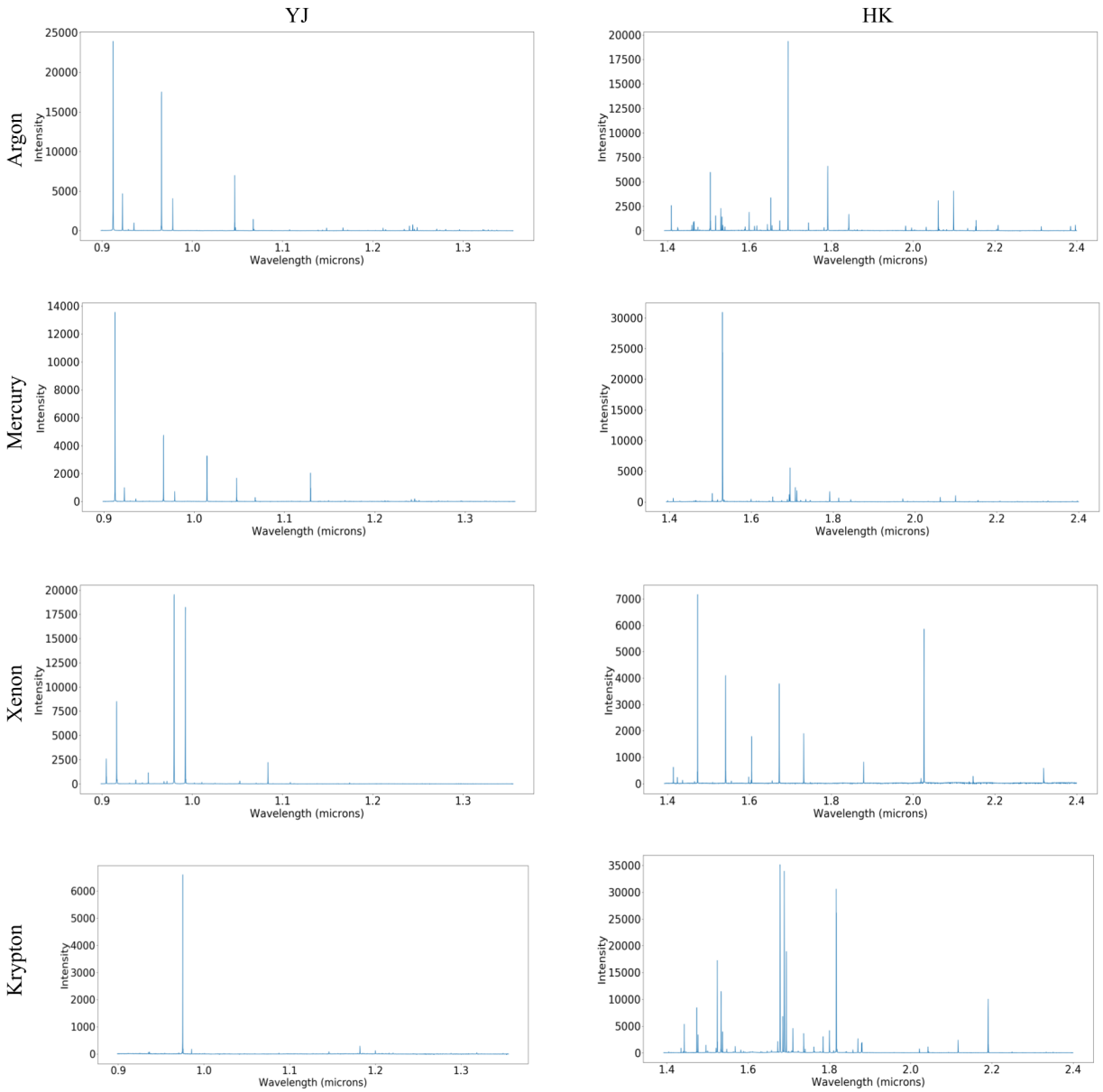


Figure 3.6: Quick reduced lab spectra for each of the spectral calibration lamps.

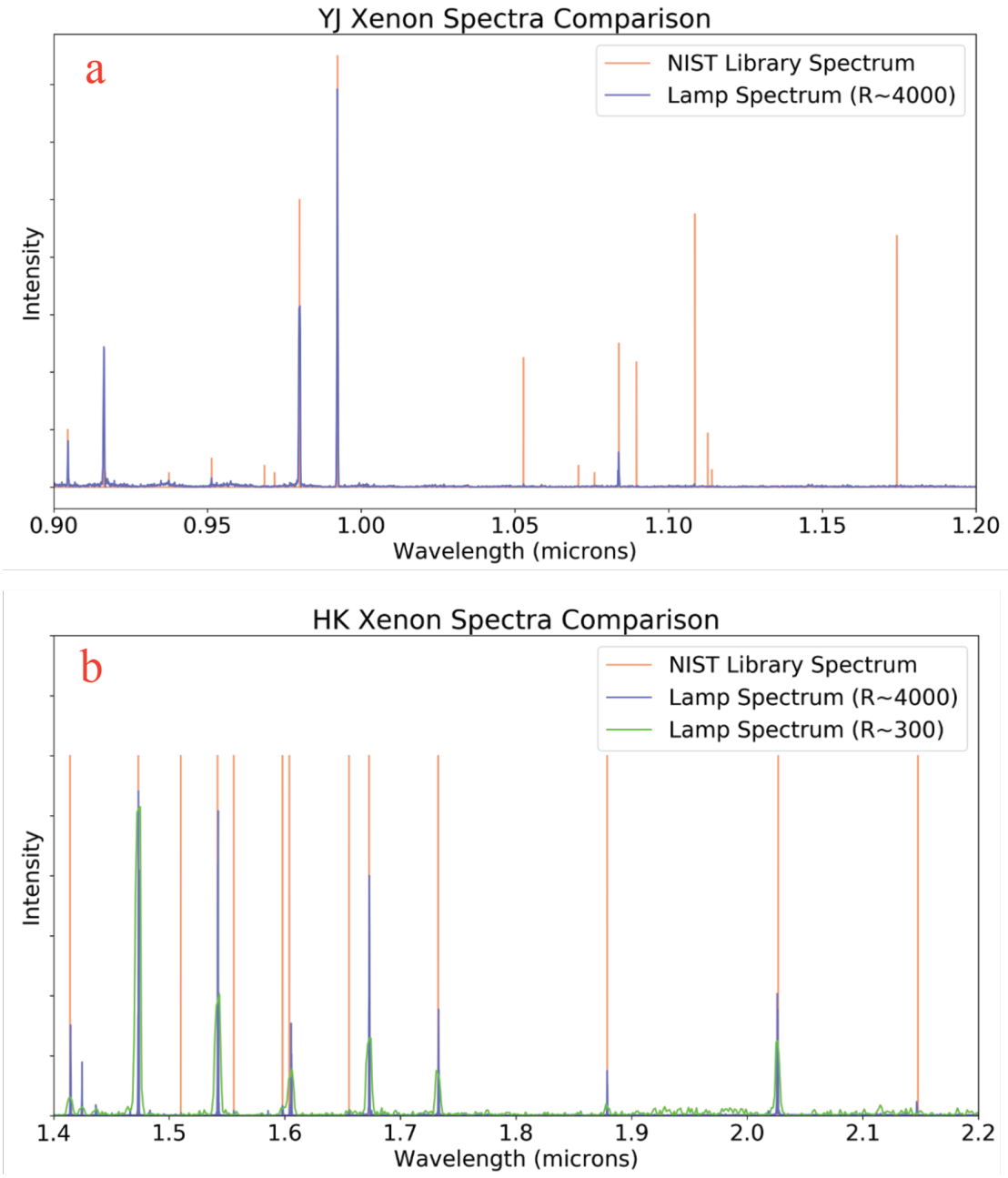


Figure 3.7: Plots from Jillian Kunze's thesis showing how the quick reduced spectra compare with NIST library spectra for both YJ (a) and HK (b) bands.[97] These plots show that the quick reduce calibration method matches well with NIST library spectra such that the measured peaks align with the NIST database.

3.3.2 Echelle Science pipeline

With any dispersive spectrograph, it is important to be able to convert a two-dimensional image of the spectrum into a well calibrated one-dimensional spectrum showing intensity versus photon energy. While using a cross-dispersed spectrograph has the huge benefit of allowing for a high resolution spectrum over a large range of wavelengths, reducing a cross-dispersed spectrum is more complicated than a single order spectrum. This section will discuss the development and testing of the RIMAS echelle spectroscopy pipeline.

3.3.2.1 Pipeline Overview

The initial plan for this data reduction pipeline was to use Spextool [137]. However, this turned out to be difficult to adapt to RIMAS due to lack of documentation, and the pipeline was written in IDL. A new pipeline, written in Python, was started from scratch at this point. Although this code eventually became the quick-reduce pipeline, turning it into a science pipeline was going to be a much larger project. After further consideration, the data reduction pipeline [52] developed for IGRINS [138] was chosen as the starting point for RIMAS. IGRINS is also a cross-dispersed NIR spectrograph, and therefore has a lot of similarities to RIMAS. Also, the IGRINS pipeline is open source and written in pure python, making it much easier to adapt and distribute to observers. The pipeline algorithms are also largely based on the ones used in Spextool.

3.3.2.2 Pipeline Algorithm: Preprocessing

Starting from the reduced ramp images produced using the ramp reduction techniques discussed in §3.2 a number of common methods are used to reduce spectral data into a useful form.

3.3.2.2.1 Preprocessing

A common method for acquiring infrared spectra is to use A-B or ON-OFF sampling. With this method, the telescope is with object nodded between two positions: along the slit for A-B sampling on and off the slit for ON-OFF sampling. ON-OFF sampling is typically chosen when the object being observed is too large to fit in two non-overlapping locations along the slit. Then, during preprocessing, the A (or ON) images are stacked, and the B (or OFF) images are stacked and the difference is taken between these stacks.[137] This sampling method is particularly useful in the infrared as it helps remove telluric emission lines. Furthermore, A-B sampling removes background, and dark current.

3.3.2.2.2 Defining Apertures

An important part of reducing data from a cross-dispersed spectrograph, is to identify each of the spectral orders. Using the IGRINS pipeline's algorithm, the boundaries of each spectral order are identified using ON-OFF sampled dome flats taken of a continuum source. Since RIMAS's spectral orders do not extend to the edges of the detector, we inserted another step where the orders are truncated in the horizontal direction based on when the signal is much lower than the peak signal for that order.

3.3.2.2.3 Dispersion Calibration

The wavelength calibration algorithm, which assigns a wavelength to each pixel based on spectral order and column, is largely unchanged from the IGRINS algorithm. First, spectral lines are acquired in ON-OFF mode of either spectral calibration lamps (as described in §3.3.3.1), or by observing telluric emission lines. Telluric emission lines will work well for the echelle spectrographs resolving power, but the lines would become too blended for use with the lower resolution spectral modes. Next, 1D spectra for each order are generated by averaging the pixel intensity along the slit, the direction of degenerate wavelength. This gives a spectrum for each order with an intensity value for each column. Emission lines are then identified using a Guassian peak finder. Using the initial wavelength calibration (§3.3.3.6), and previously identified (§3.3.3.5), each of the line wavelengths are identified in their current position. The wavelength calibration is then calculated using the same polynomial method described in §3.3.3.6.

3.3.2.3 One-Dimensional Spectrum Acquisition

Using the original algorithm from IGRINS, 2D images of spectra are converted to 1D spectra. For point like sources, weighted means are taken along the slit, the degenerate wavelength direction, of the A-B reduced image divided by its normalized spatial profile as described in Horne [139]. For A-B extended source observations, the spatial profile is determined such that the top half pixels have a value of 1, and the bottom half pixels have a value of -1. For ON-OFF extended source observations, the normalized spatial profile is taken to be 1 in all locations.

3.3.2.4 Telluric Correction

While A-B and ON-OFF sampling are useful for removing telluric emission from spectra, they do nothing to remove telluric absorption. To mitigate this, spectra from A0V stars are obtained at a similar airmass to the science target, and the profile is used to identify telluric absorption features.[140] These early A-type stars are useful for telluric correction since their intensities only deviate by a few percent from their continuum spectrum. Unfortunately, the IGRINS pipeline telluric correction algorithm was insufficient for RIMAS spectra. We discovered during testing with DeVeny[1] data (Sec. 3.3.4.4) that the IGRINS algorithm effectively required each of the absorption features to be quite narrow in wavelength. This assumption is understandable for IGRINS where the resolving power is ≈40000, and most of the telluric absorption lines are easily distinguished. However, given that RIMAS's resolving power is an order of magnitude less, the blended absorption line features become problematic when fitting a spline. To resolve this, the telluric absorption algorithm from PypeIt[2] was used in its place. PypeIt is an astronomical spectroscopy pipeline developed to handle data from many different spectrographs, and was released near the end of RIMAS's pipeline development.[141] The PypeIt method uses simulated telluric absorption spectra along with the profile of the A0V spectra to identify the telluric absorption profile. The simulated telluric absorption spectra are determined by interpolating between a grid of spectra that were previously generated using the algorithm described in Clough et al. [142] for a range of atmospheric pressures, humidities, temperatures, airmasses

[1] DeVeny is a spectrograph on LDT with a wavelength range covering 320 to 970 nm. `https://lowell.edu/research/telescopes-and-facilities/ldt/deveny-optical-spectrograph/`

[2] `https://pypeit.readthedocs.io/en/release/`

and wavelengths at LDT's location. After this grid was generated for LDT's location, this telluric absorption algorithm was successfully tested on DeVeny data.

3.3.2.5 Flux Calibration

Fluxes are normalized by reducing the spectrum of a standard star with a known spectrum, and using its spectrum to determine the flux as a function of intensity, and wavelength. This method is unchanged from the IGRINS pipeline.

3.3.3 RIMAS calibration

In order to run the spectral reduction pipeline, it is important to have a good initial calibration. This section will discuss the process of creating the calibration files: the emission lines list, the list of non-blended lines that should be used for a wavelength solution, the previous known location of those lines, and a previous wavelength solution. The algorithm for creating these files is shown in Figure 3.8.

3.3.3.1 Calibration Data Acquisition and Preprocessing

Spectral images of xenon, argon, krypton and mercury-argon low pressure gas discharge lamps [95] were acquired both individually and as a group. For each of these sources, data was acquired with the lamp on, off, off then on again. The sample-up-the-ramp data was then reference pixel corrected as described in §3.2.4 and reduced using a Fowler 2 algorithm as described in §3.2.2.

The on-off-off-on data was then preprocessed as shown in Figure 3.8 which shows

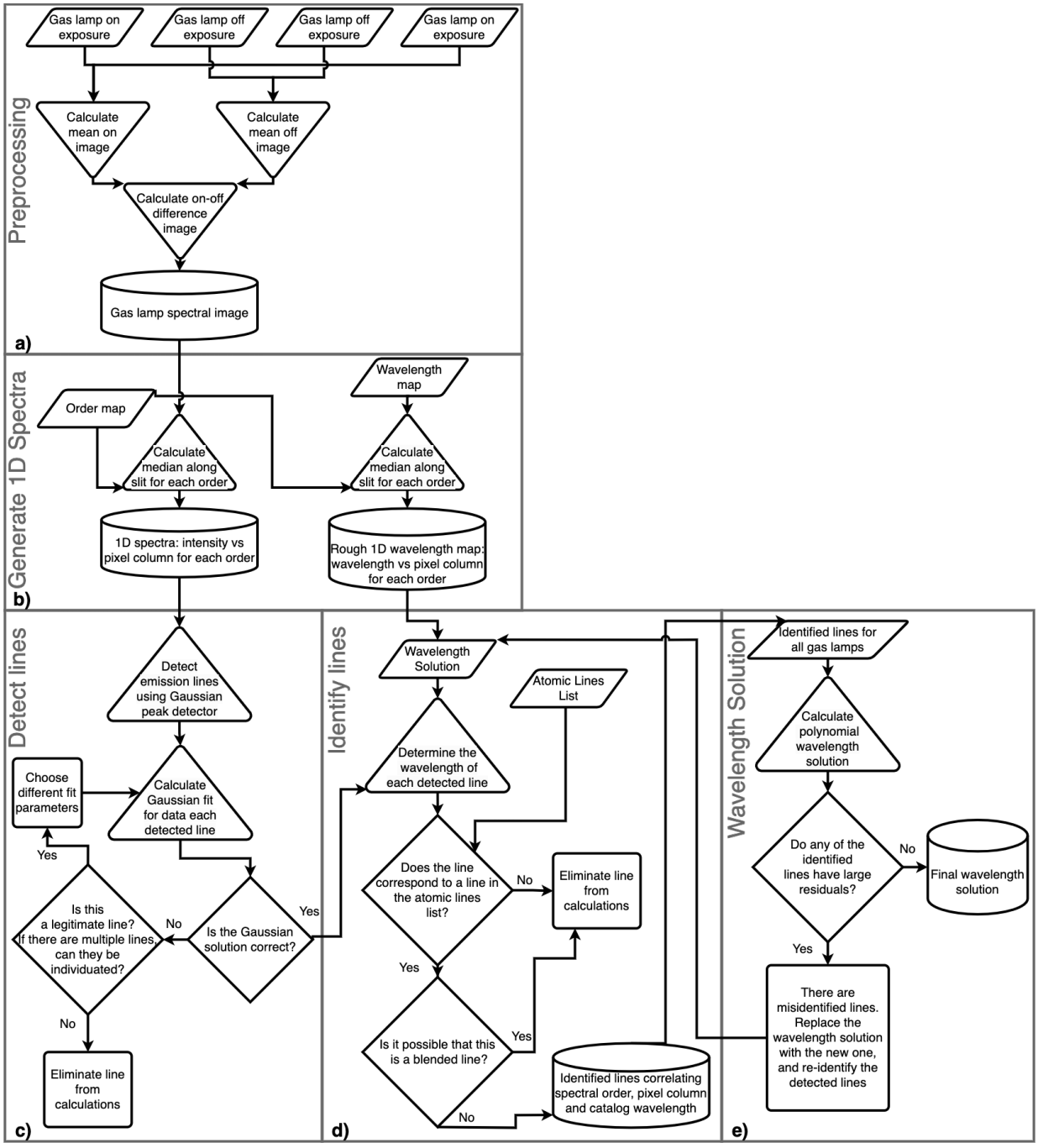


Figure 3.8: Wavelength calibration flowchart detailing the process used to arrive at a polynomial solution correlating spectral order and pixel column to wavelength.

the on images averaged together, the off images averaged together and then the difference between these data arrays is used for further calculations. The benefit of this method is that it removes the dark current and any background from the room.

3.3.3.2 One-Dimensional Spectra Generation

In order to obtain a wavelength calibration, we first require a one-dimensional spectrum for each order. To accomplish this, each of the orders' boundaries need to be identified. Although order boundaries can be determined using the algorithm in §3.3.2.2.2 this algorithm had not been successfully adapted to RIMAS when the calibration algorithms were being generated. Instead, an extended order map (Figure 3.9), generated using the method outlined in §3.3.1 was used to identify the order boundaries. This is okay for the purpose of gaining a wavelength calibration, since it is not necessary to gain an exact measure of the order boundaries since a small amount of added noise will not prevent the detection of high signal-to-noise emission lines from our calibration lamps. The extended maps are necessary because they allow for calibration files that are valid across an arbitrarily wide range on the detector. This helps allow for different cutoff values given for the order ranges as described in §3.3.2.2. Even though the wavelength calibration will not be valid to the edges of the detector, as shown in the maps, the solution will be valid over the order range determined during the aperture tracing step.

Now that the order boundaries have been identified, a spectrum for each order was generated (Figure 3.10) by aggregating the intensity of each pixel along the vertical direction, which is effectively along the slit and the direction of degenerate wavelength. In this

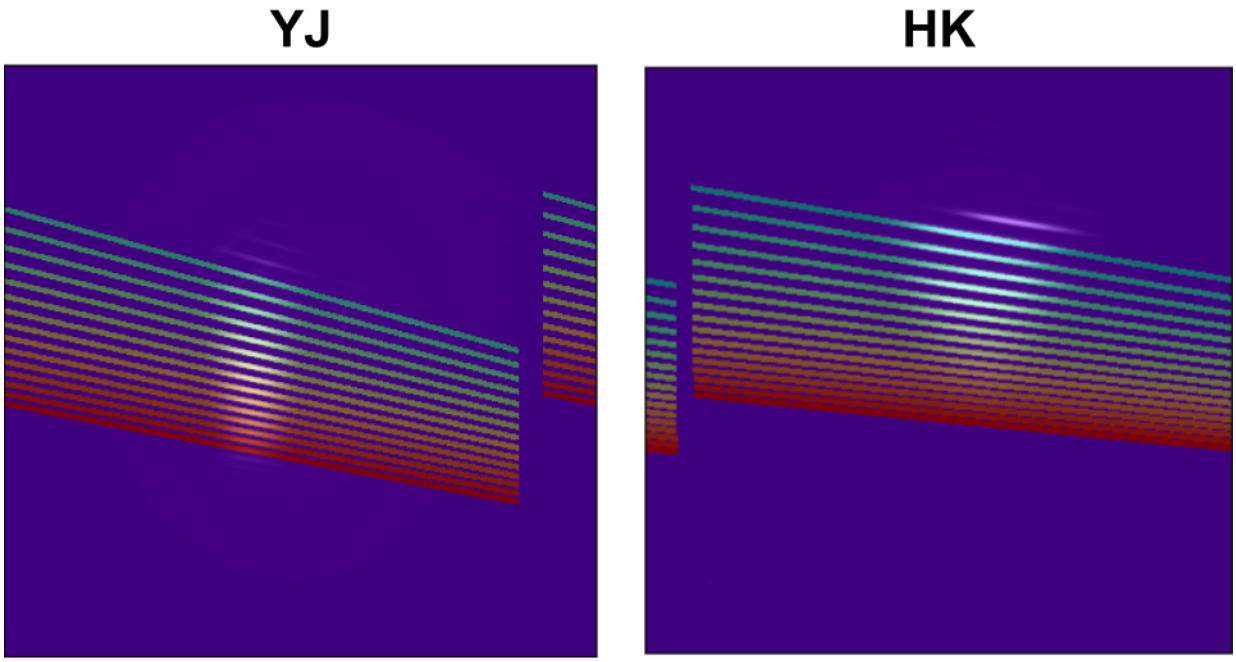


Figure 3.9: Order maps for both the YJ and HK bands overlaying the spectrum acquired from a continuum source. There are some discontinuities in these maps caused by the rollover used to align them, however this is well outside of the dispersion and does not cause any issues as a result.

case the median was chosen as it reduced the background noise. This same procedure is then performed on the extended wavelength maps (Figure 3.9 in order to obtain a rough wavelength solution for each order.

3.3.3.3 Emission Line Detection

Now that there reduced spectra to work with, emission lines from the various calibration lamps can be detected. The first step in this process is to run the spectrum for each order through the peak detector algorithm, which is part of the science pipeline and also used for the line detection in §3.3.2.2.2. Once detected, each peak is then isolated and

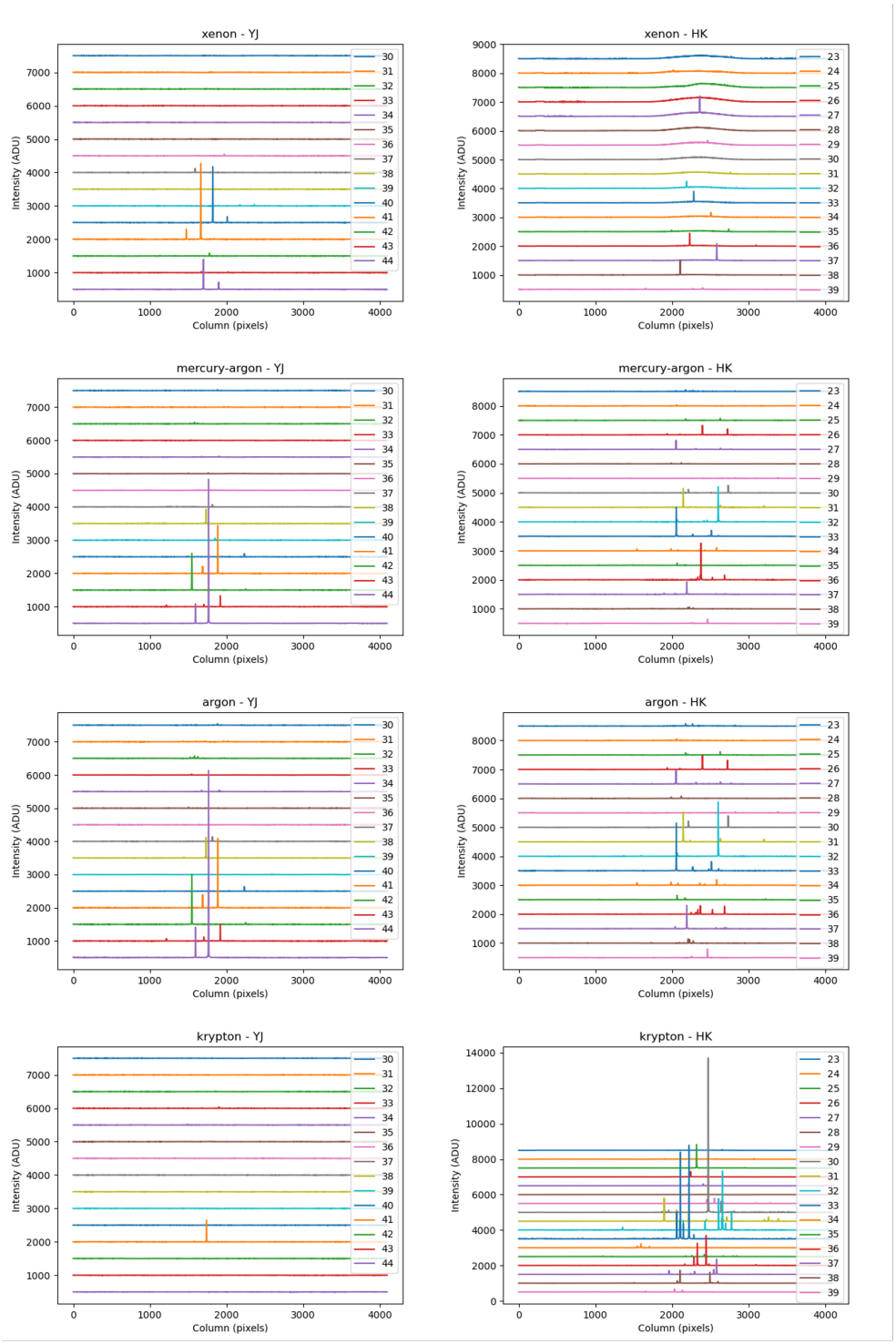


Figure 3.10: Spectra for each element observed, spectral band, and spectral order. The intensity for each order is offset by 500 for each order.

a Gaussian fit (Eq. 3.2) is determined. In Eq. 3.2, I is the intensity, A is the amplitude, x is the pixel column, $\bar{x}$ is the mean pixel column, σ is the standard deviation and I_0 is the background intensity. For this fit, I and x come from the data, and the rest are fitting parameters. If there is a bad fit, a new fit can be determined by zooming out and bringing in more background data points, zooming in to crop out other peaks, fitting multiple peaks, or using a user-defined initial guess to begin the fitting process. The plot (Figure 3.11) of this is then used to determine if this is a legitimate emission line, or if it is a blended line. If it is a blended line, it is then determined if the peaks can be distinguished. Once the peak is determined to be legitimate and distinguishable, its Gaussian fit can then be added to the list of peaks to be identified.

$$I = Ae^{(\frac{x-\bar{x}}{\sqrt{2}\sigma})^2} + I_0 \tag{3.2}$$

3.3.3.4 Atomic Lines List Catalog

In order to identify the emission lines, a good catalog is required. For the YJ spectrograph, the NIST catalog [135] was used and for the HK spectrograph the lines listed in *Wavelength Standards in the Infrared* [136] were used. It was necessary to use multiple catalogs since neither catalog covered the full wavelength range observed by RIMAS. In order to determine if using multiple catalogs would cause issues, lines that appeared in both catalogs were compared and the difference was determined to be much smaller than RIMAS's resolution element.

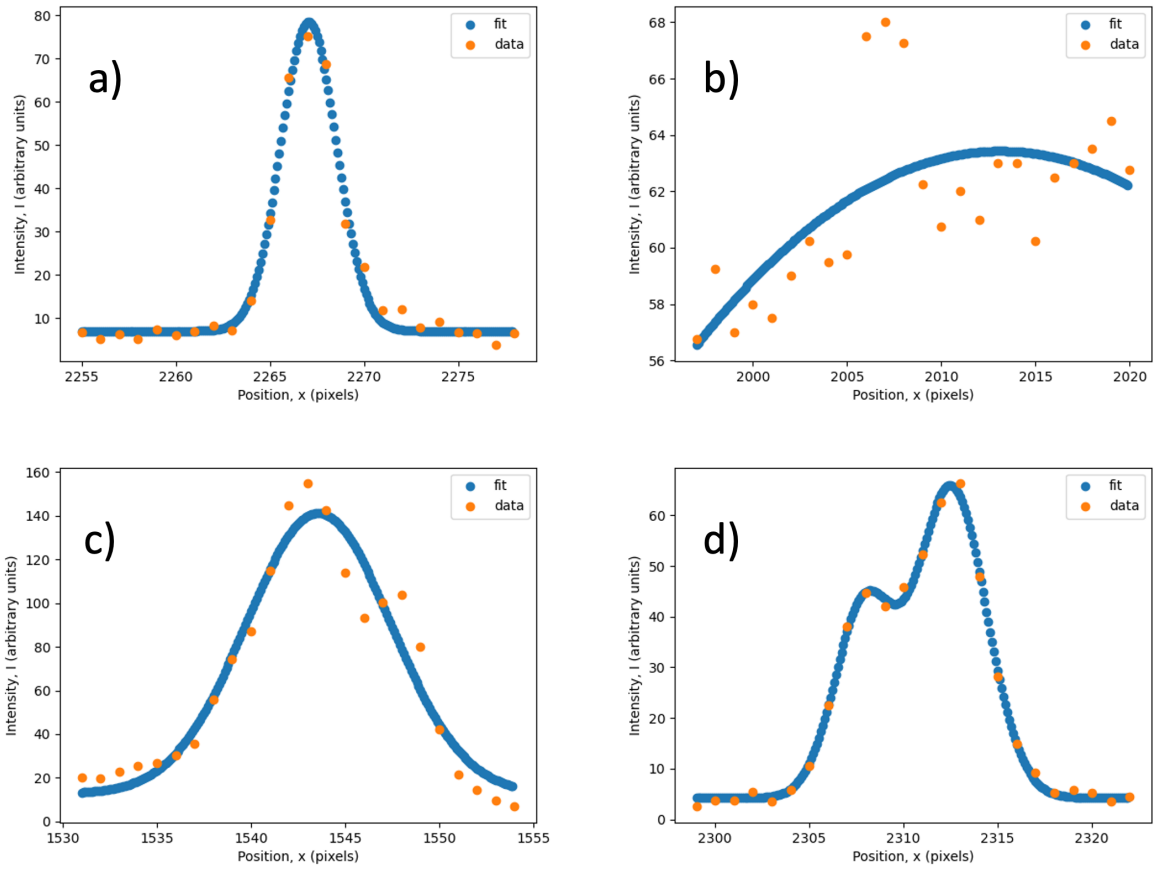


Figure 3.11: (a) Detected peak with good Gaussian fit. (b) Illegitimate detected peak. (c) Blended peaks that cannot be effectively distinguished. (d) Blended peaks that can be distinguished.

3.3.3.5 Line Identification

The next step is to determine the wavelength of each detected line. The location of each line is determined using the mean found by calculating the Gaussian fit in §3.3.3.3. For the first round of line identification, the rough wavelength solution generated from the wavelength map in §3.3.3.2 is used to estimate the wavelength of each pixel column. For subsequent iterations of line identification, the latest wavelength solution determined using the method in §3.3.3.6 is used. With this wavelength solution, and the previously determined line location, the measured wavelength is then determined. This wavelength is then cross-matched with an atomic lines list catalog. At this point the line location is plotted (Figure 3.12) alongside the closest catalog values using the standard deviation from the Gaussian fit as error bars. This allows us to determine if the line has been accurately identified, or if there is some uncertainty in this matter. If it can be confidently determined that this is an accurately identified line, it is then saved for use in the wavelength solution later.

3.3.3.6 Wavelength Solution

With the lines in each order identified for each observed element (xenon, argon, krypton and mercury), the wavelength solution can be calculated. This is done by fitting a 2D Chebychev polynomial (Eq. 3.3) to the data by matching the catalog wavelength, λ, to the measured pixel column, x, within a particular spectral order, m.

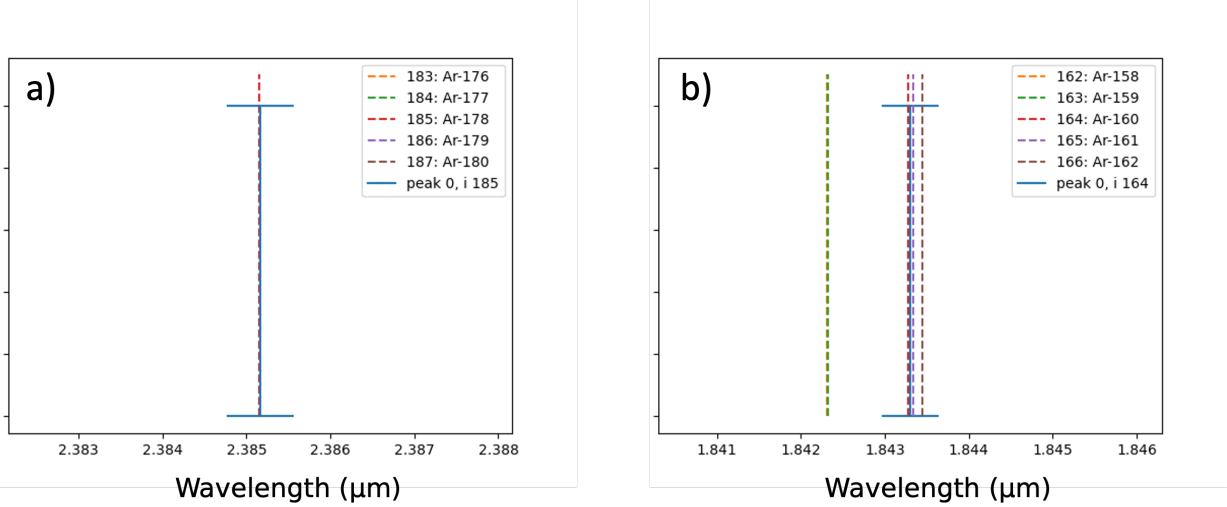


Figure 3.12: The mean location for a detected peak is plotted in blue with error bars matching its standard deviation. Alongside the detected peak, the closest lines from the catalog are also plotted and are labeled in the legend with the element and row number from the element's catalog text file. (a) Shows a successfully identified line. (b) Shows a line that cannot be successfully identified due to other peaks within the error region.

$$\lambda(m,x) = \sum_{i,j=0}^{i=d_m, j=d_x} C_{ij} T_i(m) T_j(x) \tag{3.3}$$

where $T_i(x)$ and $T_j(y)$ are Chebyshev polynomials of the first kind as defined in Eq. 3.4.

$$\begin{aligned} T_0(x) &= 1 \\ T_1(x) &= x \\ T_{i+1}(x) &= 2xT_i(x) - T_{i-1}(x) \end{aligned} \tag{3.4}$$

After testing multiple polynomial orders, it was determined that a 3$^{\text{rd}}$ degree fit was best for both pixel column and spectral order. Adding further DOF to this fit, resulted

Band	**YJ**	**HK**
Mean wavelength (µm)	1.15	1.93
Standard Error (µm)	6.52E-6	1.34E-5
Relative Error	5.67E-6	6.94E-6
Resolution Element (1/R)	2.21E-4	2.02E-4
Error Percentage of Resolution Element	2.56	3.44

Table 3.2: Table exploring the error in the wavelength solution and its relationship to the resolving power. The mean wavelength is used to calculate the relative error from the standard error. The resolving power used to calculate the resolution element was determined in §2.4.2.4.

in insignificant improvements to the standard error. A standard polynomial power series, $\lambda = \sum C_{ij} m^i x^j$, was also fit, but was found to result in a worse fit. After each fit, the identified lines were checked for outliers, and if there were outliers, the lines were re-identified with the new wavelength solution as performed in §3.3.3.5. This is especially important when using the rough wavelength map as the initial fit since it is often difficult to correctly identify emission lines with this imprecise solution. For both the HK, and YJ bands, it was found that three iterations of line identification were necessary to correctly identify detected emission lines. The residuals from this fit can be seen in Figures 3.13 and 3.14. The standard error for these fits can be seen in Table 3.2. As can be seen in the last row of this table, the error from this fit is much smaller than the resolution element.

3.3.4 Science Pipeline Testing

While the pipeline was under development, it was important to have good datasets for testing. This provided some issues that need to be overcome since it was desired to develop the pipeline before commissioning. A number of different datasets were used to help ameliorate this issue and increase the likelihood of the pipeline working well once it is working with RIMAS on-sky data.



Figure 3.13: Plots showing the residuals between the calculated fit, and catalog values of identified spectral emission lines for the echelle spectrograph's wavelength calibration. The top plot shows the residuals for the YJ spectrograph as it relates to position. The bottom plot shows the residuals for the YJ spectrograph as it relates to spectral order.

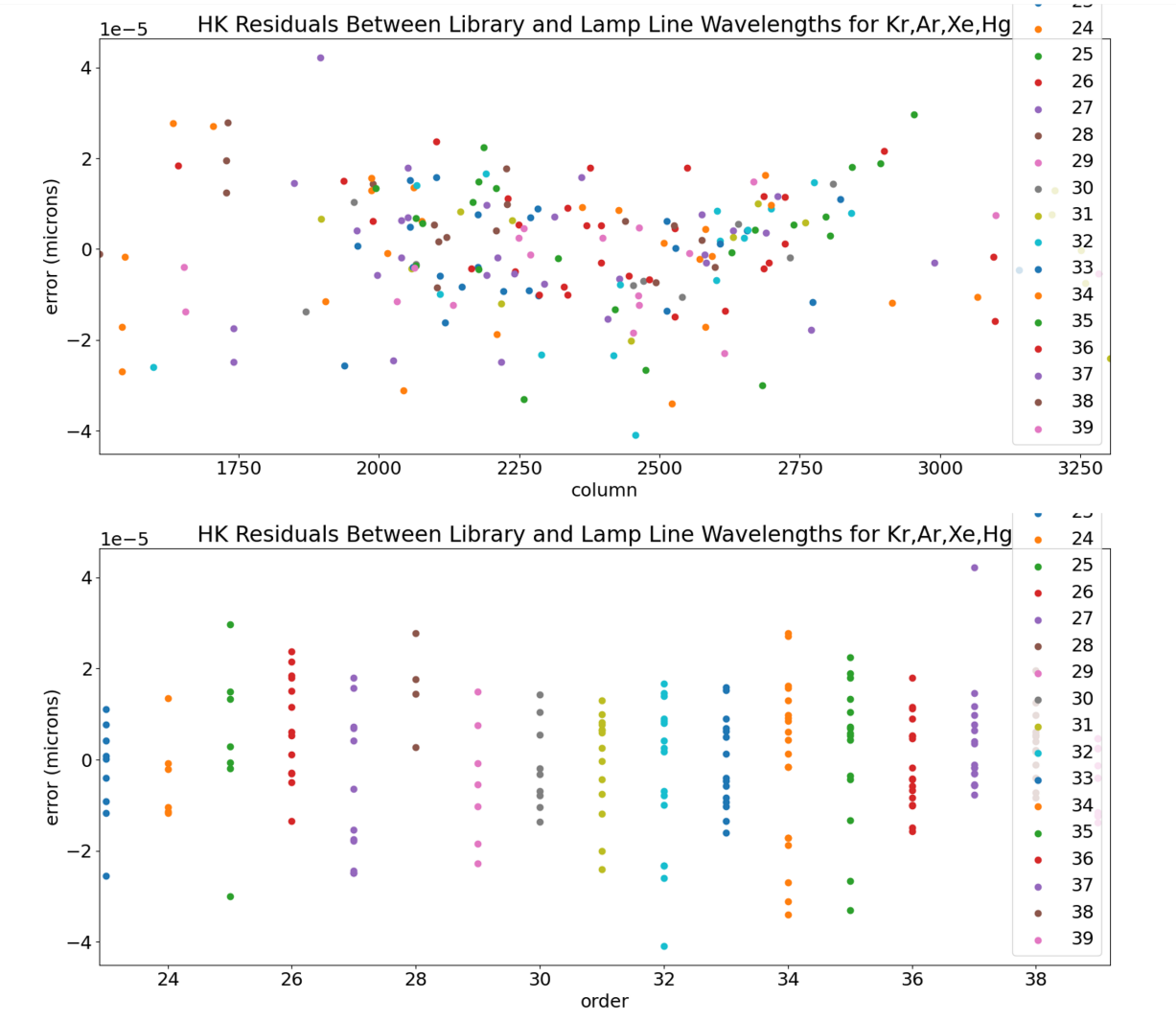


Figure 3.14: Plots showing the residuals between the calculated fit, and catalog values of identified spectral emission lines for the echelle spectrograph's wavelength calibration. The top plot shows the residuals for the HK spectrograph as it relates to position. The bottom plot shows the residuals for the HK spectrograph as it relates to spectral order.

3.3.4.1 RIMAS H2RG Lab Spectra

Initially, the data gathered using RIMAS's original H2RG detectors were used. Although this data was useful for qualitatively confirming the echelle dispersion was as expected, this data did not work particularly well for testing the pipeline as the noise created by the large quantity of shorted pixels made it difficult for any of the algorithms to work. As a result of these difficulties, this dataset was eventually abandoned for pipeline development.

3.3.4.2 Echelle++ Simulated Spectra

When it was determined that the initial set of lab data was not going to be useful, it was clear that a new dataset was needed. At this point, the loaner NIRCAM package H2RG detectors had been acquired, and the readout harnessing, mechanical structures, etc. were being developed. Unfortunately, the pandemic had begun at this point, and even if the necessary parts were acquired, there was no way to access the lab and acquire the needed data. Luckily, the Echelle++ [143] spectra simulator had recently been developed. Using Echelle++, spectra were generated for constant density flats, sky emission lines, constant density "stars", and an A0V star. All simulations inserted both photon noise and detector noise. Stellar simulations included both sky emission and sky absorption, and were simulated in both A-B-B-A and ON-OFF-OFF-ON patterns.

3.3.4.3 RIMAS H4RG Lab Spectra

After the final H4RG detectors were acquired, the next round of RIMAS lab spectra were observed as discussed in §2.4.2.1. Using this data the pipeline was further tested, so that we could be confident of the spectral order identification, and the wavelength calibration files are much closer to what will be used on the telescope.

3.3.4.4 DeVeny NIR Data

With the Echelle++ simulations and RIMAS lab data, the pipeline had been well tested on simulated stellar sources, and lab collected data. However, we still wanted to be able to test the pipeline using on-sky data to identify any important issues that were missed. To accomplish this, data was acquired using at LDT with DeVeny. For this test, DeVeny was configured to observe wavelengths towards the red end of its capabilities, and an R≈4000 grating to be as similar to RIMAS's echelle mode as possible. Data was then acquired with both ON-OFF-OFF-ON and A-B-B-A dithers of multiple standard sources so that RIMAS data reduction could be compared with catalogued spectra. This testing was mostly successful with the exception of the telluric correction algorithm. The built-in method for correcting spectra for telluric absorption was made for a much higher resolution spectrograph, IGRINS, which did not have the issue of blended absorption lines. As such, it did not handle broad absorption features in the spectra. To fix this, the telluric absorption correction algorithm from PypeIt was integrated in its place as discussed in §3.3.2.4.

3.4 Imaging Data Reduction

The data reduction pipeline for RIMAS's imaging mode[3] is based on an adaptation and improvement of the pipeline developed for LMI and RATIR [53]. With the recent upgrades, this pipeline is capable an entire night's observations with a single command, while being being flexible enough to handle exposures as they appear. The overall data reduction steps to go from multiple exposures, for a single target to a stacked and calibrated image is shown in Figure 3.15. Based on header data, the files are separated between calibration images (flats, darks, and biases), and science images. Master calibration files are then created by (1) stacking the bias frames to create, when appropriate for a given instrument, (2) subtracting this master bias from the dark calibration frames, (3) stacking the dark frames, and (4) stacking each of the flat frames by filter after the bias and dark current has been subtracted. Next, each science frame is then calibrated by subtracting the bias and dark current, and flat fielded with the normalized flat. The background from the sky is then subtracted by masking sources, and then median stacking the dithered images. This sky background is then adjusted to match the background of each individual exposure, and subtracted. Cosmic rays are then removed using a Laplacian cosmic ray identification algorithm [144]. Astrometry is then calibrated using code adapted from commonly used astrometry code initially developed for VLT.[145] The zero-point and flux calibrations are then calculated using multiple catalogs (SDSS, Pan-STARRS, 2MASS, USNO-B, and APASS) as appropriate for the field observed and the filter used. With each individual exposure fully calibrated, the images are then stacked with SCAMP [146].

[3] `https://github.com/astroumd/photometrypipeline`

Photometry can then be generated for each detected source using the same catalogs that were named above. For RIMAS, the bias subtraction and cosmic ray removal can be skipped since they are handled during the ramp reduction process.

While being prepared for RIMAS, this pipeline was upgraded in a number of ways. A number of collaborators were having issues installing the pipeline to begin with due to the AstrOmatic dependencies (Sextractor, SCAMP, SWarp, etc.), so a docker container[4] was created with each of these dependencies already compiled. Using the original python interface was a bit tricky in the docker format, so to make things more seamless a well documented command line interface was developed. This allows the docker container to be used like any other command line tool. The sky subtraction method was also improved to allow for target specific sky generation, and better masking of sources. The zero-point/flux calibration was made more accurate through improved masking of saturated sources. Finally, the code was converted from Python 2 to Python 3 in order to future proof the codebase, and make future improvements easier to implement.

[4] `https://hub.docker.com/r/joedurbak/photopipe`

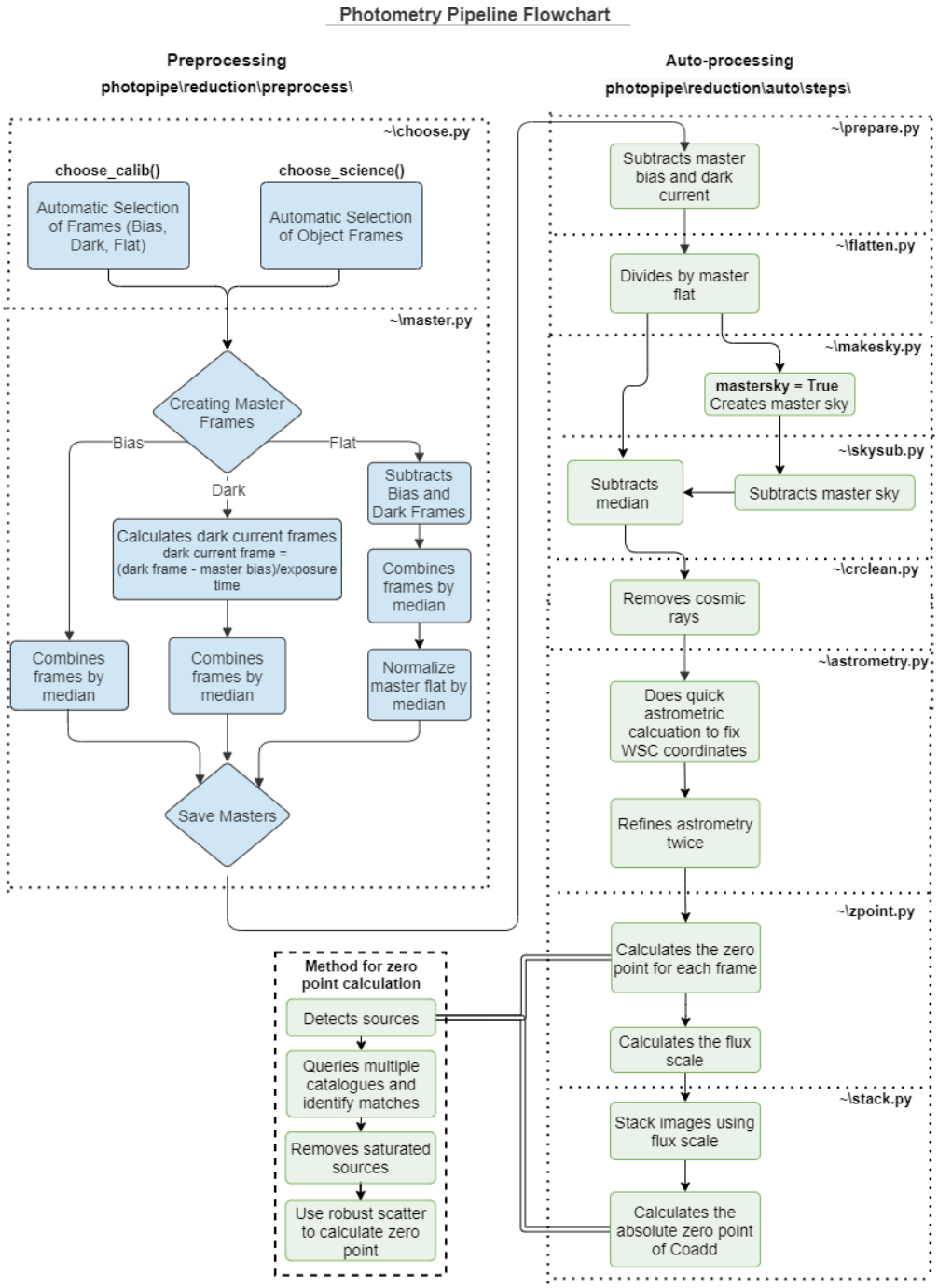


Figure 3.15: Flowchart showing the steps taken in reducing imaging data.

Chapter 4: PRIME Instrumentation

The PRime-focus Infrared Microlensing Experiments (PRIME) camera is part of the joint NASA-JAXA project supporting the RST engineering and science studies. It is installed on the 1.8 m PRIME telescope with a ≈1.5 square degree FOV dedicated to the project. The instrument is equipped with multiple broad band and narrowband filters between 0.9 µm to 1.8 µm. The instrument is installed at the South African Astronomical Observatory and has been in continuous operation since October 2022. PRIME is currently surveying the Galactic bulge for microlensing events, GW and GRB studies and other science objectives, in advance of the RST mission. The GW and GRB studies are aided by PRIME's continuous availability for ToO observations. After 1.5 years of on-sky operation, we present the use, performance and lessons learned operating RST's yield demonstration lot H4RG-10 detectors as part of the PRIME camera based on the data processing and analysis tools that we have developed. With the large field of view in the near infrared bands this instrument is a powerful tool in the Southern hemisphere and a complement to the instruments in the North and in the visible. Large portions of this chapter are only slightly edited from the SPIE paper [3] I wrote on PRIME.

4.1 Overview

Commissioned in October 2022, the PRIME consists of a 1.8 m telescope in Sutherland, South Africa, and a cryogenic NIR camera (≈100 K) in its prime focus. The observatory has been developed through a collaboration framework between NASA and the Japan Aerospace Exploration Agency (JAXA) to ensure the success of the RST microlensing mission both scientifically, and through instrumentation. At present, NIR microlensing event rate has been determined by extrapolating results from optical microlensing surveys to NIR wavelengths.[147] Constraining these values via ground-based observations, will help RST simulations by reducing uncertainty in these estimates. Furthermore, after RST launch, PRIME will observe fields simultaneously with RST to achieve parallax measure ments. PRIME is supporting RST instrumentation through the first astronomical use of the RST package H4RG detectors, and RST detector readout and control ASICs. This helps evaluate the performance of these detectors with long-term astronomical use.[54]

4.1.1 Observatory Overview

Located at the South African Astronomical Observatory (SAAO) site in Sutherland, South Africa, PRIME complements other microlensing observations in the southern hemisphere: Microlensing Observations in Astrophysics (MOA) telescope in New Zealand, the Optical Gravitational Lensing Experiment (OGLE) in Chile and the Korea Microlensing Telescope Network (KMTNet) in Chile, Australia and South Africa. Designed as an NIR twin to the optical MOA telescope, PRIME telescope consists of a 1.8 m telescope with the cryogenic camera in the prime focus. Using a five lens assembly to focus the beam,

Form factor	Prime focus reflector telescope
Diameter	1.8 m
Diameter ratio	F/2.29
Image sensor	HAWAII-4RG-10
Number of image sensor chips	4 (2x2 array)
Number of pixels per chip	4096x4096
Pixel size	10 µm
Pixel scale	0.5″/pixel
FOV	1.56 deg^2 (1.29 deg^2 without the chip gap)
Wavelength range	800 nm to 1800 nm
Filters	Z, Y, J, H, Narrow Band (1063/10 nm, 1190/11 nm, and 1644/24 nm), and blank

Table 4.1: Specifications for both the telescope and camera

PRIME has a focal length of 4125 mm. With the observatory built, the telescope installed, and the camera commissioned, PRIME is currently operating in its commissioning phase (Figure 4.1).[54]

4.1.2 Instrument Overview

Located in the prime focus of the telescope, PRIME camera is the primary instrument (Figure 4.2). The camera, which is mechanically mounted to the telescopes field derotator to compensate for the field rotation caused by the altitude-azimuth telescope mount, is a single unit consisting of a cryogenic compartment within its dewar, and a warm compartment outside of the dewar. The cold space is cooled to ≈100K using CryoTel GT coolers [120]. Within the cold space (Figure 4.3), there is a 2x2 array of RST packaged H4RG-10 detectors, and 2 filter wheels in series containing Z, Y, J, H and a composite narrow band filter. The narrow band filter has band passes of 1063 nm, 1190 nm, and 1644 nm, which are within the Y, J, and H bands respectively (Figure 4.4). The detectors are readout and controlled using 4 cryogenic ACADIA (ASIC for Control And Digitization of Imagers for Astronomy)

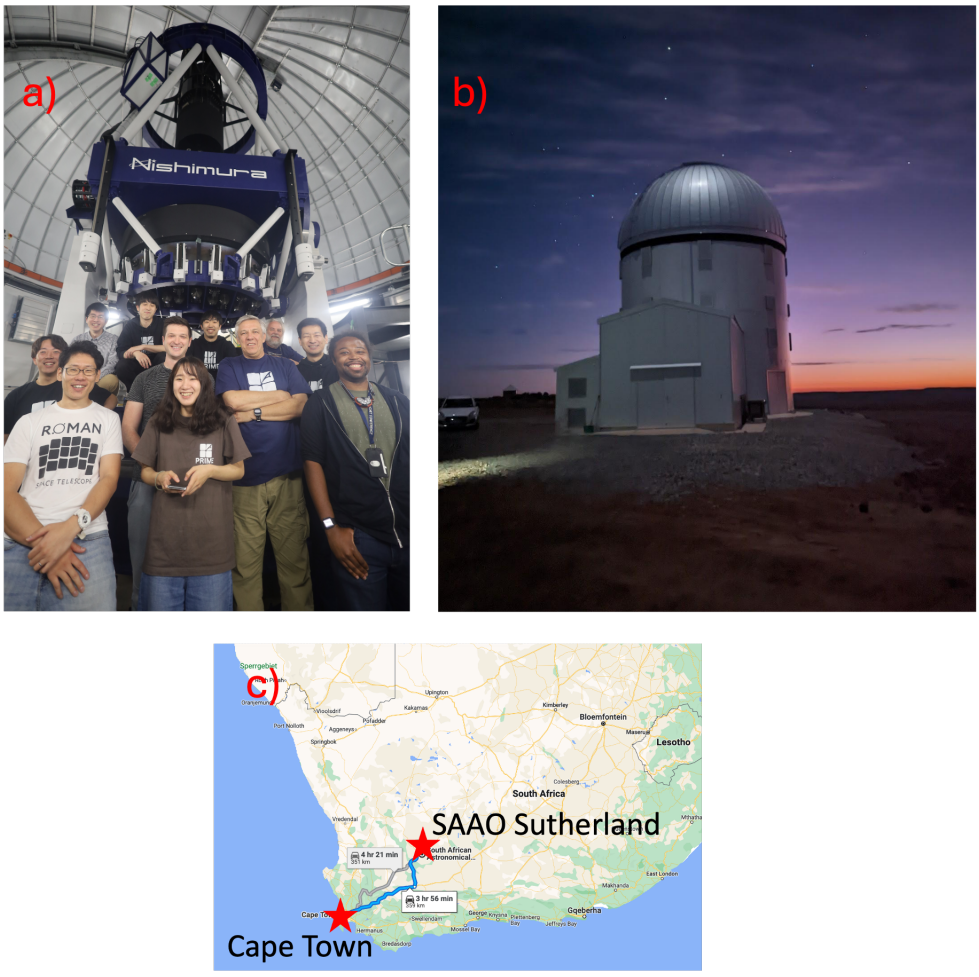


Figure 4.1: (a) Photograph of the telescope inside of the dome with the camera commissioning team in the foreground. (b) Photograph of the observatory taken at dusk. (c) Map showing the location of the observatory, and the drive from Cape Town.

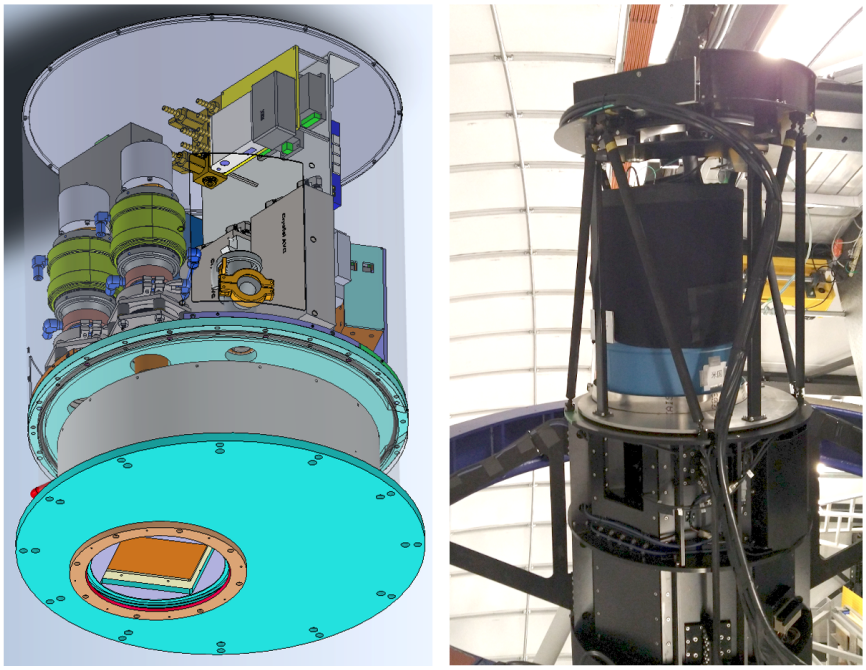


Figure 4.2: The PRIME camera can be seen on the right mounted to the telescope. The black portion is the covered electronics deck, which contains the various electronics and the bulk of the cryocoolers. This can be seen in the model on the left. The lower blue portion in the photograph on the right is the instrument dewar, which contains the detectors and filter wheels. The camera is mounted to the telescope's field derotator.

ASICs (one for each detector), and 2 room temperature Multi-Purpose Control & Interface Electronics (MACIE) FPGAs. The cryogenic ACADIAs control the detectors by supplying clocks and bias voltages, and read the detectors by converting the output analog signal to digital.[133] The room temperature MACIEs control the ACADIAs and send the detector data back to the instrument control computer.[148] This is the first astronomical use of these RST package H4RG-10 detectors.[54] Besides the MACIEs, the warm space contains communications electronics, the pressure gauge, temperature measurement and control electronics, motor controllers, and the remotely controlled power distribution unit.

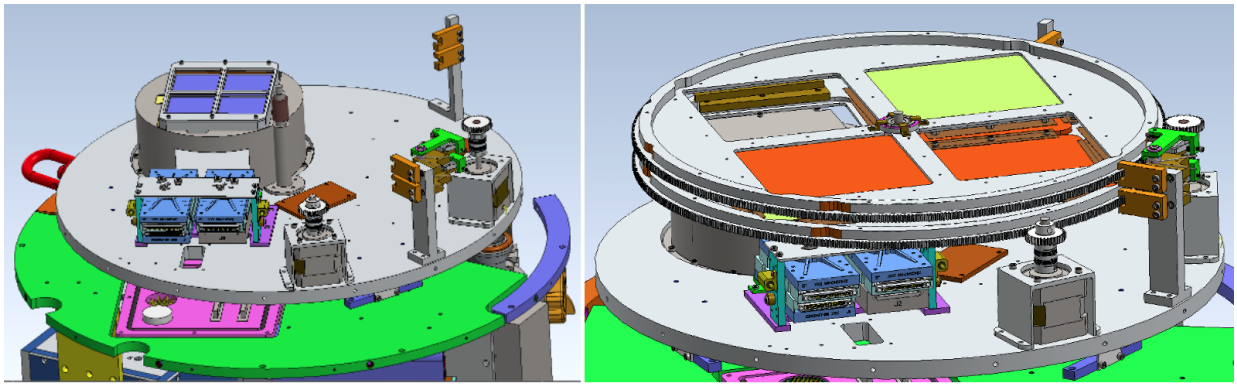


Figure 4.3: PRIME's cold assembly, which operates at ≈100 K. Right: In this space there are 2 filter wheels in series, that are controlled by the pictured motors, and held in position by the pictured registration mechanism. Left: The filter wheels are removed to show the 2 x 2 mosaic detector array, and the 4 ACADIA ASICs that control them. Not pictured: There is a cold shield covered in multi-layer insulation enveloping this assembly with a cold window allowing light through.

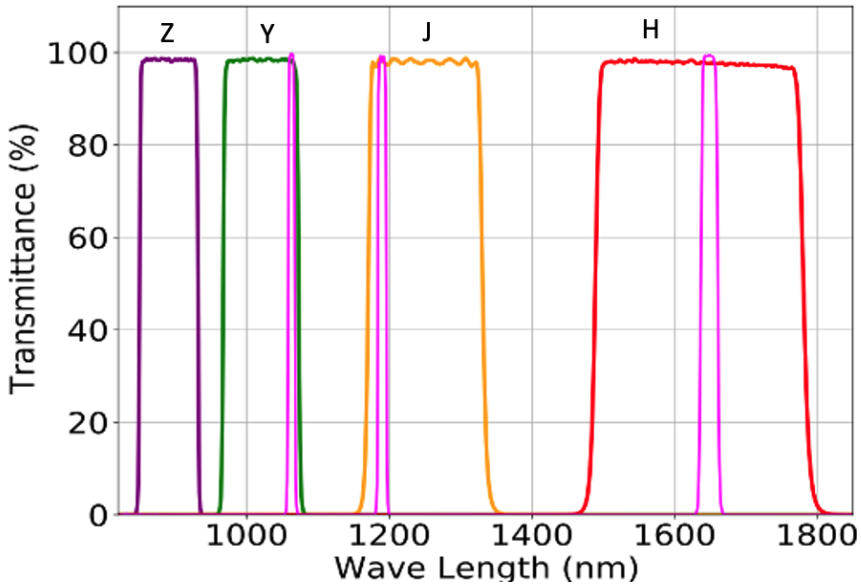


Figure 4.4: The bandpass is achieved through four IR filters, whose bands are indicated with different colors and labels. Combining a broadband filter (Z, Y, J or H) with a narrow-band filter, narrow-band observations in one of the three bandpasses indicated in pink can be archived. The filters were purchased from Optical Coatings Japan.

4.1.3 Commissioning and Servicing

PRIME camera was installed, and operational in October 2022. Unfortunately, during shipping the instrument experienced significant damage resulting in one of the ACADIAs being unresponsive, one of the detectors becoming noisy, and many unreadable channels from another detector. During commissioning, the team was able to open the instrument, and determine the root cause of most of the issues. The unreadable channels were recovered, and many loose screws within the cold space were tightened. The damaged ACADIA was determined to be unrecoverable, and the other detector remained noisy. Still, the camera was able to be mounted to the telescope, and begin taking data with a reduced FOV.

During this period with the missing detector, the collaboration was still able to begin taking science data, work on optical alignment [55], work on pipelines, and debug issues with the instrument. During the second night of observations, PRIME was able to observe GRB 221009A [47, 149, 150](Figure 4.5), the brightest GRB ever observed [47, 150]. While still waiting for replacement parts, PRIME was also able to observe GRB 230307A (Figure 4.5), the GRB with the second-highest recorded γ-ray fluence with the first GRB afterglow observed by JWST.[151] This observation helped identify that this event was related to a kilonova despite its long duration.[46] Galactic Bulge, and other adhoc observations were also begun during this period despite the reduced FOV.

In June 2023, PRIME camera was serviced to repair the remainder of the damage sustained in shipping. This involved replacing the damaged ACADIA, and the damaged harness that was causing the noisy readout. A few other optimizations were made by improving the thermal contact to the cold window, adjusting the motor to filter wheel in-

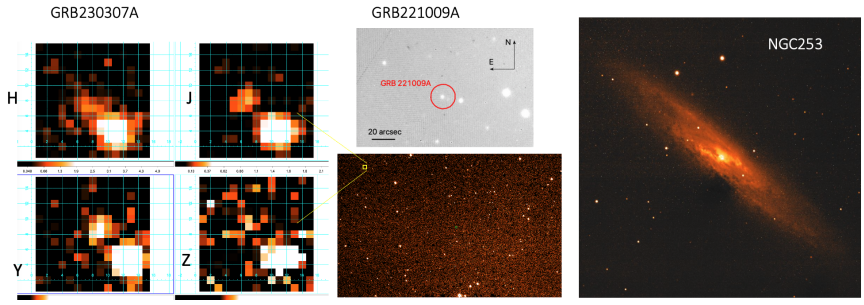


Figure 4.5: Observations, of GRB 230307A, GRB 221009A, and NGC 253 taken by PRIME. The GRB 230307A images show clear detections in H, J and Y bands. GRB 221009A was the first transient detected by PRIME. NGC 253 was observed as a test image using the previously unavailable detector, during the service mission.

terface, and adding more Acktar [152] blackout material. Using measurements gained since the initial commissioning trip, the spacer distance between the camera and the derotator was also decreased to optimize optical performance. After these repairs, the camera was able to be cooled, and mounted to the telescope again. Since this service mission, PRIME has been operating continuously with all 4 H4RG detectors operating as expected.

4.2 Camera Design

While §4.1.2 gives a short in introduction to PRIME cam, this section gives a more detailed view of the instrument. The basic layout of PRIME cam's systems is shown in Figure 4.6, which details the detector systems, filters, mechanisms, cryogenics, and housekeeping electronics for this system. PRIME camera's components were chosen so that the overall assembly would be as small as possible given the location of the instrument in the prime focus.

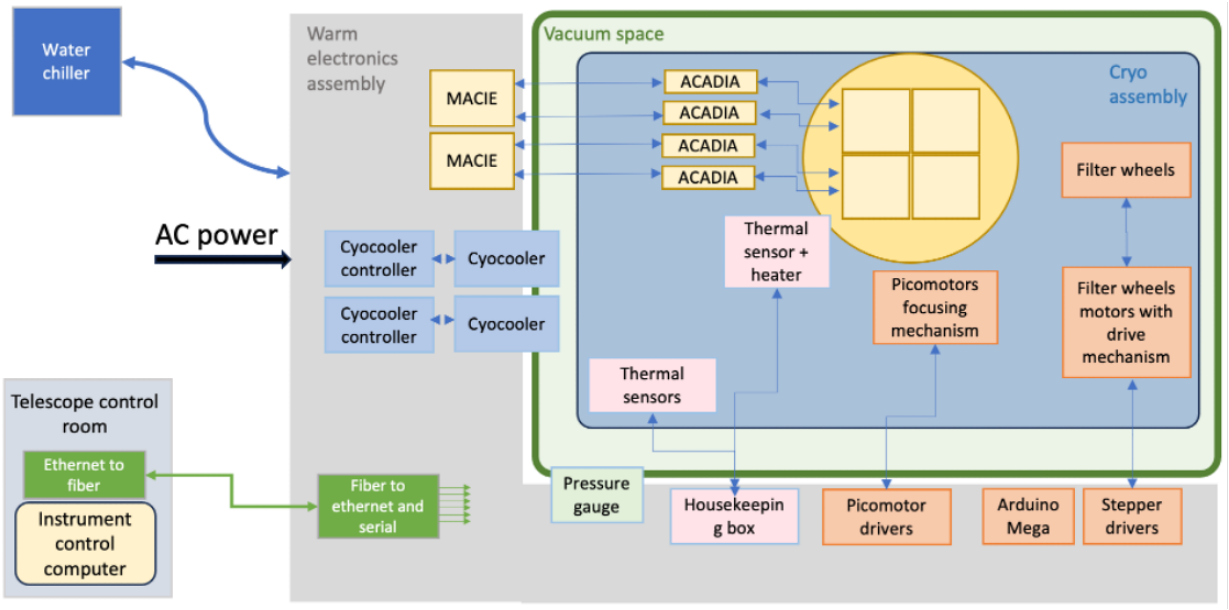


Figure 4.6: Block diagram of the PRIME camera electrical system. Yellow: detector subsystem; pink: the environmental control (temperature) and pressure monitoring; orange: the mechanical subsystem (filter wheels and motor drives). The blue-shaded rectangle identifies the cold space the green-shaded rectangle is the cryostat vacuum space; the gray shaded area is the warm electronics assembly that is mounted on top of the camera dewar.

4.2.1 Cryogenic Assembly

As can be seen in Figure 4.6, the cryogenic assembly contains the detectors, detector control ASICs (ACADIAs), detector alignment mechanisms, filter wheels, cryocoolers, thermometry and temperature control heaters. The cooling is done with the same Cryotel GT cryocoolers described in §2.4.8, which were chosen for their cooling power and compactness. Both cryocoolers have charcoal cage getters connected to their cryoheads, and only one is connected via cold strap to the cold plate. The other cryocooler is not connected to the cold plate so that it can operate at a lower temperature, and improve cryopumping. The two filter wheels operate in combination with four filter slots on each wheel. One of these slots is left open on each wheel so that the bandpass filter from the other wheel is unobstructed. The wheel closest to the window contains Y, J and H band filters, while the wheel closest to the detectors contains Z band, narrow band, and blocking filters. As described in §4.1.2 the narrowband filter is used in combination with the Y, J, and H band filters to pick one of three narrow bands. These filters are moved by the same NEMA motors, and similar registration mechanisms used for RIMAS as described in §2.4.6.1. The 2x2 array of H4RG-10 detectors are mounted to a single stainless steel plate, with slotted mounting holes to prevent warping of the detector surfaces. These detectors were aligned to be coplanar using a CMM machine operated by RST engineers, and replacing their mounting bushings with the appropriate thicknesses. The stainless steel plate is mounted to three piezoelectric linear actuators that were adjusted such that the 2x2 detector array was aligned to be parallel to the mounting plate using measurements from an alignment telescope. The detectors themselves, and the cryogenic ASICs used to read

them are described in greater detail in §4.3.

4.2.2 Electronics Assembly

The electronics (or warm) assembly contains the ASIC control FPGAs (MACIEs), PDU and power supplies, motor controllers, thermometry measurement and control, cryocooler bodies and controllers, and communications electronics. All of these items are liquid cooled using chiller plates, and build in cooling lines.

4.2.2.1 Thermometry

As described for RIMAS in §2.4.8.2, the Cryotel GT coolers temperatures, power output, and vibration are controlled by to AVC controllers located in the electronics deck. One PID temperature controlled cryocooler is strapped to the cold plate, and the other is not connected to anything, and run at constant power in order to run colder. Internal and external temperatures are measured, and heaters are controlled with a custom housekeeping box used for Balloon Experimental Twin Telescopes for Infrared Interferometry (BETTI) [153]. The housekeeping box was chosen for its compactness relative to the Lakeshore temperature controllers/monitors that were available at the start of the project.

4.2.2.2 Communications

From the start of PRIME, the plan was to send all communications to the control room via fiber in order to avoid issues with cabling range, and electrically conductive materials that could be an issue in the event of a lightning strike. Since there are robust

protocols to accomplish this with ethernet connections, ethernet switches with both copper and SFP connection were chosen. The SFP connections are compatible with a number of different mediums, but in this case we chose to use OM3 multimode fiber. Given this ethernet schema, all communications needed to be eventually converted to ethernet in the electronics deck, and USB communications needed to be changed back in the control room as shown in Figure 4.7. To accomplish this, serial device were converted to USB, and all USB devices were carried over LAN with and Icron Ranger [117] in the same way described for RIMAS in §2.4.7.3. Also, to reduce the number of fiber connections needed between the camera and the control room, a fiber to USB converter was used inside the electronics box for the housekeeping box.

4.2.2.3 PRIME Power Distribution

In the lab, we were able to control power to the individual devices using the PDUs used by RIMAS (discussed in §2.4.7.4), however this rackmount power strip form factor was too large for PRIME camera's envelope. As a replacement a WebRelay-10 Plus™ [154] was chosen for both its compactness, and its capacity for PRIME camera's voltage (up to 240 VAC) and current requirements. Using this WebRelay, each electrical component can be powered off and on remotely despite some components sharing power supplies, as shown in Figure 4.8. With the WebRelay GUI, default states and available actions for any given relay are configurable. The default state for most of the devices is to be powered on, but the cryocoolers and MACIEs defaults are set to be powered off to avoid unsafe outcomes. Since the communications are all done through the LAN switch, there is only a reset switch

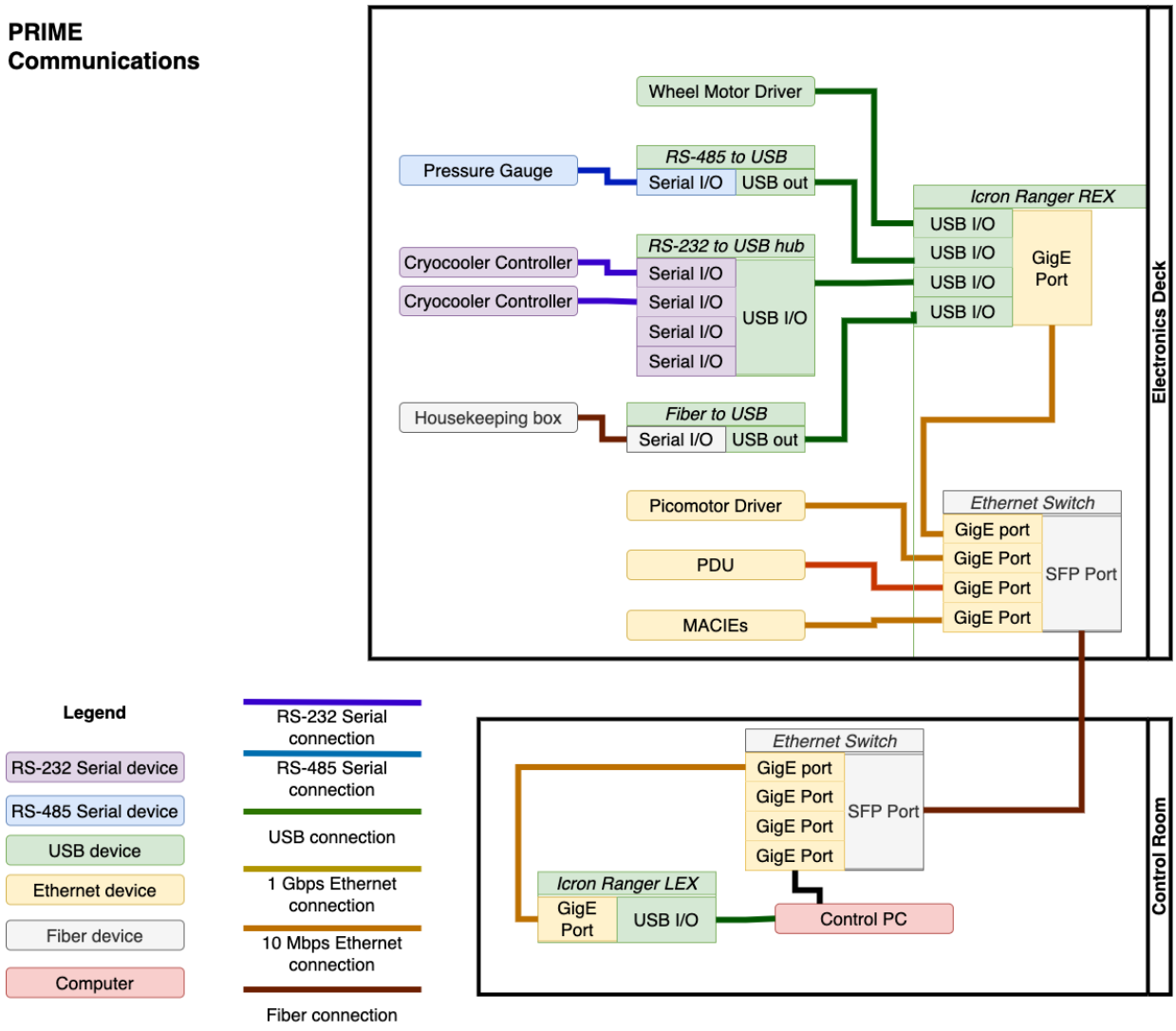


Figure 4.7: Diagram showing the communications diagram for PRIME. The Electronics deck is mounted directly to the camera dewar. The control room is in a different room within the observatory.

for this component in the GUI, and the on and off buttons are removed. The connections shown in Figure 4.8 are made using individual wires currently, but a PCB design has been created for future versions if they are needed.

4.2.2.4 Motor Controllers

The detector plane adjustment piezoelectric linear actuators are controlled using the manufacturer's controller [155]. The filter wheels are controlled using an Arduino Mega 2560 microcontroller with a Trinamic stepper motor control board using a similar interface to the one used by RIMAS, discussed in §2.4.7.6.

4.3 Detectors

As discussed previously, PRIME camera's sensors are four H4RG-10 detectors arranged in a 2x2 array. These are RST prototype detectors fabricated for the Roman IR Detector Technology Advancement Program (DTAP), aimed at optimizing the design of RST detectors.[78] These prototype arrays were used to optimized device characteristics such as the number of hot pixels, QE, total noise, interpixel capacitance, and persistence. PRIME's detectors were selected from these, which all had read noise, dark current, and QE well within requirements.

4.3.1 Detector Readout System

As described in §4.1.2, PRIME camera's 4 detectors are controlled and read by 4 ACADIAs, which are in turn read and controlled using 2 MACIEs. The initial strategy for

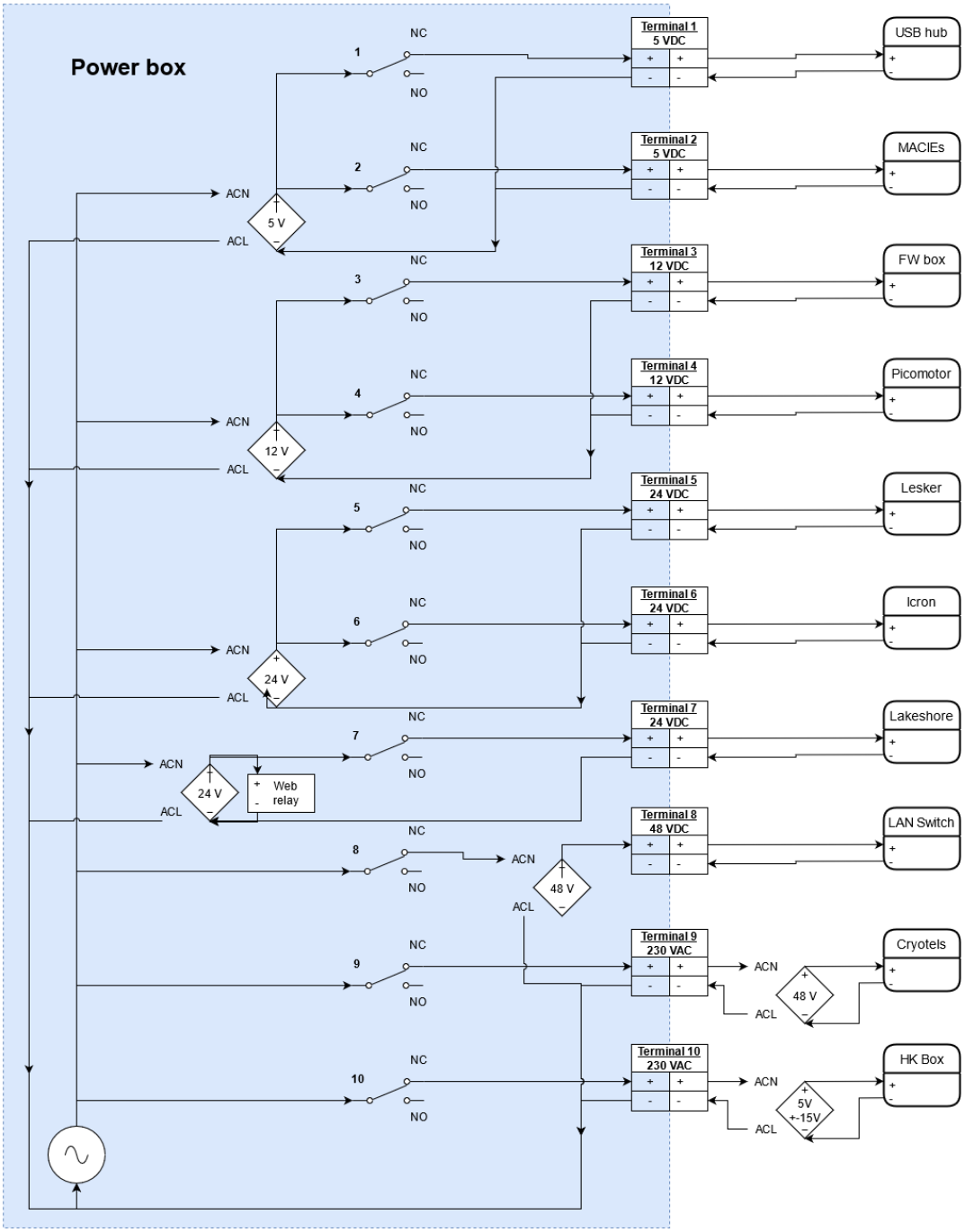


Figure 4.8: Diagram showing the power distribution diagram for PRIME. Each of the terminals is a remotely controlled relay from the WebRelay-10 that is used as a power switch. To conserve power and reduce the risk from unresponsive relays, the powered on configuration for these devices is set to Normally Closed (NC).

PRIME was to use Leach Generation IV controllers to read out and control these detectors since they were compact enough to fit with our assembly, and we should have been able to leverage code developed for these devices by the Detector Characterization Laboratory (DCL). However, the software to run the controllers was completely new since the underlying code base had changed languages from Assembly to C, and the slow manufacturing of these new systems prevented the DCL from developing the new code needed to run our detectors. Thanks to RST support, we were able to acquire the same detector readout and control ASICs being used for RST, ACADIAs. The ACADIA is a cryogenic detector control and acquisition system on an ASIC that can provide clocking and biases to the detectors and digitize up to 40 detector outputs in parallel.[133] These ACADIAs are controlled by an FPGA, which in turn takes commands, and returns data from the control computer. While RST uses a different set of FPGAs better suited to their 18 detector array, we use 2 MACIEs from the same manufacturer, Markury Scientific. These were recommended to us because they have an improved Application Programming Interface (API) in comparison to the RST FPGAs, they are more compact, and they can use the same ACADIA configuration files needed to control the detectors. The DCL also uses MACIEs, so previously tested configurations could also be used for the MACIEs, and after further development commissioned by RST, a single MACIE can control 2 ACADIAs. In PRIME's configuration, communication between the PC and MACIEs is done via GigE interface to one MACIE, which controls the other MACIE via a board-to-board interconnect.[148] This configuration is designed to synchronize all 4 ACADIAs, and their corresponding H4RG-10 detectors. The software developed to read interface between the MACIE API, and the control software is described in the next section.

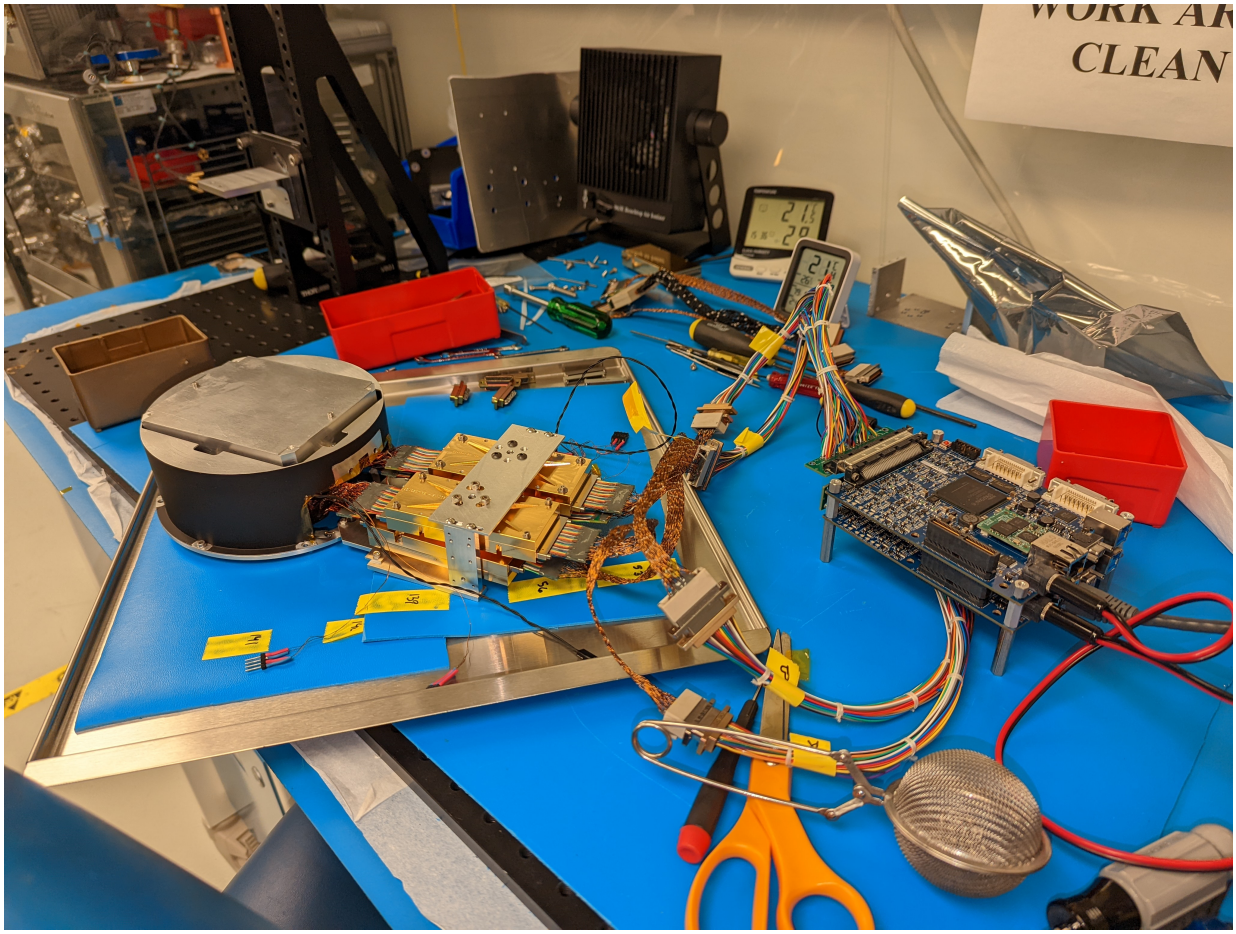


Figure 4.9: Photograph showing the fully connected readout chain on the bench. The 4 H4RG-10 detectors are to the left of the photograph inside of the baffling assembly, and a cover has been placed over them to prevent damage. The 4 ACADIAs are the 4 gold coated devices towards the middle of the photograph that are connected to the detectors via cryogenic wire created using phosphor bronze and high gauge copper conductors in twisted pairs. These are connected to the 2 MACIEs, the 2 stacked blue PCBs that are off to the right in the photograph, via phosphor bronze then, past the feedthrough, copper harnesses.

4.3.2 Detector readout software

The MACIE comes with software that allows for full testing of MACIE functionality via Graphical User Interface (GUI), including: configuring the MACIE, configuring the ACADIA, data acquisition, register reading/writing for the MACIE, and register reading/writing for the ACADIA. This GUI runs on an API, written in C, that installed alongside that software, and is very useful for integration with both control and data reduction software. Astrophysics Science Detector (asdetector[1]) was developed to serve this purpose as a high-level interface (Command Line Interface (CLI) or Transmission Control Protocol (TCP)) to acquire detector data using application specific settings.[156] To leverage existing libraries, RST data reduction codebases, and my own skill set, the MACIE API was fully wrapped in python using ctypes [157], a built-in library for python. This python wrapper was developed such that all functions could be used in a pythonic manner familiar to most Python users (e.g. returning a numpy array instead of a pointer).[2] Since the majority of MACIE API functions refer to the same attributes of a MACIE, and its dependents (the other MACIE and ACADIAs), it was natural to take an object-oriented approach to add another layer to this wrapper. ASDetector uses a base MACIE class that contains all API functions relevant to the device, and useful high level functions for initialization of ASICs, acquiring exposures, and closing the interface.[3] This parent class is inherited by child classes that are specific to the used interface (GigE, USB or CamLink),

[1] `https://github.com/joedurbak/asdetector-public`

[2] `https://github.com/joedurbak/asdetector-public/blob/main/asdetector/detector/macie/api.py`

[3] `https://github.com/joedurbak/asdetector-public/blob/main/asdetector/detector/macie/io.py`

and ASIC (ACADIA or SIDECAR). These classes are then inherited in pairs to gain the attributes for both interface, and specific ASIC (e.g. GigE-ACADIA or SIDECAR-USB). This allows for flexibility with communication methods and ASICs with minimal effort required to develop new code. At the highest level, this code is interacted with via TCP server or CLI. The TCP server communication method was chosen for its low interactivity with the camera control software written in LabVIEW,[4] [158] and the CLI is useful for quick testing/lab data acquisition. The asdetector code is also setup to do detector data reduction to reduce SUTR data using methods described in §3.2. This integration makes it simple to integrate data reduction tools created for RST.

4.3.3 Detector Characterization

A round of detector characterization/testing were done during PRIME camera development. CDS noise (Table 4.2) and dark current (Table 4.3) measurements of one of PRIME's detectors made while varying the electronics, control loops, and detector temperature. The left column in each table designates the variation from the default configuration, and the detector temperature during the measurement. The gain for these measurements is $\approx 2\ e^-/DN$. The default configuration had the detector and ACADIA temperatures PID controlled, the cryocoolers running in constant temperature mode, a turbo pump is maintaining the vacuum, and a linear power supply is used to power the MACIE. This test showed no significant noise contributions from the switching power supply, cryocooler, and less stable ACADIA temperature. Knowing this relaxed many constraints for PRIME camera's final configuration. The only significant contribution seen in this test comes from

[4] `https://github.com/GSFC-PRIME/prime`

	Mean (DN)	Median (DN)	Std. Dev (DN)	16th Per. (DN)	84th Per. (DN)
Default (95 K)	13.959	13.999	6.885	12.282	15.344
ACADIA PID Off (95 K)	13.989	14.022	6.912	12.283	15.392
Cryocooler Off (95 K)	13.961	13.888	7.298	11.713	16.026
No Pump (95 K)	13.953	13.984	6.949	12.224	15.373
Switching supply (95 K)	13.959	13.995	6.836	12.280	15.353
Default (100 K)	14.623	14.279	9.351	12.475	15.839
Default (105 K)	16.830	14.673	17.491	12.720	17.096

Table 4.2: Single Detector CDS Noise Test

increases in detector temperature. However, this noise contribution is much less than the background shot noise observed during observations. Dark current (Figure 4.11) and CDS noise (Figure 4.10) were also measured in the final configuration, which was much warmer (115 K) than the single detector test due to the 0.5 W heating contribution from each of the three extra ACADIAs needed in the final configuration. Predictably, this increased temperature resulted in higher CDS noise and dark current, but these values were still within requirements.

4.4 Data Reduction

At a basic level, PRIME requires two types of data reduction pipelines: ramp reduction software to fit multiple frames into a single exposure, and a photometry pipeline to reduce multiple exposures into a stacked and calibrated image.

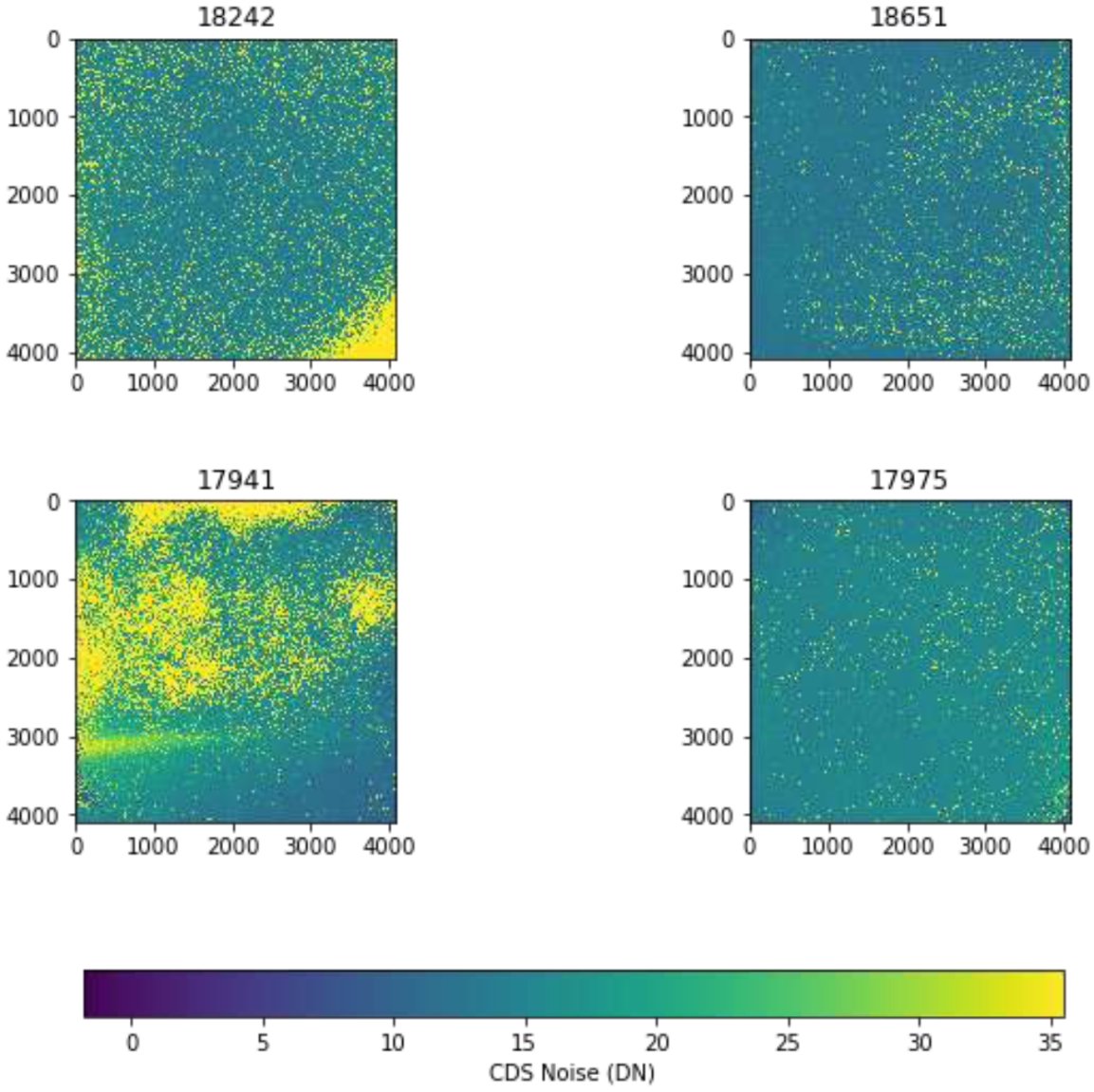


Figure 4.10: CDS noise for each of PRIME camera's detectors in the final configuration. The gain for these measurements is $\approx 2\ e^-/DN$.

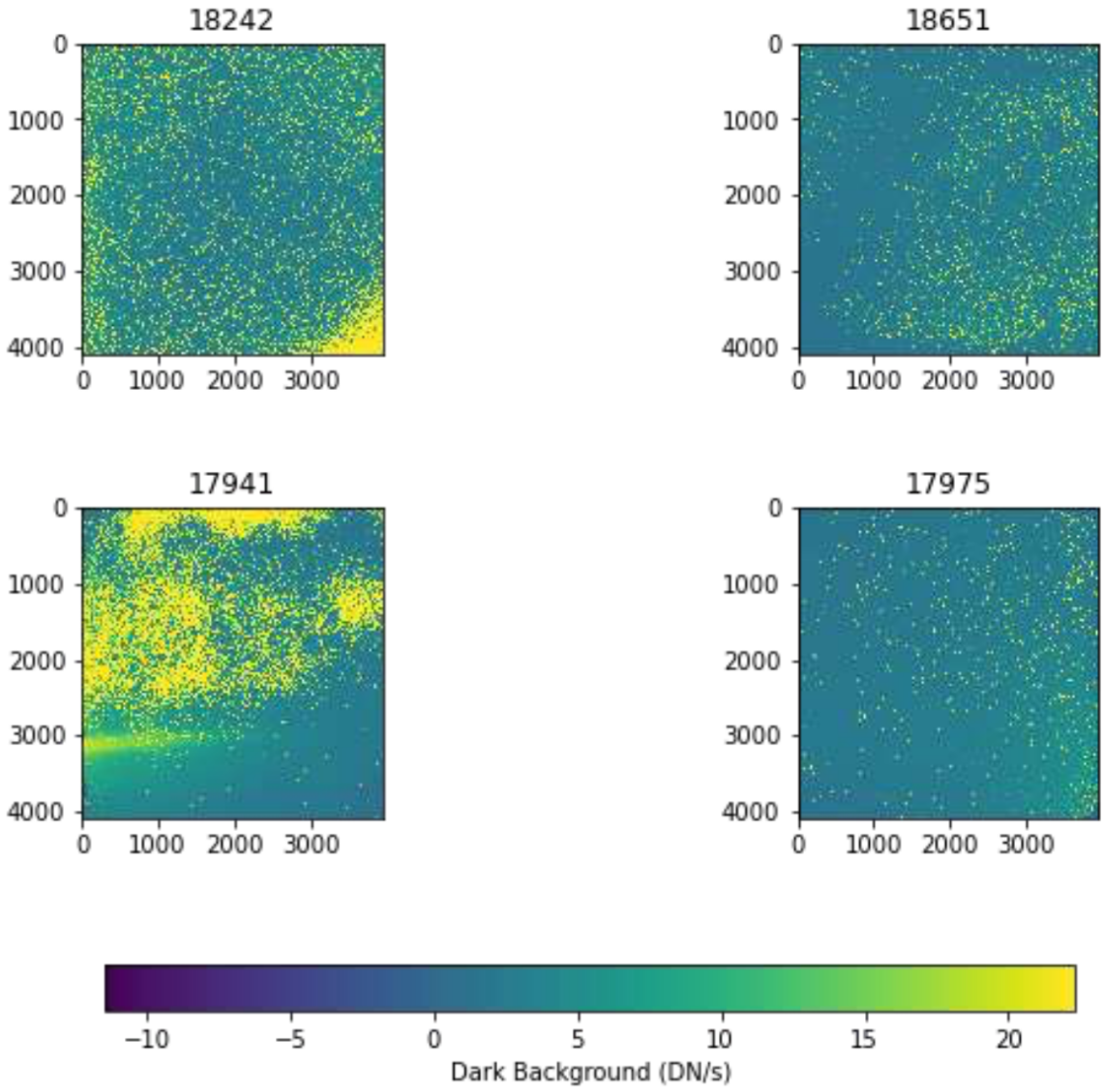


Figure 4.11: Dark current for each of PRIME camera's detectors in the final configuration. The gain for these measurements is $\approx 2\ e^-/DN$.

	Mean (DN/s)	Median (DN/s)	Std. Dev (DN/s)	16th Per. (DN/s)	84th Per. (DN/s)
Default (95 K)	2.820	1.639	3.983	1.144	3.764
ACADIA PID Off (95 K)	2.857	1.649	4.044	1.154	3.825
Cryocooler Off (95 K)	2.926	1.673	4.171	1.159	3.937
No Pump (95 K)	2.949	1.719	4.113	1.201	3.952
Switching supply (95 K)	2.834	1.687	3.912	1.177	3.766
Default (100 K)	4.054	1.735	6.581	1.171	6.024
Default (105 K)	6.429	1.862	10.915	1.180	11.284

Table 4.3: Single Detector Dark Current Test

4.4.1 PRIME Ramp Reduction

As PRIME's detector hardware is based off of RST, all exposures taken by PRIME are acquired in SUTR mode. This means that signals are read periodically (every ≈2.86 s) after resetting the pixels. Each frame up-the-ramp is reference pixel corrected using methods similar to those described by Rauscher, Fixsen and Mosby [87]. Each of the frames are then corrected for nonlinearity [159]. After each frame has been processed as described, ramp fitting and cosmic ray removal are done in real time using a memory efficient method [132].

4.4.2 PRIME Photometry Pipeline

The results in §4.5 are based on the GRB/GW follow-up team's photometry pipeline written by Orion Guiffreda [160], a baccalaureate researcher working with us, which uses the steps described here, and laid out in Figure 4.12. Initial astrometry is generated for

each ramp reduced exposure by first calculating World Coordinate System (WCS) using the telescope pointing position and rotation offset, and then running the image through a local installation of astrometry.net [161]. These images are then flat fielded using the most recently observed and stacked set of sky flats. A sky image is then generated by masking sources via sigma clipping, normalizing the sigma clipped images, and taking a median across dithered exposures for a target. Pixels that are still masked after the median stacking, are then filled with values from a spatial mean. This normalized sky is then denormalized for each exposure by multiplying by the sigma clip masked median for that exposure. This denormalized sky is then subtracted from the image. With the background removed, the astrometry is refined again using astrometry.net. The astrometry is improved yet again by identifying sources with SExtractor [162], and calculating WCS with SCAMP [146]. These astrometry calibrated images are then median stacked using SWarp [163]. Photometry is then calculated using an appropriate catalog to the observed field and filter along with PSFex [164].

4.5 Performance

With PRIME observations in progress, and data reduction being performed as detailed above, progress can be reported for both the surveys and performance. This section shows the quality of photometry currently being achieved with PRIME, and how the throughput evolves over time.

Using the data acquired during an arbitrarily chosen ToO follow-up dataset taken on 2024-03-18 of EP240315a [165], the photometric calibration fit, and corresponding residuals

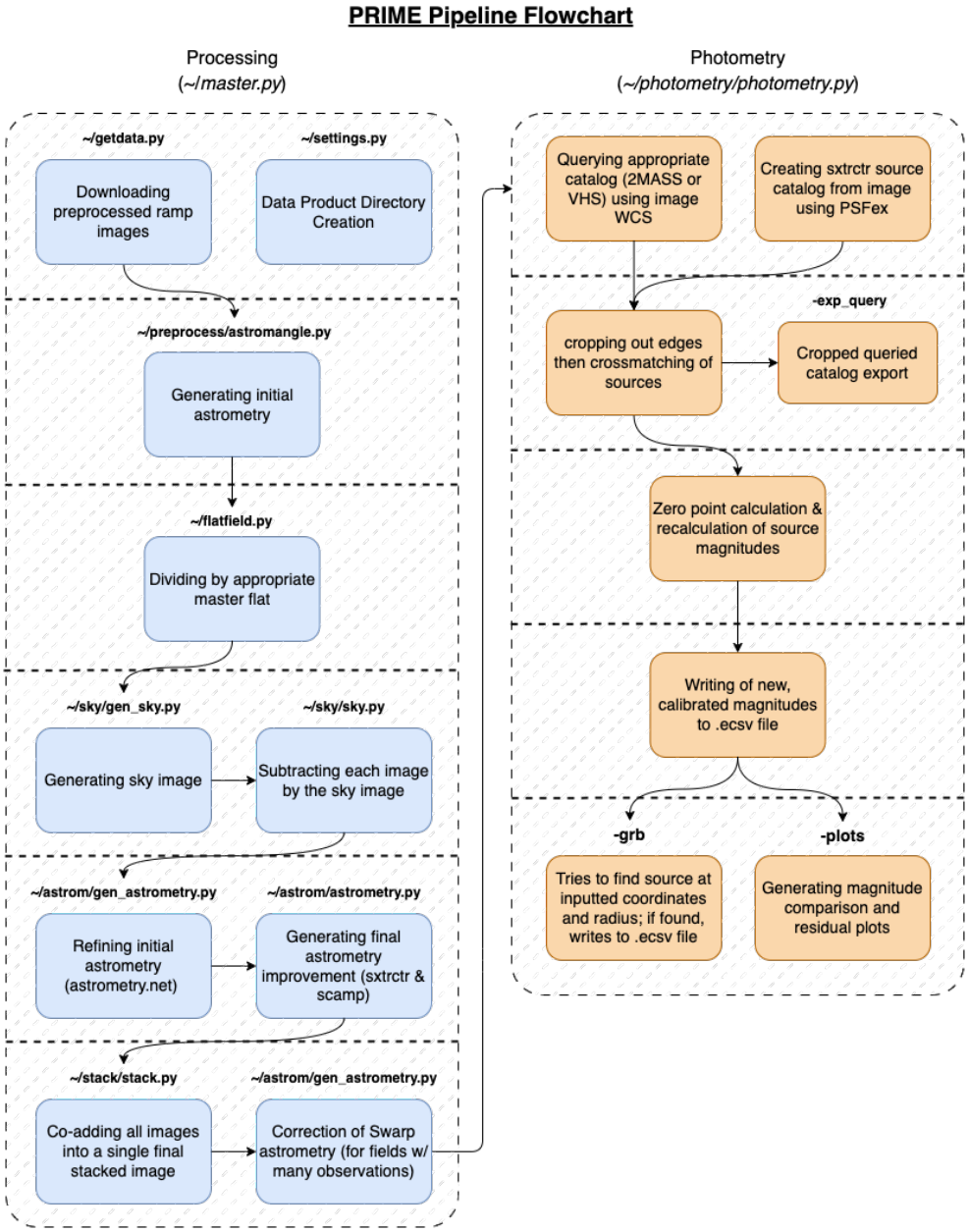


Figure 4.12: Diagram showing the steps performed by the photometry pipeline.

plot in Figure 4.13 were generated. This observation was performed in J-band, and was stacked from 90 exposures of 20 s. Photometric calibration was performed using VISTA Hemispherical Survey (VHS) [166] data. As can be seen in Figure 4.13, our calibration matches VHS, as the residual dispersion is well scattered around 0. Also, the slope of the linear fit between PRIME and VHS sources is nearly unity when the offset is set to zero.

Using another arbitrarily chosen ToO follow-up dataset taken on May 19, 2024 of EP240518a [167], the J-band limiting magnitude was calculated over time by stacking different numbers of 60 s exposures, and the results of this are shown in Figure 4.15. The limiting magnitude was determined by binning detected magnitudes into 0.1 mag bins, and selecting the magnitude at half the maximum as shown in Figure 4.14. The moon's illumination was 80%, and was located 55 deg from the observed field. The airmass was ≈1.1 during these exposures. This sensitivity is near the expectations for the instrument.

4.6 Current Observations

4.6.1 Observing Strategy

During this the observatory's commissioning phase, observations are acquired in a few different modes: Galactic Bulge (GB) survey, J-band observable sky survey, calibration fields, target of opportunity (ToO) requests, and ad hoc requests from partners. At the beginning and end of every night, sky flats are acquired in an alternating broadband filter when weather permits. The GB survey is performed whenever the bulge is observable by PRIME according to a preset grid (Figure 4.16). These observations are performed without dithering to increase throughput. When the GB is not observable, the default mode is to

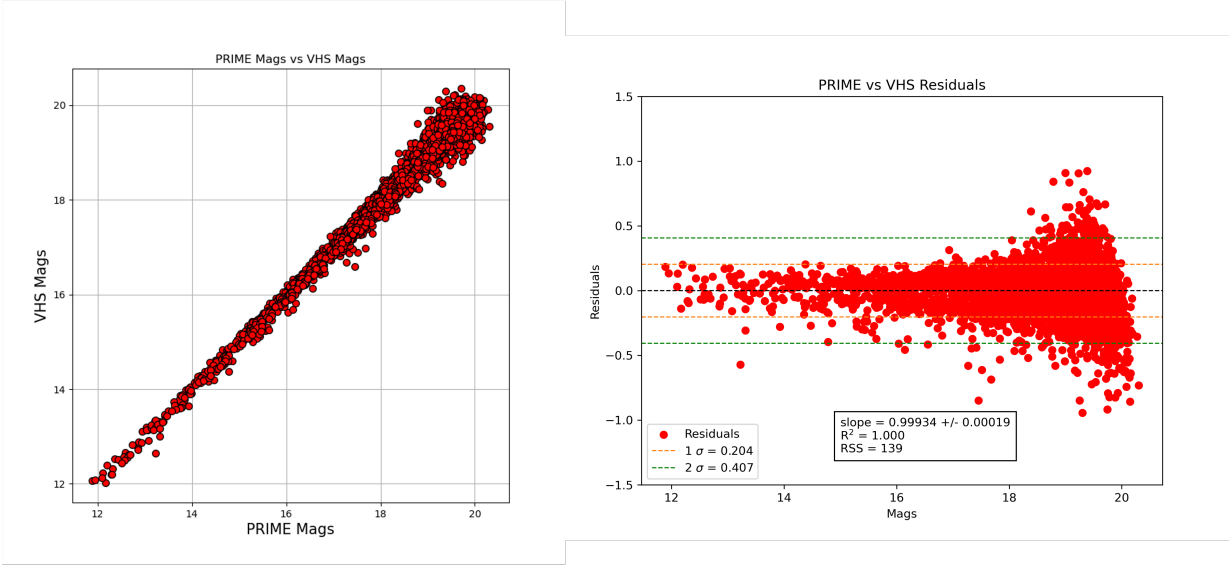


Figure 4.13: The plot on the left shows the cross-matched photometric fit of detected PRIME sources against VHS sources in J-band. The plot on the right shows the residuals of the fit.

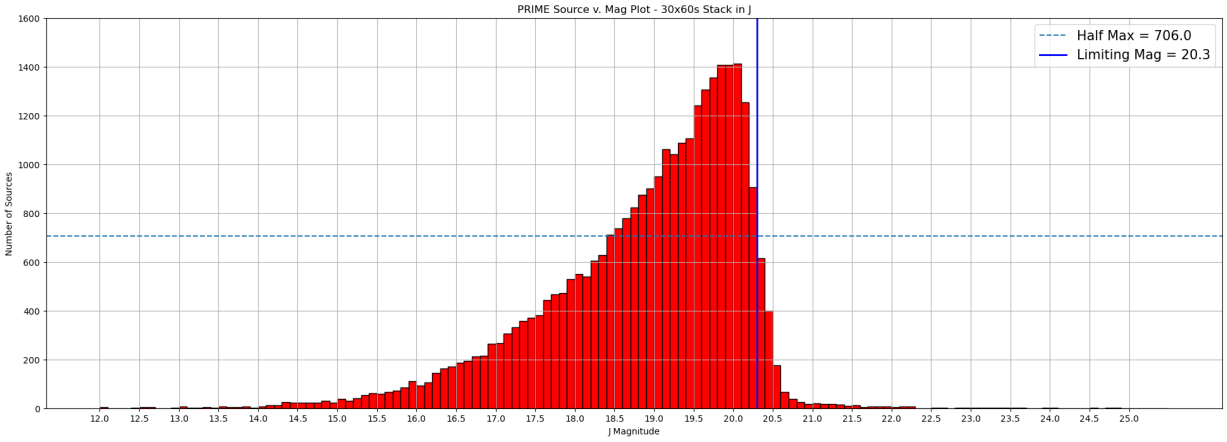


Figure 4.14: Plot showing a histogram of the detected sources in J-band after stacking thirty 60 s exposures. The limiting magnitude was determined by selecting the value at half the maximum. This histogram was created for each of the data points shown in Figure 4.15.

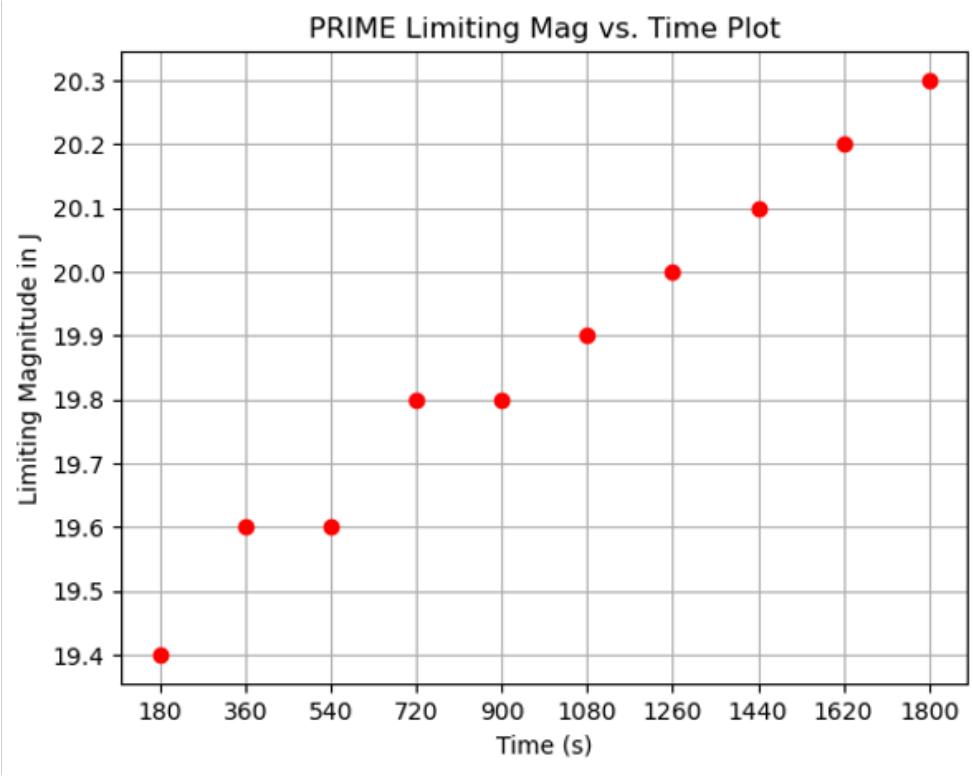


Figure 4.15: Limiting J-band mag (Vega) vs. time plot created using stacked exposures of 60 s in sets of 3, with detected sources in 0.1 mag bins.

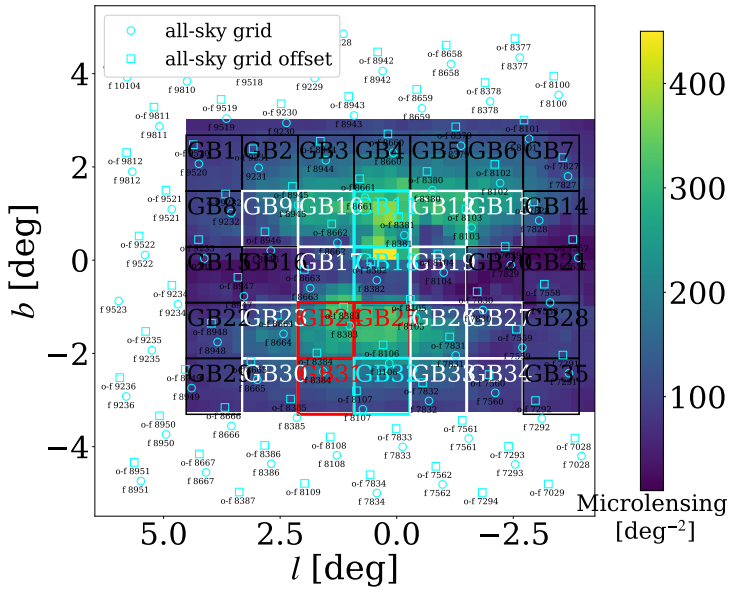


Figure 4.16: These are the various grids used by PRIME. The GB grid is used primarily for GB observations, and grid fields do not overlap. The all sky grid is the primary grid ideally used for all other observations. Pointing positions in this grid are spaced 1.136 deg apart, so that there is a small overlap in grid fields. The offset all sky grid is used when a target of interest falls within a chip gap. This field is shifted half a detectors FOV in both right ascension and declination.

obtain dithered tiled observations of the observable all sky grid (Figure 4.16) in J-band. ToO, calibration, and ad hoc observations are preferred to be taken according to the all sky grid whenever possible. If the source of interest is within the chip gap, the offset all sky grid is the net preferred option.

4.6.2 All Sky Coverage

As discussed in §4.6.1, when higher priority targets are not in the queue, the observable all sky grid is observed in J-band using 6 dithered exposures of 10 s. Based on Figure 4.15, these exposures result in a limiting magnitude >19 on the Vega scale. By an-

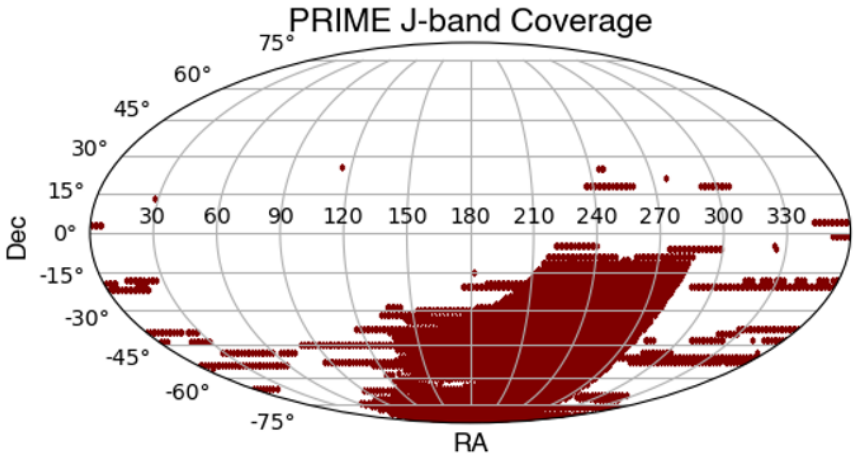


Figure 4.17: PRIME J-band coverage on the observable all sky grid. Coverage is ≈7000 deg^2 within a year of the June 2023 servicing mission. Off grid observations are not included. Limiting magnitude > 19 Vega.

alyzing the logs within a year of the servicing mission in June 2023 for unique all sky grid numbers, Figure 4.17 is generated. Multiplying the number of grid locations by 1.136 deg x 1.136 deg grid spacing, the coverage of this survey is found to be ≈7000 deg^2.

4.6.3 Observation Software

Similar to RIMAS, we want to be able to use PRIME to observe transient events as soon after initial detection as possible. To facilitate this, another GCN monitor was created for PRIME [168] based on the code discussed in §2.4.9 with observability calculations made using PRIME's location. Since PRIME is operated exclusively by Osaka University, this

monitor is not integrated into the LabVIEW instrument control software as in the RIMAS case. Instead, GCN alerts are sent to the PRIME ToO group's Slack channel, and formatted in Markdown since Markdown is natively supported in Slack. To make things even more convenient, airmass and sky plots, and observation lists are also generated and sent in the same Slack conversation with the GCN alert. The observation lists are already snapped to the appropriate grid as described in §4.6.1. Alerts are only sent for targets that are observable within the next 24 hours based on time observable above a preset elevation at night. LVK detection probability maps are tiled using gwemopt[5] [169] software, and the observation list is generated based on these pointings.

4.7 PRIME Transient Follow-Up

Since commissioning, PRIME has been used to follow-up transient events including GRB detections by Fermi and *Swift*, fast X-ray transient detections by Einstein Probe (EP), GW detections by LVK, and other similar events reported by the community in GCN circulars and Astronomer's Telegram (ATel) posts. PRIME managed to have immediate scientific impact by observing the afterglow of the brightest GRB ever observed, GRB 221009a, during the second night of observations.[149] These observations aided in determining a more accurate model for the overall structure of this GRB [47]. The afterglow from the second brightest GRB ever observed, GRB 230307a, was also detected by PRIME, and helped determine that the likely progenitor system was a lanthanide-rich kilonova despite its long duration.[46] These transient observations, along with other transient observations, are summarized in Table 4.4 along with their publications. As can be seen in

[5] `https://pypi.org/project/gwemopt/`

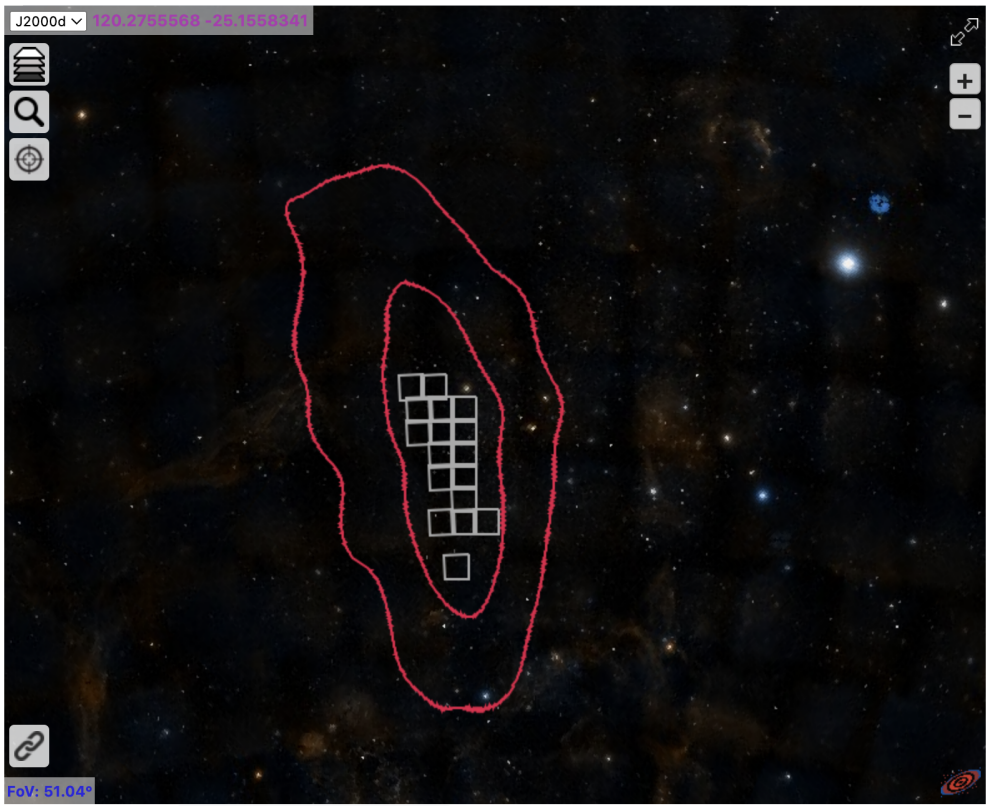


Figure 4.18: PRIME J-band tiling of S240422ed as shown on Gravitational Wave Treasure Map[b]. The innermost red outline encompasses the 50% probability region, and the outermost red outline encompasses the 90% probability region of the S240422ed detection by LVK. PRIME's coverage is shown by the white squares.

[a] https://treasuremap.space/alerts?graceids=S240422ed
[b] https://treasuremap.space/alerts?graceids=S240422ed

the table, a lot of these observations did not result in GCN circulars or ATel posts. This was due to the photometry pipeline development being in flux, and analysis taking up to a month after observation. The tiled observations of S240422ed are shown in Figure 4.18.

Table 4.4: PRIME Transient Follow Up

Transient	Observation dates	Publications
GRB 221009A	2022-10-09, 2022-11-05, 2022-11-07, 2022-11-09	GCN 32654 [149], Science Advances [47]
Swift-J103441.7	2023-01-31, 2023-02-01	
GRB 230307A	2023-03-08	Nature [46]
GRB 230812A	2023-08-15	
GRB 230815A	2023-08-19	
GRB 230827A	2024-08-27, 2024-08-28, 2024-08-29	
GRB 230906A	2023-09-06	
GRB 231117A	2023-11-17, 2023-11-18	
GRB 231210B	2023-12-10, 2024-01-14	
GRB 240122A	2024-01-23, 2024-01-24, 2024-02-04, 2024-04-01	GCN 35633 [170]
GRB 240205B	2024-02-07, 2024-02-10, 2024-02-11	GCN 35708 [171]
swift_false_alarm	2024-02-17,2024-02-18	
SRGA J144459.2-604207	2024-02-22, 2024-02-23, 2024-02-26, 2024-02-27	ATel 16499 [172]
GRB 240222A	2024-02-24	
GRB 240303A	2024-03-05	
xrf_1	2024-03-07, 2024-03-11	
EP_src2	2024-03-07, 2024-03-11	

EP 240315A	2024-03-16, 2024-03-18	GCN 35956 [173]
EP 240408A	2024-04-09, 2024-04-11	
GRB 240402B	2024-04-12, 2024-04-13	
EP 240418A	2024-04-18	
GRB 240419A	2024-04-18	
S240422ed	2024-04-23, 2024-04-24, 2024-04-25, 2024-04-27, 2024-04-28, 2024-04-29, 2024-04-30, 2024-05-01, 2024-05-07, 2024-05-09, 2024-05-12, 2024-05-15, 2024-05-16, 2024-05-18, 2024-05-19, 2024-05-20, 2024-05-21, 2024-05-22, 2024-05-23, 2024-05-24, 2024-05-25, 2024-05-26, 2024-05-27, 2024-05-28, 2024-05-29	GCN 36306 [174]
EP 240518A	2024-05-19,2024-05-21	
GRB 240702A	2024-07-06	
GRB 240805B	2024-08-05	
EP 240804A	2024-08-06	
EP 240807A	2024-08-08	GCN 37118 [175], GCN 37153 [176]
EP 240809A	2024-08-13, 2024-08-15, 2024-08-16, 2024-08-20	
GRB 240812C	2024-08-13, 2024-08-15, 2024-08-16	
EP 240816A	2024-08-17, 2024-08-23, 2024-08-24	GCN 37212 [177]
EP 240820A	2024-08-22	GCN 37250 [178]

GRB 240821A	2024-08-23, 2024-08-30, 2024-09-10	GCN 37323 [179]
GRB 240825A	2024-08-25	GCN 37303 [180]
EP 240919A	2024-09-21, 2024-09-22, 2024-09-26	
EP 241001A	2024-10-01	
GRB 241002B	2024-10-02, 2024-10-03, 2024-10-04	GCN 37700 [181], GCN 37712 [182], GCN 37736 [183]
GRB 241006A	2024-10-06	GCN 37730 [184]
GRB 241009A	2024-10-10, 2024-10-11	
EP 241021A	2024-10-22	
GRB 241105A	2024-11-06	GCN 38121 [185]
GRB 241107A	2024-11-12	
GRB 241113A	2024-11-13	GCN 38227 [186]
GRB 241115A	2024-11-18	GCN 38274 [187]
GRB 241127A	2024-11-28	GCN 38384 [188]

Chapter 5: Final Considerations

5.1 Summary

This thesis work explores the development of hardware and software to study GRBs in the NIR. As explored in §1.1.2, §1.1.4, and §2.2.1, NIR instruments are essential to multi-wavelength observations of GRBs. Towards this end, this thesis work has primarily focused on the development of two instruments, RIMAS and PRIME, to quickly perform NIR follow-up observations of GRB detections. RIMAS will soon provide quick photometric and spectroscopic measurements of NIR counterparts to GRBs. These NIR observations will be of great help in studying optically dark bursts (especially those at high redshift), and gaining detailed information about high redshift GRBs. PRIME is already developed, and performing regular observations of both its main science objective (microlensing events caused by exoplanets in the Galactic Bulge), and high energy transient events. This effort has already contributed to a few papers, and many GCN circulars detailing observations of GRB counterparts, LVK localization regions, and X-ray transients detected by Einstein Probe.

In preparing RIMAS to perform the above operations, RIMAS required thorough testing, and numerous developments to its hardware. The initial detectors were working well when characterized in Vicki Toy's thesis work [53], but they had degraded by the time

the Grisms arrived. This led to the need to integrate two different sets of replacement detectors. After this effort, the initial readout electronics became obsolete, and required replacement to avoid future issues. Upgrades were also made to make more apertures and gratings available. The cryogenic mechanisms required to focus the detectors and change apertures/filters/gratings required many rounds of development and testing to work consistently. Spectral mode testing confirmed that the spectrographs were working as expected, but they also revealed underlying issues with RIMAS's vacuum window. A large upgrade to RIMAS's cryogenic systems also made by replacing the original Gifford-McMahon cryocooler with much more compact and robust Sterling cryocoolers. Finally, most of the housekeeping electronics (communications, thermometry, vacuum gauges, humidity sensors, and power distribution) were upgraded to make the instrument more robust.

RIMAS also requires multiple types of data reduction software, which were developed over the course of this thesis work. Basic SUTR reduction software was made to reduce the many frames acquired non-destructively up the ramp during an exposure into a single image. Some future effort is required to remove fixed pattern and correlated noise along with cosmic rays from these final images, but the framework for this is already developed. The photometry data reduction software was already developed by Vicky Toy [53], but a lot of effort was made (with help from Ethan Zack, and undergraduate physics student at University of Maryland) to make the software more robust, easier to install, and the algorithms more effective. These upgrades have caused this software to already be widely used for optical observations with LMI, an optical imager on the same telescope RIMAS will be installed. The cross-dispersed spectral data reduction software was adapted from another spectrograph, IGRINS. This required robust calibration of RIMAS's spectra, and further

changes to the software's algorithms. Thorough testing of this pipeline was performed with simulated data of multiple source types, lab acquired data, and on-sky data from the DeVeny spectrograph. This testing helped confirm that the pipeline was ready for RIMAS data, and led to the discovery that a different telluric correction algorithm was required for RIMAS's resolving power.

PRIME telescope is designed specifically to perform a time domain survey of the Galactic Bulge searching for microlensing events caused by exoplanets. However, as a NIR telescope available for ToO observations in the southern hemisphere with a wide field of view and seeing limited plate scale, PRIME is a useful tool for observing high energy transients. The wide field of view is particularly useful when observing the large localization regions from Fermi GBM, and LVK. Due to the efforts described in this thesis, PRIME has been commissioned, and is already working towards these efforts. Uniquely, PRIME camera is the first astronomical instrument to use RST package H4RG-10 detectors and corresponding ASICs on-sky. This thesis describes the development of software to run these detectors, integration of the detectors into PRIME camera, and characterization of these detectors. It also covers a fair amount of the systems development required to supply power, and communicate with each of PRIME camera's subsystems. With PRIME's commissioning complete, observations have begun, and a number of high energy transients have been investigated. To facilitate this, custom software has been developed to aid with observation planning, and to quickly reduce data so that it can be shared with the community via GCN Circulars.

5.2 Future Work

5.2.1 RIMAS

The initial plans for RIMAS are straightforward: install RIMAS on LDT, obtain and analyze commissioning data, and start regular observations of GRB counterparts. RIMAS has already been accepted by Lowell pending some small adjustments (most of which have already been made), and will ship in the next few months. Once RIMAS is commissioned, it will be important to fully characterize its performance, so that its capabilities can be confirmed. After this, RIMAS should be used to observe as many GRBs as possible at the outset both to improve the chances of an interesting discovery, and to learn the idiosyncrasies involved in operating the new instrument. Based on lessons learned from performing rapid follow-up observations with LDT's optical instruments, these ToO observations are much faster if the classically scheduled observer is already using the required instrument (e.g. the instrument is already calibrated and in focus). To facilitate this and maximize the scientific output from RIMAS, it will be important to host workshops on RIMAS's operation and data reduction.

Beyond the initial stages, efforts are needed to prepare RIMAS for GW follow-up observations. During this thesis work, GW follow-up observations were performed with LDT's DeVeny spectrograph, and were aimed at classifying counterpart candidates. These observations highlighted the need to automatically reduce the data acquired of these candidates, and the need for tools to help classify the objects. To this end, a selection of template comparison, red-shifted element detection, and machine learning tools will be needed to

aid in the search for a compact merger's counterpart.

RIMAS also has a few hardware upgrades planned: a slit-viewing camera detector, and the Maryland OH Suppression IFU System (MOHSIS)[1]. A slit-viewing camera to ensure accurate pointing during spectroscopy was always in RIMAS's design, but the cryocooler upgrade prevents the effective use of the InSb detector selected for this purpose. A reasonable candidate for replacing this detector has been identified, an InGaAs detector that has been used in cryogenic conditions for other astronomical applications, and testing will be required in the lab to ensure that it can be integrated with RIMAS. MOHSIS is a fiber Bragg grating aimed at suppressing OH emission lines from the atmosphere. The H-band grating is already available, the project is funded, and the optics to integrate it are in development. A J-band grating is also planned, but this is still a work in progress. Installing MOHSIS on RIMAS would reduce the sky brightness present in the NIR, and allow for deeper measurements with RIMAS's spectrographs.

5.2.2 PRIME

As discussed above, PRIME is already in use and beginning to achieve its science goals. However, a lot of software is still needed to allow it to reach its full potential for transient detection. A good case study of this can be found in the follow-up efforts of the potential neutron star-black hole merger, LVK S240422ed. Fortunately, preparations were already made to plan tiling of the LVK localization region, and multiple epochs to a depth of $\sim$21 mag AB were observed in J-band covering a large portion of the probability region. However, due to lack of automation of the photometry pipeline, the lack of image

[1] https://www.astro.umd.edu/~veilleux/astrophotonics/MOHSIS_overview.html

subtraction software, and the lack transient detection software, PRIME was not ready to discover counterpart candidates. Efforts to create this software are already underway, but they still require a lot of development and testing. To facilitate testing and discover novel transients, a time domain survey is being planned to cover ~ 500 deg^2 in multiple bands at a cadence of a few days. This will help by providing a solid dataset that software can be developed around to process observations in real time, compare with previous epochs, and detect transients. Once this survey can be studied effectively, this process can be used on all PRIME observations.

Appendix A: Gamma Ray Burst and Gravitational Wave Follow Up with the Lowell Discovery Telescope

Although in-depth studies of GRBs and GWs were not performed during this thesis work, many contributions to this science were made via observations, data reduction, and reporting results. While waiting for RIMAS's last few components to arrive, photometric and spectroscopic observations of transients were acquired using LDT's optical instruments.

A.1 Instruments

As discussed in Chapter 2, LDT's design allows for up to five instruments to be mounted to the telescope, and available for use within minutes. This instrument suite consists of the Large Monolithic Imager (LMI), the DeVeny Spectrograph, the Extreme PREcision Spectrometer (EXPRESS), the Near-Infrared High Throughput Spectrograph (NIHTS), and will include RIMAS within the next few months. GRB and GW follow-up observations were performed using LMI and the DeVeny spectrograph. LMI is a large format imager with a 12.3′x12.3′ FOV, 0.12″/pixel, and holds 17 filters with wavelengths ranging from 0.3 to 1.0 µm.[77, 189] DeVeny is a moderate resolution spectrograph with resolving power, R, between 500 and 4000 depending on which grating is selected from the available 10.[77] The spectrograph covers wavelengths between 0.3 and 1.0 µm, and

has a motorized tilt angle stage for the grating that allows for selection of the central wavelength.[77]

A.2 GRB Follow-Up Efforts

As discussed in §1.1.2 and §1.1.4, multi-wavelength observations are key to understanding GRBs. This is enabled through timely reporting of bursts and their coordinates via GCN notices and circulars. The community then reports their low-level findings about results from follow-up observations, categorization of candidates, etc. via additional GCN circulars. Quick reporting of follow-up observations helps other observers plan their own observations as they can communicate better localization, whether the target brightness is suitable to their instrumentation, and if the particular target has interesting characteristics worthy of further study.

A.2.1 GRB observations

While preparing RIMAS and PRIME to be on sky for GRB/GW observations in the NIR, photometric and spectroscopic observations were already being acquired in the optical with LMI and DeVeny respectively. These observations have included both rapid follow-up of transient events via ToO triggers, and classically scheduled observations to observe host galaxies. The GCN circulars resulting from these rapid follow-up observations are detailed in Table A.1. Beyond the basic reporting in these GCN circulars, these observations along with the data reduction pipeline discussed in §3.4 aided in a number of studies. These studies include: studying the circumgalactic medium of high redshift galaxies using long

GRB	Publications
GRB 190106A	GCN 23744 [193]
GRB 190627A	GCN 24986 [194]
GRB 200729A	GCN 28270 [195]
GRB 200826A	GCN 28312 [196]
GRB 201006A	GCN 28572 [197]
GRB 201014A	GCN 28654 [198]
GRB 201214B	GCN 29054 [199]
GRB 201221D	GCN 29128 [200]
GRB 210504A	GCN 29946 [201]
ZTF21aayokph	GCN 29952 [202]
GRB 210704A	GCN 30451 [203]
GRB 210919A	GCN 30860 [204]
GRB 221009A	GCN 32739 [205], GCN 32799 [206]
GRB 221120A	GCN 32957 [207]
GRB 230204B	GCN 33333 [208]
GRB 230205A	GCN 33334 [209]
GRB 231117A	GCN 35099 [210], GCN 35139 [211]

Table A.1: LDT GRB Follow-Up

GRBs as line-of-sight probes [190, 191], the search for a supernova associated with GRB 221009a [150], the determination that GRB 221009a was powered by a structured jet [47], and a host galaxy study of short GRBs [192].

A.3 GW Follow-Up Efforts

Multi-messenger observations are of great interest as they give multiple insights into the fundamental physics occurring in extreme scenarios. The most obvious candidate for these observations are for binary mergers that involve a neutron star, as these are observable by LIGO, Virgo and Kagra (LVK), EM observatories, and should emit neutrinos as well. LIGO detected the first GW shortly after powering on in 2015, GW150914.[212] Later, the first binary neutron star merger was observed by LIGO, GW170817[45], and in multiple wavelengths by a number of other instruments, GRB 170817A.[20] Since then, Kamioka

Gravitational Wave Detector (KAGRA) has come online. With localizations generated with measurements from LIGO, Virgo, and KAGRA GW observatories, much better localization of GW events is now possible. These events are reported to GraceDB[1], and via GCN notices and circulars. This information is then evaluated by a number of programs, who have various ways of determining follow-up activities. For example, the Zwicky Transient Facility (ZTF) images 3750 deg^2/hr to a depth of 20.5 mag [213] to search for any optical transients within the probability region.

A.3.1 LDT GW observations

During earlier LIGO observation runs, the community would attempt to observe any significant potential GW events reported via GraceDB. However, this approach with LDT became unsustainable with the increased sensitivity of LIGO/Virgo during observing run O3. Instead, our collaboration would perform observations of any potential GW detection containing a neutron star, or a mass-gap object. These observations took two forms: an imaging galaxy search, and spectroscopic observations of potential counterparts. The imaging searches were performed using LMI, and involved observing a list of galaxies within the LIGO/Virgo localization region with similar redshift to that of the detected event. Spectroscopic measurements were acquired using DeVeny's R≈1000 grating to determine the nature of candidates identified by other programs including ZTF. The results of these searches are reported in the publications detailed in Table A.2.

[1] `https://gracedb.ligo.org/`

Signal	Publications
GW190425	GCN 24220 [214]
GW190814	GCN 25374 [215], GCN 25397 [216], MNRAS [217]

Table A.2: LDT GW Follow-Up

Appendix B: RIMAS Lab Data

A large amount of lab data was acquired to fully characterize RIMAS. A portion of these test results are provided in this appendix to give a more complete summary of RIMAS's performance.

B.1 Various Lab Spectra

B.1.1 Echelle Spectra

This section contains example spectra from RIMAS's echelle spectrograph in addition to the other spectra shown throughout this work. Spectra were acquired and combined using the same manner discussed in §2.4.2.1.

B.1.1.1 Reduced Echelle Lamp Spectra

This section contains echelle spectra taken using 80 µm slit, and reduced using the methods described in §3.3.2. These spectra are all wavelength calibrated, but not flux calibrated due to the lack of a flux calibrated standard.

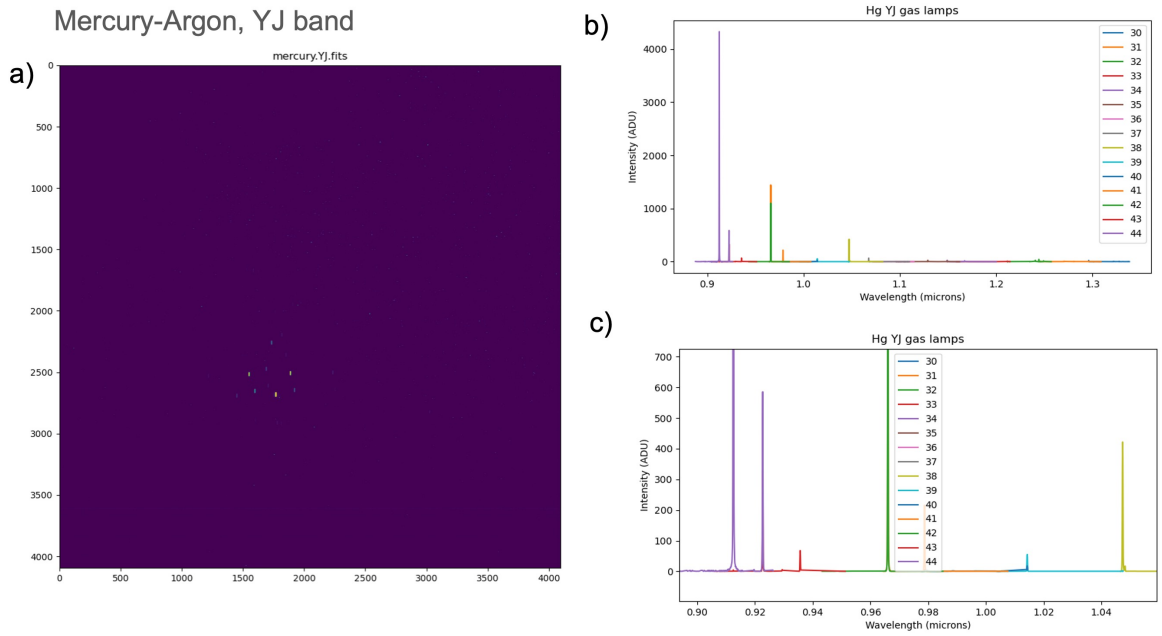


Figure B.1: Spectrum of a mercury argon low-pressure gas discharge lamp taken with RIMAS's echelle spectrograph. (a) The spectrum as it is read from the detector array. (b) The spectrum as reduced, and wavelength calibrated. No flux calibration was applied. (c) The reduced spectrum zoomed in to show the emission line features. As can be seen here, the emission lines from separate orders overlap when they are the same emission line. This shows that the spectral calibration is of good quality, and valid throughout the various spectral orders.

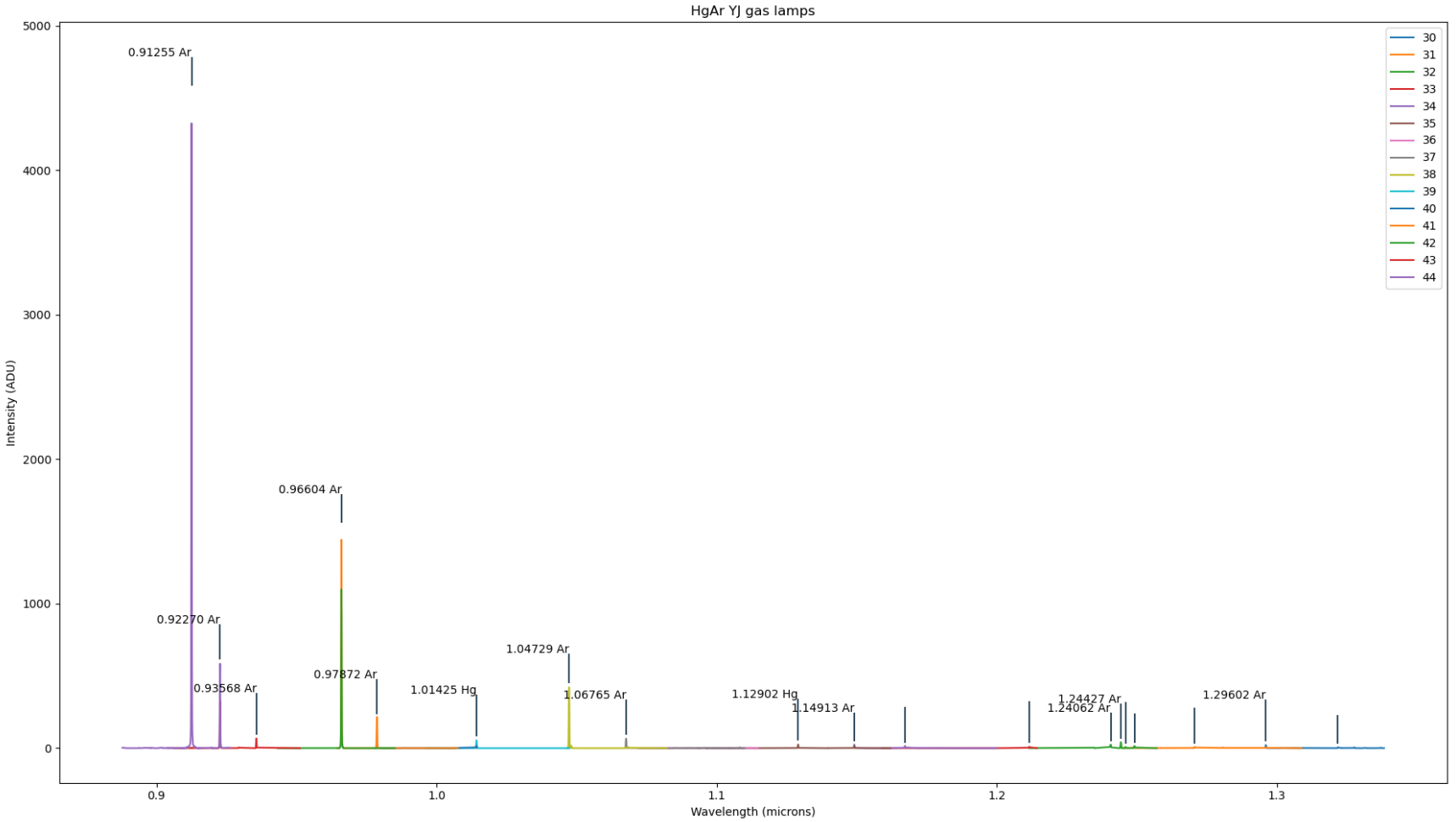


Figure B.2: Labeled spectrum of a mercury argon low-pressure gas discharge lamp taken with the YJ arm of RIMAS's echelle spectrograph. Each of the lines identified, and used for calibration have a dark line above them. The wavelengths for the brightest emission lines are given in microns.

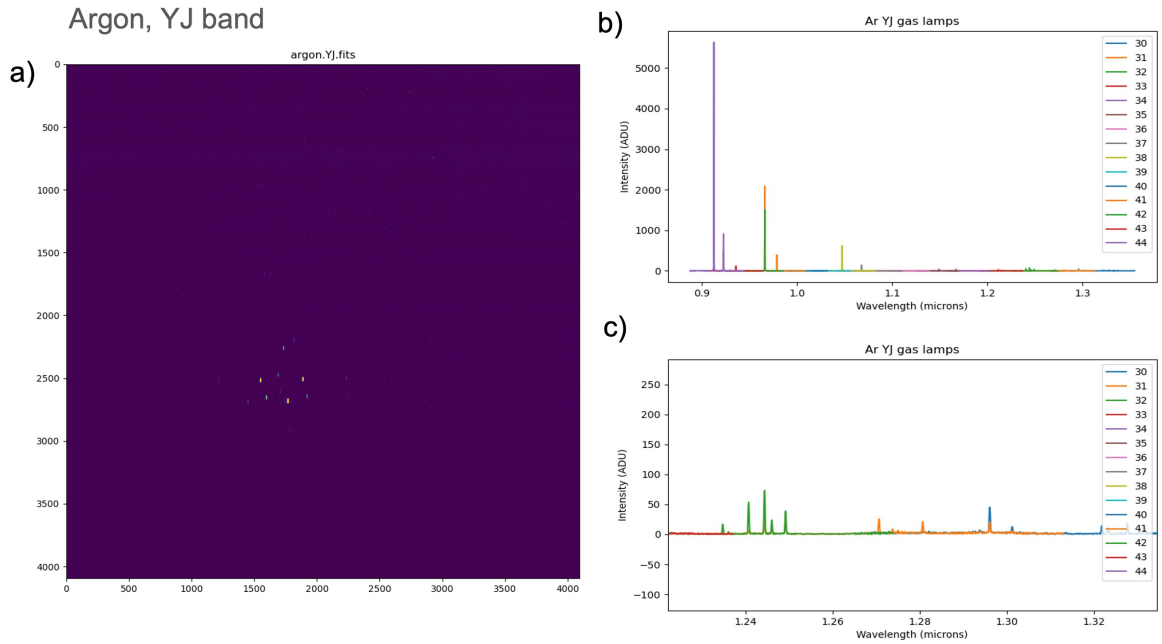


Figure B.3: Spectrum of an argon low-pressure gas discharge lamp taken with RIMAS's echelle spectrograph. (a) The spectrum as it is read from the detector array. (b) The spectrum as reduced, and wavelength calibrated. No flux calibration was applied. (c) The reduced spectrum zoomed in to show the emission line features. As can be seen here, the emission lines from separate orders overlap when they are the same emission line. This shows that the spectral calibration is of good quality, and valid throughout the various spectral orders.

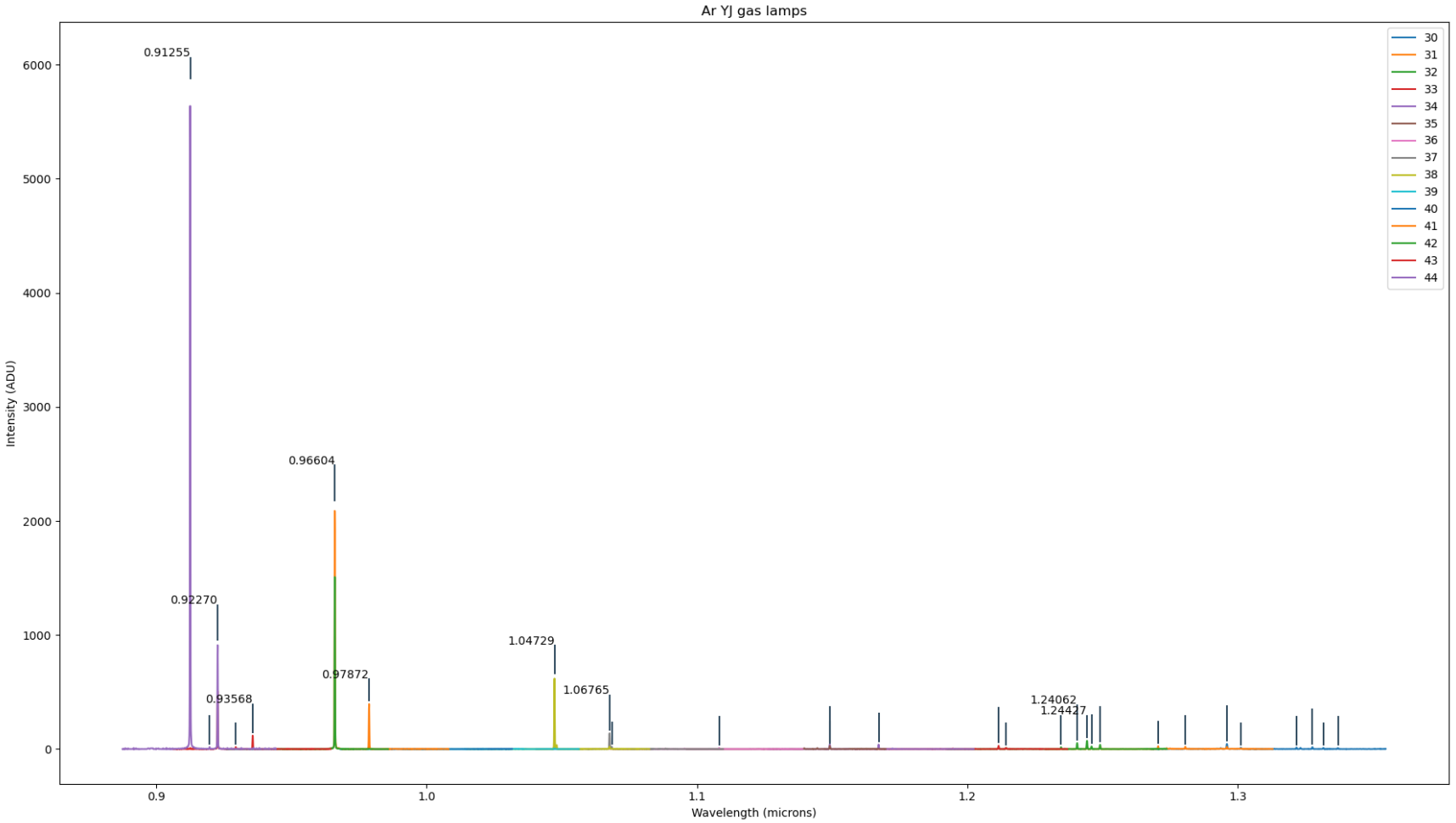


Figure B.4: Labeled spectrum of a argon low-pressure gas discharge lamp taken with the YJ arm of RIMAS's echelle spectrograph. Each of the lines identified, and used for calibration have a dark line above them. The wavelengths for the brightest emission lines are given in microns.

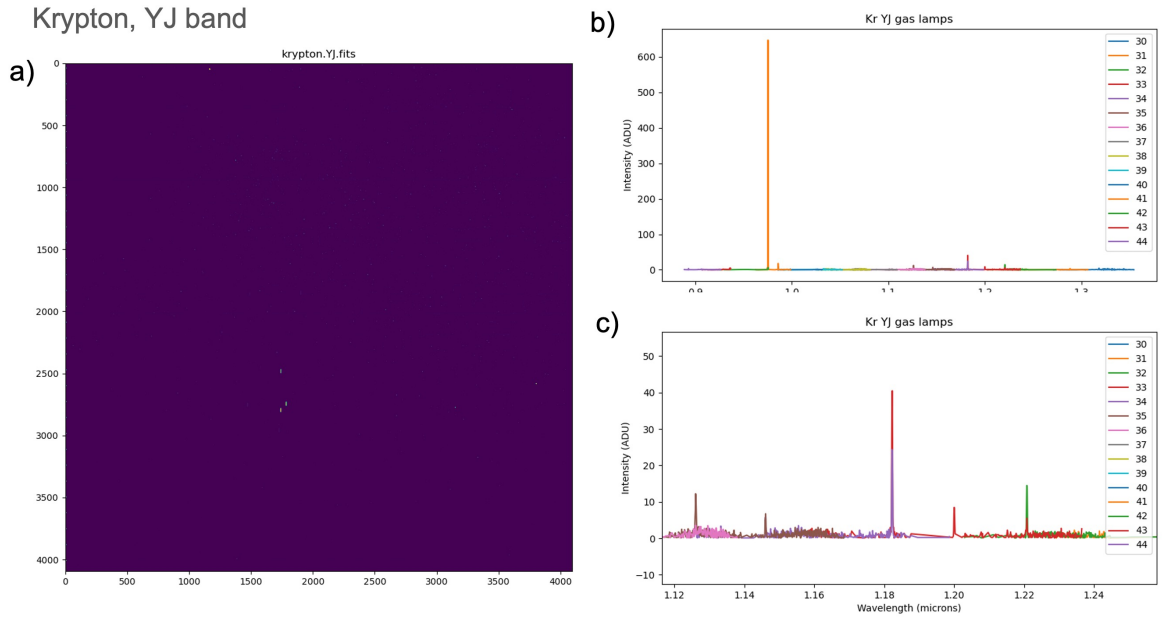


Figure B.5: Spectrum of a krypton low-pressure gas discharge lamp taken with RIMAS's echelle spectrograph. (a) The spectrum as it is read from the detector array. (b) The spectrum as reduced, and wavelength calibrated. No flux calibration was applied. (c) The reduced spectrum zoomed in to show the emission line features. As can be seen here, the emission lines from separate orders overlap when they are the same emission line. This shows that the spectral calibration is of good quality, and valid throughout the various spectral orders.

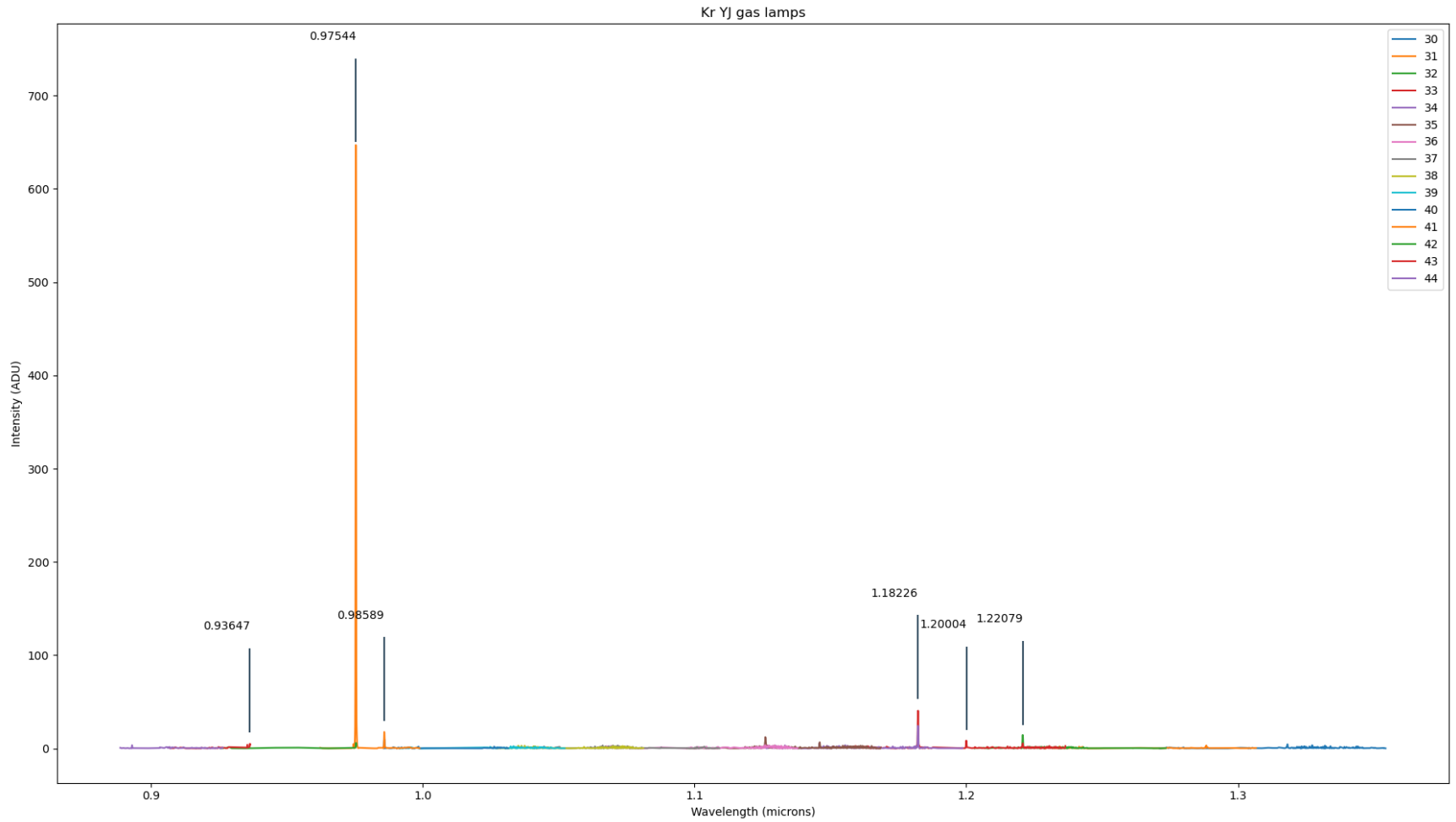


Figure B.6: Labeled spectrum of a krypton low-pressure gas discharge lamp taken with the YJ arm of RIMAS's echelle spectrograph. Each of the lines identified, and used for calibration have a dark line above them. The wavelengths for the brightest emission lines are given in microns.

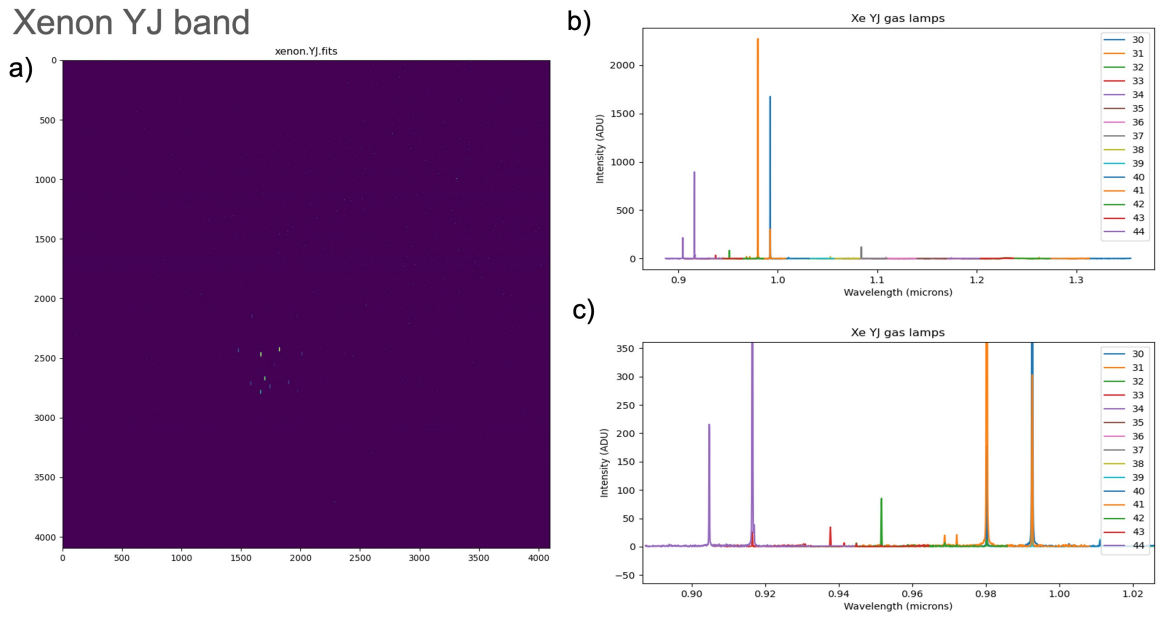


Figure B.7: Spectrum of a xenon low-pressure gas discharge lamp taken with RIMAS's echelle spectrograph. (a) The spectrum as it is read from the detector array. (b) The spectrum as reduced, and wavelength calibrated. No flux calibration was applied. (c) The reduced spectrum zoomed in to show the emission line features. As can be seen here, the emission lines from separate orders overlap when they are the same emission line. This shows that the spectral calibration is of good quality, and valid throughout the various spectral orders.

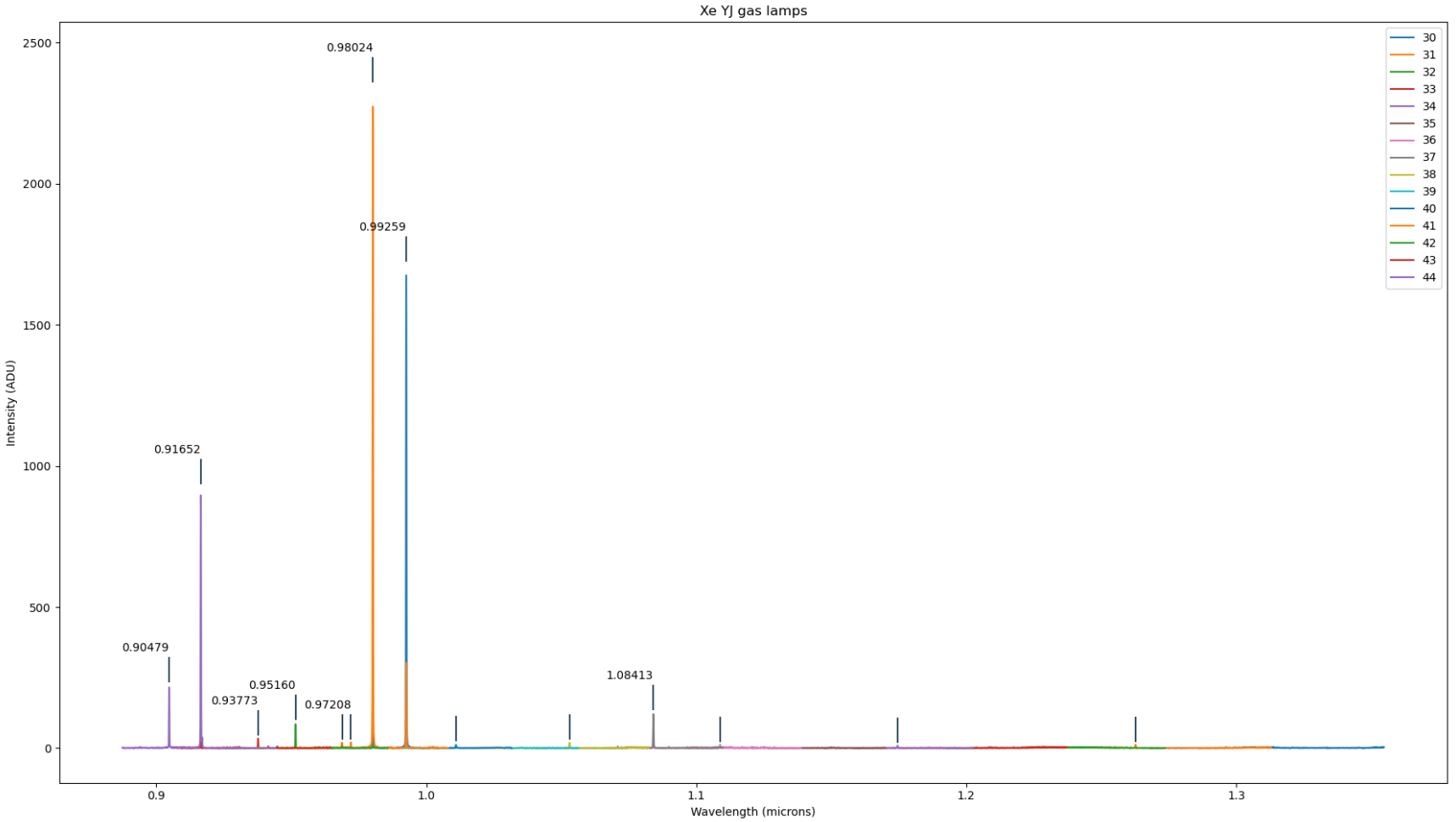


Figure B.8: Labeled spectrum of a xenon low-pressure gas discharge lamp taken with the YJ arm of RIMAS's echelle spectrograph. Each of the lines identified, and used for calibration have a dark line above them. The wavelengths for the brightest emission lines are given in microns.

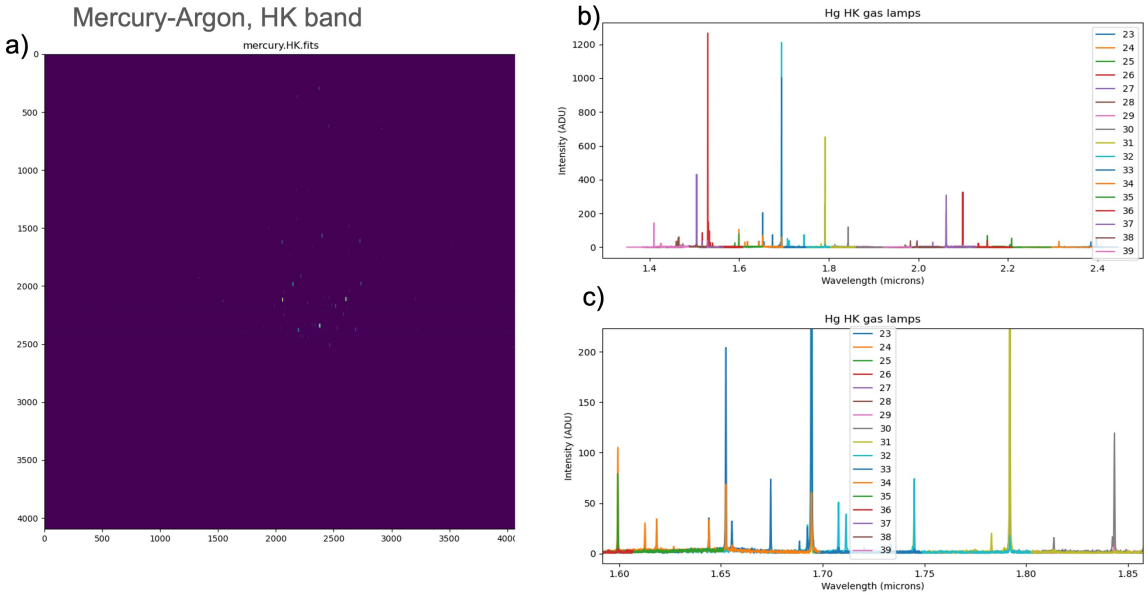


Figure B.9: Spectrum of a mercury argon low-pressure gas discharge lamp taken with RIMAS's echelle spectrograph. (a) The spectrum as it is read from the detector array. (b) The spectrum as reduced, and wavelength calibrated. No flux calibration was applied. (c) The reduced spectrum zoomed in to show the emission line features. As can be seen here, the emission lines from separate orders overlap when they are the same emission line. This shows that the spectral calibration is of good quality, and valid throughout the various spectral orders.

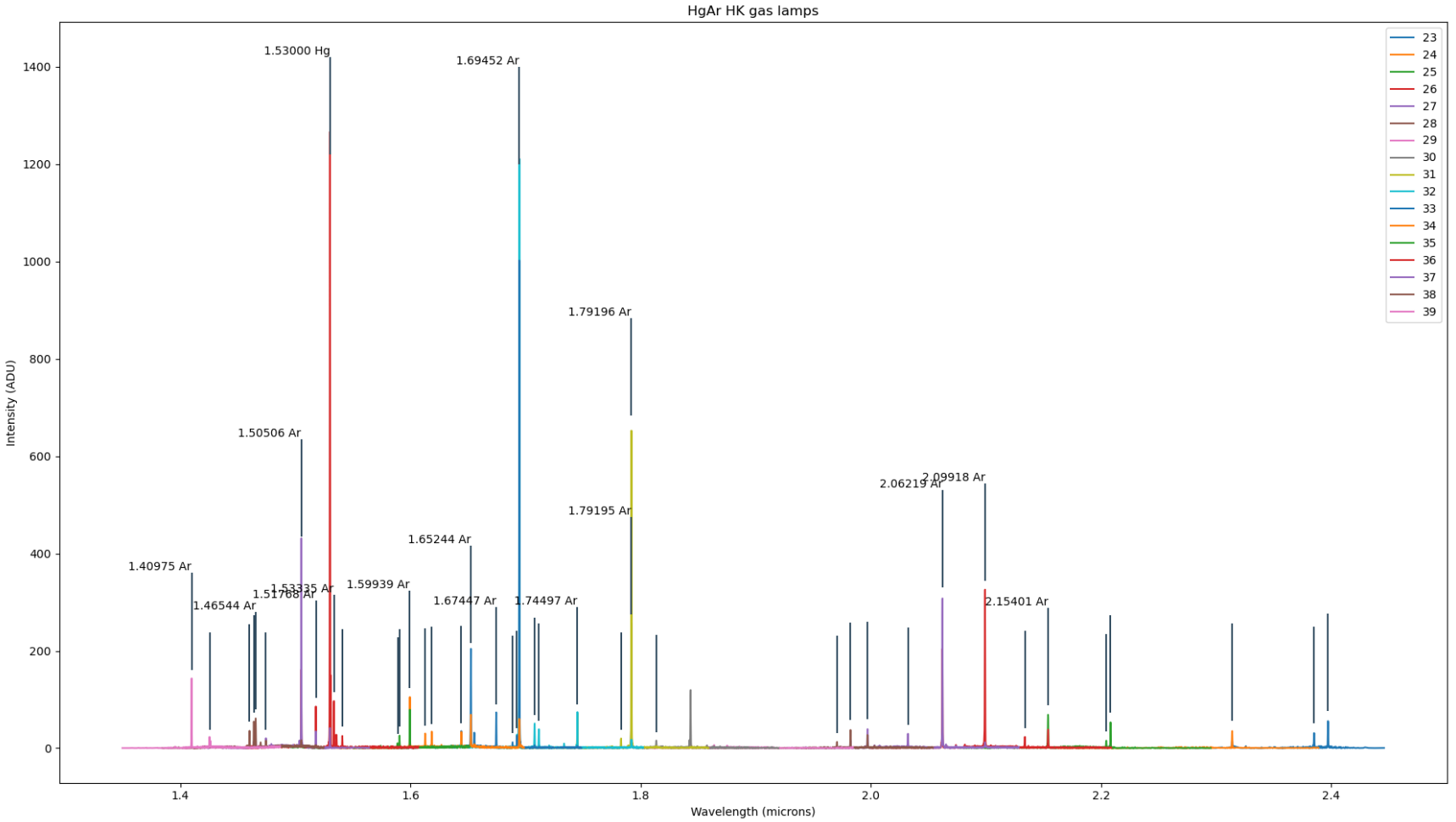


Figure B.10: Labeled spectrum of a mercury argon low-pressure gas discharge lamp taken with the HK arm of RIMAS's echelle spectrograph. Each of the lines identified, and used for calibration have a dark line above them. The wavelengths for the brightest emission lines are given in microns.

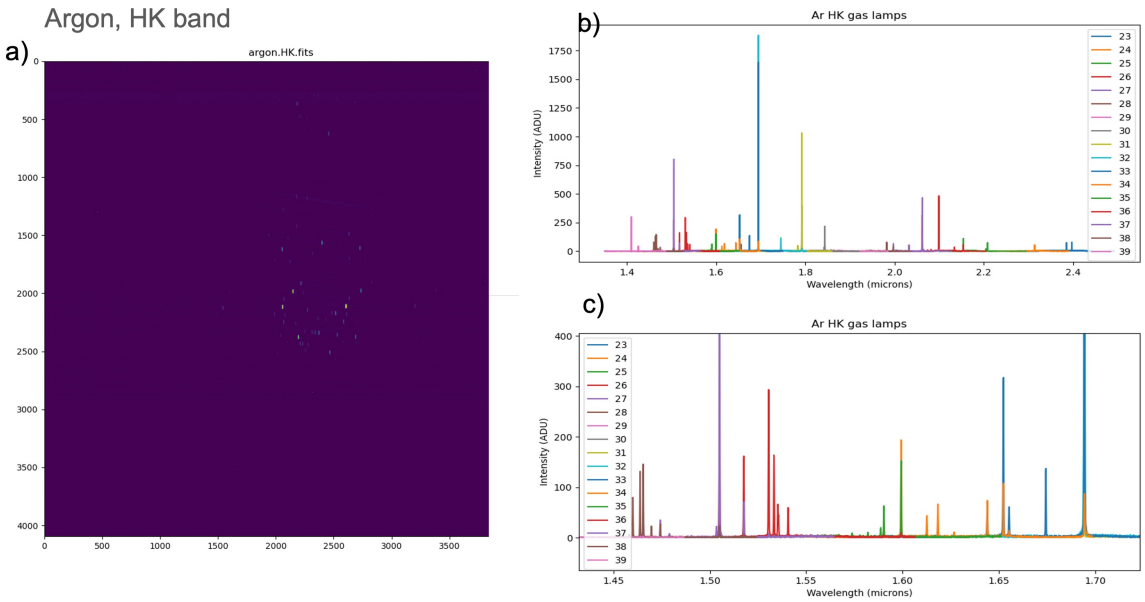


Figure B.11: Spectrum of an argon low-pressure gas discharge lamp taken with RIMAS's echelle spectrograph. (a) The spectrum as it is read from the detector array. (b) The spectrum as reduced, and wavelength calibrated. No flux calibration was applied. (c) The reduced spectrum zoomed in to show the emission line features. As can be seen here, the emission lines from separate orders overlap when they are the same emission line. This shows that the spectral calibration is of good quality, and valid throughout the various spectral orders.

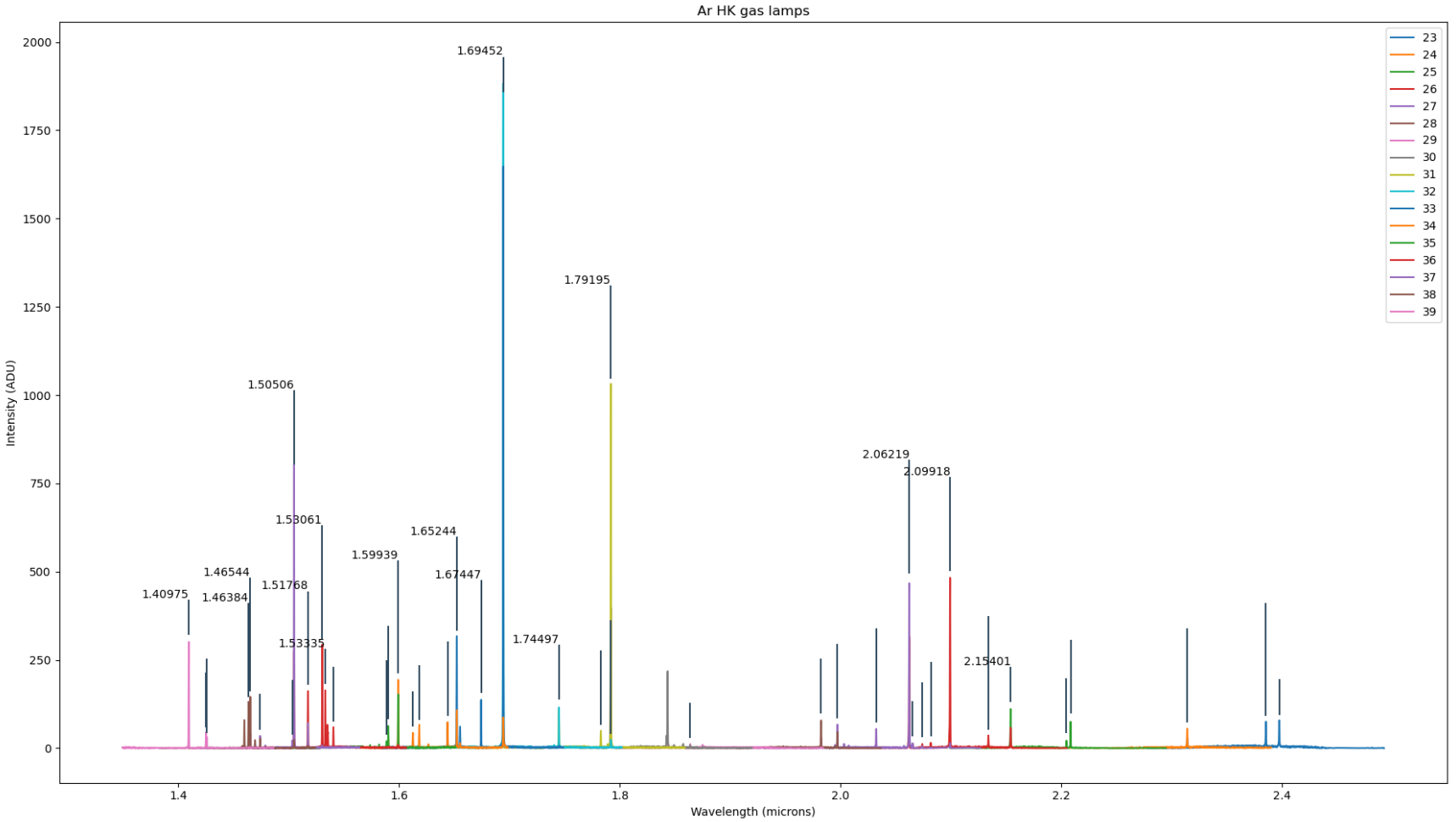


Figure B.12: Labeled spectrum of a argon low-pressure gas discharge lamp taken with the HK arm of RIMAS's echelle spectrograph. Each of the lines identified, and used for calibration have a dark line above them. The wavelengths for the brightest emission lines are given in microns.

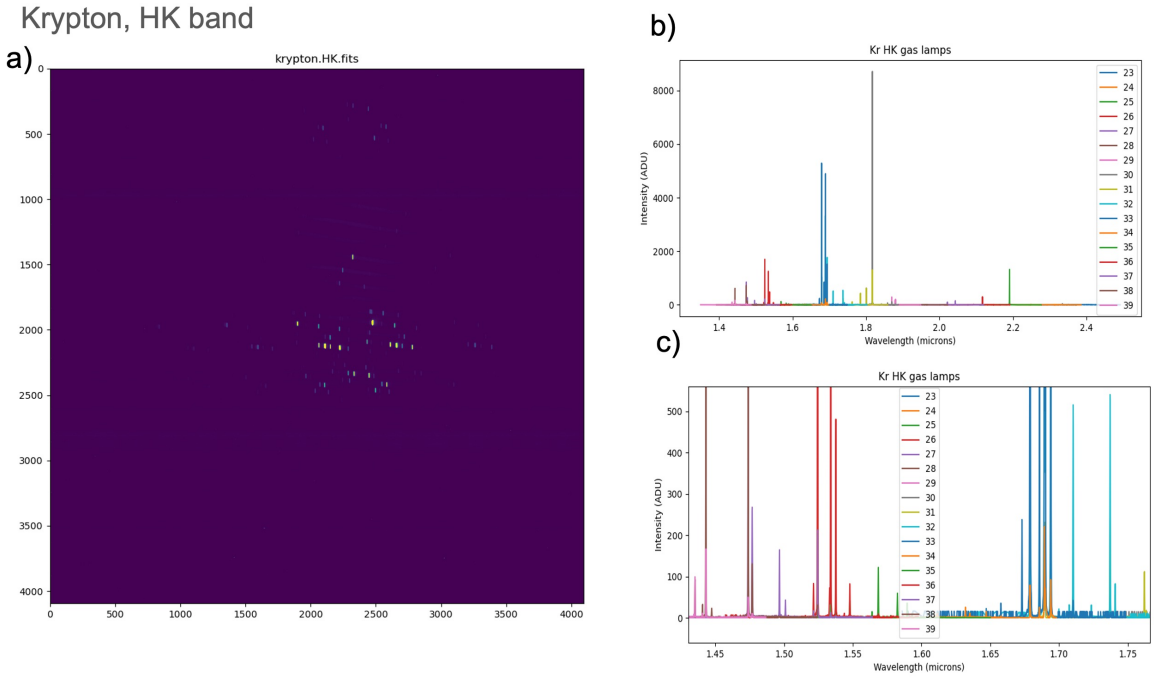


Figure B.13: Spectrum of a krypton low-pressure gas discharge lamp taken with RIMAS's echelle spectrograph. (a) The spectrum as it is read from the detector array. (b) The spectrum as reduced, and wavelength calibrated. No flux calibration was applied. (c) The reduced spectrum zoomed in to show the emission line features. As can be seen here, the emission lines from separate orders overlap when they are the same emission line. This shows that the spectral calibration is of good quality, and valid throughout the various spectral orders.

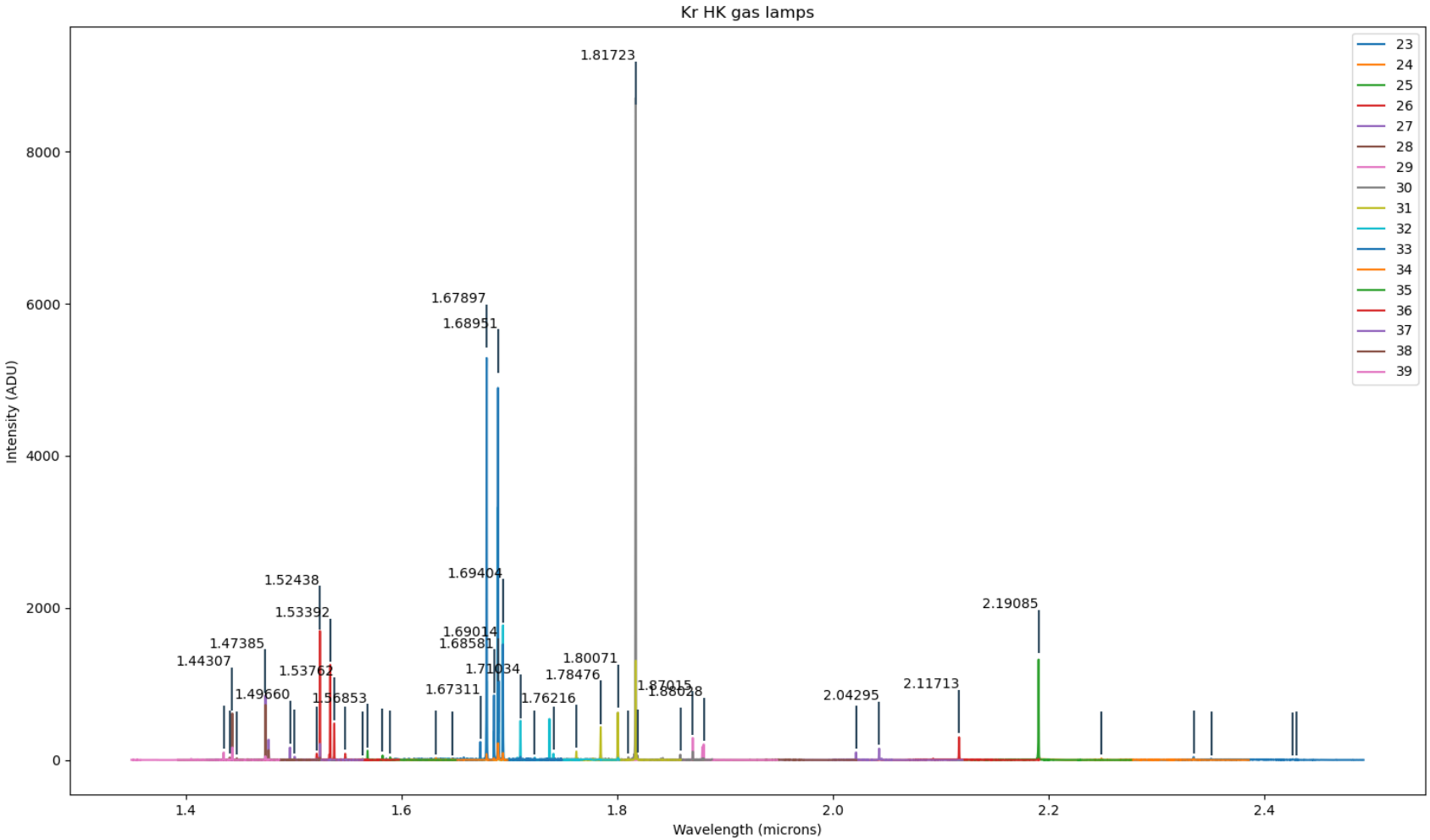


Figure B.14: Labeled spectrum of a krypton low-pressure gas discharge lamp taken with the HK arm of RIMAS's echelle spectrograph. Each of the lines identified, and used for calibration have a dark line above them. The wavelengths for the brightest emission lines are given in microns.

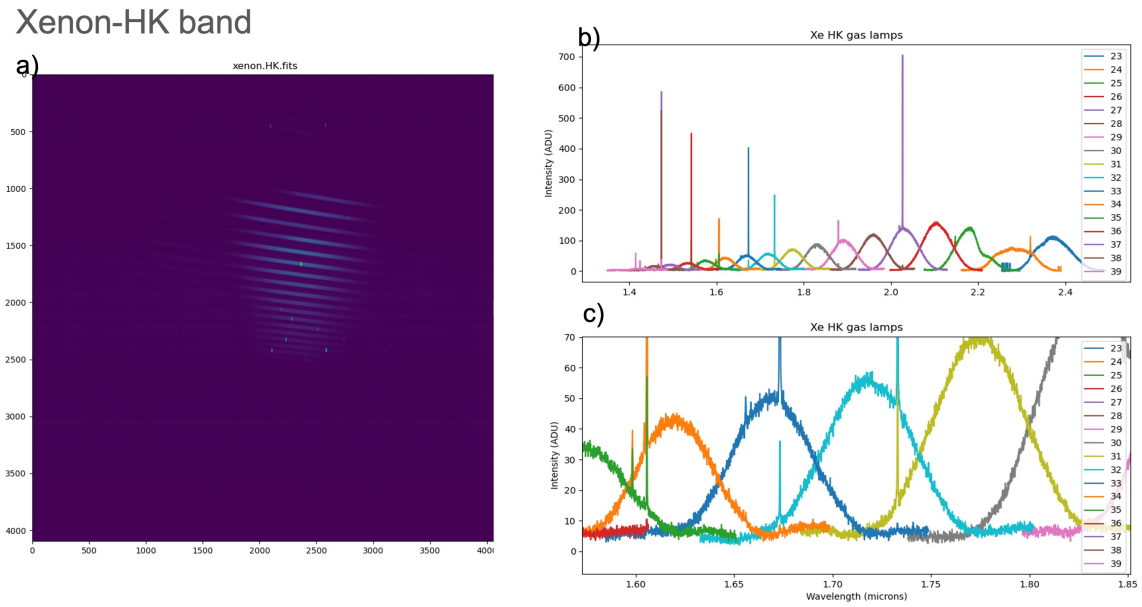


Figure B.15: Spectrum of a xenon low-pressure gas discharge lamp taken with RIMAS's echelle spectrograph. It is worth noting here that the xenon lamp had degraded, creating a thermal continuum background that can be seen here in addition to the emission lines. (a) The spectrum as it is read from the detector array. (b) The spectrum as reduced, and wavelength calibrated. No flux calibration was applied. (c) The reduced spectrum zoomed in to show the emission line features. As can be seen here, the emission lines from separate orders overlap when they are the same emission line. This shows that the spectral calibration is of good quality, and valid throughout the various spectral orders.

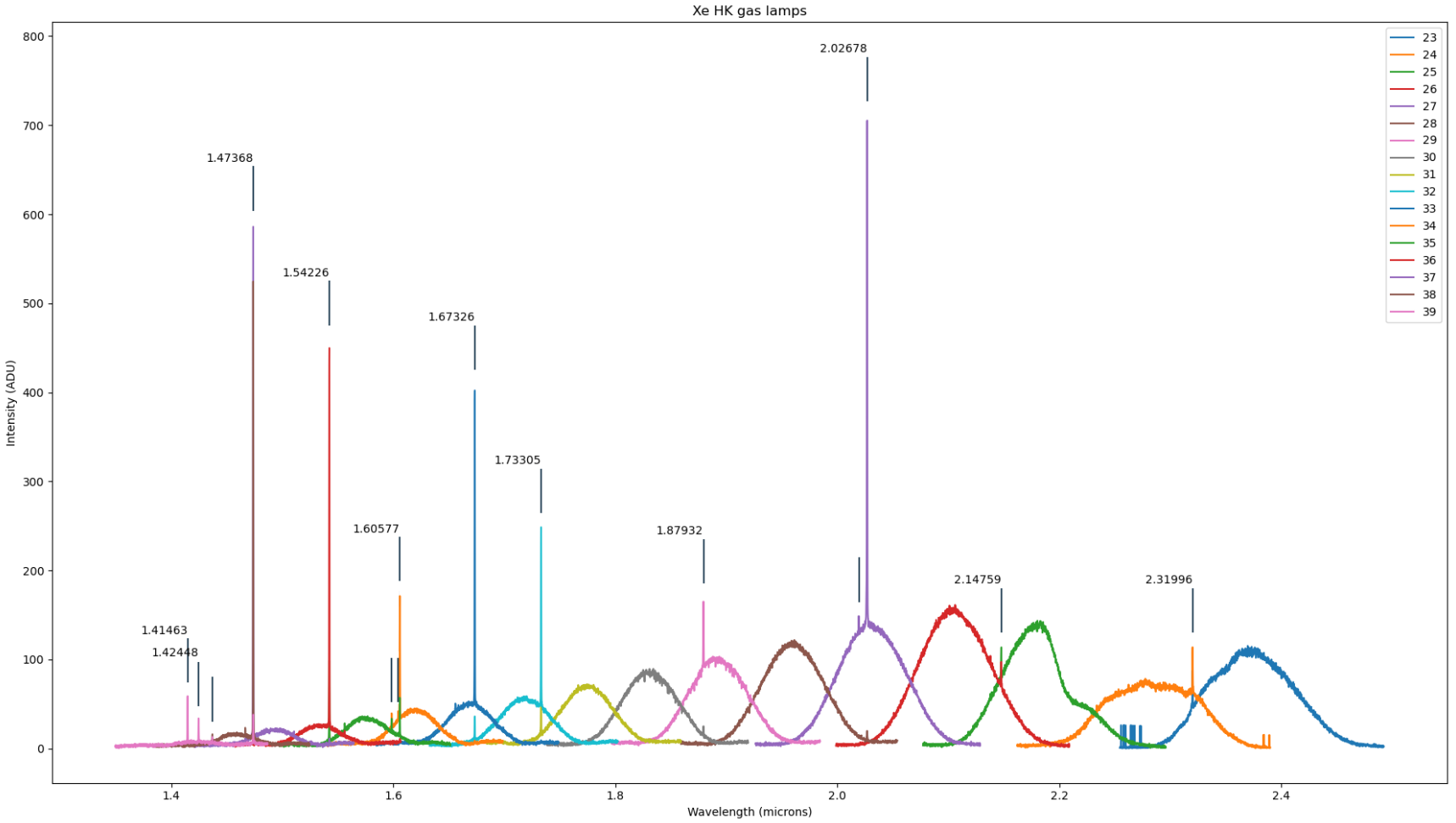


Figure B.16: Labeled spectrum of a xenon low-pressure gas discharge lamp taken with the HK arm of RIMAS's echelle spectrograph. Each of the lines identified, and used for calibration have a dark line above them. The wavelengths for the brightest emission lines are given in microns.

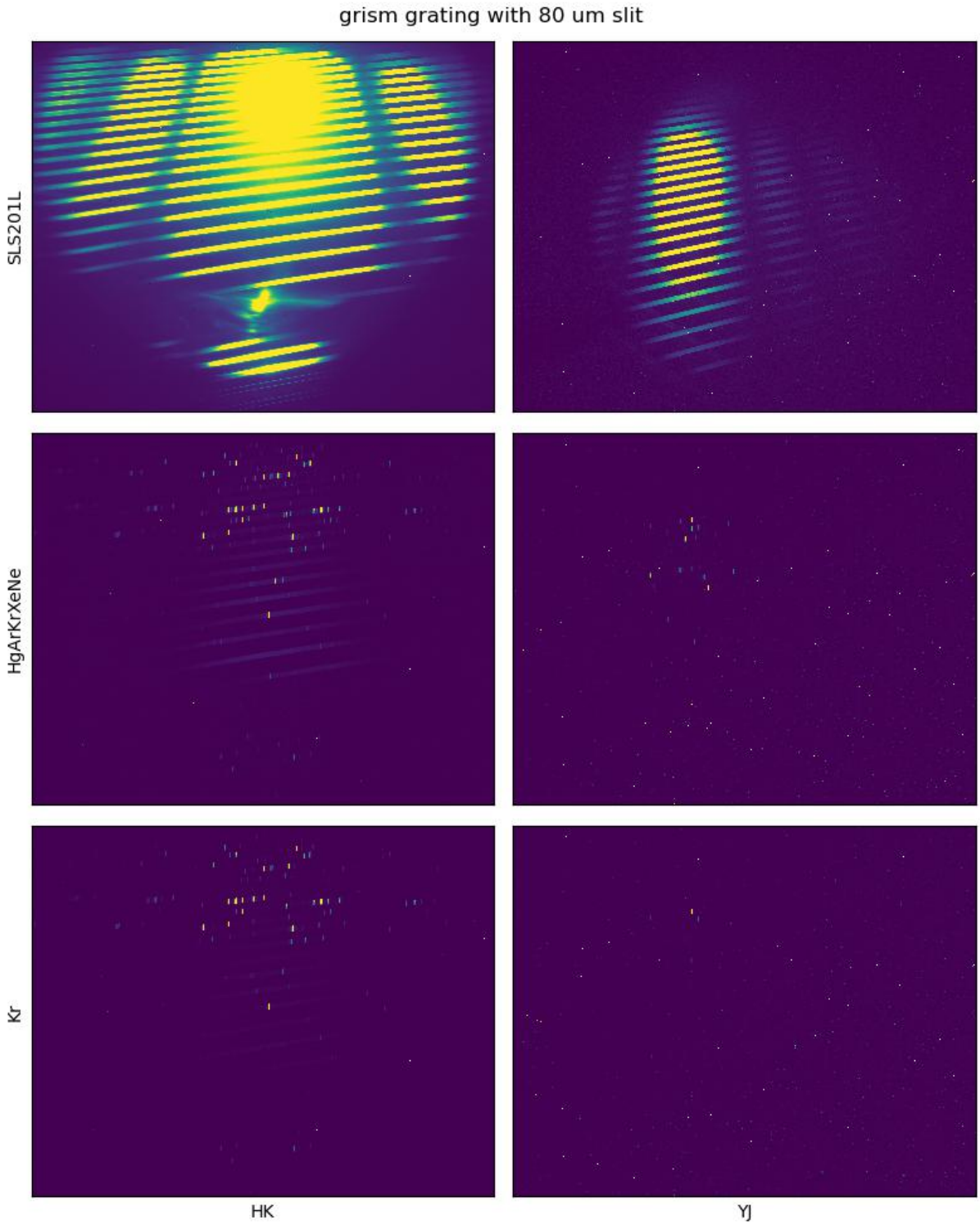


Figure B.17: Cross Dispersed Spectra taken with 80 µm slit

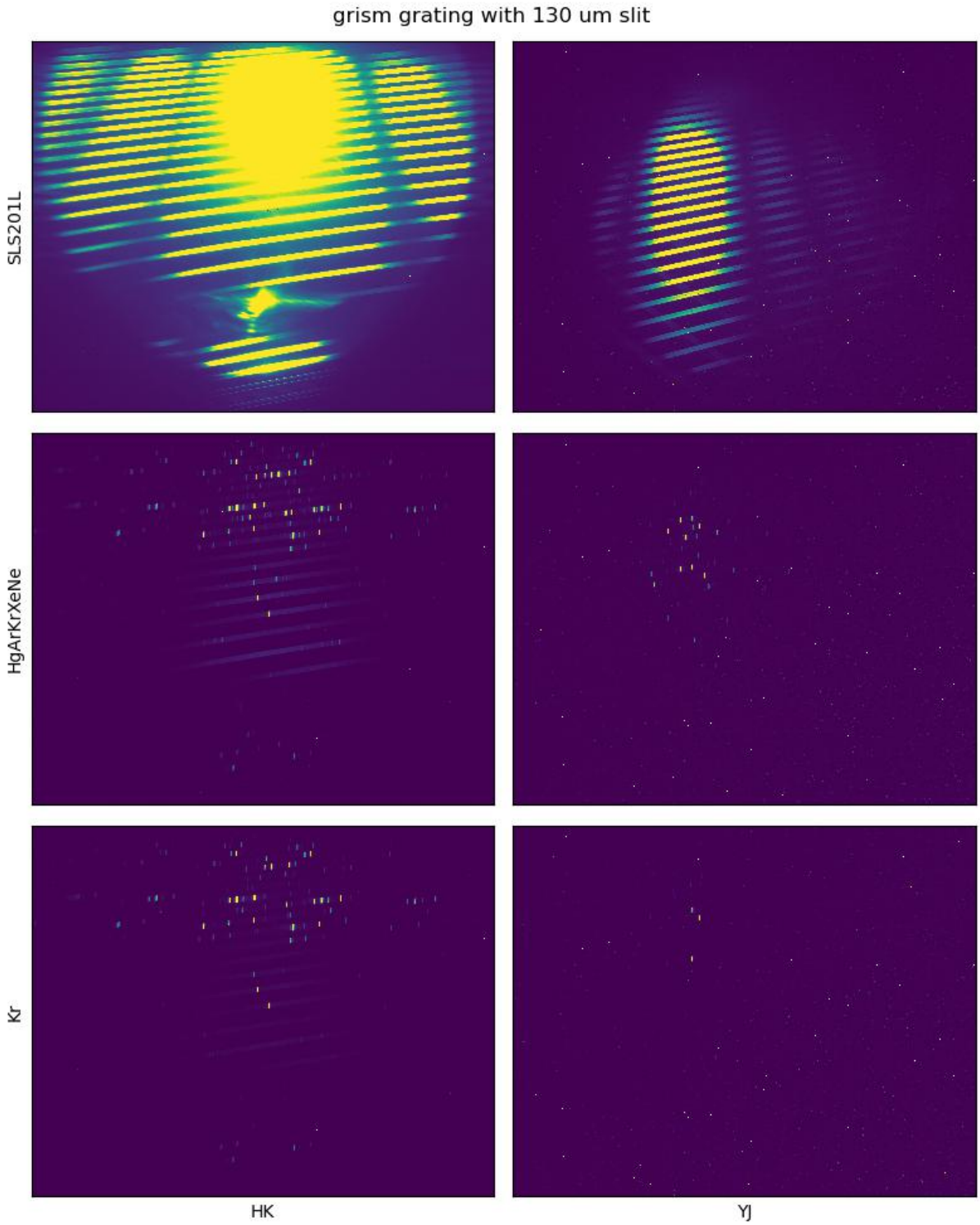


Figure B.18: Cross Dispersed Spectra taken with 130 µm slit

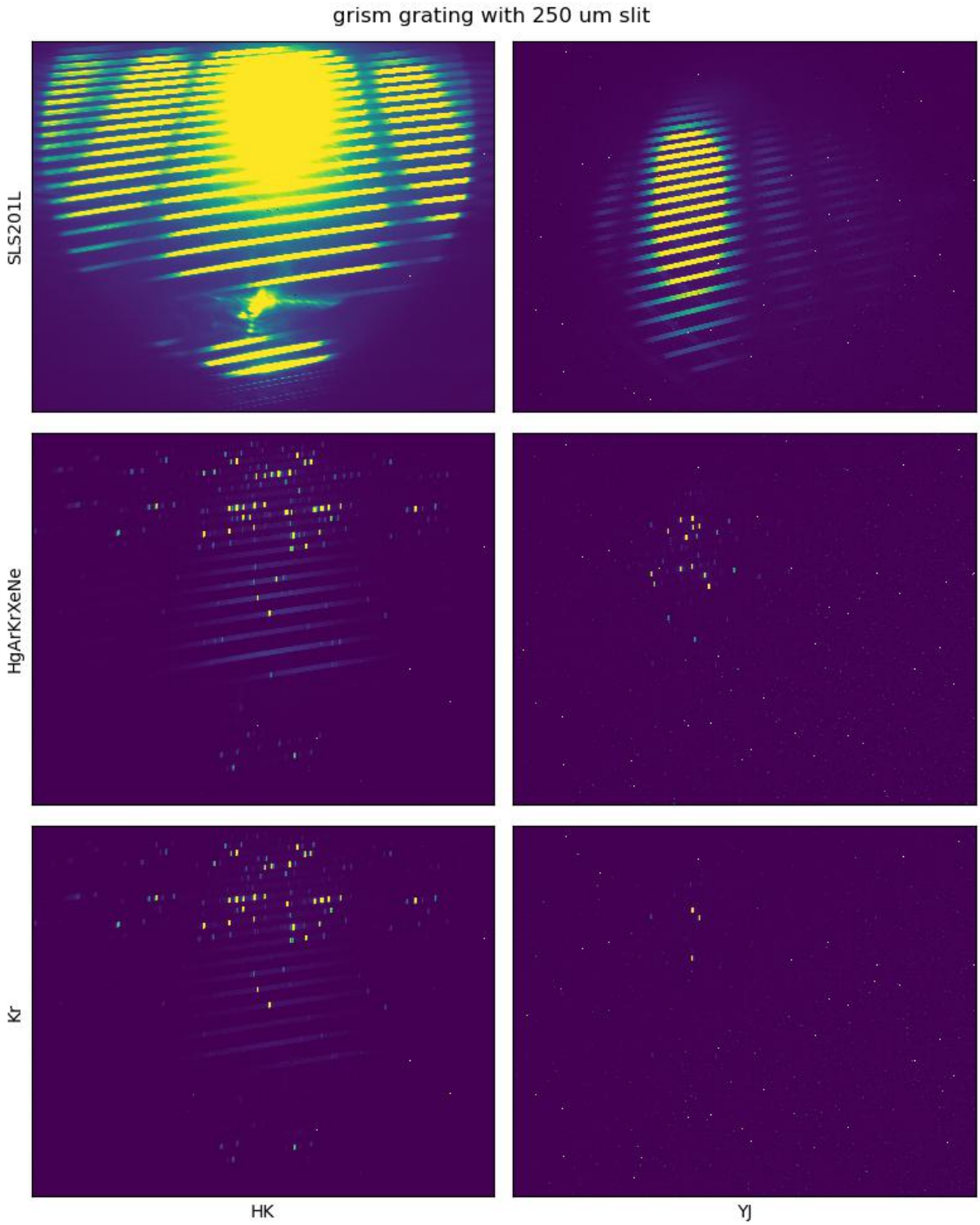


Figure B.19: Cross Dispersed Spectra taken with 250 µm slit

B.1.1.2 Additional Echelle Lamp Spectra

B.1.2 Low Resolution VPH Spectra

B.1.2.1 R≈30 Spectra

This section contains example spectra from RIMAS's lowest resolution spectrograph in addition to the other spectra shown throughout this work. Spectra were acquired and combined using the same manner discussed in §2.4.2.1.

B.1.2.2 R≈300 Spectra

This section contains example spectra from RIMAS's medium-low resolution spectrograph in addition to the other spectra shown throughout this work. Spectra were acquired and combined using the same manner discussed in §2.4.2.1.

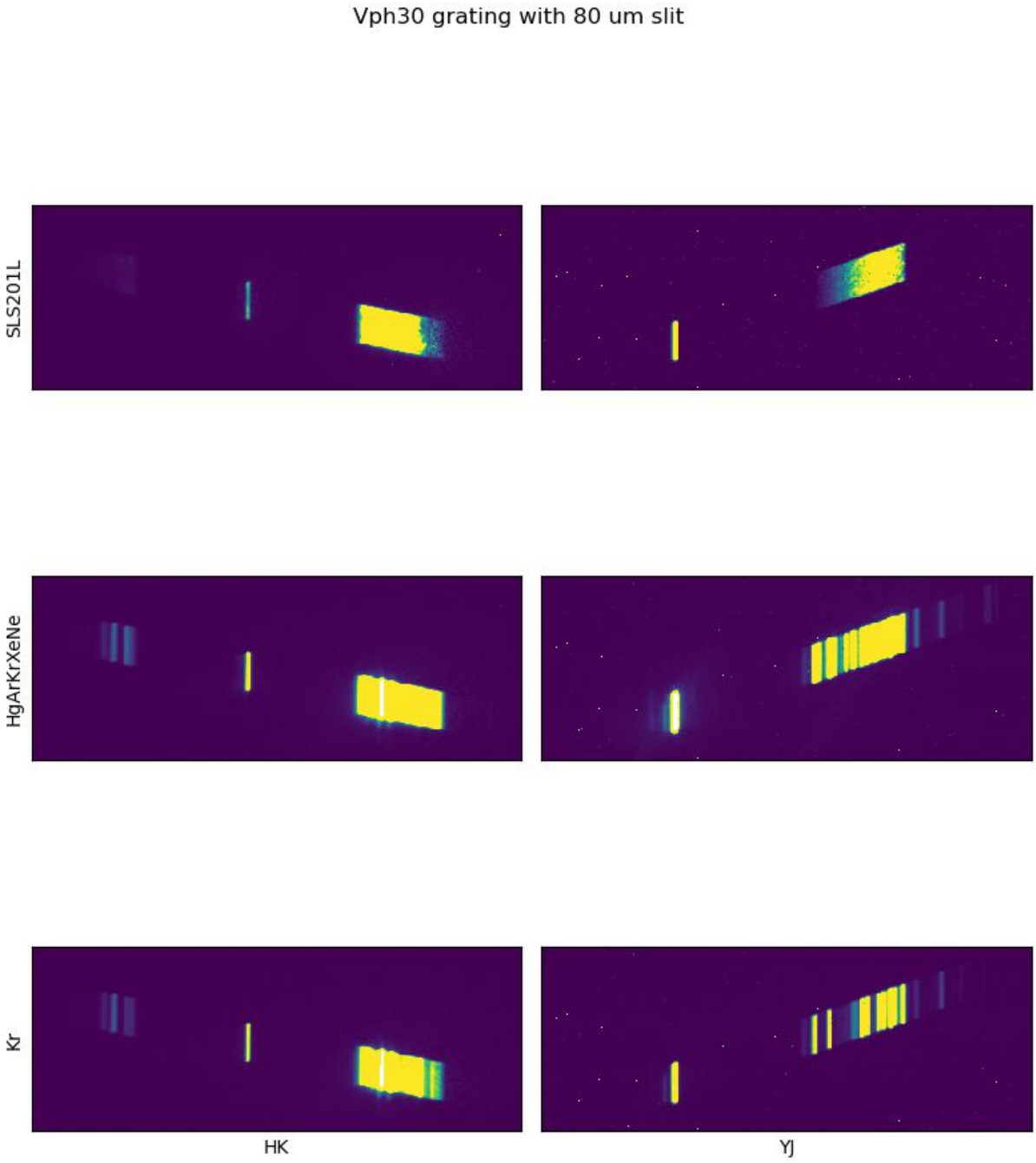


Figure B.20: R≈30 VPH Spectra taken with 80 µm slit

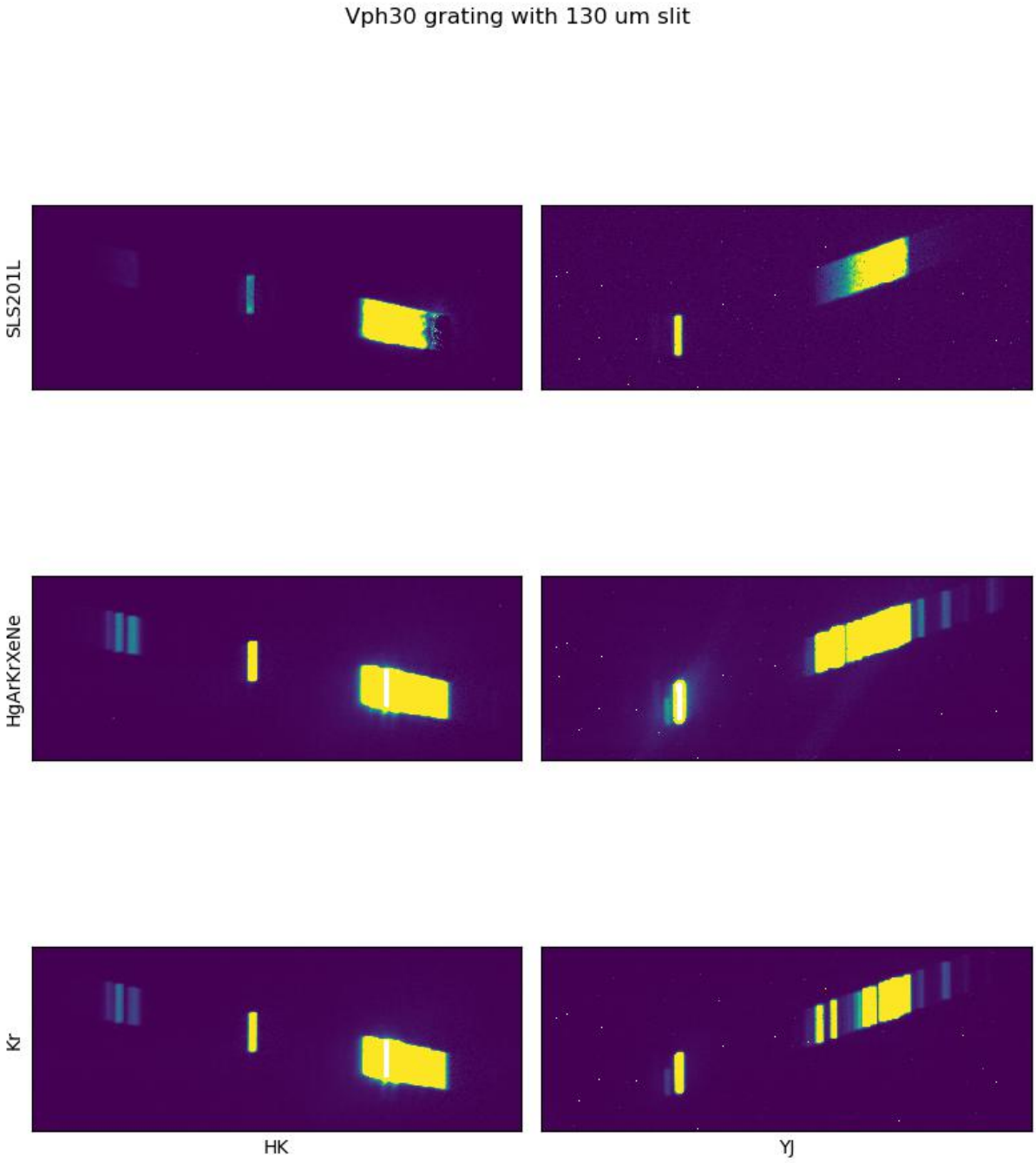


Figure B.21: R≈30 VPH Spectra taken with 130 µm slit

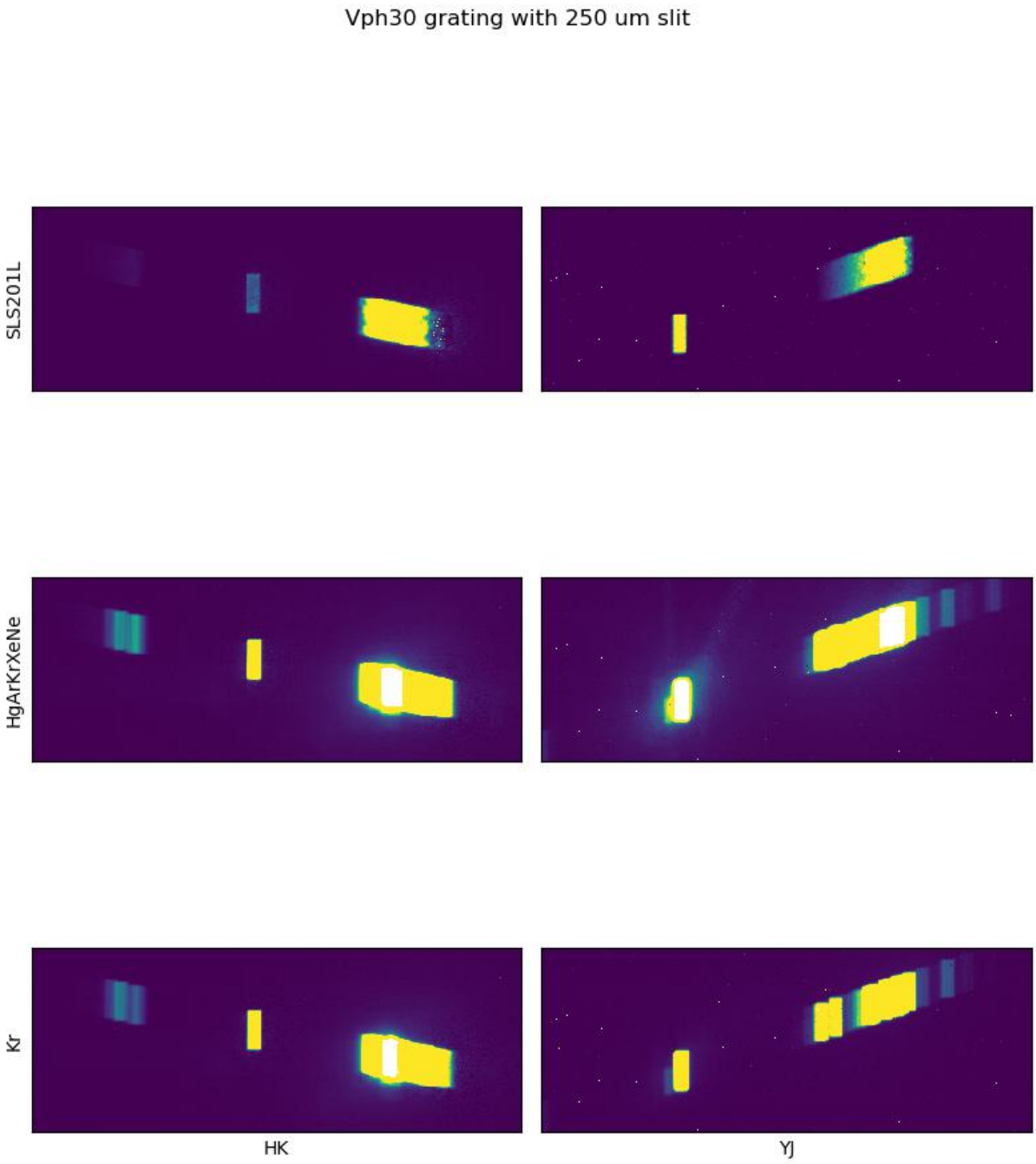


Figure B.22: R≈30 VPH Spectra taken with 250 µm slit

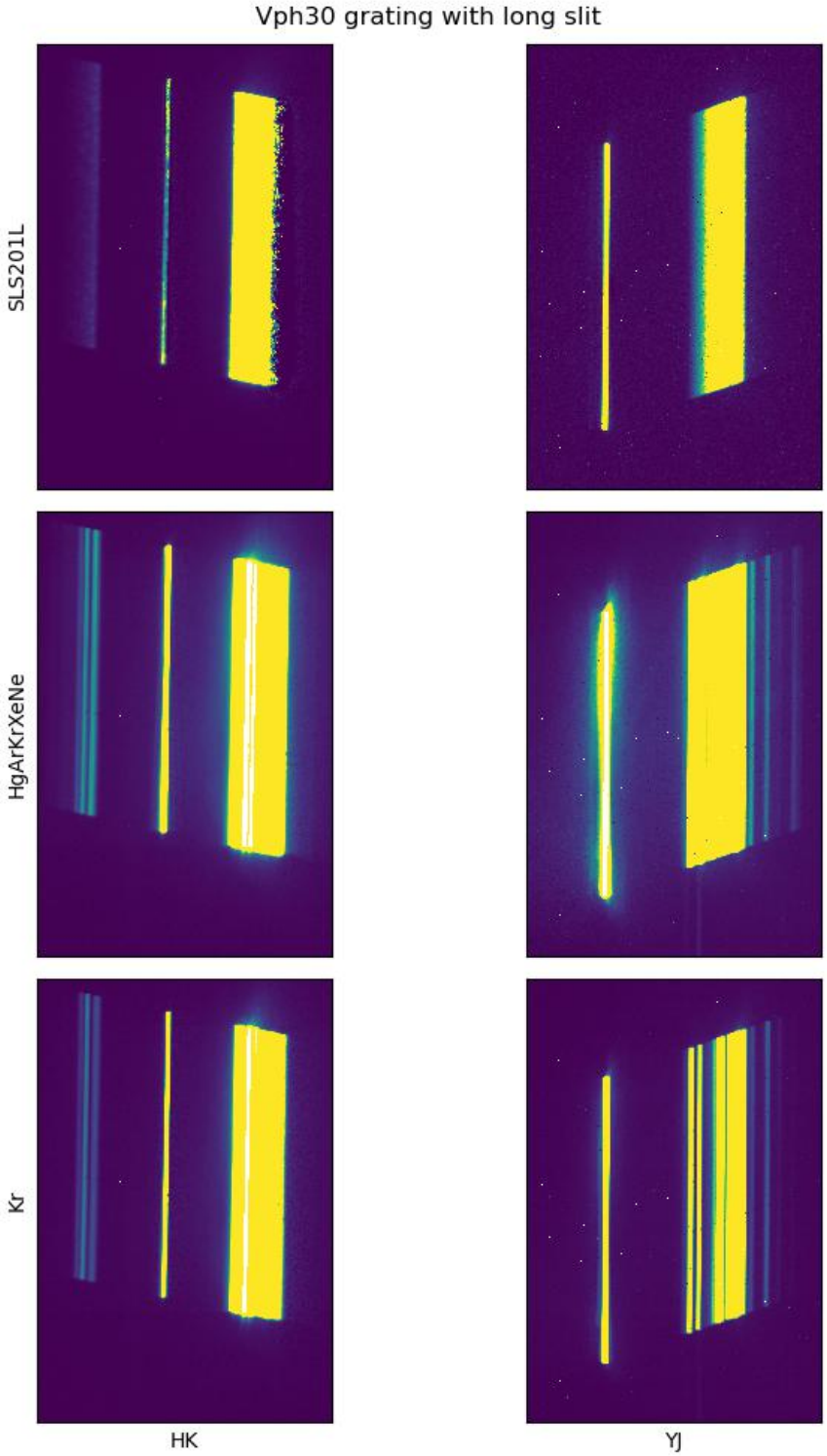


Figure B.23: R≈30 VPH Spectra taken with long slit

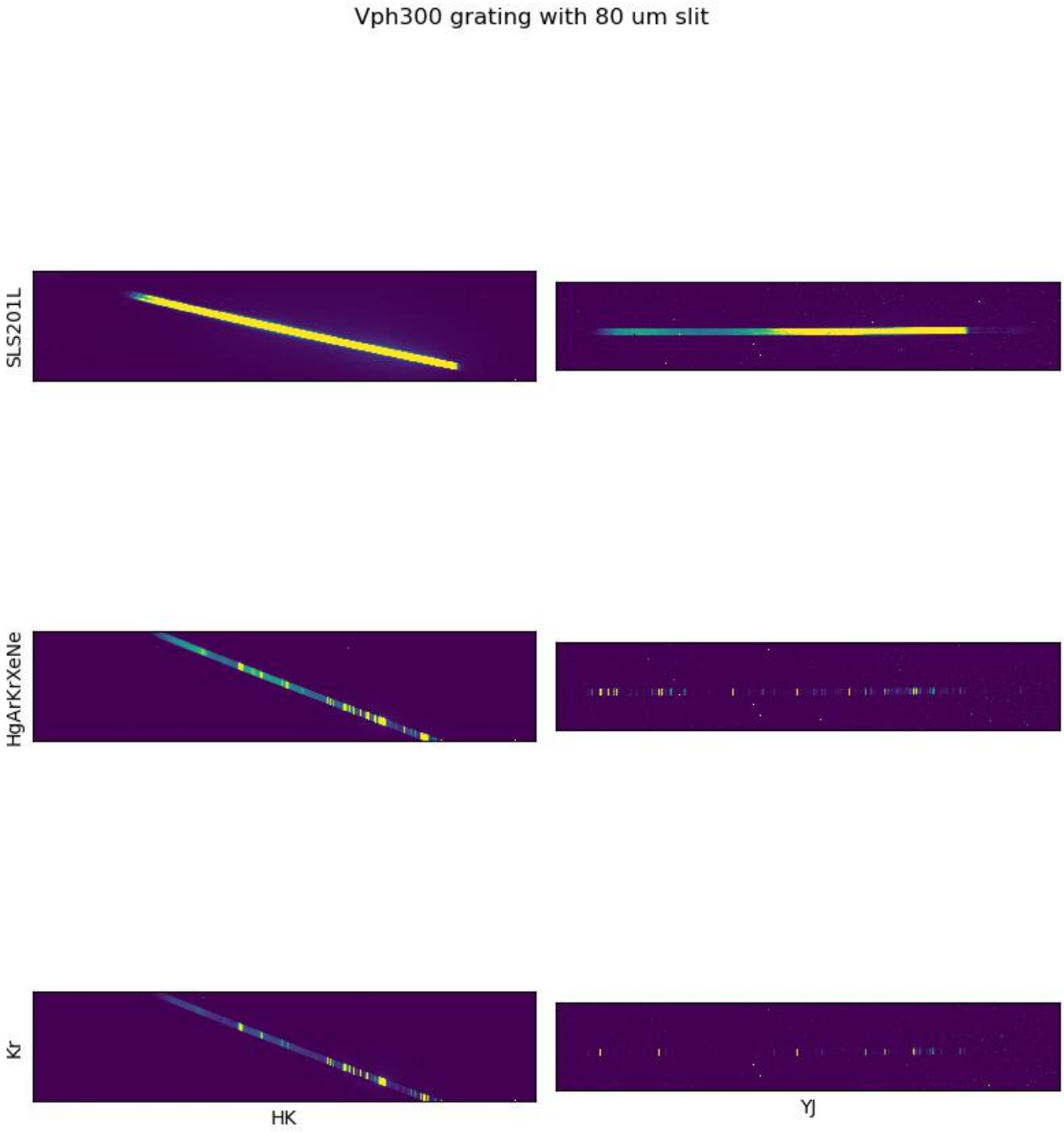


Figure B.24: R≈300 VPH Spectra taken with 80 µm slit

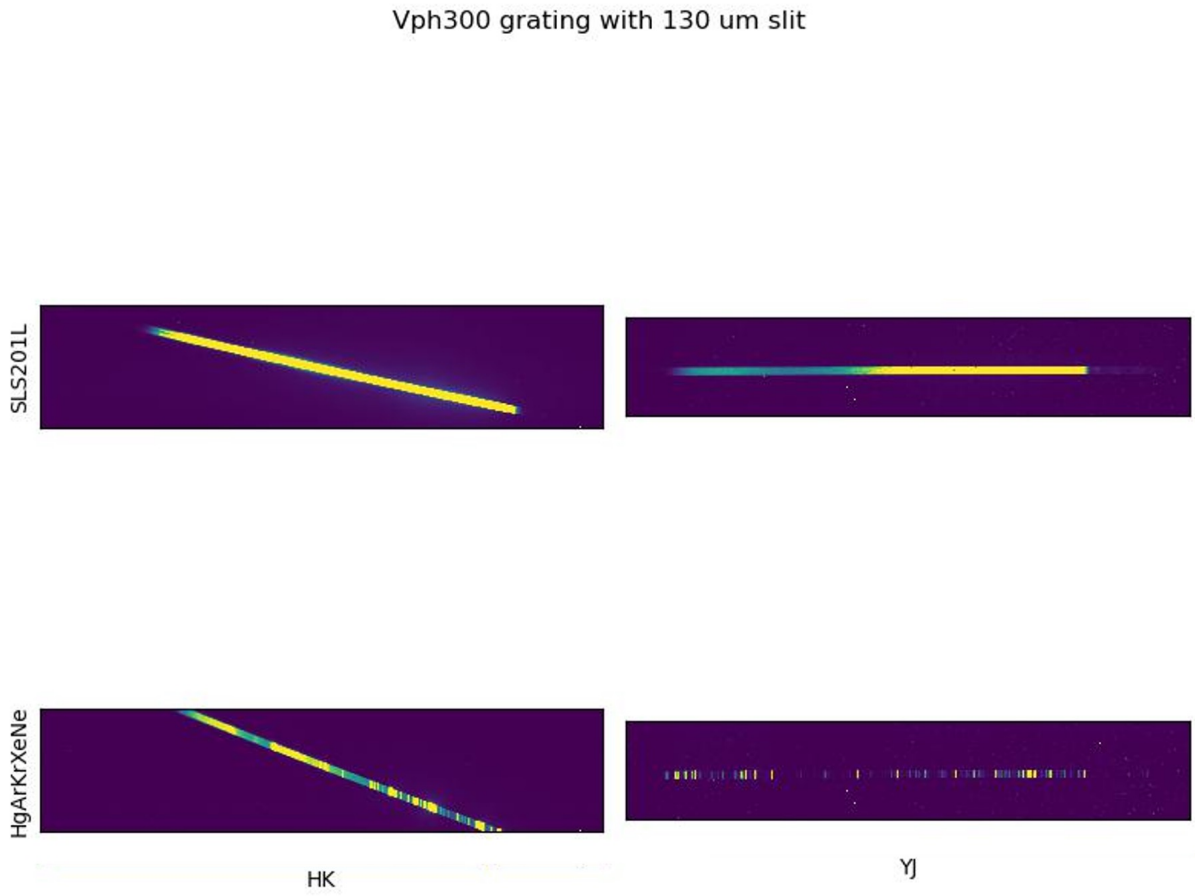


Figure B.25: R≈300 VPH Spectra taken with 130 µm slit

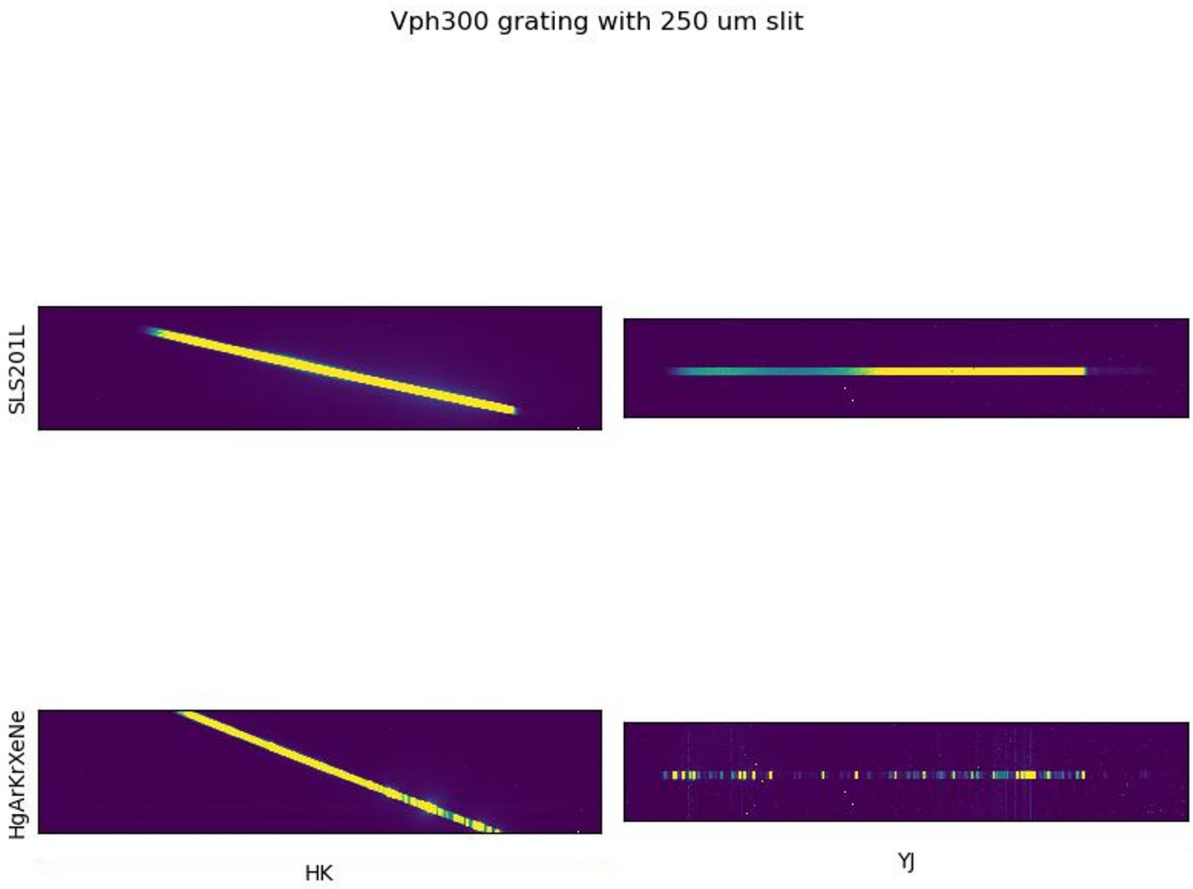


Figure B.26: R≈300 VPH Spectra taken with 250 µm slit

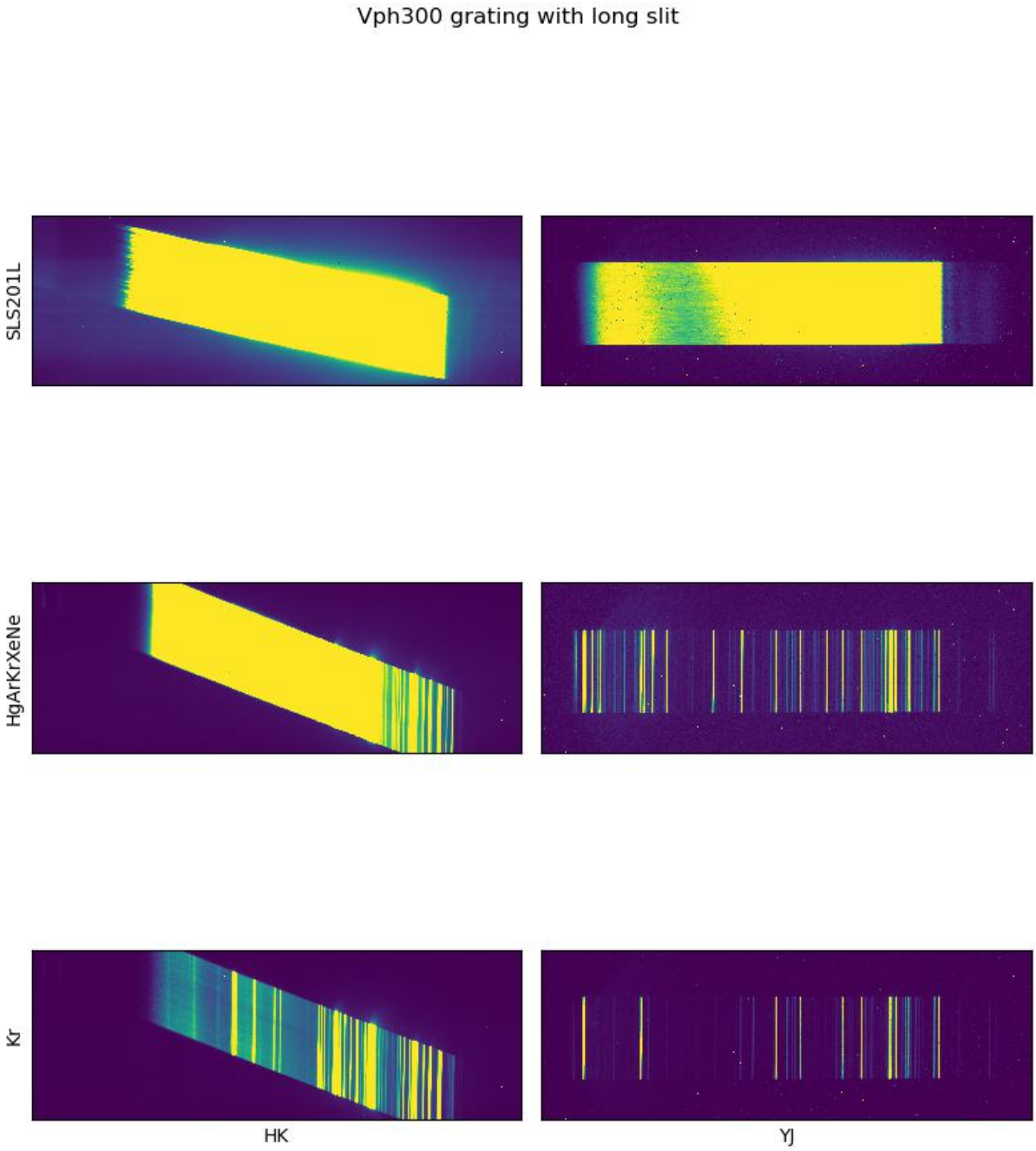


Figure B.27: R≈300 VPH Spectra taken with long slit

Bibliography

[1] Joseph Durbak, Alexander S. Kutyrev, Sylvain Veilleux, et al. RIMAS: testing, and categorization of grism spectral performance. In *Society of Photo-Optical Instrumentation Engineers (SPIE) Conference Series*, volume 11451 of *Society of Photo-Optical Instrumentation Engineers (SPIE) Conference Series*, page 114515Y, December 2020. doi: 10.1117/12.2561876.

[2] Joseph Durbak, Alexander S. Kutyrev, Sylvain Veilleux, et al. RIMAS: testing, and categorization of grism spectral performance. In Christopher J. Evans, Julia J. Bryant, and Kentaro Motohara, editors, *Ground-based and Airborne Instrumentation for Astronomy IX*, volume 12184 of *Society of Photo-Optical Instrumentation Engineers (SPIE) Conference Series*, page 1218487, August 2022. doi: 10.1117/12.2630430.

[3] Joseph Durbak, Alexander Kutyrev, Takahiro Sumi, et al. The PRIME camera: results and performance after continuous observations. In Andrew D. Holland and Kyriaki Minoglou, editors, *X-Ray, Optical, and Infrared Detectors for Astronomy XI*, volume 13103, page 1310327. International Society for Optics and Photonics, SPIE, 2024. doi: 10.1117/12.3020680. URL `https://doi.org/10.1117/12.3020680`.

[4] D.5 Neil Gehrels Swift Observatory Guest Investigator Cycle 17, Mar 2024. URL `https://nspires.nasaprs.com/external/solicitations`.

[5] J. Durbak, A. Kutyrev, S. Veilleux, et al. RIMAS — The Final Stages of Development, Instrumentation, Testing, and Categorization. In *American Astronomical Society Meeting Abstracts #235*, volume 235 of *American Astronomical Society Meeting Abstracts*, page 215.05, January 2020.

[6] S. Singer. The vela satellite program for detection of high-altitude nuclear detonations. *Proceedings of the IEEE*, 53(12):1935–1948, 1965. doi: 10.1109/PROC.1965.4470.

[7] Ray W. Klebesadel, Ian B. Strong, and Roy A. Olson. Observations of Gamma-Ray Bursts of Cosmic Origin. ApJ, 182:L85, June 1973. doi: 10.1086/181225.

[8] E. E. Fenimore, R. I. Epstein, C. Ho, et al. The intrinsic luminosity of γ-ray bursts and their host galaxies. Nature, 366(6450):40–42, November 1993. doi: 10.1038/366040a0.

[9] Adam Goldstein, Robert D. Preece, Robert S. Mallozzi, et al. The BATSE 5B Gamma-Ray Burst Spectral Catalog. ApJS, 208(2):21, October 2013. doi: 10.1088/0067-0049/208/2/21.

[10] Chryssa Kouveliotou, Charles A. Meegan, Gerald J. Fishman, et al. Identification of Two Classes of Gamma-Ray Bursts. ApJ, 413:L101, August 1993. doi: 10.1086/186969.

[11] D. Band, J. Matteson, L. Ford, et al. BATSE Observations of Gamma-Ray Burst Spectra. I. Spectral Diversity. ApJ, 413:281, August 1993. doi: 10.1086/172995.

[12] J. van Paradijs, P. J. Groot, T. Galama, et al. Transient optical emission from the error box of the γ-ray burst of 28 February 1997. Nature, 386(6626):686–689, April 1997. doi: 10.1038/386686a0.

[13] Ralph A. M. J. Wijers, Martin J. Rees, and Peter Meszaros. Shocked by GRB 970228: the afterglow of a cosmological fireball. MNRAS, 288(4):L51–L56, July 1997. doi: 10.1093/mnras/288.4.L51.

[14] N. Gehrels, G. Chincarini, P. Giommi, et al. The Swift Gamma-Ray Burst Mission. ApJ, 611(2):1005–1020, August 2004. doi: 10.1086/422091.

[15] David N. Burrows, J. E. Hill, J. A. Nousek, et al. The Swift X-Ray Telescope. Space Sci. Rev., 120(3-4):165–195, October 2005. doi: 10.1007/s11214-005-5097-2.

[16] Peter W. A. Roming, Thomas E. Kennedy, Keith O. Mason, et al. The Swift Ultra-Violet/Optical Telescope. Space Sci. Rev., 120(3-4):95–142, October 2005. doi: 10.1007/s11214-005-5095-4.

[17] N. Gehrels, E. Ramirez-Ruiz, and D. B. Fox. Gamma-Ray Bursts in the Swift Era. ARA&A, 47(1):567–617, September 2009. doi: 10.1146/annurev.astro.46.060407.145147.

[18] R. Vanderspek, T. Sakamoto, C. Barraud, et al. HETE Observations of the Gamma-Ray Burst GRB 030329: Evidence for an Underlying Soft X-Ray Component. ApJ, 617(2):1251–1257, December 2004. doi: 10.1086/423923.

[19] G. Tagliaferri, L. A. Antonelli, G. Chincarini, et al. GRB 050904 at redshift 6.3: observations of the oldest cosmic explosion after the Big Bang. A&A, 443(1):L1–L5, November 2005. doi: 10.1051/0004-6361:200500196.

[20] B. P. Abbott, R. Abbott, T. D. Abbott, et al. Gravitational Waves and Gamma-Rays from a Binary Neutron Star Merger: GW170817 and GRB 170817A. ApJ, 848(2):L13, October 2017. doi: 10.3847/2041-8213/aa920c.

[21] E. Costa, F. Frontera, J. Heise, et al. Discovery of an X-ray afterglow associated with the γ-ray burst of 28 February 1997. Nature, 387(6635):783–785, June 1997. doi: 10.1038/42885.

[22] J. S. Bloom, S. G. Djorgovski, and S. R. Kulkarni. The Redshift and the Ordinary Host Galaxy of GRB 970228. ApJ, 554(2):678–683, June 2001. doi: 10.1086/321398.

[23] A. S. Fruchter, A. J. Levan, L. Strolger, et al. Long γ-ray bursts and core-collapse supernovae have different environments. Nature, 441(7092):463–468, May 2006. doi: 10.1038/nature04787.

[24] N. Gehrels, C. L. Sarazin, P. T. O'Brien, et al. A short γ-ray burst apparently associated with an elliptical galaxy at redshift z = 0.225. Nature, 437(7060):851–854, October 2005. doi: 10.1038/nature04142.

[25] A. Cucchiara et al. A Photometric Redshift of z ˜ 9.4 for GRB 090429B. ApJ, 736: 7, July 2011. doi: 10.1088/0004-637X/736/1/7.

[26] K. Z. Stanek, T. Matheson, P. M. Garnavich, et al. Spectroscopic Discovery of the Supernova 2003dh Associated with GRB 030329. ApJ, 591(1):L17–L20, July 2003. doi: 10.1086/376976.

[27] Bin-Bin Zhang, Yi-Zhong Fan, Rong-Feng Shen, et al. GRB 120422A: A Low-luminosity Gamma-Ray Burst Driven by a Central Engine. ApJ, 756(2):190, September 2012. doi: 10.1088/0004-637X/756/2/190.

[28] D. A. Perley, S. B. Cenko, A. Corsi, et al. The Afterglow of GRB 130427A from 1 to 10^{16} GHz. ApJ, 781(1):37, January 2014. doi: 10.1088/0004-637X/781/1/37.

[29] D. M. Coward, E. J. Howell, M. Branchesi, et al. The Swift gamma-ray burst redshift distribution: selection biases and optical brightness evolution at high z? MNRAS, 432(3):2141–2149, July 2013. doi: 10.1093/mnras/stt537.

[30] P. Jakobsson, J. Hjorth, J. P. U. Fynbo, et al. The line-of-sight towards GRB 030429 at z =2.66: Probing the matter at stellar, galactic and intergalactic scales. A&A, 427:785–794, December 2004. doi: 10.1051/0004-6361:20041233.

[31] Andrew Levan, Andrew Fruchter, James Rhoads, et al. Infrared and Optical Observations of GRB 030115 and its Extremely Red Host Galaxy: Implications for Dark Bursts. ApJ, 647(1):471–482, August 2006. doi: 10.1086/503595.

[32] D. A. Perley, S. B. Cenko, J. S. Bloom, et al. The Host Galaxies of Swift Dark Gamma-ray Bursts: Observational Constraints on Highly Obscured and Very High Redshift GRBs. AJ, 138(6):1690–1708, December 2009. doi: 10.1088/0004-6256/138/6/1690.

[33] K. M. Svensson, A. J. Levan, N. R. Tanvir, et al. The dark GRB 080207 in an extremely red host and the implications for gamma-ray bursts in highly obscured environments. MNRAS, 421(1):25–35, March 2012. doi: 10.1111/j.1365-2966.2011.19811.x.

[34] Re'em Sari, Tsvi Piran, and Ramesh Narayan. Spectra and Light Curves of Gamma-Ray Burst Afterglows. ApJ, 497(1):L17–L20, April 1998. doi: 10.1086/311269.

[35] P. Mészáros. Gamma-Ray Bursts: theoretical issues and developments. Mem. Soc. Astron. Italiana, 90:57, January 2019. doi: 10.48550/arXiv.1904.10488.

[36] T. Piran. Gamma-ray bursts and the fireball model. Phys. Rep., 314(6):575–667, June 1999. doi: 10.1016/S0370-1573(98)00127-6.

[37] M. J. Rees and P. Meszaros. Relativistic fireballs - Energy conversion and time-scales. MNRAS, 258:41, September 1992. doi: 10.1093/mnras/258.1.41P.

[38] P. Meszaros and M. J. Rees. Relativistic Fireballs and Their Impact on External Matter: Models for Cosmological Gamma-Ray Bursts. ApJ, 405:278, March 1993. doi: 10.1086/172360.

[39] M. J. Rees and P. Meszaros. Unsteady Outflow Models for Cosmological Gamma-Ray Bursts. ApJ, 430:L93, August 1994. doi: 10.1086/187446.

[40] S. E. Woosley. Gamma-Ray Bursts from Stellar Mass Accretion Disks around Black Holes. ApJ, 405:273, March 1993. doi: 10.1086/172359.

[41] A. I. MacFadyen and S. E. Woosley. Collapsars: Gamma-Ray Bursts and Explosions in "Failed Supernovae". ApJ, 524(1):262–289, October 1999. doi: 10.1086/307790.

[42] Bruno Giacomazzo, Rosalba Perna, Luciano Rezzolla, et al. Compact Binary Progenitors of Short Gamma-Ray Bursts. ApJ, 762(2):L18, January 2013. doi: 10.1088/2041-8205/762/2/L18.

[43] V. V. Usov. Millisecond pulsars with extremely strong magnetic fields as a cosmological source of γ-ray bursts. Nature, 357(6378):472–474, June 1992. doi: 10.1038/357472a0.

[44] N. R. Tanvir, A. J. Levan, A. S. Fruchter, et al. A 'kilonova' associated with the short-duration γ-ray burst GRB 130603B. Nature, 500(7464):547–549, August 2013. doi: 10.1038/nature12505.

[45] B. P. Abbott, R. Abbott, T. D. Abbott, et al. Multi-messenger Observations of a Binary Neutron Star Merger. ApJ, 848(2):L12, October 2017. doi: 10.3847/2041-8213/aa91c9.

[46] Yu-Han Yang, Eleonora Troja, Brendan O'Connor, et al. A lanthanide-rich kilonova in the aftermath of a long gamma-ray burst. Nature, 626(8000):742–745, February 2024. doi: 10.1038/s41586-023-06979-5.

[47] Brendan O'Connor, Eleonora Troja, Geoffrey Ryan, et al. A structured jet explains the extreme GRB 221009A. *Science Advances*, 9(23):eadi1405, June 2023. doi: 10.1126/sciadv.adi1405.

[48] R. Sari and T. Piran. The early afterglow. A&AS, 138:537–538, September 1999. doi: 10.1051/aas:1999342.

[49] E. Molinari, S. D. Vergani, D. Malesani, et al. REM observations of GRB 060418 and GRB 060607A: the onset of the afterglow and the initial fireball Lorentz factor determination. A&A, 469(1):L13–L16, July 2007. doi: 10.1051/0004-6361:20077388.

[50] En-Wei Liang, Shuang-Xi Yi, Jin Zhang, et al. Constraining Gamma-ray Burst Initial Lorentz Factor with the Afterglow Onset Feature and Discovery of a Tight Γ_0-E $_{\gamma,iso}$ Correlation. ApJ, 725(2):2209–2224, December 2010. doi: 10.1088/0004-637X/725/2/2209.

[51] En-Wei Liang, Ting-Ting Lin, Jing Lü, et al. A Tight L_{iso} - $E_{p,z}$ - $Gamma_0$ Correlation of Gamma-Ray Bursts. ApJ, 813(2):116, November 2015. doi: 10.1088/0004-637X/813/2/116.

[52] Jae-Joon Lee. plp: Version 2.0, 2015. URL `https://zenodo.org/record/18579`.

[53] Vicki Toy. *Gamma-Ray Bursts: Lighting Up the High-Redshift Universe*. PhD thesis, University of Maryland-College Park, 2017.

[54] Alexander Kutyrev, Takahiro Sumi, Giuseppe Cataldo, et al. The PRIME project large format near infrared camera for the microlensing events survey. In *Society of Photo-Optical Instrumentation Engineers (SPIE) Conference Series*, volume 12680 of *Society of Photo-Optical Instrumentation Engineers (SPIE) Conference Series*, page 126802O, October 2023. doi: 10.1117/12.2692417.

[55] Hibiki Yama, Daisuke Suzuki, Shota Miyazaki, et al. Optical Alignment Method for the PRIME Telescope. *Journal of Astronomical Instrumentation*, 12(3):2350004, January 2023. doi: 10.1142/S2251171723500046.

[56] John Capone, D. Content, A. Kutyrev, et al. RIMAS - Optical Design Development of the Imager/Spectrometer for the Discovery Channel Telescope. In *American Astronomical Society Meeting Abstracts #219*, volume 219 of *American Astronomical Society Meeting Abstracts*, page 446.14, January 2012.

[57] John I. Capone, David A. Content, Ori D. Fox, et al. The development and analysis of cryogenic optical systems for the rapid infrared imager/spectrometer. In James B. Heaney and E. T. Kvamme, editors, *Cryogenic Optical Systems and Instruments 2013*, volume 8863 of *Society of Photo-Optical Instrumentation Engineers (SPIE) Conference Series*, page 88630D, September 2013. doi: 10.1117/12.2023123.

[58] O. M. Littlejohns, N. R. Butler, A. Cucchiara, et al. Identifying High-redshift Gamma-Ray Bursts with RATIR. AJ, 148(1):2, July 2014. doi: 10.1088/0004-6256/148/1/2.

[59] The GCN/TAN System, October 2017. URL `https://gcn.gsfc.nasa.gov/gcn_describe.html`.

[60] R. H. Becker et al. Evidence for Reionization at z˜6: Detection of a Gunn-Peterson Trough in a z=6.28 Quasar. AJ, 122:2850–2857, December 2001. doi: 10.1086/324231.

[61] G. Hinshaw et al. Nine-year Wilkinson Microwave Anisotropy Probe (WMAP) Observations: Cosmological Parameter Results. ApJS, 208:19, October 2013. doi: 10.1088/0067-0049/208/2/19.

[62] D. Q. Lamb and D. E. Reichart. Gamma-Ray Bursts as a Probe of the Very High Redshift Universe. ApJ, 536:1–18, June 2000. doi: 10.1086/308918.

[63] J. L. Racusin, S. V. Karpov, M. Sokolowski, et al. Broadband observations of the naked-eye γ-ray burst GRB080319B. Nature, 455(7210):183–188, September 2008. doi: 10.1038/nature07270.

[64] J. S. Bloom et al. Observations of the Naked-Eye GRB 080319B: Implications of Nature's Brightest Explosion. ApJ, 691:723–737, January 2009. doi: 10.1088/0004-637X/691/1/723.

[65] D. A. Kann, N. Masetti, and S. Klose. The Prompt Optical/Near-Infrared Flare of GRB 050904: The Most Luminous Transient Ever Detected. AJ, 133:1187–1192, March 2007. doi: 10.1086/511066.

[66] M. McQuinn et al. Probing the neutral fraction of the IGM with GRBs during the epoch of reionization. MNRAS, 388:1101–1110, August 2008. doi: 10.1111/j.1365-2966.2008.13271.x.

[67] N. R. Tanvir et al. A γ-ray burst at a redshift of z˜8.2. Nature, 461:1254–1257, October 2009. doi: 10.1038/nature08459.

[68] R. Salvaterra et al. GRB090423 at a redshift of z˜8.1. Nature, 461:1258–1260, October 2009. doi: 10.1038/nature08445.

[69] D. A. Perley et al. The Host Galaxies of Swift Dark Gamma-ray Bursts: Observational Constraints on Highly Obscured and Very High Redshift GRBs. AJ, 138:1690–1708, December 2009. doi: 10.1088/0004-6256/138/6/1690.

[70] J. Greiner et al. The nature of "dark" gamma-ray bursts. A&A, 526:A30, February 2011. doi: 10.1051/0004-6361/201015458.

[71] R. Chornock et al. GRB 130606A as a Probe of the Intergalactic Medium and the Interstellar Medium in a Star-forming Galaxy in the First Gyr after the Big Bang. ApJ, 774:26, September 2013. doi: 10.1088/0004-637X/774/1/26.

[72] O. E. Hartoog et al. VLT/X-Shooter spectroscopy of the afterglow of the Swift GRB 130606A. Chemical abundances and reionisation at z ˜6. A&A, 580:A139, August 2015. doi: 10.1051/0004-6361/201425001.

[73] A. J. Castro-Tirado et al. GRB 130606A within a sub-DLA at redshift 5.91. astro-ph/1312.5631, December 2013.

[74] R. Chornock et al. GRB 140515A at z=6.33: Constraints on the End of Reionization From a Gamma-ray Burst in a Low Hydrogen Column Density Environment. astro-ph/1405.7400, May 2014.

[75] S. B. Cenko et al. Dark Bursts in the Swift Era: The Palomar 60 Inch-Swift Early Optical Afterglow Catalog. ApJ, 693:1484–1493, March 2009. doi: 10.1088/0004-637X/693/2/1484.

[76] E. Bowell. Lowell Observatory's Discovery Channel Telescope. *Society for Astronomical Sciences Annual Symposium*, 24:145, May 2005.

[77] Thomas A. Bida, Edward W. Dunham, Philip Massey, and Henry G. Roe. First-generation instrumentation for the Discovery Channel Telescope. In Suzanne K. Ramsay, Ian S. McLean, and Hideki Takami, editors, *Ground-based and Airborne Instrumentation for Astronomy V*, volume 9147 of *Society of Photo-Optical Instrumentation Engineers (SPIE) Conference Series*, page 91472N, July 2014. doi: 10.1117/12.2056872.

[78] Gregory Mosby, Bernard J. Rauscher, Chris Bennett, et al. Properties and characteristics of the Nancy Grace Roman Space Telescope H4RG-10 detectors. *Journal of Astronomical Telescopes, Instruments, and Systems*, 6:046001, October 2020. doi: 10.1117/1.JATIS.6.4.046001.

[79] John Capone. *Near-Infrared Instrumentation for Rapid-Response Astronomy*. PhD thesis, University of Maryland-College Park, 2016.

[80] Alicia Canipe, Massimo Robberto, and Bryan Hilbert. A New Non-Linearity Correction Method for NIRCam. Technical Report JWST-STScI-005167, January 2017.

[81] R. Blank, S. Anglin, J. W. Beletic, et al. The HxRG Family of High Performance Image Sensors for Astronomy. In J. R. Kuhn, D. M. Harrington, H. Lin, et al., editors, *Solar Polarization 6*, volume 437 of *Astronomical Society of the Pacific Conference Series*, page 383, April 2011.

[82] J. Green, P. Schechter, C. Baltay, et al. Wide-Field InfraRed Survey Telescope (WFIRST) Final Report. *arXiv e-prints*, art. arXiv:1208.4012, August 2012. doi: 10.48550/arXiv.1208.4012.

[83] Bernard J. Rauscher, Carl Stahle, Robert J. Hill, et al. Commentary: JWST near-infrared detector degradation— finding the problem, fixing the problem, and moving forward. *AIP Advances*, 2(2):021901, June 2012. doi: 10.1063/1.4733534.

[84] Lawrence G. Burriesci. NIRCam instrument overview. In James B. Heaney and Lawrence G. Burriesci, editors, *Cryogenic Optical Systems and Instruments XI*, volume 5904 of *Society of Photo-Optical Instrumentation Engineers (SPIE) Conference Series*, pages 21–29, August 2005. doi: 10.1117/12.613596.

[85] Markus Loose, L. Lewyn, Hakan Durmus, et al. SIDECAR low-power control ASIC for focal plane arrays including A/D conversion and bias generation. In Masanori Iye and Alan F. M. Moorwood, editors, *Instrument Design and Performance for Optical/Infrared Ground-based Telescopes*, volume 4841 of *Society of Photo-Optical Instrumentation Engineers (SPIE) Conference Series*, pages 782–794, March 2003. doi: 10.1117/12.462601.

[86] ARC, Inc., May 2024. URL https://www.astro-cam.com/index.php.

[87] Bernard J. Rauscher, Dale J. Fixsen, and Gregory Mosby. Simple improved reference subtraction for H4RG, H2RG, and H1RG near-infrared array detectors. *Journal of Astronomical Telescopes, Instruments, and Systems*, 8:028002, April 2022. doi: 10.1117/1.JATIS.8.2.028002.

[88] CableEye Automation-Ready Cable & Harness Testers — Catalog, July 2024. URL https://www.camiresearch.com/catalog.html.

[89] Paul J. Kuzmenko, Steve L. Little, Alexander S. Kutyrev, and John I. Capone. Technique for diamond machining large ZnSe grisms for the Rapid Infrared/Imager Spectrograph (RIMAS). In Ramón Navarro and James H. Burge, editors, *Advances in Optical and Mechanical Technologies for Telescopes and Instrumentation II*, volume 9912 of *Society of Photo-Optical Instrumentation Engineers (SPIE) Conference Series*, page 99120C, July 2016. doi: 10.1117/12.2231834.

[90] Winfried Posselt, Wolfgang Holota, Ernst Kulinyak, et al. NIRSpec: near-infrared spectrograph for the JWST. In John C. Mather, editor, *Optical, Infrared, and Millimeter Space Telescopes*, volume 5487 of *Society of Photo-Optical Instrumentation Engineers (SPIE) Conference Series*, pages 688–697, October 2004. doi: 10.1117/12.555659.

[91] Bongkon Moon, Weisong Wang, Chan Park, et al. Immersion grating mount design for IGRINS and GMTNIRS. In Ramón Navarro, Colin R. Cunningham, and Eric Prieto, editors, *Modern Technologies in Space- and Ground-based Telescopes and Instrumentation II*, volume 8450 of *Society of Photo-Optical Instrumentation Engineers (SPIE) Conference Series*, page 845048, September 2012. doi: 10.1117/12.925702.

[92] Yinxin Zhang, Wanzhuo Li, Wenhao Duan, et al. Echelle grating spectroscopic technology for high-resolution and broadband spectral measurement. *Applied Sciences*, 12(21), 2022. ISSN 2076-3417. doi: 10.3390/app122111042. URL https://www.mdpi.com/2076-3417/12/21/11042.

[93] Christopher Palmer. *Diffraction Grating Handbook*. MKS Instruments, Inc, Rochester, New York, 8 edition, 2020.

[94] Paul J. Kuzmenko, Steve L. Little, and Alexander S. Kutyrev. Machining a YJ band grism in ZnSe for the Rapid Infrared Imager Spectrograph (RIMAS): improvements in technique. In *Society of Photo-Optical Instrumentation Engineers (SPIE) Conference Series*, volume 11451 of *Society of Photo-Optical Instrumentation Engineers (SPIE) Conference Series*, page 114515B, December 2020. doi: 10.1117/12.2560578.

[95] Typical Spectra of Oriel Instruments Spectral Calibration Lamps, August 2012. URL https://www.newport.com/medias/sys_master/images/images/h55/hfd/8797293281310/Typical-Spectra-of-Spectral-Calib-Lamps.pdf.

[96] SpectralCalc.com. Spectral Calculator-Hi-resolution gas spectra, 2024. URL https://spectralcalc.com/blackbody_calculator/blackbody.php.

[97] Jillian Kunze. *Calibration and Data Simulation for RIMAS, the Rapid Infrared Imager - Spectrometer*. Bachelor's thesis, University of Maryland-College Park, 2020.

[98] J. Gordon Robertson. Quantifying Resolving Power in Astronomical Spectra. PASA, 30:e048, September 2013. doi: 10.1017/pasa.2013.26.

[99] Newport Corporation. UV Fused Silica Window, 2024. URL https://www.newport.com/f/uv-fused-silica-parallel-windows.

[100] Richard Pogge, Apr 2008. URL https://www.astronomy.ohio-state.edu/pogge.1/Ast161/Unit5/atmos.html.

[101] Wasatch Photonics. Transmission Gratings — VPH — Volume Phase Holographic Gratings, 2024. URL https://wasatchphotonics.com/product-category/gratings-and-diffractive-optics/.

[102] *Temperature Sensor SELECTION GUIDE*. Lake Shore Cryotronics, Inc., June 2017.

[103] *User's Manual Model 325 Temperature Controller*. Lake Shore Cryotronics, Inc., July 2017.

[104] *User's Manual Model 331 Temperature Controller*. Lake Shore Cryotronics, Inc., May 2009.

[105] *User's Manual Model 218 Temperature Monitor*. Lake Shore Cryotronics, Inc., July 2017.

[106] *User's Manual Model 336 Temperature Controller*. Lake Shore Cryotronics, Inc., July 2017.

[107] N. Minorsky. DIRECTIONAL STABILITY OF AUTOMATICALLY STEERED BODIES. *Journal of the American Society for Naval Engineers*, 34(2):280–309, 1922. doi: https://doi.org/10.1111/j.1559-3584.1922.tb04958.x. URL https://onlinelibrary.wiley.com/doi/abs/10.1111/j.1559-3584.1922.tb04958.x.

[108] Adafruit Si7021 Temperature & Humidity Sensor Breakout Board, May 2024. URL https://www.adafruit.com/product/3251.

[109] MicroPython pyboard lite v1.0, May 2024. URL https://store.micropython.org/product/PYBLITEv1.0.

[110] MicroPython language and implementation, May 2024. URL https://docs.micropython.org/en/latest/reference/index.html.

[111] Joe Durbak. joedurbak/htsensor: Initial release, 2024. URL https://zenodo.org/doi/10.5281/zenodo.11123662.

[112] *Air Temperature and Humidity Sensor - Data Sheet, Product Mode: S-TH-01*. seeed, 2011.

[113] *Compact FullRange™ Gauge - PKR 251*. Pfeiffer Vacuum, April 2004.

[114] *Kurt J. Lesker Company Ionization Gauge / Dual Convection With Integrated Controller & Display 392 Series Ionization Vacuum Gauge*. Kurt J. Lesker Company, 2011.

[115] *972B DualMag™ Vacuum Pressure Transducer Models with RS-232/RS-485, EtherCAT®, or Digital Display - Operation and Installation Manual*. MKS Instruments, Inc., February 2020.

[116] *5-port, 8-port and 16-port Gigabit Ethernet Unmanaged Switches*. NETGEAR, Inc., 2020.

[117] *USB 2.0 Icron Ranger® 2304*. Icron, 2022.

[118] design1st.com. CableEye Automation-Ready Cable & Harness Testers — Catalog, July 2024. URL https://www.design1st.com/Design-Resource-Library/engineering_data/ThermalEmissivityValues.pdf.

[119] CH-208R 10K CRYOCOOLER SERIES, Mar 2024. URL https://www.shicryogenics.com/product/ch-208r-10k-cryocooler-series.

[120] CryoTel GT, March 2024. URL https://www.sunpowerinc.com/products/stirling-cryocoolers/cryotel-cryocoolers/gt.

[121] R. A. Haefer. REVIEW ARTICLE: Cryogenic vacuum techniques. *Journal of Physics E Scientific Instruments*, 14(3):273–288, March 1981. doi: 10.1088/0022-3735/14/3/002.

[122] An Invitation To Receive GCN/TAN Notices and Circulars, Sep 2022. URL https://gcn.gsfc.nasa.gov/invitation.html.

[123] The GCN/TAN System, Oct 2017. URL https://gcn.gsfc.nasa.gov/gcn_describe.html#tc5.

[124] GCN: NASA's Time-Domain and Multimessenger Alert System, Mar 2024. URL https://gcn.nasa.gov.

[125] GCN Circulars, Mar 2024. URL https://gcn.nasa.gov/circulars.

[126] Jan 2024. URL https://gcn.gsfc.nasa.gov/GCN.gif.

[127] Joe Durbak. joedurbak/labview_gcn_monitor: v1.0.0-initial, 2024. URL https://zenodo.org/doi/10.5281/zenodo.10783621.

[128] Leo Singer. pygcn 1.1.3, Jul 2022. URL https://pypi.org/project/pygcn/.

[129] Brett M. Morris, Erik Tollerud, Brigitta Sipőcz, et al. astroplan: An Open Source Observation Planning Package in Python. AJ, 155(3):128, March 2018. doi: 10.3847/1538-3881/aaa47e.

[130] Albert M. Fowler and Ian Gatley. Noise reduction strategy for hybrid IR focal-plane arrays. In T. S. J. Jayadev, editor, *Infrared Sensors: Detectors, Electronics, and Signal Processing*, volume 1541 of *Society of Photo-Optical Instrumentation Engineers (SPIE) Conference Series*, pages 127–133, November 1991. doi: 10.1117/12.49326.

[131] NASA/IPAC. Spitzer: IRAC Instrument Handbook, 2024. URL `https://irsa.ipac.caltech.edu/data/SPITZER/docs/irac/iracinstrumenthandbook/images/IRAC_Instrument_Handbook021.png`.

[132] J. D. Offenberg, D. J. Fixsen, and J. C. Mather. Memory-Efficient Up-the-Ramp Processing with Cosmic-Ray Rejection. PASP, 117(827):94–103, January 2005. doi: 10.1086/427566.

[133] Markus Loose, Brian Smith, Greg Alkire, et al. The ACADIA ASIC: detector control and digitization for the Wide-Field Infrared Survey Telescope (WFIRST). In Andrew D. Holland and James Beletic, editors, *High Energy, Optical, and Infrared Detectors for Astronomy VIII*, volume 10709 of *Society of Photo-Optical Instrumentation Engineers (SPIE) Conference Series*, page 107090T, July 2018. doi: 10.1117/12.2313067.

[134] Jillian Kunze, Alexander Kutyrev, and Joseph Durbak. Exploration of the Calibration and Development of the Spectral Extraction Procedure for the Rapid IMAger - Spectrometer. In *American Astronomical Society Meeting Abstracts #233*, volume 233 of *American Astronomical Society Meeting Abstracts*, page 146.11, January 2019.

[135] Alexander Kramida and Yuri Ralchenko. NIST Atomic Spectra Database, NIST Standard Reference Database 78, 1999. URL `http://www.nist.gov/pml/data/asd.cfm`.

[136] K. Narahari Rao, Curtis J. Humphreys, and D. H. Rank. *Wavelength standards in the infrared*. Academic Press Inc., 1966.

[137] Michael C. Cushing, William D. Vacca, and John T. Rayner. Spextool: A Spectral Extraction Package for SpeX, a 0.8-5.5 Micron Cross-Dispersed Spectrograph. PASP, 116(818):362–376, April 2004. doi: 10.1086/382907.

[138] In-Soo Yuk, Daniel T. Jaffe, Stuart Barnes, et al. Preliminary design of IGRINS (Immersion GRating INfrared Spectrograph). In Ian S. McLean, Suzanne K. Ramsay, and Hideki Takami, editors, *Ground-based and Airborne Instrumentation for Astronomy III*, volume 7735 of *Society of Photo-Optical Instrumentation Engineers (SPIE) Conference Series*, page 77351M, July 2010. doi: 10.1117/12.856864.

[139] K. Horne. An optimal extraction algorithm for CCD spectroscopy. PASP, 98:609–617, June 1986. doi: 10.1086/131801.

[140] William D. Vacca, Michael C. Cushing, and John T. Rayner. A Method of Correcting Near-Infrared Spectra for Telluric Absorption. PASP, 115(805):389–409, March 2003. doi: 10.1086/346193.

[141] J. Xavier Prochaska, Joseph Hennawi, Ryan Cooke, et al. pypeit/PypeIt: Release 1.0.0, April 2020.

[142] Shepard A. Clough, Michael J. Iacono, and Jean-Luc Moncet. Line-by-Line Calculations of Atmospheric Fluxes and Cooling Rates: Application to Water Vapor. J. Geophys. Res., 97(D14):15,761–15,785, October 1992. doi: 10.1029/92JD01419.

[143] Julian Stürmer, Andreas Seifahrt, Zachary Robertson, et al. Echelle++, a Fast Generic Spectrum Simulator. PASP, 131(996):024502, February 2019. doi: 10.1088/1538-3873/aaec2e.

[144] Pieter G. van Dokkum. Cosmic-Ray Rejection by Laplacian Edge Detection. PASP, 113(789):1420–1427, November 2001. doi: 10.1086/323894.

[145] Perley, Daniel. autoastrometry.py - a fast astrometric solver, 2012. URL `https://sites.astro.caltech.edu/~dperley/programs/autoastrometry.py`.

[146] E. Bertin. Automatic Astrometric and Photometric Calibration with SCAMP. In C. Gabriel, C. Arviset, D. Ponz, and S. Enrique, editors, *Astronomical Data Analysis Software and Systems XV*, volume 351 of *Astronomical Society of the Pacific Conference Series*, page 112, July 2006.

[147] Jennifer C. Yee, Michael Albrow, Richard K. Barry, et al. NASA ExoPAG Study Analysis Group 11: Preparing for the WFIRST Microlensing Survey. *arXiv e-prints*, art. arXiv:1409.2759, September 2014. doi: 10.48550/arXiv.1409.2759.

[148] Markury Electronics. Multi-Purpose ASIC Control & Interface Electronics (MACIE) Hardware Manual Rev. 4.0, 2018.

[149] J. M. Durbak, A. S. Kutyrev, I. Andreoni, et al. GRB 221009A or Swift J1913.1+1946: PRIME near-infrared detection. *GRB Coordinates Network*, 32654:1, October 2022.

[150] Gokul P. Srinivasaragavan, Brendan O'Connor, S. Bradley Cenko, et al. A Sensitive Search for Supernova Emission Associated with the Extremely Energetic and Nearby GRB 221009A. ApJ, 949(2):L39, June 2023. doi: 10.3847/2041-8213/accf97.

[151] Andrew J. Levan, Benjamin P. Gompertz, Om Sharan Salafia, et al. Heavy-element production in a compact object merger observed by JWST. Nature, 626(8000):737–741, February 2024. doi: 10.1038/s41586-023-06759-1.

[152] Edmund Optics. Acktar Light Absorbent Foil. `https://www.edmundoptics.com/f/Acktar-Light-Absorbent-Foil/14802/`, 2019. [Online; accessed 28-March-2019].

[153] Maxime Rizzo, S. Rinehart, D. J. Benford, et al. The Balloon Experimental Twin Telescopes for Infrared Interferometry (BETTII): targets and calibration. In *American Astronomical Society Meeting Abstracts #223*, volume 223 of *American Astronomical Society Meeting Abstracts*, page 148.06, January 2014.

[154] ControlByWeb®. WebRelay-10 Plus™ — Industrial Grade Remote Control, Jun 2024. URL `https://controlbyweb.com/webrelay-10/`.

[155] Newport. Vacuum Compatible Picomotor™ Piezo Linear Actuators, Jun 2024. URL `https://www.newport.com/f/vacuum-picomotor-actuators`.

[156] Joe Durbak. joedurbak/asdetector-public: v1.0.0-initial, 2024. URL `https://zenodo.org/doi/10.5281/zenodo.13234066`.

[157] Python Software Foundation. ctypes - A foreign function library for Python, 2024. URL `https://docs.python.org/3/library/ctypes.html`.

[158] Eric Lyness. prime, 2024. URL `https://github.com/GSFC-PRIME/prime`.

[159] Ryusei Hamada and et. al. New nonlinearity correction method considering nonlinear dark currents. In *Society of Photo-Optical Instrumentation Engineers (SPIE) Conference Series*, volume 13096 of *Society of Photo-Optical Instrumentation Engineers (SPIE) Conference Series*, June 2024.

[160] Orion Guiffreda and Joseph Durbak. Oriohno/prime-photometry: Photometry pipeline for prime telescope, Jun 2024. URL `https://github.com/Oriohno/prime-photometry`.

[161] Dustin Lang, David W. Hogg, Keir Mierle, et al. Astrometry.net: Blind Astrometric Calibration of Arbitrary Astronomical Images. AJ, 139(5):1782–1800, May 2010. doi: 10.1088/0004-6256/139/5/1782.

[162] E. Bertin and S. Arnouts. SExtractor: Software for source extraction. A&AS, 117: 393–404, June 1996. doi: 10.1051/aas:1996164.

[163] Emmanuel Bertin. SWarp: Resampling and Co-adding FITS Images Together. Astrophysics Source Code Library, record ascl:1010.068, October 2010.

[164] Emmanuel Bertin. PSFEx: Point Spread Function Extractor. Astrophysics Source Code Library, record ascl:1301.001, January 2013.

[165] W. J. Zhang, X. Mao, W. D. Zhang, et al. Einstein Probe detected of a fast X-ray transient EP240315a. *GRB Coordinates Network*, 35931:1, March 2024.

[166] R. G. McMahon, M. Banerji, E. Gonzalez, et al. First Scientific Results from the VISTA Hemisphere Survey (VHS). *The Messenger*, 154:35–37, December 2013.

[167] Q. Y. Wu, A. Li, Y. Liu, et al. EP240518a: EP-WXT detection of a new X-ray transient. *GRB Coordinates Network*, 36512:1, May 2024.

[168] Joe Durbak. joedurbak/prime-gcn-monitor: v1.0.0, 2024. URL `https://zenodo.org/doi/10.5281/zenodo.13218706`.

[169] Michael W. Coughlin et al. Optimizing searches for electromagnetic counterparts of gravitational wave triggers. *Mon. Not. Roy. Astron. Soc.*, 478(1):692–702, 2018. doi: 10.1093/mnras/sty1066.

[170] O. Guiffreda, J. Durbak, A. S. Kutyrev, et al. GRB240122A: PRIME near infrared detection. *GRB Coordinates Network*, 35633:1, January 2024.

[171] O. Guiffreda, J. Durbak, A. S. Kutyrev, et al. GRB 240205B: PRIME near infrared detection. *GRB Coordinates Network*, 35708:1, February 2024.

[172] O. Guiffreda, K. De, J. Durbak, et al. PRIME discovery of a likely fading near-infrared counterpart to SRGA J144459.2-604207. *The Astronomer's Telegram*, 16499:1, March 2024.

[173] O. Guiffreda, J. Durbak, A. S. Kutyrev, et al. X-ray transient EP240315a: PRIME near infrared detection. *GRB Coordinates Network*, 35956:1, March 2024.

[174] O. Guiffreda, J. Durbak, E. Troja, et al. LIGO/Virgo/KAGRA S240422ed: PRIME near-infrared observations. *GRB Coordinates Network*, 36306:1, April 2024.

[175] O. Guiffreda, J. Durbak, A. S. Kutyrev, et al. X-ray Transient EP240807a: PRIME near-infrared upper limits. *GRB Coordinates Network*, 37118:1, August 2024.

[176] O. Guiffreda, J. Durbak, A. S. Kutyrev, et al. EP240807a: PRIME H-band upper limits. *GRB Coordinates Network*, 37153:1, August 2024.

[177] O. Guiffreda, S. Atri, J. Durbak, et al. EP240816a: PRIME upper limits. *GRB Coordinates Network*, 37212:1, August 2024.

[178] S. "U. Rome" Atri, J. Durbak, O. Guiffreda, et al. EP240820a: PRIME J-band Observations. *GRB Coordinates Network*, 37250:1, August 2024.

[179] J. Durbak, E. Troja, S. "U. Rome" Atri, et al. GRB 240821A: PRIME near-infrared observations. *GRB Coordinates Network*, 37323:1, August 2024.

[180] O. Guiffreda, J. Durbak, S. Atri, et al. GRB 240825A: PRIME near-infrared detection. *GRB Coordinates Network*, 37303:1, August 2024.

[181] J. Durbak, O. Guiffreda, S. Atri, et al. GRB 241002B: PRIME near-infrared detection. *GRB Coordinates Network*, 37700:1, October 2024.

[182] J. Durbak, O. Guiffreda, S. Atri, et al. GRB 241002B: PRIME near-infrared detection in 2nd epoch. *GRB Coordinates Network*, 37712:1, October 2024.

[183] O. Guiffreda, J. Durbak, S. Atri, et al. GRB 241002B: PRIME near-infrared detection in 3rd epoch. *GRB Coordinates Network*, 37736:1, October 2024.

[184] J. Durbak, O. Guiffreda, S. Atri, et al. GRB 241006A: PRIME near-infrared upper limits. *GRB Coordinates Network*, 37730:1, October 2024.

[185] J. Durbak, O. Guiffreda, S. Atri, et al. GRB 241105a: PRIME near-infrared upper limits. *GRB Coordinates Network*, 38121:1, November 2024.

[186] J. Durbak, O. Guiffreda, A. S. Kutyrev, et al. GRB 241113A: PRIME near-infrared upper limits. *GRB Coordinates Network*, 38227:1, November 2024.

[187] J. Durbak, O. Guiffreda, A. S. Kutyrev, et al. GRB 241115a: PRIME near-infrared upper limits. *GRB Coordinates Network*, 38274:1, November 2024.

[188] J. Durbak, E. Troja, O. Guiffreda, et al. GRB 241127A: PRIME near-infrared detection. *GRB Coordinates Network*, 38384:1, November 2024.

[189] Philip Massey, E. W. Dunham, T. A. Bida, et al. As Big and As Good As It Gets: The Large Monolithic Imager for Lowell Observatory's 4.3-m Discovery Channel Telescope. In *American Astronomical Society Meeting Abstracts #221*, volume 221 of *American Astronomical Society Meeting Abstracts*, page 345.02, January 2013.

[190] P. Gatkine, S. Veilleux, D. Perley, et al. Outflow-Galaxy Connection at z = 2-6 using GRB hosts. In *American Astronomical Society Meeting Abstracts*, volume 237 of *American Astronomical Society Meeting Abstracts*, page 308.04, January 2021.

[191] Pradip Gatkine, Sylvain Veilleux, Daniel Perley, et al. The CGM-GRB Study. II. Outflow-Galaxy Connection at z 2-6. ApJ, 926(1):63, February 2022. doi: 10.3847/1538-4357/ac408e.

[192] B. O'Connor, E. Troja, S. Dichiara, et al. A deep survey of short GRB host galaxies over z 0-2: implications for offsets, redshifts, and environments. MNRAS, 515(4): 4890–4928, October 2022. doi: 10.1093/mnras/stac1982.

[193] S. Dichiara, P. Gatkine, J. M. Durbak, et al. GRB 190106A: Discovery Channel Telescope observations. *GRB Coordinates Network*, 23744:1, January 2019.

[194] S. Dichiara, P. Gatkine, J. M. Durbak, et al. GRB 190627A: Discovery Channel Telescope late time observations. *GRB Coordinates Network*, 24986:1, July 2019.

[195] S. Dichiara, P. Gatkine, J. Durbak, et al. GRB 200729A: Lowell Discovery Telescope observations. *GRB Coordinates Network*, 28270:1, August 2020.

[196] S. Dichiara, S. B. Cenko, E. Troja, et al. GRB 200826A: Lowell Discovery Telescope observations of ZTF20abwysqy. *GRB Coordinates Network*, 28312:1, August 2020.

[197] S. Dichiara, S. B. Cenko, E. Troja, et al. GRB 201006A: Lowell Discovery Telescope upper limits. *GRB Coordinates Network*, 28572:1, October 2020.

[198] S. Dichiara, S. B. Cenko, E. Troja, et al. GRB 201014A: Lowell Discovery Telescope afterglow imaging. *GRB Coordinates Network*, 28654:1, October 2020.

[199] S. Dichiara, E. Troja, P. Gatkine, et al. GRB 201214B: Lowell Discovery Telescope optical observations. *GRB Coordinates Network*, 29054:1, December 2020.

[200] S. Dichiara, E. Troja, S. B. Cenko, et al. GRB 201221D: Lowell Discovery Telescope afterglow observations. *GRB Coordinates Network*, 29128:1, December 2020.

[201] B. O'Connor, S. Dichiara, E. Troja, et al. GRB 210504A: Lowell Discovery Telescope optical observations. *GRB Coordinates Network*, 29946:1, May 2021.

[202] B. O'Connor, S. Dichiara, E. Troja, et al. Lowell Discovery Telescope Observations of ZTF21aayokph (AT2021lfa). *GRB Coordinates Network*, 29952:1, May 2021.

[203] B. O'Connor, E. Troja, E. Zack, et al. GRB 210704A: Lowell Discovery Telescope Optical Observations. *GRB Coordinates Network*, 30451:1, July 2021.

[204] A. Gottlieb, S. Dichiara, S. B. Cenko, et al. GRB 210919A: Lowell Discovery Telescope upper limits (correction to GCN 30859). *GRB Coordinates Network*, 30860:1, September 2021.

[205] B. O'Connor, S. B. Cenko, E. Troja, et al. GRB 221009A: Lowell Discovery Telescope Afterglow Detection. *GRB Coordinates Network*, 32739:1, October 2022.

[206] B. O'Connor, S. B. Cenko, E. Troja, et al. GRB 221009A: Continued LDT Afterglow Monitoring. *GRB Coordinates Network*, 32799:1, October 2022.

[207] B. O'Connor, I. Andreoni, S. B. Cenko, et al. GRB 221120A: LDT Optical Afterglow Candidate. *GRB Coordinates Network*, 32957:1, November 2022.

[208] B. O'Connor, E. Hammerstein, S. B. Cenko, et al. GRB 230204B: Lowell Discovery Telescope Observations. *GRB Coordinates Network*, 33333:1, February 2023.

[209] B. O'Connor, E. Hammerstein, S. B. Cenko, et al. GRB 230205A: Lowell Discovery Telescope Observations. *GRB Coordinates Network*, 33334:1, February 2023.

[210] I. Andreoni, G. Srinivasaragavan, B. O'Connor, et al. GRB 231117A: Lowell Discovery Telescope Observations. *GRB Coordinates Network*, 35099:1, November 2023.

[211] B. O'Connor, I. Andreoni, G. Srinivasaragavan, et al. GRB 231117A: LDT Confirmation of Optical Fading. *GRB Coordinates Network*, 35139:1, November 2023.

[212] B. P. Abbott, R. Abbott, T. D. Abbott, et al. Tests of General Relativity with GW150914. Phys. Rev. Lett., 116(22):221101, May 2016. doi: 10.1103/PhysRevLett.116.221101.

[213] Matthew Graham and Zwicky Transient Facility (ZTF) Project Team. The Zwicky Transient Facility: Overview and Commissioning Activities. In *American Astronomical Society Meeting Abstracts #231*, volume 231 of *American Astronomical Society Meeting Abstracts*, page 354.16, January 2018.

[214] S. Dichiara, P. Gatkine, J. Durbak, et al. LIGO/Virgo S190425z: DCT ZTF19aarykkb spectroscopy. *GRB Coordinates Network*, 24220:1, January 2019.

[215] S. Dichiara, E. Troja, S. B. Cenko, et al. LIGO/Virgo S190814bv: No candidates from DCT galaxy targeted search and observations of DECam-GROWTH candidates. *GRB Coordinates Network*, 25374:1, August 2019.

[216] S. Dichiara, E. Troja, S. B. Cenko, et al. LIGO/Virgo S190814bv: No candidates from image subtraction in DCT galaxy targeted search. *GRB Coordinates Network*, 25397:1, August 2019.

[217] A. L. Thakur, S. Dichiara, E. Troja, et al. A search for optical and near-infrared counterparts of the compact binary merger GW190814. MNRAS, 499(3):3868–3883, December 2020. doi: 10.1093/mnras/staa2798.